Emission line properties of type-2 AGN in the Lockman-SpReSo survey

A Thesis Submitted to the
Office of Postgraduate Programme of
Space Science and Geospatial Institute,
Entoto Observatory and Research Center,
Department of Astronomy and Astrophysics,
in affiliation with Addis Ababa University

By

Bereket Assefa Moltote

In partial fulfillment of the degree of Master of Science in
Astronomy and Astrophysics

September 2024
Addis Ababa, Ethiopia

Emission line properties of type-2 AGN in the Lockman-SpReSo survey

By

Bereket Assefa

Dr. Mirjana Povic

Main Supervisor

September, 2024

We the undersigned committee hereby approved that we have read and recommended to the office of graduate program for acceptance of thesis entitled "**Emission line properties of type-2 AGN in the Lockman-SpReSo survey**" by **Bereket Assefa** in partial fulfillment for the requirements for the degree of **Masters in Astronomy and Astrophysics.**

Approved by

_____	_____
Chair Person	
_____	_____
External Examiner	
_____	_____
Internal Examiner	
_____	_____
Main Supervisor	
_____	_____
Director General	

Date of approval: **September 9, 2024**

Author's Declaration

I hereby declare that this study is original and has not been submitted for any other degree award to any other University. It is a true copy of the thesis, including any required final revisions, as accepted by my examiners. Permission is herewith granted to Entoto Observatory and Research Center, Space Science and Geospatial Institute, affiliated with Addis Ababa University to circulate and to have copied for non-commercial purposes, at its discretion, the above title upon the request of individuals or institutions.

_____

Author's Signature

_____

Date

Table of Contents

Abstract

Active galactic nuclei (AGN) are some of the brightest sources in the Universe, emitting light at all wavelengths due to their complex structure. Deep multiwavelength extragalactic surveys are therefore crucial for understanding the full physics of AGN and their role in the formation and evolution of galaxies. The Lockman-SpReSo survey is one of the deepest multiwavelength spectroscopic surveys in the far-infrared (FIR). It is a unique sample of AGN with deep FIR and optical spectroscopic data obtained using Herschel and Gran Telescopio de Canarias (GTC) 10 m telescopes, respectively. This research investigates the spectroscopic properties of FIR-selected type-2 AGN detected in the Lockman Hole field using the Lockman-SpeRSo survey. We identified and measured various emission lines, including Balmer lines, forbidden lines, and some UV lines. Our analysis revealed that FIR-detected type-2 AGN exhibits similar strongest emission lines to optically-selected AGN. We constructed a comprehensive catalogue of emission line measurements for 71 sources, which will be made publicly available. We found correlations between emission line luminosities and AGN luminosity, SFR, and IR luminosity, suggesting connections between the AGN, surrounding gas, star formation, and dust properties. Additionally, we observed higher luminosities in FIR-detected AGN compared to optically-selected sources from SDSS DR8.

Keywords: Active galaxies, Multi-wavelength data, Lockman-SpReSo survey, Optical spectroscopic data, FIR emitters

Acknowledgements

First and foremost, I would like to thank my heavenly father for everything he has done in my life and giving me courage during all my studies in the second place I want to thank my family and my husband for being supportive throughout my study. It was an honor to have Dr. Mirjana Povic as a supervisor to my thesis. From the beginning to the end, her constant support and wise counsel were key to developing our project in a good way. Her in-depth knowledge of the subject was extremely helpful as I worked my way through the research process. She was very kind and courageous throughout my difficult data analysis, and I thank her for her assistance amid my difficulties. I also want to thank the Lockman team for assisting me in getting the data and providing guidance.

Acronyms

List of Abbreviations

ADAF	Advection-dominated accretion flow
AGN	Active Galactic Nuclei
BC	Blue cloud
BH	Black hole
BLR	Broad line region
BLRG	Broad line radio galaxies
BTP	Baldwin-Phillips-Terlevich
CAS	Concentration, Asymmetry, Smoothness
CIB	Cosmic infrared background
CMD	Color-magnitude diagram
CNN	Conventional neural network
COSMOS	Cosmic Evolution Survey
DSFGs	Dusty star-forming galaxies
ET	Early-type
EW	Equivalent width
FMR	Fundamental metallicity relation
FRI	Fanaroff and Riley class I
FRII	Fanaroff and Riley class II
FSRQs	Flat spectrum radio quasars
FWHM	Full Width Half Maximum
GTC	Gran Telescopio de Canarias
GV	Green valley
HST	Hubble Space Telescope
IA-UNAM	Instituto de Astronomıa of the Universidad Nacional Autonoma de Mexico
IFS	Integral field spectroscopy
IR	Infrared
IRAC	Infrared Array Camera
IRAF	Image Reduction and Analysis Facility
IRAS	The Infrared Astronomical Satellite
ISM	Interstellar medium
ISO	Infrared Space Observatory
JWST	James Webb Space Telescope
LD	Luminosity distance
LINERs	Low-Ionization Nuclear Emission Line Regions
LMFIT	Non-Linear Least-Squares Fitting
LOFAR	LOw-Frequency ARray
LT	Late-type

MHD	Magnetohydrodynamics
MIPS	Multi-band Imaging Photometer
MOS	Multi-object spectroscopy
MS	Main sequence
MZR	Mass-metallicity relation
NLR	Narrow line region
NLRG	Narrow-line radio galaxies
NOAO	National Optical Astronomy Observatory
OVV	Optically violent variable
PACS	Photodetector Array Camera and Spectrometer
QSO	Quasars
QSQ	Radio-quiet quasars
RLQ	Radio-loud quasars
RS	Red sequence
SDSS	Sloan Digital Sky Survey
SED	Spectral energy distribution
SF	Star formation
SFH	Star formation history
SFR	Star formation rate
SMBH	Supermassive black hole
SMG	Submillimeter galaxy
S/N	signal-to-noise ratio (S/N)
SPIRE	Spectral and Photometric Imaging Receiver
SPLAT	Spectral Analysis Tool
sSFR	Specific star formation rate
SSP	Stellar synthesis population analysis
TOPCAT	Tool for Operations on Catalogs And Tables
UV	Ultraviolet
VO	Virtual Observatory
WHT	William Herschel Telescope
WISE	Wide-field Infrared Survey Explorer

Constants

Ω_Λ **(0.7)**	Normalised cosmological constant
Ω_m **(0.3)**	Density ratio of the universe
H_0 **(70 kms^{-1}Mpc^{-1})**	Hubble constant

List of Figures

List of Tables

Publications, proceedings, and presentations

The paper is in preparation and will be submitted to the Astronomy and Astrophysics (A&A) journal for review shortly after the thesis defense, in collaboration with the entire Lockman-SpReSo survey team.

International and national presentations related to this MSc work

- We have gained an opportunity to present this work at the 4th annual African Astronomical Society (AfAS) Conference in Marrakech, Morocco, April 15-20, 2024, as an oral contribution. Secondly, we also gained the opportunity to present our work at the ”AGN Populations Across Continents and Cosmic Time” conference at Durham University in the UK, from July 8-12, 2024. At this conference, we gave a poster presentation and a ”sparkle” talk. Additionally, we gained another opportunity to have a poster presentation at the XXXII IAU GA 2024 in South Africa from August 6-15, 2024.

Chapter 1

Introduction

1.1 Background

Compact sources in centers of galaxies with significant accreting supermassive black holes (SMBH) with masses above $10^6 M_\odot$ and large luminosity (e.g., above $10^{42} erg/sec$) across all electromagnetic spectrum referred to as active galactic nuclei (AGN). Galaxies hosting an AGN are known as active galaxies, they are characterized by their large nuclear activity. AGN are crucial to the evolution of galaxies. The co-evolution of the AGN and host galaxy is driven by the SMBH feeding mechanism(s) and AGN feedback (e.g., Xu et al., 2003; Peterson, 2006; Tadhunter, 2008; Meléndez et al., 2008; Ho, 2008; Schawinski et al., 2014; Netzer, 2015; Mickaelian, 2015; Padovani et al., 2017; Blandford et al., 2019; Mahoro et al., 2019; Mountrichas et al., 2021).

There are two classes of AGN based on optical emission line characteristics, type-1 and type-2 AGN. Type-1 AGN are characterized by the broad component in their emission lines (beside the narrow component) coming from the broad line region (BLR) (Peterson, 2006). On the other side, type-2 AGN emission comes from the narrow line region (NLR), while the BLR emission is blocked by a dusty torus (e.g., Sulentic et al., 2000; Tadhunter, 2008; Ho, 2008; Schawinski et al., 2014; Netzer, 2015; Mickaelian, 2015; Padovani et al., 2017; Blandford et al., 2019; Nour, 2023). To understand the physical processes of AGN it is necessary to use multiwavelength data with well-defined source samples. Numerous studies are pointing out the importance of deep multiwavelength extragalactic surveys for studying galaxy formation and evolution (e.g., Heckman & Best, 2014), AGN properties, including the ongoing changing look of AGN (Ajay et al., 2022), AGN activity in post-merger remnants (e.g., Li et al., 2023), and the interplay between AGN and star formation (e.g., Pović et al., 2016; Mahoro et al., 2017, 2019).

Many of the unsolved questions in galaxy evolution are related to AGN studies. Further AGN studies are crucial for answering some of the still open questions about AGN, including: what is the impact of AGN on their host galaxies?, what is the origin of the accretion material?, the triggering mechanisms of AGN?, and what is the length of the active phase in galaxies?, among others AGN emit strong radiation at all wavelengths due to their complex structure (e.g., Kuraszkiewicz et al., 2004; Schneider, 2006; Netzer, 2015; Padovani et al., 2017; Blandford et al., 2019).

The Lockman-SpReSo is one of the deepest, multiwavelength spectroscopic surveys in optical of far infrared (FIR) selected galaxies. It aims to provide one of the most extensive optical spectral follow-ups of the FIR sources observed by Herschel Space Observatory. FIR sources were selected from Herschel observations of Lockman Hole field with an optical counterpart. The collection consists of 956 Herschel FIR sources and an additional 188 field objects. These

include optical equivalents of sub-millimeter galaxies as well as point X-ray sources, variable star candidates, high-velocity halo star candidates, radio sources, and extremely red quasi-stellar objects. The OSIRIS instrument on the 10.4 m Gran Telescopio de Canarias (GTC) was used in multi-object spectroscopy (MOS) mode. Two multi-fibre spectrographs, the AF2-WYFFOS at the William Herschel Telescope (WHT) and the HYDRA instrument at the WIYN telescope, were used to observe the bright component. Lockman-SpReSO observations, carried out from 2014 to 2018, were completed, and all data have been properly reduced and calibrated. From the analysis of the spectroscopic data, a total of 357 objects' spectroscopic redshifts, ranging from $z_{spec} = 0.0290$ to $z_{spec} = 4.9671$, have been determined, while for other sources, photometric redshifts have been measured. From SED-fitting the IR luminosity and the stellar masses of the sources were derived (Gonzalez-Otero et al., 2023). Using this survey, it is possible to study the relationship between fundamental FIR and optical properties, such as extinction, star formation rate (SFR), and gas metallicity.

In this work, we want to go a step further and better understand the properties of FIR type-2 AGN in the Lockman-SpReSo survey and, in particular, their spectroscopic properties in optical. This is a unique sample of AGN with deep FIR and optical spectroscopic data. We will first obtain the emission spectra of AGN by running the Starlight code[1] (e.g., Cid Fernandes et al., 2005, and references therein) and by subtracting the continuum plus absorption spectra. Using the strong emission lines, we will measure the line intensity, full width at half maximum (FWHM) and the equivalent width (EW) of all identified emission lines. We will provide for the first time a catalog of type-2 AGN in the Lockman-SpReSo survey.

1.2 Motivation

Type-2 AGN are obscured by dust. Studying their emission lines in the FIR is a useful technique for both their detection and better understanding of their properties, and study the correlation between there FIR and optical properties. This provides new possibilities for investigating the accretion disk and the hidden mechanism powering the AGN luminosity. Understanding the intricate processes taking place in the host galaxy is largely dependent on FIR observations.

Through examination of the FIR signature, we are able to differentiate between the energy output originating from the AGN and the input originating from active star formation inside the dusty galactic environment. This makes easier to comprehend how the strong radiation from AGN stimulate the formation of new stars and may cause a starburst event. Analyzing type-2 AGN help us understand more about the effects of these intense stages on galaxy formation and evolution. The FIR emission itself is affected by the properties of the surrounding dust. By analyzing the spectrum and intensity of the FIR emission, we can learn more about the composition, temperature distribution, and total mass of the dust surrounding the AGN. This, in combination with the optical emission lines from the NLR, can give us a complete characterisation of type-2 AGN properties.

1.3 Objectives

1.3.1 General objective

The main objective of this research is to characterize the emission line properties of type-2 AGN in the Lockman-SpReSo survey, to construct the catalogue with measured spectroscopic

[1] http://www.starlight.ufsc.br/

properties, to better understand the correlation between optical and FIR properties of type-2 AGN.

1.3.2 Specific objectives

In order to achieve the main objective, the following specific objectives are set:

- To obtain the emission line spectra of all identified AGN in the Lockman-SpReSo survey.
- To determine the line intensity, FWHM, and EW of all identified emission lines in type-2 AGN spectra.
- To construct a catalogue of type-2 AGN in the Lockman-SpReSo survey, to be made publicly available.
- To find a correlation between the emission line properties with other galaxy properties such as SFR, AGN luminosity, and FIR properties.
- To compare between FIR- and optically-selected type-2 AGN.

1.4 Significance of the work

This study will create the first catalogue of type-2 AGN in the Lockman-SpReSo survey, featuring the latest FIR and optical spectroscopic data, including emission line measurements and derived parameters. The public catalogue will support various AGN studies, such as investigations into the NLR and dusty torus. This work is significant for its use of new, high-quality data with a high signal-to-noise ratio in both FIR and optical wavelengths.

1.5 Organisation of the thesis

This thesis is structured as follows: in chapter 1, the general overview, objectives of the study, and the significance of the work are described. In chapter 2, we provide the literature review about the general properties of galaxies and general properties of AGN and active galaxies, including the properties of type-2 AGN. Data and methodology, used are explained in chapter 3 and 4 respectively, whereas chapter 5, summarises the analysis carried out. The main results are described and discussed in chapter 6, while chapter 7 gives summary of the work carried out and future plans.

Chapter 2

Literature Review

2.1 General properties of galaxies

2.1.1 Morphology of galaxies

Hubble tuning fork is one of the earliest and most used galaxy classification systems (Hubble, 1926, 1936). Morphological classifications of galaxies help us to understand galaxy formation, star formation activity, presence and fraction of interactions and mergers, dynamical and chemical evolution of galaxies, etc. (e.g., Conselice et al., 2000; Kelly, 2004; Wijesinghe et al., 2010; Buta, 2013; Conselice, 2014; Cavanagh et al., 2021; Kartaltepe et al., 2023).

Depending on how they appear in optical light, there are 4 principal types, grouped into 2 broad types (Hubble, 1926, 1936), late-type (LT) and early-type (ET) galaxies. LT galaxies contain a younger stellar population and include spiral and irregular galaxies, while ET include mainly elliptical and lenticular galaxies, being dominated by older stellar populations and small amounts of gas and dust (e.g., Pović et al., 2013; Schawinski et al., 2014; Mahoro et al., 2022). These two major categories link the morphology of galaxies to many stellar and structural characteristics (e.g., Khosroshahi et al., 2000; Lee et al., 2010; Schawinski et al., 2014; Mahoro et al., 2019; Cheng et al., 2021; Kartaltepe et al., 2023). Figure 2.1 shows Hubble classification into elliptical, lenticular, spiral, and irregular galaxies. In the continuation, we describe briefly each of the morplogical types of galaxies.

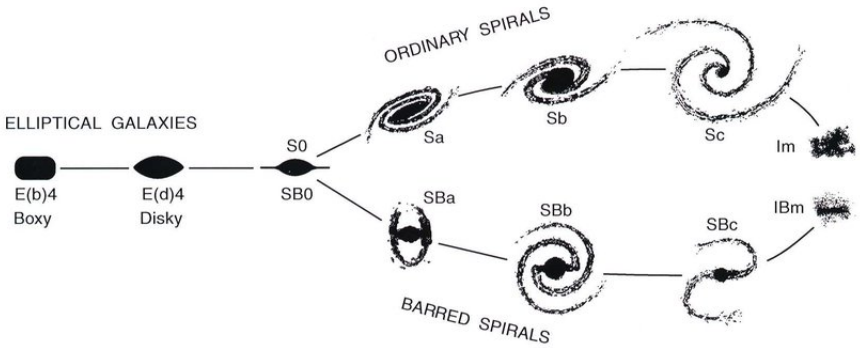

Figure 2.1: Revision of Hubble's 1936 morphological classification scheme. Credit: Kormendy, 1996.

Elliptical galaxies

Elliptical galaxies are the oldest galaxies with high metallicity and a low rate of new star formation (e.g., Trager et al., 2000; Khochfar, 2005; Lee et al., 2010; Pollo, 2015). They are characterised by a large central bulge, weak or non-existent disc, lack of spiral arms and nuclear bars, absence of open stellar clusters[1] and the existence of globular clusters[2] in both the halo and the bulge, they are characterized by a huge central bulge, weak or non-existent disc, lack of spiral arms, and nuclear bars (e.g., Khosroshahi et al., 2000; Conselice, 2006; Lee et al., 2010; Schawinski et al., 2014; Conselice, 2014; Cheng et al., 2021; Kartaltepe et al., 2023, and references therein). The primary explanation for the formation of elliptical galaxies is the morphological alteration of spiral galaxies through major mergers (Lacerna et al., 2020; Pfeffer et al., 2023; Li et al., 2023). Figure 2.2 shows elliptical galaxies with different elliptical classification. In the Hubble classification system, the most spherical galaxies are designated E0, and the flattest, E7 (Buta, 2013; Pollo, 2015), using En as:

$$E_n = \frac{(10(a-b))}{a}, \tag{2.1}$$

where a and b are the projected major and minor axes, respectively.

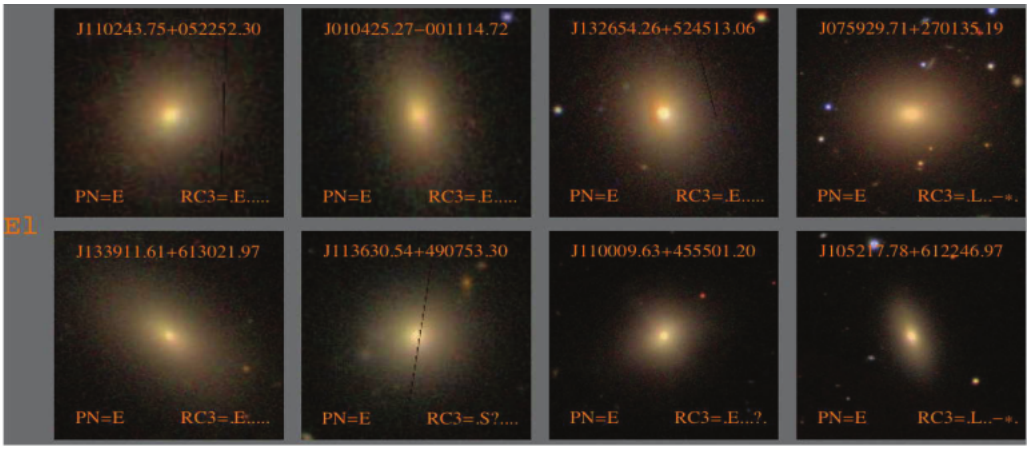

Figure 2.2: Example of different types of eliptical galaxies. Credit: Nair & Abraham, 2010.

Lenticular galaxies (S0)

Lenticular galaxies (S0) are intermediate type between elliptical and spiral galaxies. They contain a large-scale disc but do not have a large-scale spiral arm, sometimes called, armless spiral galaxies (e.g., Buta, 2013; Pollo, 2015; Saha, 2018; Sil'chenko et al., 2019; Ge et al., 2020; Rathore et al., 2022; Xu et al., 2022). Lenticular galaxies are a disc galaxies that have used up or lost most of their interstellar matter and have very little ongoing star formation. Galaxy mergers, both major and minor, have been shown to produce S0 galaxies, although there formation are still not fully understand. Even so many characteristics of S0s, including their structure, dynamics, and scaling relations, are explained via mergers (e.g., Ge et al., 2020; Pfeffer et al., 2023). Figure 2.3, shows different examples of nearby lenticular galaxies.

[1] Open stellar clusters are clusters of young clusters of stars, and locations of new star formation.
[2] Globular clusters are old clusters of stars that have remained in a gravitationally bound system.

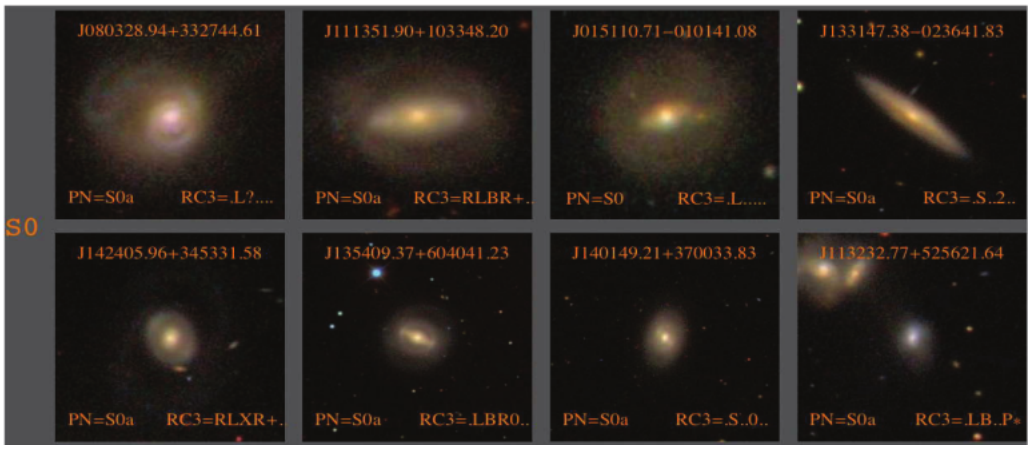

Figure 2.3: Example of lenticular galaxies. Credit: Nair & Abraham, 2010.

Spiral galaxies

Spiral galaxies are characterized by a bright bulge at the center and a compressed disk containing spiral arms. They have three main components: bulge, disk, and halo (e.g., Conselice et al., 2000; Kelly, 2004; Wijesinghe et al., 2010; Buta, 2013; Conselice, 2014; Shen, 2020; Cavanagh et al., 2021; Pak et al., 2021; Kartaltepe et al., 2023). Another characteristic of spiral galaxies is a predominance of blue light, which (if not an AGN) may indicate an active star formation consequently, the galaxy's age (Schawinski et al., 2014). Based on the presence of nuclear bars spiral galaxies have two principal groups: normal spirals (SA) and barred spirals (SB) (Conselice, 2014). The normal spiral has three classes. **Type 'a' (Sa)** are characterised by huge bright central bulge with a spiral arm which are strongly tightened, **type 'b' (Sb)** are characterised by a moderate nuclear bulge and a moderately wound spiral arm, while **type 'c' (Sc)** are characterised by a smaller central bulge and highly loose wound spiral arms (e.g., Wijesinghe et al., 2010; Buta, 2013). A barred spiral galaxy is a type of spiral galaxy which have a bar-like pattern of stars crossing the center. Some classes of barred spirals are: **type 'a' (SBa)**, galaxies with large central bulges and tightly wound spiral arms with bar-like patterns, **type 'b' (SBb)**, galaxies with moderate central bulge and a moderately wound spiral arms with a bar-like pattern, **type 'c' (SBc)**, galaxies with smaller central bulge and loosly wound spiral arms with bar-like pattern (e.g., Schneider, 2006; Wijesinghe et al., 2010; Buta, 2013; Pollo, 2015). Finally, the intermediate types of spiral galaxies also exist, SAB, with some indications (but not clear presence) of nuclear bars and with the same sub-classes as explained above. In addition, **'Sd'** and **'Sm'** sub-classes of spiral galaxies also exist as the boundary between spiral and irregular galaxies, and the intermediate sub-classes between Sa and Sb (Sab), Sb and Sc (Sbc), Sc and Sd (Scd), and Sd and Sm (sdm). Figure 2.4 shows the classification of spiral galaxies.

Irregular galaxies (Irr)

Irregular galaxies are unique and don't have enough structure (e.g., clear central bulge and/or disc and spiral arms) to be classifed into any of the above types (Buta, 2013). Irregular galaxies contain a large amount of gas and dust. Many new stars are born in a short period of time, they have young stellar populations and open stellar clusters (Pollo, 2015). There are 3 types of irregular galaxies: **Irr-I**, galaxies which have some structure, but they aren't aligned clearly with the Hubble classification scheme, **Irr-II**, galaxies which don't have any structure and may have been disrupted, and **dwarf irregular galaxies (dirr)** which are similar to the previous two types, but with much smaller sizes, masses, brightness, and numbers of stars (Conselice, 2006). Figure

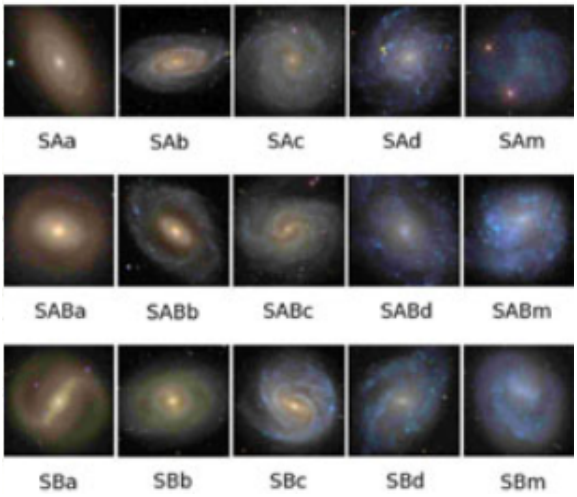

Figure 2.4: Example of different types of spiral galaxies. Credit: Buta, 2013.

2.5 shows an example of different types of irregular galaxies.

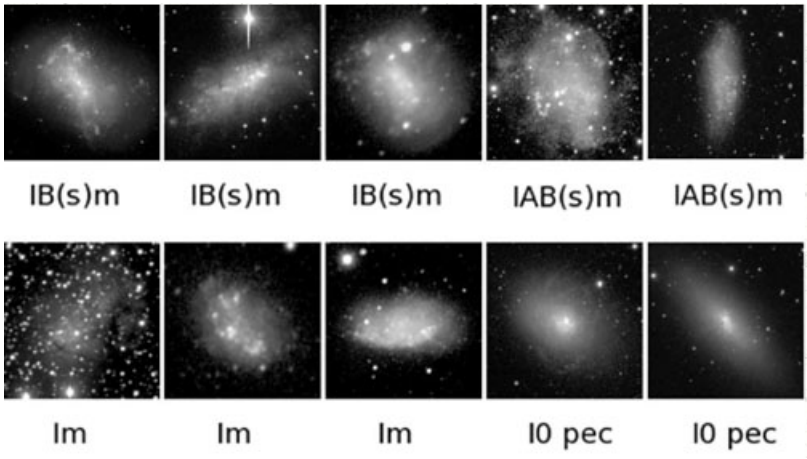

Figure 2.5: Example of irregular galaxies. Credit: Buta, 2013.

Peculiar galaxies

Peculiar galaxies are galaxies that have larger gas content than typical galaxies with normally strong star formation, the nuclear region is dominated by intermediate and old stellar populations, and they are commonly interacting galaxies, distorted by tidal effects (e.g., Casasola et al., 2004; Wenderoth et al., 2022). These galaxies vary greatly, sometimes they are so blue that any underlying old population is entirely dominated by newly formed stars, and other times they are so red that much of the activity must be obscured by dust clouds. These galaxies are uncommon, but they are particularly interesting because some of them might be undergoing the kinds of transformations and rapid star formation that characterized typical galaxies in their early stages of formation (Wenderoth et al., 2022). Low surface brightness galaxies, starburst and post-starburst galaxies, nucleus-dominated N-type galaxies, cD galaxies (supermassive elliptical galaxies surrounded by stellar halos, seen in the nuclei of huge clusters), and a whole zoo of galaxies whose spectra are dominated by radiation from wavelength ranges other than the optical are also among the peculiar galaxy type (Pollo, 2015). Figure 2.6 shows some examples of peculiar galaxies.

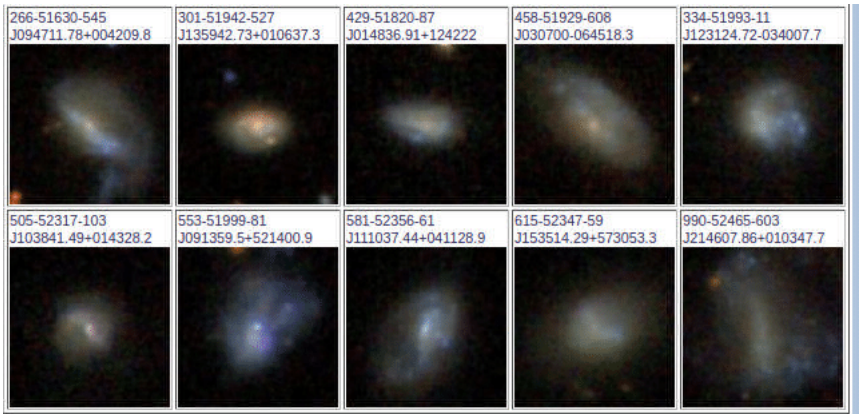

Figure 2.6: Example of peculiar galaxies. Credit: Getachew-Woreta et al., 2022.

2.1.2 Methods of morphological classification

There are different methods of morphological classification of galaxies, such as visual inspection, parametric, non-parametric method, and machine learning.

Visual inspection classifies galaxies, traditionally by visual inspection of photometric images. One example is the Galaxy Zoo[3] project, designed initially for classifying nearly one million galaxies in the Sloan Digital Sky Survey (SDSS) through an online interface enabling the separation of galaxies into elliptical, spiral, or unclassified. This method is limited for high redshift galaxies, and for large survey data, in addition, it is subjective and time-consuming (e.g., Kelly, 2004; Lintott et al., 2008, 2011; Pović et al., 2013; Willett et al., 2013; Conselice, 2014; Mahoro et al., 2019; Cavanagh et al., 2021; Cheng et al., 2021).

Parametric classification is characterising a galaxy by simulating the light using a predetermined analytical model such as, e.g., Sersic function (e.g., Sersic, 1968; Baes, 2011). By fitting the galaxy with a two-component profile, the free parameters can be calculated, such as the bulge, disk components and bulge-to-disk (B/D) or bulge-to-total (B/T) light ratios, which correlate with qualitative Hubble-type classifications. However, both one-component and multiple-component fitting methods fail for irregular, tidally perturbed, and merging galaxies. In addition, well-resolved images are needed for galaxy decomposition, so this method has limitations when classifying galaxies at high redshift or galaxies that have low S/N images.

Non-parametric methods of classification are based on analysing the various galaxy quantities that correlate with the distribution of light and/or galaxy shape, and do not need any specific analytic model (Pović et al., 2015). The common classification is through concentration, asymmetry, smoothness (CAS) system (e.g., Conselice et al., 2000; Lotz et al., 2004; Pović et al., 2015; Ferrari et al., 2015; Zhong et al., 2022, and references therein). The concentration index C correlates with the concentration of light in a galaxy and the B/D (or B/T) ratio of a galaxy, the asymmetry index A (Abraham et al., 1996) is sensitive to the shape of a galaxy and can distinguish ET galaxies (E /S0/S0a) from later types (Sa/Sb/Sc/Sd) and can classify irregular and interacting galaxies, while the smoothness (or clumpiness) parameter S (Conselice et al., 2000) is sensitive to irregular (clumped) structures within the galaxy. Different types of concentration indices have been defined, but the two most commonly used are the Abraham concentration index Abraham et al. (1996) defined as the ratio of fluxes, and the Conselice-Bershady concentration index (Bershady et al., 2000) defined as the ratio of two different radii enclosing different galaxy

[3] https://data.galaxyzoo.org/

fluxes (usually at 80% and 20%). For a summary of the most commonly used morphological parameters in the non-parametric classification, see Pović et al. (2015). These non-parametric characteristics are also detectable at higher redshifts, which makes them suitable for studying the evolution of galaxies through cosmic time (Conselice, 2014). Other non-parametric ways of quantifying galaxy morphology is Gini coefficient. The technique was initially modified by Abraham et al. (2003) for the purpose of classifying galaxy morphology. Its objective was to measure the relative flux distribution inside the galaxy-associated pixels. The brightest pixels are not assumed to be at the geometric center of the galaxy picture, but there is a correlation with concentration (Lotz et al., 2004). M20 (moment of light) is also another indicator that characterizes the second-order moment of the galaxy's brightest 20%. M20 does not enforce circular symmetry and is more sensitive to merger such as multiple nuclei, yet being similar to the concentration index (Lotz et al., 2004). The advantages of measuring those indicators is, independent of wavelength or redshift, they may be applied to any galaxy and do not impose any functional shape on the surface brightness distribution of a galaxy (e.g., see Nersesian et al., 2023).

Machine learning. Machine learning techniques are useful for automatically categorizing galaxies based on their properties without human interference. They can handle big data sets and data at high redshift using labeled datasets and programmed algorithms with more accuracy (Vavilova et al., 2021). In many cases the datasets contain examples, such as images of galaxies and labels like "spiral" and "elliptical." The algorithm learns to recognize correlations and patterns between the labels and the characteristics taken from the data, such as the shape of the image and brightness distribution, the model can then predict labels for newly discovered galaxy images (Reza, 2021). There are three main types of machine learning classifications: supervised learning, unsupervised learning, and semi-supervised learning. Among the methods most commonly used in supervised learning are random forests, support vector machines, and linear discriminant analysis (de Diego et al., 2020). Random forests (Miller et al., 2017) combine multiple decision trees (Barchi et al., 2020) for robust classifications, while support vector machines (Huertas-Company et al., 2008) use a high-dimensional feature space to determine the ideal distance between classes (e.g., Pović et al., 2015; Domínguez Sánchez et al., 2018; Amado et al., 2019; Carrasco et al., 2021; Reza, 2021). Classifiers using linear discriminant analysis look for the optimal linear boundaries to divide the data, this has been applied recently to detect galaxy mergers, classification of galaxies in spiral and elliptical morphological types, classification of Hickson's compact groups of galaxies (de Diego et al., 2020). However, it is very difficult to retrieve data from a larger number of categories. Instead of concentrating on a particular morphological classification, supervised studies are used more for identifying specific features that are present in the images (Fraix-Burnet, 2023). Unsupervised methods identify intrinsic categories in unlabeled data based on their similarities. One of the most used unsupervised methods is neural networks. Neural networks is an image-based categorisation having exceptional precision in classification from deep imaging surveys specifically using conventional neural network (CNN) (Dieleman et al., 2015). Many hidden layers, each with a specific number of neurons that can execute tensor operations, make up a CNN (Ball et al., 2004). CNNs are an example of artificial neural networks, which are a powerful tool used for various tasks, including categorizing galaxy morphologies, identifying mergers, and locating gravitational lenses (Pfeffer et al., 2023). Finally, to enhance classification accuracy, semi-supervised learning can be used by combining labeled and unlabeled data (e.g., Reza, 2021; Jiang et al., 2023, and reference therein). Through the application of these machine learning approaches, it becomes possible to classify galaxy shapes with increasing accuracy, leading to a greater understanding of galaxy formation and evolution.

2.1.3 Redshift

Redshift is an astronomical distance-measuring parameter, the most commonly used to measure distances to galaxies, which helps to study the evolution of the Universe and gives a direct kinematic measurement for cosmic acceleration (Kim et al., 2015). Redshift of a galaxy describes how light shifts toward longer (shorter) wavelengths as objects in space move farther away from us (toward us). The concept is mainly due to the combination of Doppler motions and the expansion of the Universe (Hubble, 1926, 1936). To calculate the redshift z, in terms of wavelength, is given by:

$$z = \frac{\lambda_0 - \lambda_e}{\lambda_e}, \tag{2.2}$$

where the expression of the redshift in terms of frequency is:

$$z = \frac{v_0 - v_e}{v_e}, \tag{2.3}$$

where z indicates the redshift, λ_0 is the observed wavelength, λ_e is the emitted wavelength, v_o, stands for the observed frequency, and v_e stands for the rest frame frequency. The most precise measurements of redshift can be obtained through the spectroscopic emission and absorption lines, but photometric data and SED fittings can be used as well (e.g., Garilli et al., 2010; Schneider et al., 2010; Tarrío, 2020: Dey et al., 2022).

2.1.4 Brightness parameters

Brightness, or the amount of emitted light, is one of the main parameters of celestial bodies. To characterise the brightness of galaxies, the most commonly used parameters are apparent and absolute magnitudes, fluxes, and luminosities.

Apparent magnitude describes how bright an object appears in the sky from Earth. The apparent magnitude of a celestial object, such as a star or galaxy, is the brightness measured by an observer. The brightness of an object is indicated by its magnitude, whose small numbers correspond to brighter objects, while higher numbers correspond to fainter objects. It can be measured as:

$$m - m_0 = -2.5 \log_{10}(\frac{F}{F_0}), \tag{2.4}$$

where m is apparent magnitude, m_0 is a reference magnitude, F is the observed flux in the same band, and F_0 is the flux for a celestial standard source (bands).

Absolute magnitude (M) is the actual/intrinsic brightness of a star or galaxy. If we know a galaxy's luminosity distance, we can determine its absolute magnitudes as:

$$m = M + KQ + 5log(LD - 1). \tag{2.5}$$

By rearranging equation 2.5, then the absolute magnitude is

$$M = m - KQ - 5log(LD - 1), \tag{2.6}$$

where KQ is the k-correction[4], and LD is the luminosity distance in parsec.

[4]"K correction" is the term used to describe the changes between observed and rest-frame broad-band photometric

Flux (F) is defined as the amount of energy or radiation passing through a surface of galaxy per unit of time, or the total amount of energy intercepted by the light detector to measure its brightness. How bright a galaxy looks to us is determined by its flux. Flux decreases as we get farther from the galaxies (Schneider, 2006).

In the AB photometric system, we can measure flux from the AB k-corrected apparent magnitude for a given galaxy as:

$$m(AB) = -2.5\log(f_\nu) - 48.6. \tag{2.7}$$

From this equation, the monochromatic flux is measured in a frequency distribution, f_ν, as:

$$f_\nu = 10^{-0.4\times(m+48.6)}, \tag{2.8}$$

where f_ν is flux in units of $erg/sec/cm^2/Hz$. After estimating the f_ν, flux in $[erg/sec/cm^2]$ can be measured.

Luminosity (L) is an important physical parameter of a galaxy, defined as the amount of light or energy radiated into space per second, and therefore it gives information about the intrinsic brightness of an astronomical object (Schneider, 2006). L is defined as (Hogg, 1999):

$$LD = \sqrt{\frac{L}{4\pi F}}, \tag{2.9}$$

where L is bolometric luminosity, F defined as flux and LD is defined by the relationship between bolometric (i.e., integrated over all frequencies) flux S and L.

2.1.5 Colors of galaxies

Colors in astronomy are defined as a difference of magnitude measured in two different filters, which can form a clear sequence on optical color-color diagrams (Pollo, 2015). Broadband filters and color index and multi-wavelength imaging are some of the examples for measuring colors. Most of ET galaxies are characterized by more red colors and LT galaxies with bluer colors. This can however change depending on other galaxy properties, such as the AGN emission and recent star formation in ET galaxies, or extinction and inclination effects in LT galaxies (e.g., Kormendy, 1996; Pović et al., 2013; Cheng et al., 2021). The advantage of using galaxy colors to describe the galaxy population over morphological types is that because they are more easily quantifiable, the measurements are robustly reproducible, and there are models that allow us to directly tie them to star formation history (SFH) with little or no speculation (e.g., Balogh et al., 2004; Pollo, 2015). In addition, colors of galaxies provide us with valuable information concerning the present-day composition of stars.

Color-mass diagram

In large surveys, at both low and higher redshifts, a bi-modal distribution of galaxies has been observed when using any of the parameters such as colors, luminosity, stellar mass, SFR, or sSFR (e.g., Mahoro et al., 2017, 2019). The two principal regions are named ”blue cloud” (BC), being mainly populated by LT galaxies, and ”red sequence” (RS), being mainly populated by ET galaxies. There is a region known as the ”green valley” (GV) that lies between the BC and RS, and it has a diverse population of galaxies (e.g., Balogh et al., 2004; Pović et al.,

data.

2012; Schawinski et al., 2014; Mahoro et al., 2017, 2019). A morphology-based analysis (e.g, Schawinski et al., 2014) reveals that, once the morphologies change from disk to spheroid and star production is rapidly quenched, only a tiny number of blue ET galaxies migrate over the GV quickly. While their SFR are slowly declining, the vast blue star-forming galaxies still have large disks and LT morphology. Figure 2.7 shows the distribution of galaxies in the colour-stellar mass diagram in the SDSS survey, showing the bi-polar distribution of galaxies with RS and BC, being populated mainly by ET and LT galaxies, respectively, and with the GV region in between (marked with the two solid green lines).

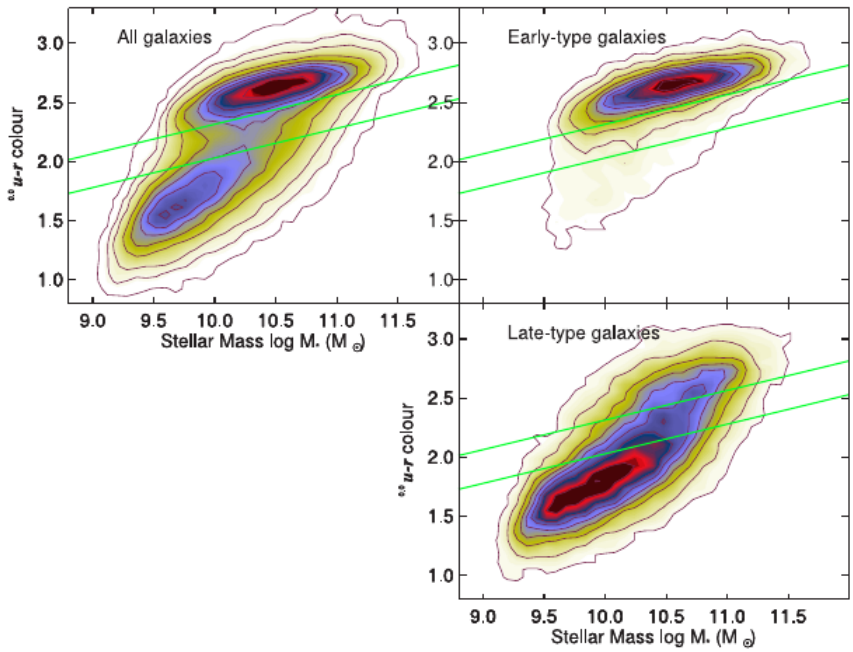

Figure 2.7: Distribution of galaxies in the color-stellar mass diagram in the SDSS survey for a total sample of galaxies (top left), ET (top right), and LT (bottom) galaxies. Credit: Schawinski et al., 2014.

2.1.6 Total mass of galaxies

Two primary components make a galaxy's total mass: 15% is made up of baryonic matter, while the remaining 85% is composed of dark matter (e.g., Zasov et al., 2017). Dark matter makes up the majority of a galaxy's mass, however understanding dark matter is still challenging, whereas baryonic matter is the total mass of stars (stellar mass), gas, and dust (Cautun et al., 2020). Stellar mass is one of the most fundamental parameters of a galaxy, it provides a measure of the evolution processes of galaxies (Mobasher et al., 2015; Hartmann et al., 2016). The stellar mass of a galaxy accumulates within the processes such as the formation of stars via gas and dust or the interaction of galaxies (minor and major mergers) (e.g., Kauffmann et al., 2003). The most common technique for determining the stellar mass of galaxies is to match their observed SEDs, which cover the UV, optical, and IR wavelength range, to templates created from stellar population synthesis models (e.g., Cid Fernandes et al., 2005; Mobasher et al., 2015; Mahoro et al., 2017; Kim, 2020; Leroy et al., 2021). A galaxy stellar mass has a different range, dwarf galaxies are the smallest and least massive kind of galaxies ranging between $10^6 - 10^{10} M_\odot$. Massive galaxies, known as giant elliptical galaxies range between (10^{11}–$10^{14} M_\odot$ or more) (Sreejith et al., 2018).

2.1.7 Star-formation rate

Star-formation rate (SFR) is the gas mass that is converted into stars per unit of time (Hirashita et al., 2003), and star formation in a galaxy takes place over a finite period of time. Specifically, the SFR is defined as the number of solar-mass stars created in a galaxy per year. ET galaxies having old stars will have decreasing SFR over time, because more and more matter is bound in stars and thus no longer available to form new stars, but in the LT galaxies they have higher SFR (e.g., Brinchmann, 2000; Madau, 2014). Using a total FIR luminosity of galaxies, we can measure the SFR. Another SFR indicator is the UV luminosity, which is one of the well-known and frequently utilized tracers of massive stars because massive stars are a powerful source of UV photons. In addition, SFR can be measured in optical using the Hα emission line produced by gas that has been ionized by massive-star radiation (e.g., Hirashita et al., 2003; Conselice, 2014; Mahoro et al., 2017; Papovich et al., 2019). Recent studies suggest that with radio wavelengths, it is possible to track the entire SFR in galaxies, both obscured and unobscured and to study the fuel driving the SFH of the Universe (e.g., Schneider, 2006; Netzer, 2015, and references therein).

2.1.8 Metallicity of galaxies

A galaxy's metallicity is defined as the abundance of elements heavier than hydrogen and helium (e.g., see Arcones, 2023, and references therein). The system's history of star formation and the galaxies age impact the total metal abundance, in which young stars are metal-poor and old stars are metal-rich (e.g., Garcia et al., 2023). The most prominent characteristic of galaxies that give us precise information on the previous history of galaxy formation, SFH, and the galactic evolutionary stage is metallicity (Sommariva et al., 2012). ET galaxies are metal-rich systems, distinguished by having high [α/Fe] ratios in the dominant star population and super-solar [Mg/Fe] in the nucleus of luminous galaxies (Molero et al., 2023).

Fundamental metallicity relation (FMR), a relationship between mass and metallicity of star-forming galaxies, demonstrates that metallicity has an inverse relationship with SFR and directly depends on stellar mass and gas cycling through the interstellar medium (ISM). Within a given stellar mass, high-redshift galaxies are likely to be more metal-poor than local ones because the mass metallicity relation (MZR) evolves dramatically with redshift (e.g., Guseva et al., 2009; Andrews, 2013; Curti et al., 2023; Baker et al., 2023). Through large spectroscopic surveys, the NIR metallicity of high redshift galaxies can be studied (De Vis et al., 2019; Curti et al., 2023).

There are different ways of determining metallicity, like calibration of strong line diagnosis of the temperature sensitive aurora lines. These techniques make use of Balmer lines as well as nebular emission lines, such as [OII]3727, [OIII]5007, and [NII]6583. Through the direct calculation of the electron temperature, also known as T_e method and strong-lines, the gas phase metallicity can be determined in both star-forming regions (also known as HII regions) and star-forming galaxies. Measurements of aurora lines, such as [OIII]4363, [NII]5755, and [SIII]6312, are necessary for the T_e method because these lines are faint (100 times weaker than Hβ) and can only be seen in objects with significant ionization and/or low metallicity. The oxygen abundance in relation to hydrogen is typically used to calculate the gas-phase metallicity and is expressed in units of $[12 + log(O/H)]$ (e.g., Guseva et al., 2009; Andrews, 2013; Pérez-Montero et al., 2019; Armah et al., 2023).

2.1.9 Age and stellar populations

Stellar populations in a galaxy are normally classified into young (with average stellar ages $<$ 10^8 Gyr), intermediate (with ages $10^8 - 10^9$ or 10^{10} Gyr), and old (with ages $>$ 10^9 or 10^{10} Gyr, depending on the works) (e.g., Pović et al., 2016; Cazzoli et al., 2018; Mahoro et al., 2022, and references therein). In most cases, the stellar populations are characterized by means of broadband photometry, optical spectroscopy and NIR spectroscopy (e.g., Wuyts et al., 2007; Schawinski et al., 2014; Mahoro et al., 2017).

Stellar populations of galaxies provide detailed information about the large-scale galaxy formation processes. While stars found in the disk have metallicities, stars found in the halos of the galaxies have high metallicities. This difference, interpreted as an evidence that the halo stars (population II) formed first, before much chemical enrichment by deaths of massive stars had taken place, as it is the case in the disk with population I stars (e.g., Schneider, 2006; Schawinski et al., 2014; Mahoro et al., 2022). Old stellar populations are found in such as environments, such as globular clusters and in the halos and bulges of galaxies. On other hand,, young stars are found in the galaxy disk and in open stellar clusters (e.g., Milone et al., 2012; Getman et al., 2014; Stanway, 2018; Bastian, 2018).

Stellar population analysis is an effective method used to study stellar populations through the spectra of galaxies (e.g., Pović et al., 2016; Mahoro et al., 2022). Results can be achieved by modeling the entire spectrum or by taking measurements of the absorption index that depend on different stellar population factors (e.g., Kauffmann et al., 2003; Parikh et al., 2021). We can study the composition, age and stellar populations of galaxies using observable characteristics of the source SED, including photometric colors and spectroscopic emission lines (e.g., Stanway, 2018).

2.2 Active galactic nuclei

Active galactic nuclei (AGN), are extremely energetic sources in the centers of galaxies, fed through the accretion processes of matter onto a SMBH. AGN exhibit distinctive observational signatures that span the entire electromagnetic spectrum. Galaxies hosting an AGN are known as active galaxies. The source of the AGN luminosity is created by the accretion of matter onto SMBH (e.g., Peterson, 2006; Ho, 2008; Tadhunter, 2008; Schawinski et al., 2014; Mickaelian, 2015; Netzer, 2015; Padovani et al., 2017; Blandford et al., 2019; Mahoro et al., 2019; Mountrichas et al., 2021, and references therein). Understanding AGN luminosity function is crucial to understand formation and evolution of a galaxies and Universe as a whole (e.g., Fontanot et al., 2023). To study AGN it is essential to have a solid understanding of radiation and multi-wavelength SED, since the emitted light has been observed at all wavelengths, as mentioned above (e.g., Padovani et al., 2017, and references therein).

2.2.1 General properties of active galaxies and AGN

AGN features a lot of fascinating characteristics. These include extremely high luminosity and variability (Netzer, 2015), which make them some of the most luminous sources in the Universe and make them visible up to very high redshifts (at z $>$ 13 with James Webb Space Telescope (JWST) (e.g., Juodžbalis et al., 2023). Small emission regions, order of a milli-parsec found in most bands, as implied by their rapid fluctuation, suggest that there is high energy density, strong evolution of luminosity functions, and detectable emission, covering the whole electromagnetic spectrum. AGN are more powerful emitters than the nuclei of normal galaxies (Padovani et al.,

2017). Since they are some of the brightest, SMBH most dependable, and most energetic sources in the Universe, AGN are used to examine high redshift objects. The physical properties of AGN are determined based on the following parameters: mass of the BH, rate of accretion onto the SMBH, presence of a jet, and the angle at which the galaxy is viewed (Netzer, 2015). The principal differences between non-active (normal) galaxies, without signs of AGN emission, and active galaxies that host an AGN in their center, are:

- The energy of normal galaxies is equal to the sum of the energies released by all stars inside that galaxy, however, this is not the case for active galaxies. The main source of their energy is due to the accretion of matter into the SMBH at the center of the host galaxy (e.g., Netzer, 2015, and references therein). SMBHs may be found in both active and inactive galaxies, however, active galaxies often contain a larger mass of SMBHs because of a possible relationship between accretion rate, SMBH mass, and galactic activity (e.g., Kormendy, 2013).
- Due to star and interstellar gas emissions, the normal galaxy mostly produces light in the optical band, but for active galaxies, the non-thermal emission from a central nucleus outperforms the thermal emission from stars and interstellar gas and goes well beyond the optical band, from radio to gamma rays (e.g., Netzer, 2015; Padovani et al., 2017, and references therein).
- Active galaxies are a small subset that exhibits strong and broad emission lines with velocity dispersion of the emitting gas of several thousand kilometers/second (e.g., Netzer, 2015; Cho et al., 2020).
- Another difference between normal galaxies and active galaxies is in the active galaxies there exist strong, relativistic jets originating from the center basically from the SMBH (e.g., Laughlin et al., 2004; Padovani et al., 2017).
- Another important distinction between active galaxies and non-active galaxies is variability. Active galaxies show sudden and often dramatic changes in brightness across different wavelengths due to fluctuations in the rate of accretion, which result in variations in the amount of energy produced (e.g., Netzer, 2015; Padovani et al., 2017; Burke et al., 2021).

2.2.2 Standard model of AGN and its main components

The standard model is a single, comprehensive system that has been used to explain the wide range of AGN classes (e.g., Antonucci, 1993). In models of AGN, the SMBH and an accretion disk resembling a giant doughnut, located in the doughnut's hole and a cold region composed of gas and dust are included. The core elements of AGN, are presented in Figure 2.8 and include:

- **Supermassive black hole (SMBH)** is the primary building block of the majority of galaxies (Greene, 2006), located at the center of galaxies (Melia, 2001; Fontanot et al., 2023). SMBHs are encircled by an accretion disc and serve as a main energy source for AGN. They have high gravitational field, which pulls matter from the surrounding and accretes mass onto it (e.g., Tadhunter, 2008; Schawinski et al., 2014; Mickaelian, 2015; Netzer, 2015; Padovani et al., 2017; Blandford et al., 2019). Understanding the mass of a SMBH can provide us a better understanding on the formation and evolution of SMBHs and their host galaxies (e.g., Ferrarese, 2000; Greene, 2006; Ho, 2008; Best, 2012). The mass of the SMBH can be measured through

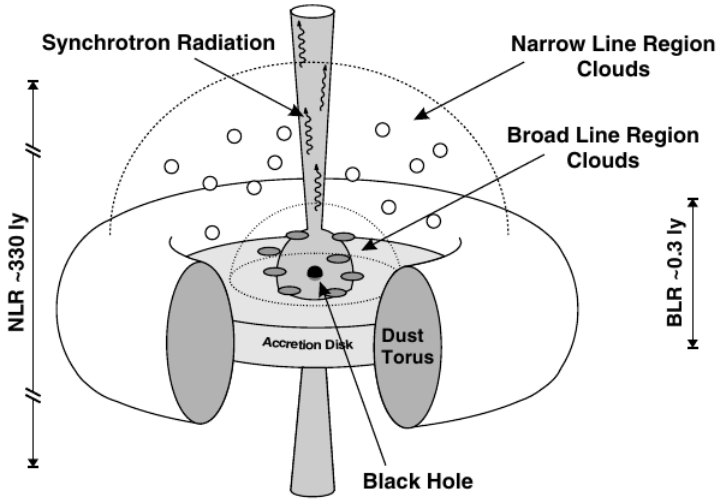

Figure 2.8: The standard model of AGN. Credit: Smith et al., 2008.

different methods, e.g., using the reverberation mapping of the BLR in type-1 AGN (Peterson, 2006; Haas et al., 2011) or through the intensity of different emission lines. Different studies have shown that there is a co-evolution between the SMBH and its host galaxy, in particular between the mass of the SMBH and the mass and luminosity of the bulge (e.g., Kormendy, 2013; McConnell, 2013; Smethurst et al., 2024).

– **Accretion disk** is the major source of power in which matter with even a small amount of angular momentum, attracted by the SMBH gravity, spirals in and forms a disk. It is believed that the accretion disc is the origin of the X-ray, UV, and optical continuous emission, which ionizes the gas in both the broad-line and the narrow-line region. It may also serve as the starting point for winds and jets (e.g., Ghisellini, 2013; Netzer, 2015; Padovani et al., 2017; Fabj et al., 2020). Thin doughnuts (thick disks), Shakura-Sunyaev (thin) disks, slim disks, and advection-dominated accretion flows (ADAFs) are some of the models describing the accretion disc. The thin doughnuts (thick disks) model was developed by Paczynski et al. (1996) and his collaborators. The disks described have a toroidal (doughnut-shaped) structure, consisting of a narrow funnel along the rotation axis and a fat central body. The thin-disk Shakura-Sunyaev and Novikov-Thorne models imply radiatively efficient accretion (Shakura, 1973). According to this principle, all of the heat produced by viscosity at a certain radius is reflected; no additional cooling mechanism is required since the local radiative cooling balances the viscous heating. This model assumes a geometrically thin, optically thick, and steady disk. Due to the immense gravitational pull of the central black hole, these disks can be quite hot. This model helps describe the structure and spectrum emitted by the disk (e.g., Shakura, 1973). In the late 1988, Abramowicz et al. (1988) proposed the concept of slim accretion disk models, which describe an optically thick, geometrically not very thin quasi-Keplerian accretion flow onto a black hole in high Eddington ratio sources.This model describes the slim discs are the result of high accretion rates due to radiation pressure, electron scattering, and the significance of heat transfer by rapidly moving gases. In the ADAF solution, effective cooling is included; it goes so far as to penetrate almost all of the viciously wasted energy into the SMBH instead of radiating it out. The ADAF is applicable when the brightness (and typically the mass accretion rate) are low, in contrast to the slim disk approach, which is typically invoked at high luminosity's (e.g., Nenkova et al., 2008; Yuan et al., 2008; Abramowicz, 2013).

- **X-ray corona** is a hot plasma which encircles the accretion disk and produces X-rays via the inverse Compton scattering of the optical-UV disk photons (e.g., Ghisellini, 2013; Nour, 2023; Fontanot et al., 2023). They have been suggested to originate from the surface of an accretion disc, and they are frequently seen in the X-ray spectra of AGN (e.g., Ballantyne, 2020).
- **Obscuring torus** located at a distance from the SMBH, obscures radiation coming from the SMBH and re-emits it in the IR bands (e.g., Antonucci, 1985; Ho, 2008; Ghisellini, 2013; Netzer, 2015; Ramos Almeida et al., 2017). The torus is depicted as a large doughnut-like component, presumably populated by molecular clouds accreted from the galaxy (Elitzur, 2006). Simple torus model, clumpy torus model, bi-conical wind model, self-regulated torus model are some of the models for describing the obscuring torus. The simple torus model is as it is described by the unification model by Antonucci (1993), and Urry & Padovani (1995) Clumpy torus model, taking into account the existence of clumps inside the dusty structure, this model improves upon the basic torus. This model provides a better explanation for the observed differences in obscuration between AGN and the patchy obscuration found in certain systems. According to this model, an AGN categorization is determined entirely by chance; a source may exhibit type-1 characteristics even when seen from orientations that are near the equatorial plane (e,g., Granato et al., 2004, Nenkova et al., 2008; Ramos Almeida et al., 2014). Because a smooth dust distribution would cause collisions that would raise the temperature to levels too high for the dust to survive, clumpy models are a more possible representation of the actual dust distribution (e.g., Feltre et al., 2012). The bi-conical wind model, the torus is a bi-conical structure with out-flowing winds along the rotating axis rather than a complete ring, refs for this model. In addition to causing obscuration, these winds may also be the cause of ionization cones that have been seen in some AGN. The relationship between the dusty torus and the radiation field from the core engine is included in this model. In the self-regulated torus model, the torus's overall structure and obscuring qualities may be impacted by the strong radiation's ability to heat and push particles outward refs for this model. Recognizing the torus's responsiveness to the core environment, this model offers a more dynamic perspective of the torus.
- **Broad Line Region (BLR)** is the region where broad emission lines are created. Broad lines are observed due to Doppler shift. This happens when a small rapidly moving dense gas cloud region located at a small distance from the SMBH, intercepts the ionizing radiation of the disk, and re-emit it in the form of lines (Pancoast et al., 2012; Ghisellini, 2013). They are dust-free gas clouds traveling at luminosity-dependent distances of 0.01–1pc from the SMBH (Pancoast et al., 2012; Netzer, 2015). Therefore, the BLR is photoionized gas heated by radiation from the restricted accretion disk that fuels the SMBH at the center of AGN, located in the upper part of the accretion disk (see Figure 2.8). The BLR is a special laboratory for studying the accretion process onto the SMBH (e.g., Balmaverde, 2014; Netzer, 2015; Pâris et al., 2017, and references therein). The reverberation-mapping technique can be used to determine the size and structure of this region (Peterson, 2006, Li et al., 2022). In addition, the BLR can be studied using IR spectroscopy and spectropolarimetric measurements (Antonucci, 1985), specifically large components in the hydrogen recombination lines may be detected using near-IR spectroscopy across a less narrow line of sight (Ramos Almeida et al., 2009). At some wavelengths, such as millimeter or IR, dust obscuration may have less impact on some wide emission lines from the BLR. For such case multiwavelength study of the BLR is also another tool. The spectral analysis is also another way of studying the strength, profile and variability of the

emission from the BLR, hence it make it possible to study the physical conditions (density, temperature, velocity) within the BLR, even if it's partially obscured (Wang et al., 2023).

– **Narrow Line Region (NLR)** develops from circling clouds which are less dense and moving with less speed at a larger distance. Since the orbiting cloud is ionized gas that stretches from the edge of the torus to the direction of the torus' opening (ionization cones), most of this gas consists of dust (e.g., Sulentic et al., 2000; Netzer, 2015). There are two likely sources of emission clouds in NLR of AGN: local gas clouds associated with star formation (like the emission regions in HII galaxies) and/or ionized gas clouds associated with central galactic outflows (Zhang, 2022). The narrow emission spectrum, is dominated by forbidden lines. Almost all optical surveys use narrow emission lines to identify and categorize AGN (e.g., Bennert et al., 2006; Greene et al., 2011; Liu et al., 2013; Hainline et al., 2016). Examining the Doppler shift of the emission lines within the NLR can be used for studying gas clouds within the NLR. The variations in the measured wavelength of a line may be used to map the movements of the gas in the NLR since they indicate a change in direction of the gas, either towards or away from us (blueshift or redshift). One effective method for figuring out the physical parameters in the NLR of AGN is spatially resolved emission-line spectroscopy (e,g., Peterson (2006)). In recent years, Integral Field Spectroscopy (IFS) has emerged as one of the most effective ways for studying AGN. Using IFS data from the CALIFA surveys (e.g., García-Lorenzo et al., 2015; Morales-Vargas et al., 2023), SAMI surveys (e.g., Tescari et al., 2018; Zovaro et al., 2024), and MaNGA surveys (e.g., He et al., 2018; Wylezalek et al., 2020; Albán, 2023; Peluso et al., 2023), researches investigate different facts of AGN.

– **Relativistic jets.** The term "jet" refers to the energetic beam of particles that is ejected from the SMBH and accretion disk in opposite directions at speeds that are nearly equal to the speed of light (Ghisellini, 2013). They are the most extreme example of the power that an AGN SMBH can produce (e.g., Netzer, 2015; Romero et al., 2017; D'Ammando, 2019; Hada, 2019). When a SMBH rotates and an accretion disk becomes strongly magnetized, relativistic AGN jets might be created, and the emission from these jets is extremely beamed (e.g., Romero et al. (2017)). It is thought that the enormous energy output from AGN jets have a significant influence on the evolution of galaxies across cosmic time (Lin et al., 2023). In Magnetohydrodynamics (MHD) models, the jet is seen as a magnetized fluid in which the interaction of moving charged particles with magnetic fields is critical and the particle acceleration views how the jet particles accelerate to extremely high speeds (Mościbrodzka, 2019).

2.2.3 Types of AGN

The properties of AGN vary widely among them, they are not all identical. Depending on their radio power, they can be categorized as radio-loud and radio-quiet AGN (Kellermann et al., 2016). Since the presence or absence of powerful relativistic jets is the primary physical distinction between these two classes, the maximal photon energy of the two classes differs significantly (Padovani et al., 2017; Miraghaei, 2020). Figure 2.9 shows one of examples of different types of AGN depending on their radio and optical properties, while Figure 2.10 shows the typical spectra for the different classes of AGN described below.

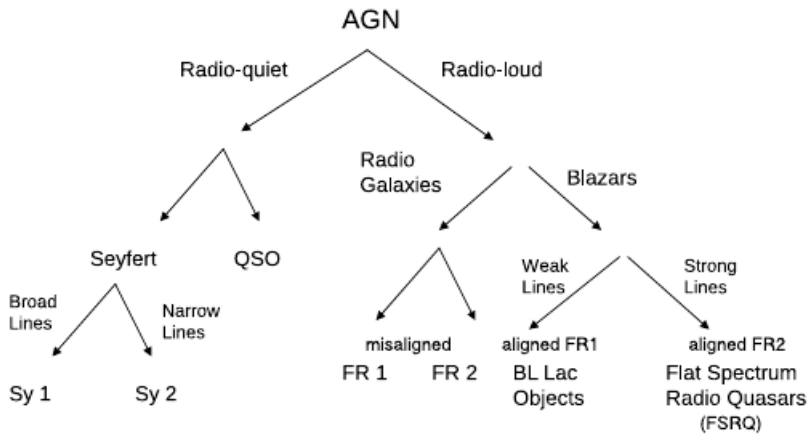

Figure 2.9: Classification of galaxies based on their radio emission. Credit: Dermer, 2016.

Radio-quiet AGN

are characterized by weak or absent radio emission and weak relativistic radio jet with thermal emission. Either directly or indirectly, the thermal emission is related to the accretion disk, which dominates the multi-wavelength emission of radio-quit AGN (e.g., Padovani et al., 2017; Hardcastle et al., 2019; Miraghaei, 2020). Some of radio-quiet AGN are:

- **Seyfert galaxies.** The presence or lack of broad optical emission lines has been used to categorize Seyfert 1 and Seyfert 2 galaxies (e.g., Heckman & Best, 2014; Netzer, 2015). Both have permitted emission lines, such as Balmer lines, [HeII]4686 and [HeI]5876, [FeII], and forbidden emission lines: [OII]3727, [OIII]4959, 5007, [SII]6717, 6731, and [NII]6548, 6584 (Peña-Herazo et al., 2022). While Seyfert galaxy with broad lines such as Balmer lines (Hδ, Hγ, Hβ, and Hα) and narrow permitted (such as [OIII], [NeIII], [OII], [OI], [NII], [SII]) and forbidden lines are Seyfert 1, while Seyfert 2 galaxies exclusively have only narrow permitted and forbidden line emission (e.g., Peterson, 2006; Meléndez et al., 2008; Bamford et al., 2008; Bianchi et al., 2012; Elitzur, 2012; Heckman & Best, 2014; Netzer, 2015).
- **Quasars (QSO)** are very luminous radio sources having distinct emission line properties. The emission line present in quasars are balmers line, Lyα 1216, [HeI]5876, [HeII]4686, [CIV]1549, [CIII]1909, [NV]1240, [NIII], [OIII]5007, [OI]6300, [MgII] 2800, [MgI]5183, [FeII]1044, [FeI]6302, [NeV]3429, [NeIII]4610, [Al III]1859, [SiIII]1892 (e.g., Forster et al., 2001; Coatman et al., 2016). Specifically, the strongest emission lines are [CIV]1549, [CIII]1909, [MgII]2800 (e.g., Coatman et al., 2016; Pâris et al., 2017; Huang et al., 2023).
- **Radio-quiet quasars (QSQ),** are characterized by their weak radio emission, radio jet and flux densities comparable to those in the optical, and by lower energies (e.g., Barvainis et al., 2005; Lister et al., 2016; Blandford et al., 2019).
- **Low ionization nuclear emission-line regions (LINERs),** are a source of weak, narrow, low-ionization emission lines from gas that has been ionized by a non-stellar source. They have low AGN luminosity, order of 10^{42} erg/sec/cm^2 (e.g., Netzer, 2015; Pović et al., 2016; Blandford et al., 2019). They are found mainly in elliptical galaxies in the local Universe, and often the spiral galaxies and the diagnostic Baldwin-Phillips-Terlevich (BTP) diagram are used to identify them (Baldwin et al.,

1981) in combination with the WHAN diagram (Cid Fernandes et al., 2011). Dilute AGN photoionization and shocks have both been proposed as methods for producing LINER spectra. A small percentage of them exhibit distinct broad components in their Hα lines, indicating the existence of an AGN broad line region (Ho, 2008). LINERs are often categorized by their narrow emission-line ratios, such as [OIII]5007/Hβ, [NII]6584/Hα, and [OI]6300/Hα (Pović et al., 2016). Typical strong emission lines in this group are [NII]6584, [SII]6731, and the Balmer lines (Netzer, 2015).

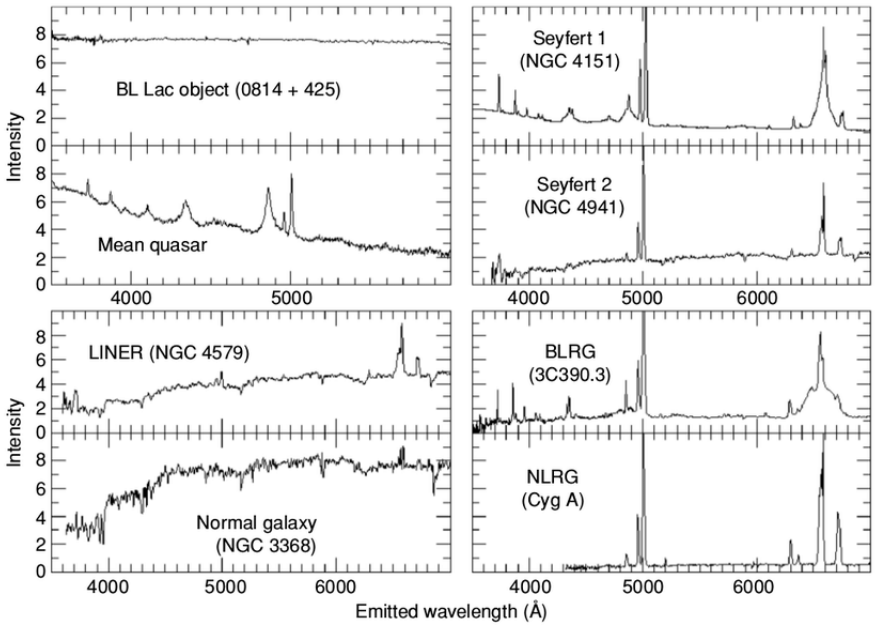

Figure 2.10: Example of optical spectra of different types of AGN. Credit: Andika, 2016

Radio-loud AGN

are characterized by a powerful relativistic jet of charged particles and magnetic field that are created as a result of the accretion of matter onto a galaxy's SMBH in combination with non-thermal emission. Therefore, the energy observed is produced from radio emission through the synchrotron process (e.g., Padovani et al., 2017; Hardcastle et al., 2019; Miraghaei, 2020). They are normally hosted by large elliptical galaxies. The radio-loud classes include radio-loud quasars, blazars, and radio galaxies (Chiaberge et al., 2015).

- **Radio-loud quasars (RLQ)** are quasars forming a powerful jet (Barvainis et al., 2005) and becoming radio-loud as a result of the SMBH spinning rapidly (Netzer, 2015).
- **Blazars** are AGN with jets directed directly toward us, with no emission lines, they are highly variable, and emit radiation across the entire electromagnetic spectrum (e.g., see Netzer, 2015; Chang et al., 2023, and references therein). Blazars are classified into two: BL Lac objects and optically violent variables (OVVs). Most of the radiation we detect from these sources is the Doppler-boosted non-thermal radiation emitted within the jet (e.g., Urry & Padovani, 1995; Tadhunter, 2008; Dermer, 2016; Paliya et al., 2019; Chang et al., 2023).
- **Radio galaxies** are AGN with jets that are pointing in different directions (Hardcastle, 2020). The dominant source of the radio emission in radio galaxies is synchrotron radiation from relativistic jets (e.g., Padovani et al., 2017). Radio AGN are typically found in massive, quiescent galaxies with older stellar populations, (Shen et al.,

2017). Single or twin radio lobes are frequently seen along with these emissions (Hardcastle, 2020). Based on their radio morphology, they are classified as Fanaroff and Riley class I (FRI), limb-brightened and class II (FRII) edge-brightened. FRI radio sources have radio powers that are, on average, lower than those of FRII sources. Based on their optical emission spectra, radio galaxies are also classified as broad-line radio galaxies (BLRG) and narrow-line radio galaxies (NLRG) (e.g., Tadhunter, 2008; Dermer, 2016; Padovani et al., 2017). Figure 2.11 shows the classification of radio galaxies using CNN for SDSS-selected sources. In addition to the radio classifi-

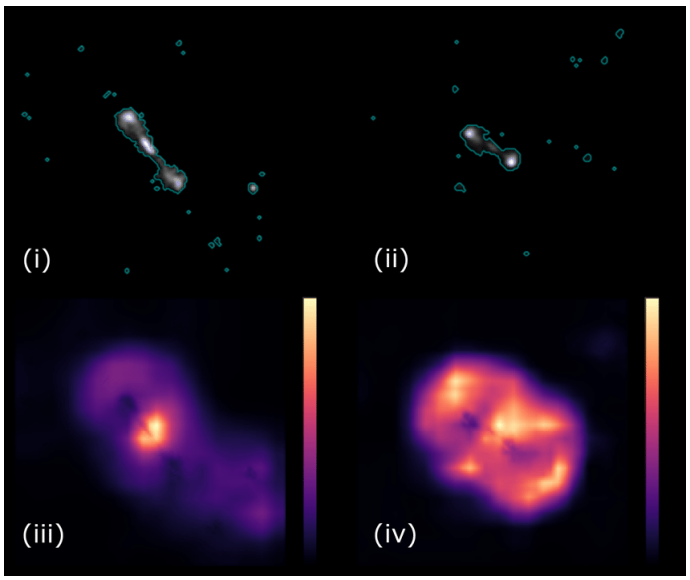

Figure 2.11: Example FRI (i) and FRII (ii) sources. The averaged attention maps for the FRI and FRII sources are represented in plots (iii) and (iv), respectively. Credit: Bowles et al., 2021.

cation, according to optical properties of emission lines, AGN are classified as type-1 or type-2, with distinct characteristics:

– **Type-1 AGN,** have a central point source that is luminous and non-stellar, visible at all wavelengths and exhibits broad permitted and semi-forbidden emission lines, which results in lines with FWHM of 1000 – 20,000 km/sec (or more). Nearly all type-1 AGN with low to medium luminosity exhibit in addition strong, narrow emission lines with high ionization, many of which are forbidden lines (e.g., Bamford et al., 2008; Elitzur, 2012; Netzer, 2015; Nour, 2023; Abdulrahman et al., 2023). A large portion of the emission in type-1 AGNs comes from gas in the accretion disc that is located extremely near to the black hole (Kauffmann, 2019).

– **Type-2 AGN,** emit strong narrow (300 – 1,000 km/sec) NIR-optical-UV emission lines that are somewhat broader than those observed in emission-line galaxies of similar types, according to their optical spectra (e.g., Tadhunter, 2008; Netzer, 2015; Abdulrahman et al., 2023), originating from the circling clouds comprising the NLR (Bamford et al., 2008; Nour, 2023). In type-2 AGNs, the accretion disk is hidden by dust, and the emission lines detect highly ionized gas in the host galaxy (Kauffmann, 2019). A torus-like structure with dust-dominant features blocks the view of type-2 AGN. Therefore, despite being discovered in spectro-polarimetric tests, the BLRs are seen to be largely hidden in type-2 AGN (Elitzur, 2012).

2.2.4 The unification model of AGN

The standard unification model of AGN was introduced by Antonucci (1993). The basic principle of the unification model is that type-2 and type-1 AGN belong to the same class of objects and differ primarily in terms of how they are oriented in relation to an obscuring medium and observer. A full representation of Seyfert galaxies, radio galaxies, quasars, and blazars is provided by the unification model of AGN. The discovery of hidden broad emission lines from type-2 AGN in optical polarized spectra leds to the unification model (e.g., Antonucci, 1985; Elitzur, 2012; Bianchi et al., 2012; Beckmann, 2012; Abdulrahman et al., 2023). Figure 2.12 gives a presentation of the unification model. According to the

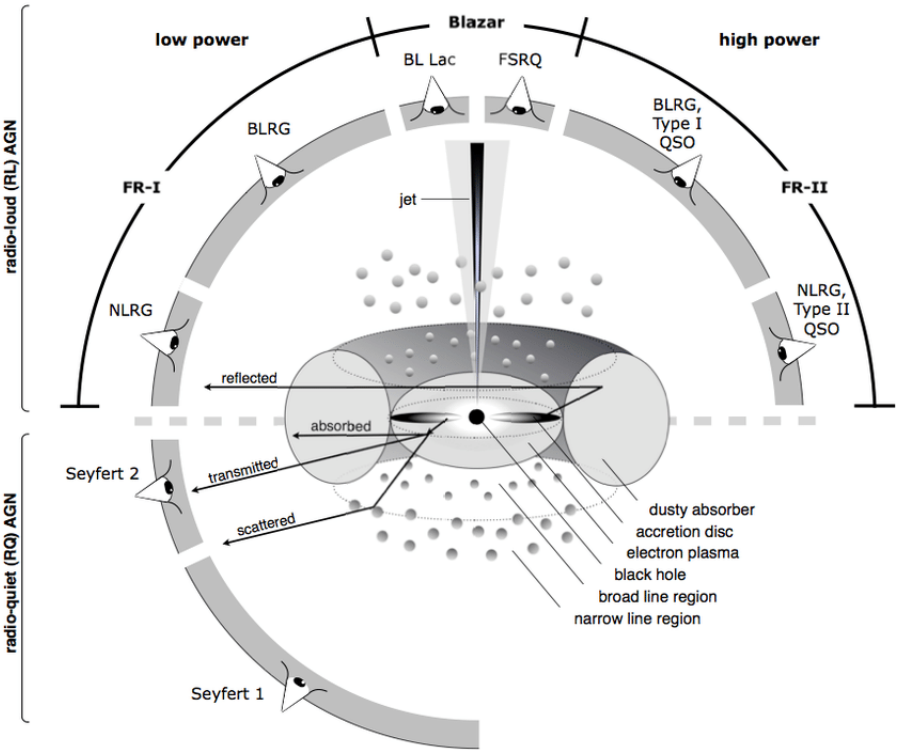

Figure 2.12: The unification model of AGN. Credit: Beckmann, 2012.

unification model, AGN are represented as SMBHs surrounded by an accretion disk of hot plasma emitting visible and UV radiation. The BLR is a dense region of high-velocity gas clouds and radiation fields, and twin relativistic plasma jets are formed by material ejected from the accretion disk. The SMBH and its accretion disk fuel nuclear activity in a donut-shaped structure, with dusty clouds surrounding the central engine. Sources seen from the front are classified as type-1 objects, while sources seen from the side are classed as type-2 objects (e.g., Elitzur, 2006; Beckmann, 2012; Netzer, 2015; Noda et al., 2023). Recent observations in FIR and optical through variability studies (e.g., changing-look AGN) have shown that the type-1/type-2 classification might not be the result of the orientation effect alone, but of actual physical differences between the two types (e.g. see Netzer, 2015).

2.2.5 AGN selection mechanisms using X-ray, optical, radio and IR data

AGN can be recognized using a variety of observational methods in different bands, where different bands may represent various stages in the formation of AGN (Liu et al., 2022).

As mentioned above, the optical/UV band is associated with emission from the accretion disk, the X-ray band traces the emission of a (putative) corona, and the IR band is primarily sensitive to obscuring material and dust. Both obscured and unobscured AGN can be found using MIR and FIR (e.g., Stern et al., 2012). On the other hand, gamma ray and high flux density radio samples provide AGN releasing significant non-thermal jet or associated lobe-related radiation (Kramarenko et al., 2022). Figure 2.13, shows how AGN can be seen at all wavelength ranges from radio to gamma-rays.

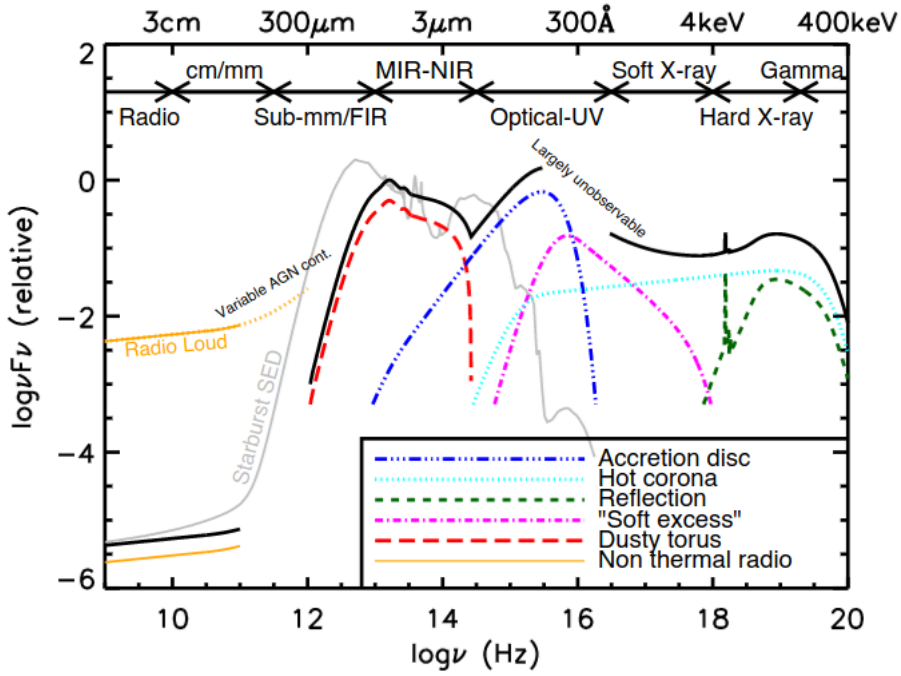

Figure 2.13: Schematic illustration of an AGN SED, mainly driven by the SEDs of radio-quiet quasars that have been detected. The numerous colored curves indicate the distinct components, while the black solid curve represents the entire SED. Credit: Harrison, 2014.

X-ray selection

Due to the fact that AGN frequently outshine light from even the most active star-forming galaxies at X-ray wavelengths, X-ray selection provides a reliable approach to screen AGN (Mendez et al., 2013). X-rays have a deep penetrating power even at large column densities. Due to their great penetration and little dilution from host galaxies, they are used to identify all, including low luminous AGN (Xue et al., 2016). Therefore, X-ray selection gives the most unbiased samples of AGN. The commonly used methods for AGN selection in X-rays include X-ray luminosity, X-ray to optical flux ratio, and emission in hard X-rays. X-ray luminosity involves analyzing the total X-ray emission. Objects emitting more X-rays above a certain threshold are considered potential AGN candidates (e.g., Brandt et al., 2015; Birchall et al., 2022, and reference therein). However, the specific luminosity threshold may vary based on the object's redshift and the X-ray survey's sensitivity. A widely used reference point of X-ray luminosity is 10^{42} erg/s after redshift correction (Mushotzky, 2004). The X-ray to optical flux ratio technique involves comparing the amount of visible light (optical flux) with the amount of X-ray radiation (X-ray flux) emitted by an object (e.g., Pović et al., 2009; Pović et al., 2012; Lusso et al., 2010). Objects with a higher X-ray to optical flux ratio are identified as AGN, this technique is less affected by dust obscuration compared to X-ray luminosity since dust absorbs more

light at optical wavelengths (Brandt et al., 2015). Another technique is looking for very hard X-rays ($> 10keV$) in the spectrum of a possible AGN (Kayal, 2024). High-energy X-rays have a greater chance of penetrating dust obscuration and providing evidence for an AGN, even if the source is partially obscured (e.g., Wang et al., 2021; Krezinger et al., 2024).

Optical selection

Color-based selection of AGN in optical is not efficient due to stellar contamination (Sánchez-Sáez et al., 2019). Variability-based selection can be one of the mechanisms used to categorize high-redshift AGN such as quasars. Combining both optical colors and variability parameters improves the classification efficiency and completeness, but this is also limited to low-luminosity and obscured AGN populations (Sánchez-Sáez et al., 2019). The main AGN selection in optical comes from the use of the emission line ratios and BPT diagrams (e.g., Kauffmann et al., 2003; Kewley et al., 2006). Figure 2.14 shows the optical classification using BPT diagrams which is based on the four optical line ratios [OIII]/Hβ, [NII]/Hα, [SII]/Hα, and [OI]/Hα using of samples from Kewley et al. (2006). Optical data are often combined with X-ray data for selecting AGN, e.g., through the X-ray-to-optical flux ratio (e.g., Pović et al., 2009; Pović et al., 2012; Mahoro et al., 2017).

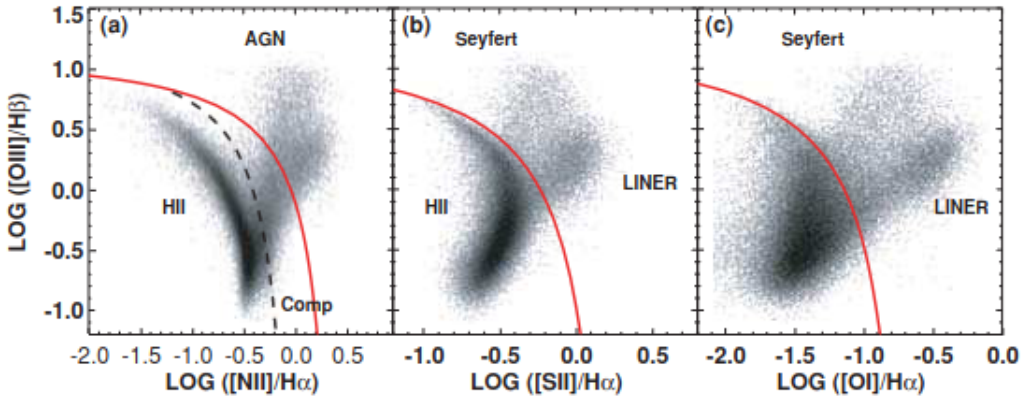

Figure 2.14: (a) Diagnostic diagram for SDSS galaxies with S/N $>$ 3 showing [NII]/Hα vs. [OIII]/Hβ. The dotted line is the Kauffmann et al., 2003 classification line while the solid line represents the Kewley et al., 2001 extreme starburst line. Two diagnostic diagrams are provided: (b) the [SII]/Hα vs. [OIII]/Hβ; and (c) the [OI]/Hα versus [OIII]/Hβ. Credit: Kewley et al., 2006.

IR selection

The IR measurements provide details on the characteristics of dust, which mostly produces blackbody radiation at temperatures around 1500K (Ogawa et al., 2021). They are helpful for identifying a specific subgroup of AGN, and to find dust-obscured AGN (Bickley et al., 2023). There has been significant progress recently in the identification of IR AGN using the broadband photometry in MIR, including the selection techniques based on Spitzer IRAC colors, WISE colors, SED decomposition technique, and Herschel observations in FIR (e.g., Assef et al., 2013; Li et al., 2020). MIR observations are effective at identifying those severely obscured, specifically undetected in X-rays (e.g., Netzer, 2015; Ji et al., 2022; Zhong et al., 2022). The MIR selection of AGN is based on separating the roughly power-law AGN spectra from the blackbody star spectrum of galaxies. AGN can

be distinguished from stars and galaxies using MIR data, which also has the advantage of being sensitive to sources with the highest redshift and being less prone to dust extinction (Stern et al., 2012). This was made possible by the Spitzer Infrared Array Camera (IRAC), which had high sensitivity and effective mapping, and simple color cuts have been used to detect AGN in IR (Stern et al., 2012; Assef et al., 2013; Lyu et al., 2022).

In addition, from the IRAC color-color diagram which was constructed by Donley et al. (2012), on a sizable sample of galaxies in the COSMOS field, it is possible to select IR AGN. Numerous previous surveys with IRAC photometry have shown that this selection have successfully detected IR AGN at high redshifts (see, e.g., Stern et al., 2012; Ji et al., 2022). The IR technique also used as a clear prediction of any torus model in a broad IR SED with a total luminosity (Netzer, 2015). Figure 2.15, showing an example of MIR color-color diagram of COSMOS field, sources selected by WISE showing WISE W1 − W2 plotted against IRAC [5.8] − [8.0]. In which W1 − W2 $\geq$ 0.8 to be selected as AGN using WISE and 123 are AGN according to their IRAC colors.

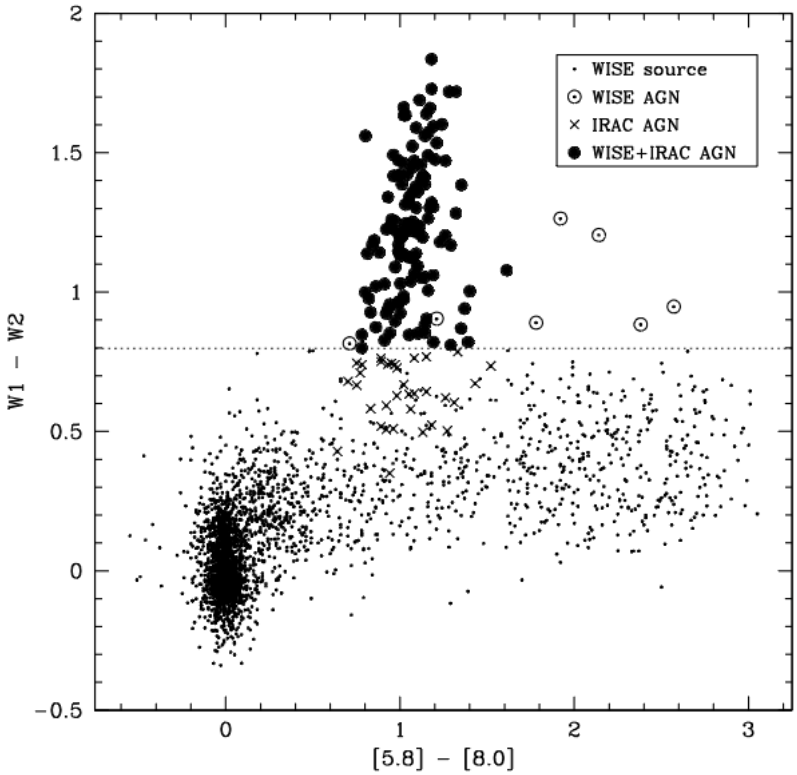

Figure 2.15: An example of AGN selection in MIR. Credit: Stern et al., 2012.

Radio selection

Since the radio wavelength are less influenced by dust and can pass through the dusty atmospheres around the AGN, radio surveys provide a means of looking for the obscured nuclei (Park et al., 2008). Since the radio emission is produced by synchrotron radiation, which is created by high-energy electrons within jets or lobes that radiate from the central area of AGN basically from SMBH, radio selection is useful tool to study the relativistic jet and lobes (e.g., Padovani et al., 2017; Krezinger et al., 2024). Strong evidence for the presence of an AGN is provided by these jets, which frequently have an extended lobe and a compact core (Padovani et al., 2017).

2.3 Infrared luminosity of AGN

In the MIR and FIR, thermal (dust) emission contributes significantly to the bolometric luminosity of AGN. Large dust grains are the source of the FIR emission, and all of them are heated by stars that have formed recently or in the past. Therefore, it is crucial to determine whether the source fueling the IR emission originates from scattered star formation in the host galaxy or (re-)radiated light from the AGN in order to obtain a quantitative picture of the contribution of AGN to the overall energy production of distant galaxies (Sturm et al., 2002). In the FIR and submillimeter wavelength ranges, we receive about half of the light emitted from evolving galaxies in the early Universe (Lutz, 2014). The Infrared Astronomical Satellite (IRAS) mission was the first to employ FIR emission as a tool to investigate galaxy formation (Lutz, 2014). The first deep surveys at MIR and FIR wavelengths were obtained by the IR Space Observatory (ISO); these surveys found a strong evolution of the luminosity function out to $z \approx 1$, and they supported a possible extrapolation that these dusty galaxies make up the cosmic infrared background (CIB). Additionally, ISO was the first to apply rich MIR spectra as a technique for examining the physical parameters and energy sources of dusty galaxies (Genzel, 2000). With launching of Spitzer, massive galaxies at redshifts z $>$ 6 have been discovered, which have also directly detected dust-enshrouded star formation, re-solved the cosmic background into the dusty infrared-luminous galaxies that comprise it, and measured the universe's star formation history up to $z > 3$ (Soifer et al., 2008).

Space missions with small 60 – 80 cm diameter primary mirrors, like ISO, Spitzer, and AKARI, were strongly limited by source confusion when aiming for the crucial deep FIR surveys, with this mission IR luminosity can introduce a large bias into high redshift samples (Lutz, 2014). During its operation from 2009 to 2013, the European Space Agency's Herschel Space Observatory significantly reduced confusion levels by meeting the need for a combination of sensitivity and big aperture (3.5 m) spanning the complete FIR and submillimeter wavelength range for the first time (Pilbratt et al., 2010). Many of AGN studies in FIR have been derived from Herschel photometric surveys and focused observations made with the Photodetector Array Camera and Spectrometer (PACS) (70, 100, and 160 μm; Poglitsch et al., 2010) and Spectral and Photometric Imaging Receiver (SPIRE) (250, 350, and 500 μm; Griffin et al., 2010) instruments employing their camera modes.

The IR emission comes from both the accretion disk and objects surrounding the SMBH, such as the torus (e.g., Padovani et al., 2017; Ramos Padilla et al., 2020). Because of the dusty environment around the accretion disk, which reprocesses received X-rays from the central engine and re-radiates these photons at IR wavelengths, AGNs are frequently luminous in the mid-IR (Park et al., 2008). IR luminosity is an accurate method for identifying galaxies with AGN, including obscured AGN (e.g., Bornancini et al., 2022). Studies have shown that measuring AGN luminosity using IR emission is more accurate than other methods because IR emission is not absorbed by dust and gas, can penetrate through the dusty atmosphere e.g., Park et al., 2008; Iwasawa et al., 2011; Netzer, 2015; Matsuoka, 2015). Using a MIR based approach for AGN selection, Stern et al., 2005 established an empirical criterion based on the distribution of over 10,000 spectroscopically detected sources from the AGN and galaxy evolution survey to distinguish active galaxies from other sources. Although different studies show the relation between SF and FIR AGN luminosity, which leads to further insight on galaxy evolution (e.g., Matsuoka, 2015; Dai et al., 2018).

2.4 Summary of the main findings on type-2 AGN, in the optical and infrared

Despite the difficulties caused by dust obscuring, studying type-2 AGN with optical spectroscopy has produced important results. One of the most important finiding is that the confirmation of the obstruction of type-2 AGN by dust. An examination of the optical spectrum indicates a reddening in comparison to unobscured AGN, which is indicative of dust obstructing the light coming from the central engine. Certain type-2 AGN still show modest, narrow emission lines from the NLR, these lines yield important details about the ionized gas surrounding the SMBH. They provide information about the temperature, movements, and composition of the gas (Mignoli et al., 2013). The ionized gas in the AGN's nuclear light region is likely linked to the nuclear star formation and surrounds SMBH studying this region makes it possible to obtain information about the host galaxy's star formation history indirectly by analyzing the metal content of the ionized plasma in the AGN NLR (Feltre et al., 2017). The NLR, which is less affected by dust obscuration, may be a more reliable measuremnt of activity in type-2 AGN.

Type-2 AGN can be used in FIR surveys with AKARI and Herschel to explore the relationship between star formation and SMBH accretion luminosity. It is found that FIR and AGN luminosities show a positive linear relationship across a large dynamic range when predicting AGN luminosities from the emission lines (Matsuoka, 2015). Optical spectrum in combination with infrared offers important information on the dust obscuration, the characteristics of the surrounding gas, and the black hole's surrounding geometry. The spectroscopic properties of type-2 AGN have shown the correlation between black hole accretion luminosities and SF by utilizing a sample of type-2 AGNs at $z < 0.22$, identified by the FIR surveys conducted with Herschel and AKARI. Furthermore, studies have been carried out on the scaling relations between SMBH masses and emission line properties, such as narrow emission line luminosity, in type-1 and type-2 AGN, to determine whether these relations persist when the central areas are hidden, indicating that both forms of black hole accretion may have a similar underlying physical process (e.g., Kaspi et al., 2005). On the other side, true physical differences have been found between type-1 and type-2 AGN (e.g., see Netzer, 2015 for a review).

Chapter 3

Data sources and instrumentation

Lockman-SpReSo survey

Lockman-SpReSO is one of the deepest optical spectroscopic surveys of FIR-selected galaxies ever made. Furthermore, it is a deep optical spectroscopic survey of a comprehensive sample of galaxies previously detected at the highest depth in X-ray, FIR, and sub-millimeter using, respectively, XMM, Spitzer, Herschel, and radio observations spanning the central 24 x 24 arcmin^2 of the Lockman Hole field (northeastern region) (e.g., Gonzalez-Otero et al., 2023). Overall, the Lockman-SpReSO survey is dedicated to providing high-quality optical spectroscopic follow-up of the FIR sources from the Herschel Space Observatory-PEP survey. This survey involves deep PACS observations of galaxy clusters and field galaxies at 70, 100, and 160 μm. Compared to other deep spectroscopic surveys, the Lockman-SpReSO survey is 1.2 times deeper than the VVDS ultra-deep survey. It also offers larger spectral coverage and continuum sensitivity compared to AEGIS-DEEP and z-COSMOS surveys. These benefits are primarily due to the use of a powerful instrument like OSIRIS and the collecting surface of a 10-meter class telescope. Even with the later releases, the sensitivities of the Lockman survey are higher than those of surveys with smaller collecting areas, such as the SDSS survey (Le Fèvre et al., 2013; Gonzalez-Otero et al. 2023). Furthermore, our of the optical counterparts of the Herschel FIR sources, the Lockman-SpReSO survey is the most comprehensive, extensive, and statistically significant to date.

The Lockman-SpReSo survey consists of a sample of 114 AGN with deep FIR and optical spectroscopic data out of a sample of 1144 galaxies in total. The primary goal of the Lockman-SpReSO survey is to provide a robust optical counterparts in images from the GTC/OSIRIS instrument in the SDSS r band, up to r = 24.5 mag (in AB system) of 956 objects that were chosen from the Herschel's FIR observations of the Lockman Hole field, together with a sample of additional 188 field FIR sources from the Herschel-PEP survey, for determining the evolution of fundamental parameters like extinction, SFR, and gas metallicity (Gonzalez-Otero et al., 2023, 2024).

In the following, we briefly describe the Lockman Hole field and its FIR and, in particular, optical observations carried out under our team. Since optical spectroscopic data are the main data used in this work, we also provide a brief description of the reduction of faint and bright sources. We also briefly present the final multi-wavelength catalogue compiled by the Lockman-SpReSo collaboration used in this work. Finally, we describe the sample selection of type-2 AGN used in this thesis.

3.1 Lockman Hole feild

The Lockman Hole is a sky area that is about 15deg^2 in size (60 times larger than the full moon) and is located in the constellation Ursa Major. The Lockman Hole is the cosmic window that allows for the acquisition of the clearest and deepest views of the universe at various wavelengths. As such, it has historically been the main focus of several deep surveys, providing excellent multiwavelength data sets (e.g., Egami et al., 2008; Mahony et al., 2016; Bonato et al., 2021; Jurlin et al., 2021; Belvedersky et al., 2022; Gonzalez-Otero et al., 2023). These data are crucial for describing the physical and evolutionary characteristics of the different source populations found, primarily AGN and star-forming galaxies (Mahony et al., 2016). Figure 3.1, shows the Lockman hole field observed by LOw-Frequency ARray (LOFAR), a large radio telescope.

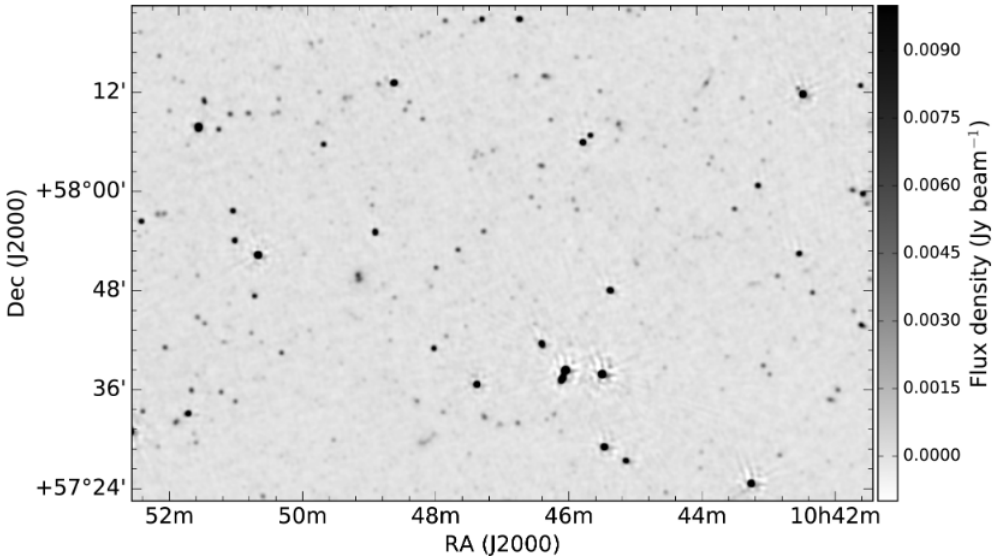

Figure 3.1: Part of the Lockman Hole field covering an area of 1.5 x deg^2. Credit: Mahony et al., 2016.

3.2 Infrared observations

Observations in FIR have been obtained using the Herschel telescope, as mentioned above. Herschel is an ESA's FIR and submillimeter space observatory that has significant NASA involvement (Dicken et al., 2023). It has two research instruments, PACS and SPIRE. PACS instrument can achieve integral-field spectroscopy and imaging photometry in the 60 - 210 μm wavelength range. It can photograph two bands simultaneously and has an instantaneous spectral coverage of about 1500 km/s and a spectral resolution of about 175 km/s. When imaging a field of 47" × 47", it is resolved into 5 × 5 pixels in spectroscopy mode. SPIRE instrument consists of a two-part system, including an imaging photometer that could capture images at 250, 350, and 500 μm, and an imaging spectrometer that could acquire spectra from 190 to 670 μm. The spectrometer offered two observing modes: low resolution, covering the full wavelength range with lower resolution, and high resolution, providing higher spectral resolution but covering a smaller wavelength range. To comprehend the significance of AGN in galaxy evolution, the Herschel observations are essential because a wide range of diagnostic data is available in the FIR/sub-mm wavelength region (Dicken et al., 2023).

The Lockman-SpReSO survey uses observations from the Herschel/PACS Evolutionary Probe (PEP) Data Release (DR1) program, which was conducted by Lutz et al., 2011. The PEP pro-

gram involved deep FIR photometric survey using Herschel telescope, focusing on deep PACS observations at 70, 100, and 160 μm of galaxy clusters and field galaxies. These observations identified sources with strong optical counterparts down to approximately 24.5 in r band and provided data on the field's central 24 x 24 arcmin^2 region at 100 and 160 μm. For the Lockman-SpReSo survey, a catalogue of Herschel/PACS fluxes detected by the PEP project at 100 and 160 μm, as well as Spitzer/MIPS (Multi-band Imaging Photometer) at 24 μm, was used. This catalog includes positions and fluxes and, after applying the constraint imposed by the coordinates and discarding MIPS sources with no fluxes at 100 and 160 μm, the survey obtained a total of 1181 sources for the FIR catalogue (referred to as the PEP-catalogue).

3.3 Optical observations

The OSIRIS spectrograph mounted on the 10.4 m GTC telescope at the Roque de los Muchachos Observatory in La Palma, Canary Islands were used in our optical observations (Cepa et al., 2008). For the spectroscopic modes, low-resolution grisms (250, 500, and 1000), with intermediate (R = 2500) and high-resolution (R = 5000) were employed. The GTC is the largest optical telescope in the northern hemisphere with a segmented main mirror comparable to a circular aperture with a diameter of ten meters. The instrument is mounted at the telescope's Cassegrain focal station. In addition to traditional broad-band imaging and long-slit spectroscopy, OSIRIS offers charge-shuffling, multi-object spectroscopy, and imaging with narrow-band tunable filters. With a total field of view of 7.8 × 8.5 arcmin^2 (7.8 × 7.8 arcmin^2 unvignetted) and 7.5 × 6.8 arcmin^2 for direct imaging and MOS, respectively, OSIRIS spans the wavelength range from 0.36 μm to 1.05 μm (Lombardi et al., 2022).

Using OSIRIS instrument, the Lockman SpReSo survey aimed to achieve a S/N $>$ 3 in the continuum for all objects. The observation time varied depending on object brightness, with 1 to 1.4 hours per mask for brighter objects and up to 3 hours per mask for fainter objects. The sample was divided into two parts based on magnitude: faint subset ($20 \leq r \leq 22$ mag, 993 sources) and bright subset ($16.8 \leq r \leq 20.6$ mag, 151 sources), with a small overlap existing for r = 20 to 20.6 mag for 93 sources.

The **faint subset** was observed using the OSIRIS instrument at the GTC telescope. The blue and red regions of the optical spectrum were observed at various resolutions using a mix of masks and grisms. To remove the sky background, they were viewed using a narrower 3 arcsec slit and an ON-OFF-ON observing mode. A total of 48 masks were created to cover 92% of the faint subgroup objects to achieve a S/N $>$ 3. Observations were performed with the airmass 1.2 and excellent seeing conditions 1 arcsec. The **bright objects** were observed using two separate telescopes with multi-object spectrographs: 4.2m William Herschel Telescope with the AutoFib2+WYFFOS (AF2), and 3.5m WIYN telescope with the HYDRA spectrograph. The targets were divided by color (blue and red) and observed in multiple configurations, but not all observations were completed. To fill in the gaps, the WIYN telescope with the HYDRA spectrograph was used, observing objects not seen by the WHT/AF2 and some overlapped objects for comparison. All observations aimed for a higher S/N $>$ 3 compared to the faint subset, likely due to the expectation of these objects being at a lower redshift. To remove the sky background for the brighter sources, 10 arc-second slits were used. All observations are explained in detail in (Gonzalez-Otero et al., 2023).

Since different instruments and telescopes were used to collect the data, the nature of the data varies for each subset of the survey. As a result, each set of data, for faint and bright subsample of sources, went through a separate data reduction process, although in some cases the same techniques have been used. The all data reduction and calibration (wavelength and flux)

process was explained in (Gonzalez-Otero et al., 2023). The ultimate goal of data processing was to produce a final 1D spectrum of each source that would disclose the characteristics of continuum, emission, and absorption lines, and their nature. The procedure involves obtaining the average spectrum, since for each source multiple observations were available. Figure 3.2 shows an example of OSIRIS 1D spectra in blue and red of an individual source at redshift of 0.421, while Figure 3.3 shown an example of HYDRA1D spectrum of another source at redshift of 0.029. In this work we used already reduced and calibrated spectra obtained obtained through the Lockman-SpReSo collaboration.

The final LH catalogue is the result of merging three catalogues: the PEP catalogues, FT catalogues (Fotopoulou et al., 2012), and OSIRIS catalogues. The process involves two steps to create the final multi-wavelength catalogue. Firstly, the PEP catalogue is compared with the OSIRIS mosaic target list, resulting in 991 matched targets. Secondly, the PEP catalogue is compared with the FT catalogue, revealing 1063 common objects. After removing duplicates, 956 primary sources are compiled, which are the FIR counterparts. Finally, the final catalog consists of a total of 1144 sources, as summarized in Table 3.4, combining the primary catalogue (FIR counterparts) and complementary sources from the OSIRIS mosaic.

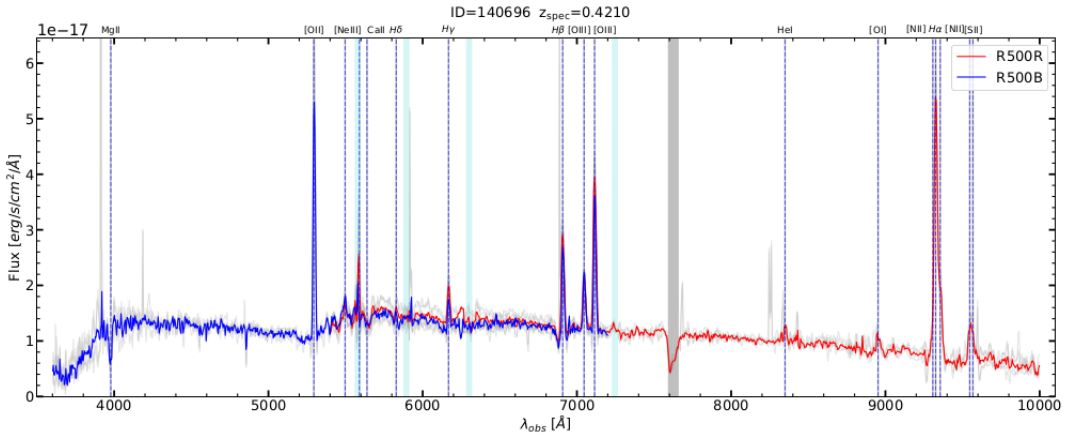

Figure 3.2: Example of the final 1D OSIRIS blue and red spectra obtained for a faint subset source at z = 0.421. Credit: Gonzalez-Otero et al., 2023.

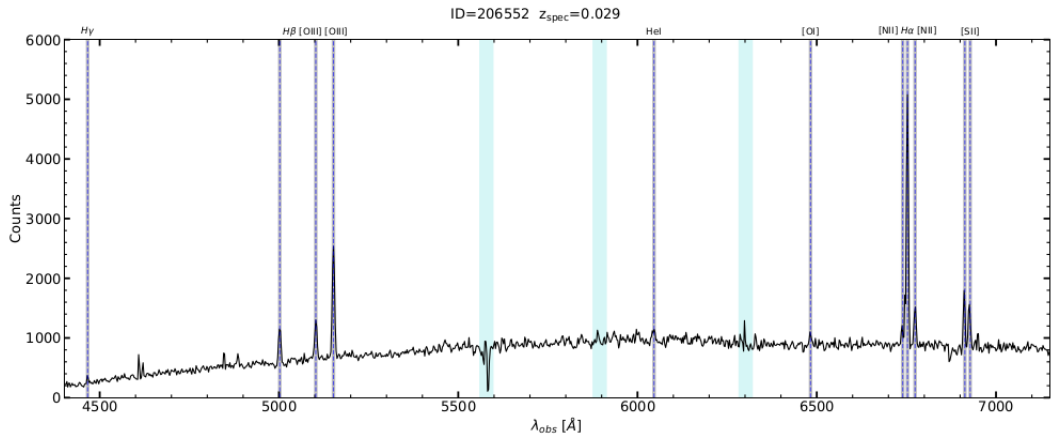

Figure 3.3: Example of the final 1D OSIRIS blue and red spectra obtained for a faint subset source at z = 0.029. Credit: Gonzalez-Otero et al., 2023.

The Lockman-SpReSo survey obtained spectroscopic redshift measurements for 357 sources. The spectroscopic redshift measurements were measured using two methods. The first method used existing data for single spectral lines, which has been used for 89 sources. The second method

involved using multiple spectral lines and was applied to the remaining 268 sources.In Figure 3.4, the table shows the number of observed sources as faint and bright subsets, the measured spectroscopic redshift, and the principal source catalogue.

CAT	Preliminary object Type	Catalogue	Observed	Observed faint	Observed bright	Object cont.	z_{spec}	z_{spec} faint	z_{spec} bright	z_{sup}
1	X-rayPoint + CatVarStars	45	43	41	6	39	30	28	4	3
2	High-Velocity Stars	93	85	14	80	80	1	–	1	–
3	Radio Galaxies	17	13	13	1	7	5	5	1	1
4	FIR	902	838	772	106	503	305	258	76	90
5	1 + 4	12	11	11	1	11	7	7	1	3
7	3 + 4	4	4	3	1	4	3	2	1	1
12	1 + 2	1	1	1	1	1	1	1	–	–
20	RedQSOs(W4)	23	21	21	–	2	2	2	–	–
21	RedQSOs(FIRST)	5	5	5	–	1	–	–	–	–
23	20 + 3	2	1	1	–	1	–	–	–	–
24	20 + 4	38	33	33	–	5	1	1	–	1
25	21 + 2	1	1	–	1	1	1	–	1	–
26	21 + 3	1	1	1	–	1	1	1	–	–
	TOTAL	1144	1057	916	197	656	357	305	85	99

Figure 3.4: This table has been adapted from Gonzalez-Otero et al., 2023. It gives the summary of observed objects, including their type and measured redshifts.

3.4 Type-2 AGN sample selection

Our initial sample of AGN, detected in FIR with optical counterparts, has been selected from Gonzalez-Otero et al. (2023) catalogue. In this work, the authors selected in total 114 AGN using SED fitting from IR templates of Dale et al. (2014). A ratio of spectral lines in the BPT diagram also has been used to separate AGN from SFGs. We downloaded all AGN 1D reduced spectra (in both blue and red parts of the spectrum) using the Lockman-SpReSo survey database. From the total sample of AGN, using visual inspection of spectra and the presence/absence of broad components in their emission lines we classified all AGN as type-1/type-2, respectively. Out of 114 AGN, 43 have been classified as type-1 and 71 as type-2. These selected type-2

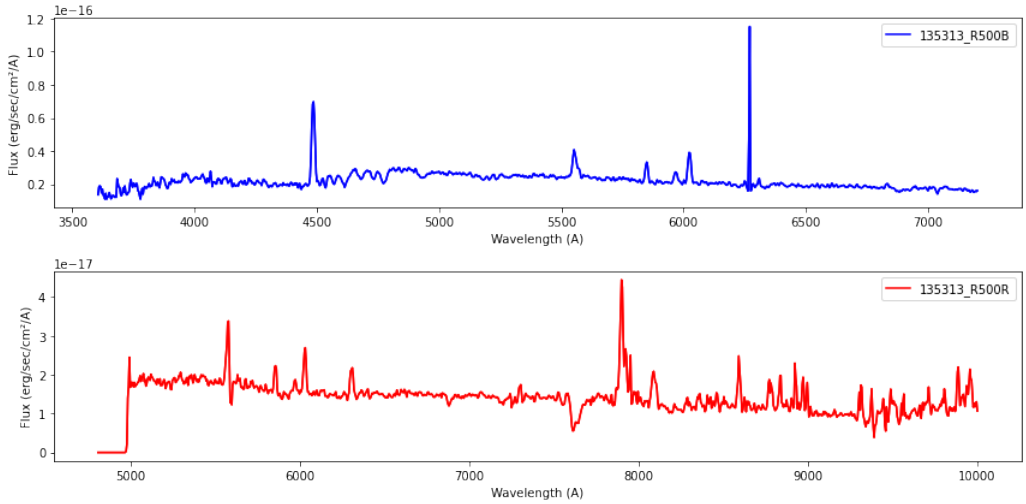

Figure 3.5: Example of the blue (top) and red (bottom) spectra of one type-2 AGN in our sample at z_{spec} = 0.2202.

AGN form a sample analysed in this work. Figure 3.5 shows an example of one selected type-2

AGN spectra in blue (top) and red (bottom) part of the optical spectrum, before being moved to the rest-frame. The spectroscopic redshift distribution of the total sample and type-2 AGN sample is shown in Figure 3.6 (in red solid, and blue lines, respectively) the median redshifts for both samples are quite similar, with the total sample at $\approx$ 0.44 and the type-2 AGN at $\approx$ 0.45. Figure 3.7 shows the magnitude distribution of both the total sample and type-2 AGN

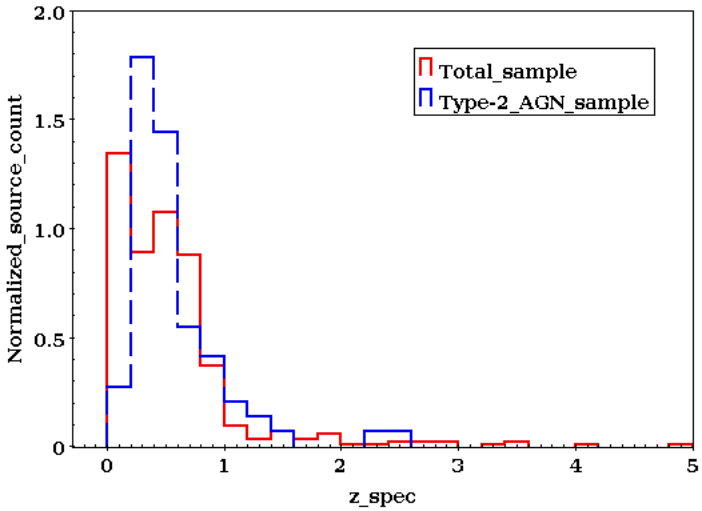

Figure 3.6: Redshift distribution of total (red solid line) and type-2 AGN (blue dashed line) samples in the Lockman-SpReSO survey.

samples in the B (left) and R (right) filters. In the blue filter, the median magnitude for type-2 AGN is (22.61) compared to the total galaxy sample (23.67). In the red filter, both samples show similar median magnitudes, 21.48 for the total sample and 21.22 for type-2 AGN, with a total sample covering a larger range of values.

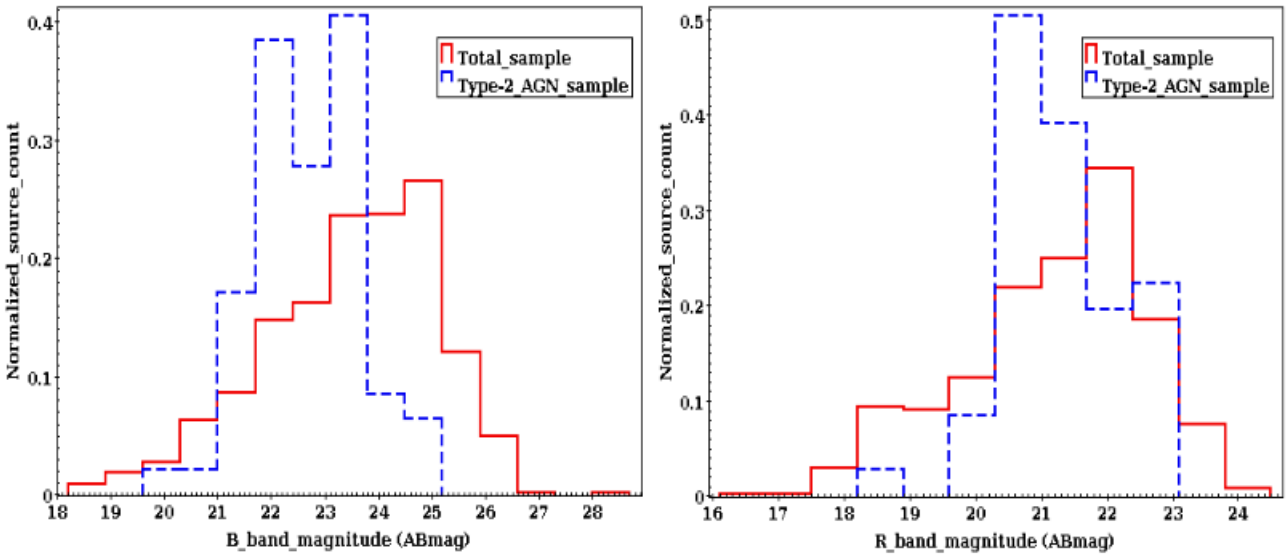

Figure 3.7: Magnitude distribution in B and R bands for the total sample (red solid lines) and type-2 AGN sample (blue dashed lines).

Chapter 4

Methodology

In this chapter, we describe the method and the software used in this work, basically the tools. Firstly, we extract the sample from Gonzalez-Otero et al. (2023), as described in the previous section. Secondly, the spectra are inspected using IRAF and SPLAT to identify sources and confirm the nature of type-2 AGN. Thirdly, the blue and red spectra are combined using SPLAT. Fourthly, we run the STARLIGHT code for all combined type-2 AGN to obtain the emission-line spectra, allowing us to examine a variety of features. Using LMFIT, we measure the properties of identified emission lines, such as the EW, FWHM, and intensity by fitting the line with a single Gaussian function. To ensure accuracy, we test our line measurements in both IRAF and SPLAT to make sure that everything is correct. For catalogue compilation, we use TOPCAT. In continuation, we describe in more detail the tools that we use, while the details regarding each step are given in capter 5.

- **STARLIGHT: Spectral Stellar Populations Synthesis Code**
  STARLIGHT is a FORTRAN 77 program and a spectral synthesis code, that fits an observed spectrum O_λ to a model M_λ, that merges up to N_* single stellar populations (SSPs) with distinct ages and metallicities from different stellar population synthesis models (Cid Fernandes et al., 2005). STARLIGHT is a code used to derive stellar population and stellar age, it is a stellar population synthesis code used for fitting spectra and for analysis of SED (e.g., Cid Fernandes et al., 2005; Pović et al., 2016; Mahoro et al., 2022).

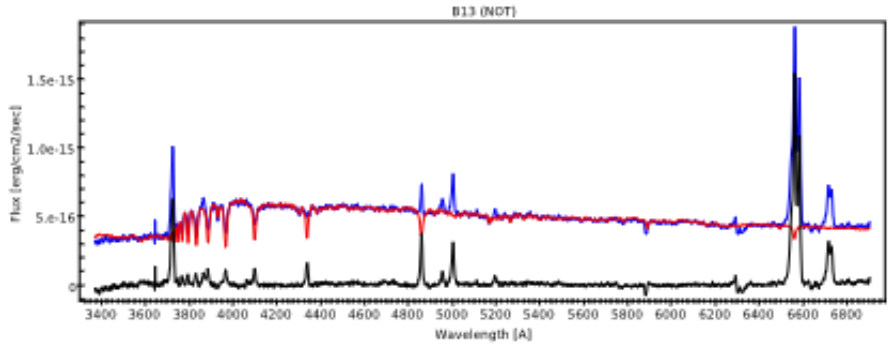

Figure 4.1: Example of STARLIGHT fits. Credit: Pović et al., 2016.

Useful findings have been obtained for a wide range of objects, including ultra-compact blue dwarf galaxies, low luminosity AGN, and normal galaxies (from elliptical to spiral). It can also be used to determine the characteristics of the stellar population mixes, create a stellar template to facilitate the measurement of emission lines, or even calculate velocity

dispersion (Cid Fernandes et al., 2005). In this work, we used STARLIGHT to obtain the emission-line spectrum by subtracting absorption and continuum part of the spectra from the original spectra, obtained from the best fit, from the original spectrum. We followed the same process as explained in Pović et al. (2016). To do the fitting, STARLIGHT collects N_* spectra from a user-specified base of individual populations to find linear combinations that correspond to an input observed spectrum. Figure 4.1 gives an example of one spectrum fitted using STARLIGHT, where the original spectrum is shown in blue, the best template found by STARLIGHT is in red, and the final emission spectrum is in black (Pović et al., 2016). This is exactly the process that we are following in this work as well. For a good stellar template to remove from data and to facilitate emission line analysis, these parameters are required: the full synthetic spectrum M_λ, the population vector for light-fractions $\vec{x}$, mass-fraction population vector $\vec{\mu}$, stellar velocity shift (v_*) dispersion and extinction of stars. During the process of fitting, emission lines, bad pixels and unknown features are masked by assigning $W_{lambda} = 0$ to those regions and getting a good fit for the continuum plus the absorption spectra. Finally, from the code output, we can get the 'population vector' (xj), which is the fraction of the total light that each simple stellar populations (SSP) contributes to the fitting (Mahoro et al., 2022).

- **LMFIT**[1] **(Non-Linear Least-Squares Fitting)**
  LMFIT is a Python package that provides a simple and flexible approach to curve-fitting problems. It is a useful tool for developing complex fitting models for non-linear least-squares problems (Newville et al., 2016). LMFIT's improvements to optimization and data fitting challenges include the use of parameter objects as variables rather than simple floats, the ease with which fitting algorithms may be changed, and the enhanced curve-fitting and confidence interval estimation possible with the Model class. Additionally, LMFIT has a large number of pre-built models for typical line forms (Newville et al., 2016). In our case, we used it to calculate the intensity, FWHM, and EW of identified emission lines, including their errors. This fitting has been done through the Gaussian fittings of emission lines. Figure 4.2 shows an example of a portion of the spectrum within a specified range, fitted using LMFIT. The original spectra are represented in blue, and the Gaussian curve is represented in red.

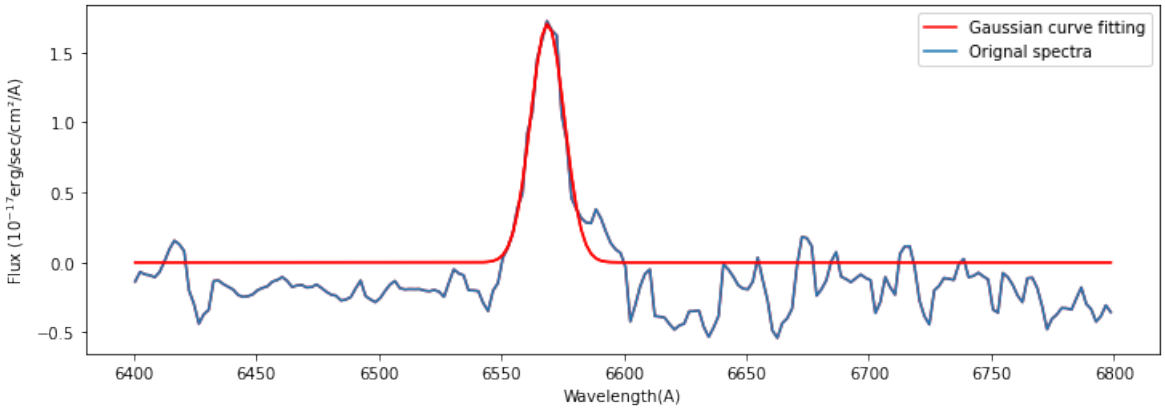

Figure 4.2: Example for LMFIT fitting adapted from Gonzalez-Otero et al. (2023) catalogue for source 128229.

- **IRAF**[2] **(Image Reduction and Analysis Facility)**

[1] https://github.com/lmfit/lmfit-py
[2] https://iraf-community.github.io/

The IRAF system offers a wide range of tools for the reduction and analysis of optical data, which is created by the National Optical Astronomy Observatory (NOAO). In addition, it is a good tool for general image processing and graphics applications (Tody, 1986). In our case, we use IRAF to calculate the line intensity, FWHM, and EW of identified emission line. Similar as above, this fitting has been done through the Gaussian fittings of emission lines. In particular, we found that in case of multiple lines IRAF works better than LMFIT to provide the emission line fits. Therefore, IRAF was used for fitting the Ha+[NII] triplet and [SII] doublet emission lines. Figure 4.3 shows an example of IRAF Gaussian fitting for Ha+[NII] triplet and [SII] doublet emission lines within a specified range.

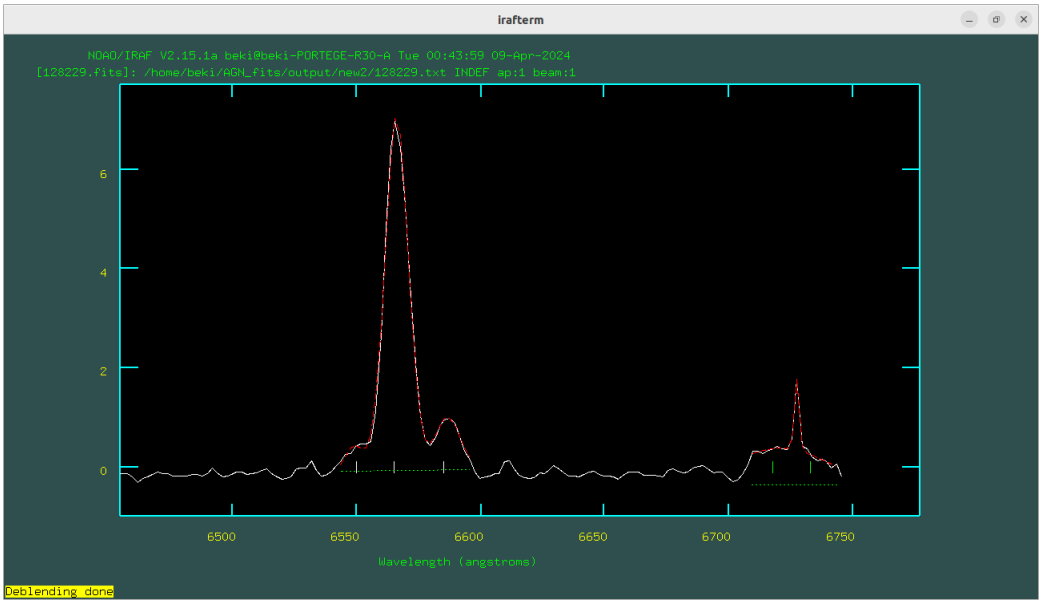

Figure 4.3: Example for IRAF fitting adapted from Gonzalez-Otero et al. (2023) catalogue for source 128229.

- **SPLAT-VO[3]: (Spectral Analysis Tool - Virtual Observatory)**
  SPLAT-VO is a graphical tool that allows to view, compare, modify, and analyze astronomical spectra. It is an extension of SPLAT (Spectral Analysis Tool, ascl:1402.007) and is equipped with features that enable it to function as a component of the Virtual Observatory (VO). Two versions of SPLAT-VO are available: one for interacting with VO tools like TOPCAT (ascl:1101.010), and another for retrieving and querying spectra from SSAP servers (Castro-Neves, 2014). The SPLAT-VO graphical application can analyze, alter, and compare astronomical spectra saved in different formats such as FITS, TEXT, and NDF/NDX. This tool can search for spectral data in a specific area of the sky, interact with the VO, read spectra from local disk files, or download them from the Internet. SPLAT-VO offers a range of analysis facilities, including the ability to fit Gaussian, Lorentzian, and Voigt profiles to emission and absorption lines, filter spectra using average, median, and line-shape window functions, perform wavelet denoising, and compute statistics. Background estimation can be accomplished by fitting a polynomial to specific parts of a spectrum or drawing an interpolated spline. Additionally, SPLAT-VO has a database of laboratory line positions to help with the identification of lines (Draper et al., 2013; Draper, 2014). In our work, we used SPLAT-VO to visualize the spectra and crosscheck the emission line spectra analysis. Figure 4.4 shows an example of SPLAT-VO Gaussian line fitting within the selected range.

[3]https://github.com/Starlink/starjava

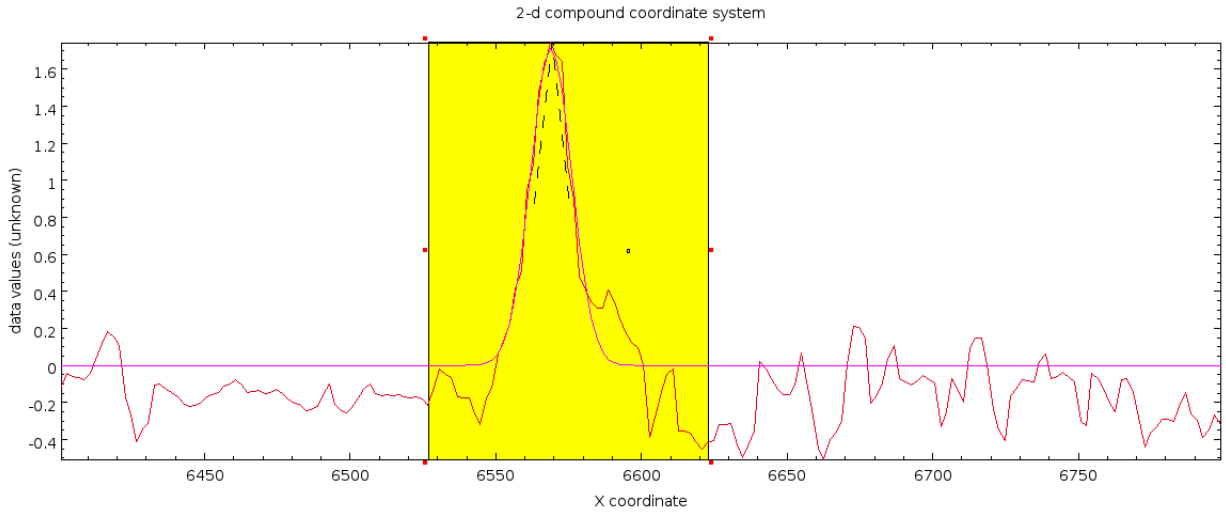

Figure 4.4: Example for SPLAT-VO fitting adapted from Gonzalez-Otero et al. (2023) catalogue for source 128229.

- **Python**

  Python is a powerful object-oriented programming language with a simple syntax that is simple to learn. Dynamic typing, very high-level data types, exceptions, modules, and classes are all present. Python is a free program. It is compatible with several other operating systems, including GNU (GNU/Linux), Unix, and Microsoft Windows (Van Rossum, 2009). For our case, we used python for data representation and analysis.

- **TOPCAT**[4] **(Tool for OPerations on Catalogues And Tables)**

  TOPCAT is a tool developed under the virtual observatory for examining, analyzing, and altering tables. It offers tools for manipulating information and data in large catalogues including visualization, cross-matching, sorting, and row selection (Taylor, 2005). In our case, we used it for making catalogs, including the final catalogue of type-2 AGN emission lines, and for statistical analysis.

[4]http://www.starlink.ac.uk/topcat/

Chapter 5

Analysis

The main part of our analysis consists of measuring the properties of identified emission lines of type-2 AGN. After extraction of spectra in blue and red part, we took a special care with their combination. Before running the STARLIGHT code, the spectra have been combined, moved to the rest-frame, corrected for galactic extinction, and K-corrected. We then run the STARLIGHT code, after masking the strong emission lines and any artefacts, to find the best fit to the continuous and absorption part of the spectrum. The best fit has been then subtracted from the original spectrum to obtain the emission line spectrum only, which finally was used for measuring teh properties of emission lines such as their intensity, FWHM, EW, and their corresponding errors. Finally, we constructed a catalogue of all measured emission lines. In the following, we describe all steps in detail.

5.1 Extraction and combination of spectra

All spectra of 71 selected type-2 AGN were obtained from Gonzalez-Otero et al. (2023). All our type-2 AGN were observed with a blue and red filter, so we extracted both blue and red spectra from the Lockman-SpReSo database. We first performed a visual inspection of all spectra to get an idea of their quality and appearance. To run the STARLIGHT code and find the best fit we need a wide range of wavelengths, covering both the blue and the red part of the spectrum, so in all cases we went through the combination of spectra.

We found two cases during the combination of spectra. Firstly, in the case of the 54 sources, there was an overlap between the blue and red continuum, which facilitated the combination of spectra. An example is shown in figure 5.1 (top plot). In this type of case, we did not have to do any continuum correction, but kept the full spectrum with the highest S/N, usually in the blue part, and added on top of it only the part of the red spectrum not covered by the blue filter, as shown in Figure 5.1 (bottom plot). Secondly, in the case of 17 sources in total, there is a gap between the two continuums in blue and red, as can be seen in Figure 5.2 (top plot). In these cases, we first equalise the two continua by subtracting or adding the middle blue or red continuum, and then follow the same procedure as in case 1. Figure 5.2 (bottom plot) shows the example of the final combined spectrum. Finally, all combined spectra have been converted into ascii files, with the corresponding wavelength and flux values, using IRAF.

5.2 STARLIGHT fittings and extraction of emission line spectra

In this section we describe the spectral fittings we carried out using the STARLIGHT code. As mentioned above, the main aim of STARLIGHT fittings is to find the best fit corresponding to

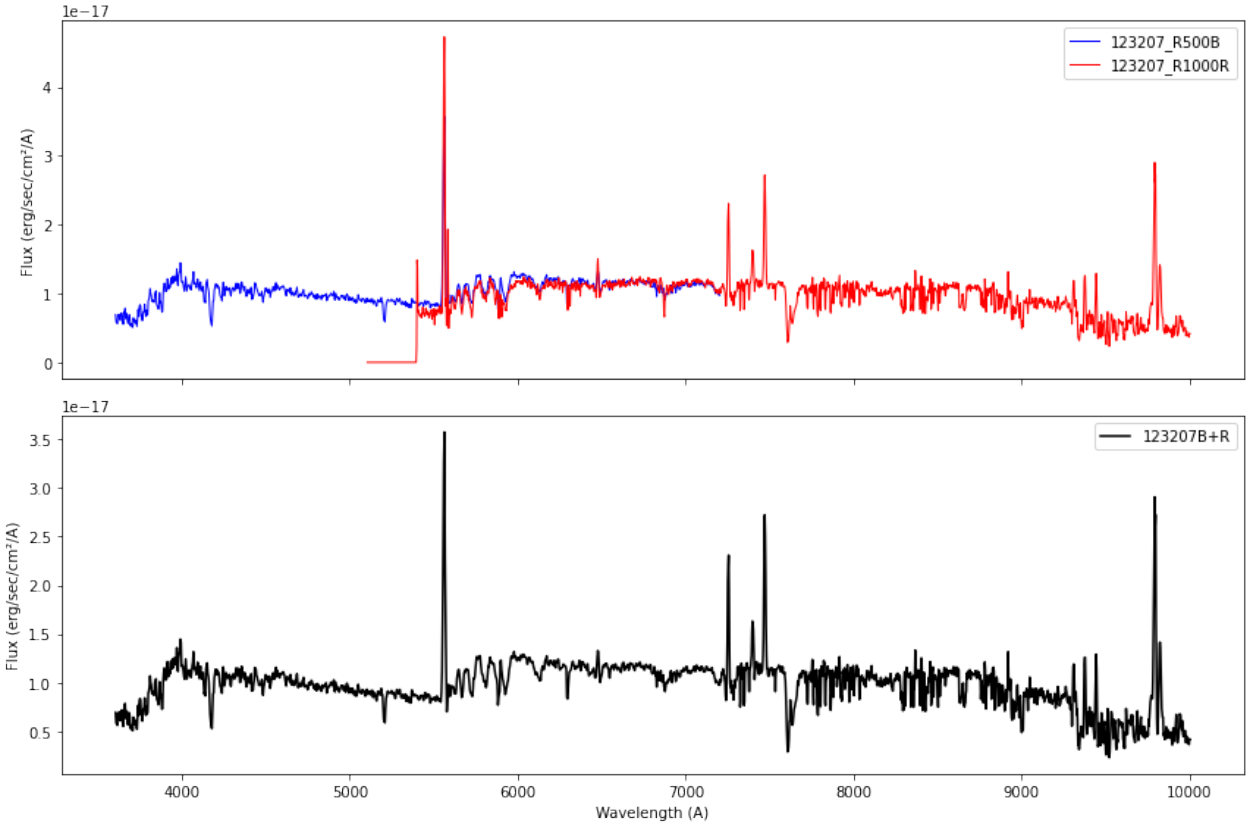

Figure 5.1: Example of the combined blue and red spectra (top), and the final combined spectrum used (bottom) of 123207 source.

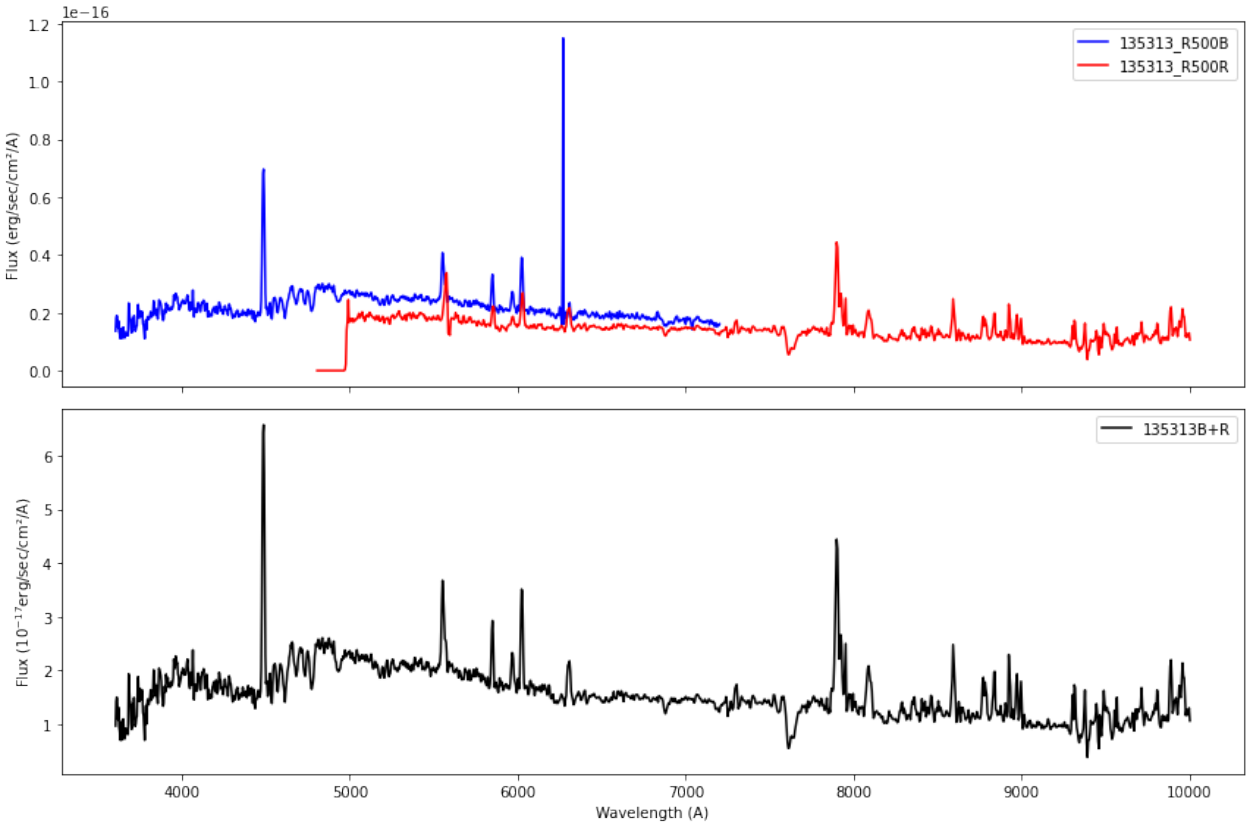

Figure 5.2: Example for fluctuation of the flux regardless of overlap (top), and the final combined spectrum used after correction for the continuum (bottom) of 135313 source.

the stellar contribution in the spectra of our type-2 AGN (continuum plus absorption spectra) and to derive the emission spectra only. Before executing the STARLIGHT code, we go through several steps which are briefly described in the following:

- **Step 1.** We use a python code to do extinction correction of all spectra combined, move them to the rest-frame and perform the k-correction. More information about the code can be seen in Pović et al. (2016). The extinction correction is used to remove dust contamination, especially in the blue part of the spectrum. The rest-frame correction moves the observed spectrum to its rest-frame, allowing the emission lines to manifest themselves at their intrinsic (laboratory) wavelengths. The k-correction is used to deal with cosmic expansion, as it corrects the observed spectrum of higher-redshift AGN to account for the expansion effect of the universe. This restores the original positions of the wavelengths in the rest-frame, allowing a better observation of the emission lines. Figure 5.3 shows an example of two spectra (shown in Figures 5.1 and 5.2) after being extinction corrected, k-corrected and moved to the rest-frame. All emission lines are now at their rest-frame wavelengths.

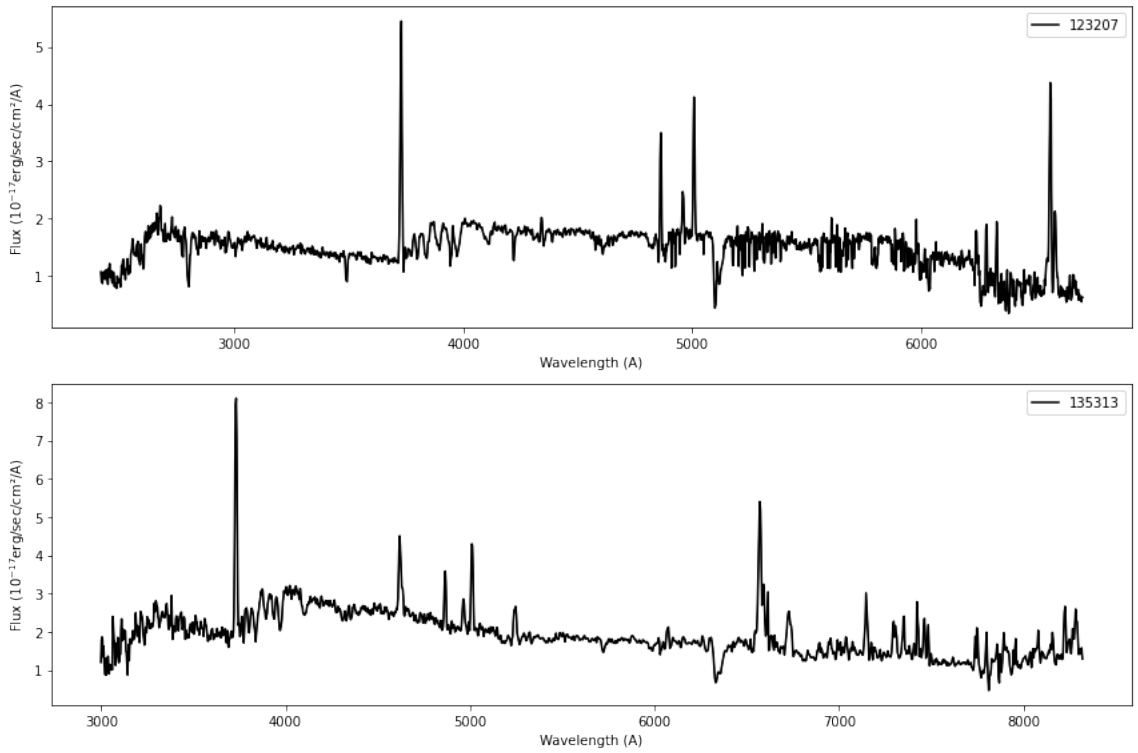

Figure 5.3: Example spectra of 123207 (top) and 135313 (bottom) sources after extinction correction, k-correction and moving of the spectra to the rest-frame.

- **Step 2.** creates a mask file. This process consists of identifying the regions that should not be modelled with STARLIGHT, such as emission lines, bad pixels, artefacts, etc. This is done by creating a plain text file in .sm format consisting of rows indicating the start and end wavelengths of each masked region and describing the wavelength regions to be omitted from the modelling. This allows STARLIGHT to provide a cleaner picture of the underlying stellar continuum, removing the type-2 AGN contribution and allowing the model to accurately fit the observed stellar contributions to the spectrum. As a result, the model can concentrate on accurately fitting the observed stellar contributions to the spectrum, producing a more realistic representation of the actual stellar populations and thus providing the best-fit absorption spectrum as the best fit. Figure 5.4 shows an example

of the STARLIGHT fittings of the 123207 and 135313 sources, where the violet areas present the regions of the input spectra that have been masked and therefore not used in the STARLIGHT fittings.

Step 3. consists of the preparation of the ”base” file. The base file tells STARLIGHT which templates should be used and combined to fit the input data. This is determined by specifying the number of stellar ages and metallicities to use and the template database. In our case, we use the templates from, with solar metallicity of Z = 0.02 and with 25 stellar ages, from 10^6 to 18^9.

Step 4. consists of preparing a configuration file for fitting every single source. This file contains the specified normalisation lambdas. The normalisation lambdas refer to the part of the spectrum where there are no emission and absorption lines, and where only the continuum part is present.

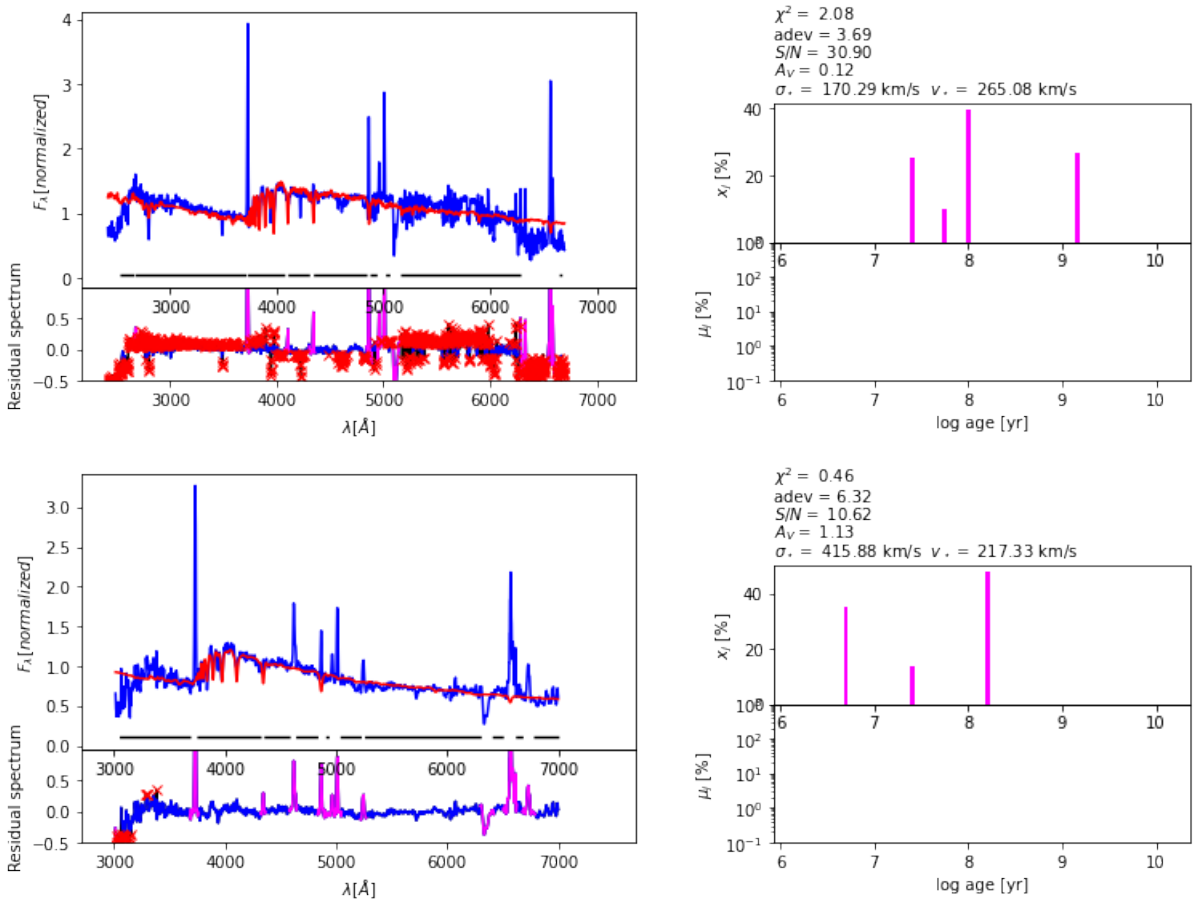

Figure 5.4: The example of STARLIGHT fittings of 123207 (top) and 135313 (bottom) sources, where the top left plot shows the original spectrum in blue and the best fit in red, the bottom left plot the residual with masked regions (in violet), and the right plot the obtained stellar populations.

Step 5. is the preparation of a grid file. This file contains all the information and the location of the other files that will be used by the STARLIGHT code to fit the input spectra. It includes the base directory in which the base file is located, the directory in which the input spectra to be fitted are located, the mask directory in which the mask files are located, and the output directory where the STARLIGHT output files will be stored. The grid file also includes the lower- and upper-lambda of the S/N window where the S/N will be measured and the lower- and upper-lambda for the STARLIGHT fitting. The last lower- and upper-lambdas specify the part of the input spectrum to be fitted. For our study, we use

this to cut the red part of the spectrum where there are strong sky emission lines and blue when there is a lot of noise in the spectrum. In addition, in the grid file we also specify the Calzetti law (Calzetti et al., 1994) to be used for the extinction correction in all cases. After finalising all the steps described above, we run the STARLIGHT code. With this, we obtained a best-fit model that represents the underlying stellar continuum emission for each type-2 AGN host galaxy. This model essentially reflects the combined light from all stars of different within the AGN host galaxy. Figure 5.4 shows the results obtained with STARLIGHT following all the steps mentioned above in the case of overlapping (top) and fluctuating (bottom) sources. The results include the chi-square value (x^2), goodness of fit (adev parameter), S/N ratio, and extinction parameter (Av). In both examples, in the upper left graph, the input spectrum is shown in blue and the best fit obtained with STARLIGHT in red. The residual is shown in the lower left graph, also showing all masked regions in violet. The right-hand plot shows the result for stellar populations of different ages obtained from the best fit, but this information was not used in this work and is shown here only as an additional information. For the STARLIGHT fits of all other sources, see the Appendix. Finally, after obtaining the best STARLIGHT fit, we proceeded to extract the

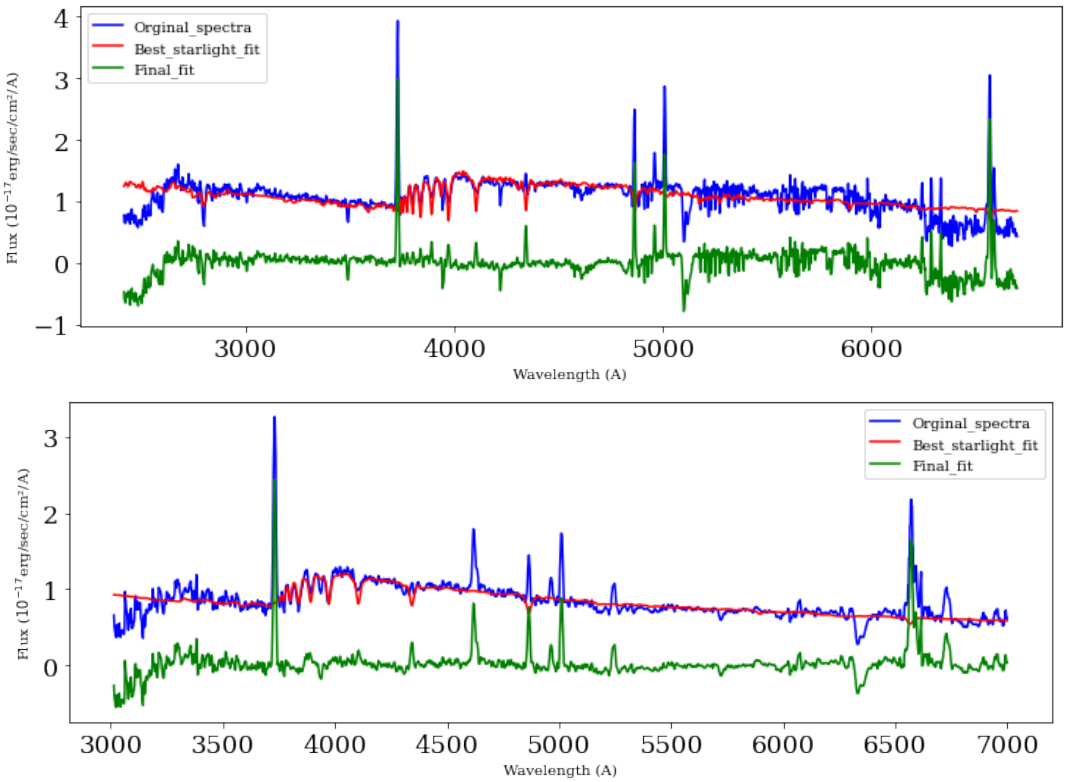

Figure 5.5: Example of the extracted emission spectra (in green) of 123207 (top) and 135313 (bottom) type-2 AGN after subtracting the best fit (in red) from the input spectra (in blue).

emission line spectra of all type-2 AGN. We subtracted the best-fit stellar model from the observed AGN spectrum, which removed the contribution from the modeled stellar continuum and absorption spectrum. This process left us with the resulting spectrum dominated by emission lines, revealing the real AGN emission line spectrum. For 3 sources with a shorter wavelength range, we didn't run STARLIGHT. Instead, we directly measured the emission line after combining and moving, k-correction, and extinction correction (see Figure 5.8). Figure 5.5 shows the extracted emission spectra (in green) of overlapping (top) and fluctuating (bottom) sources after subtracting the best fit (in orange) from the input spectra (in blue). For the rest of the sample, the figures are given in the Appendix.

5.3 Measurements of emission line properties

After obtaining the emission line spectra of all type-2 AGN in our sample, we proceeded to measure the emission line properties. To do so, we used the tools LMFIT, IRAF and SPLAT (see section 4) for the line measurements, with LMFIT being the main tool. The results were cross-checked with the other two tools. For each identified emission line, we measured the line intensity, FWHM and EW. We performed the following steps:

- **Identification of sky lines**
  In many cases, we observe strong emission lines coming from the sky (hereafter referred to as sky lines), as an emission from the Earth's atmosphere. These sky lines may affect the process of identifying emission lines related to AGN activity, and may also fall in the same wavelength range as some of the AGN emission lines. Therefore, we first proceeded to the identification of the sky lines. For this purpose, we used a detailed ESO catalogue of the sky emission lines, which covers all sky lines in the wavelength range $\approx$ 3100 - 10400Å. The figure 5.6 shows as an example a small wavelength range with sky emission lines identified in the ESO database. To identify the sky lines in our spectra, we use the wavelengths of lines as measured in the original spectra, before the spectra have been moved to the rest-frame.

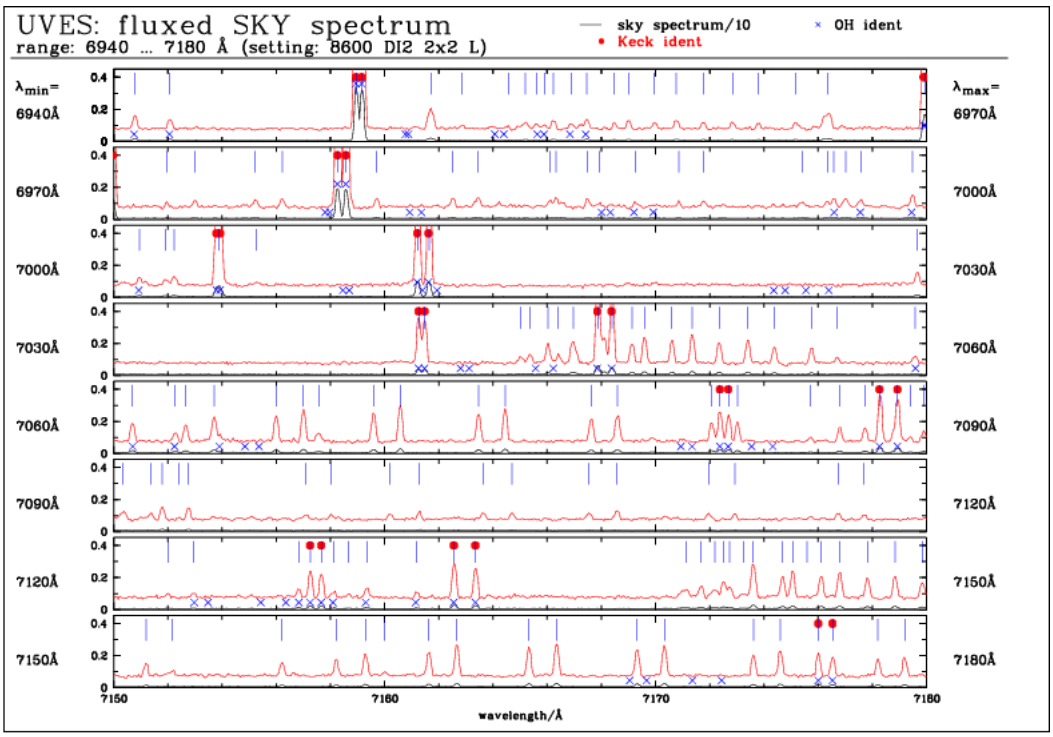

Figure 5.6: Example of the sky emission lines in the ESO database, in the indicated wavelength range. Image credit: ESO.

- **Identification and measurement of emission lines**
  After identification of sky lines, we proceed to identify emission lines in our sources primarily based on their rest-frame wavelengths, as detailed in Vanden Berk et al. (2001). Common lines analysed are Balmer lines (Hα, Hβ, Hγ, Hδ), and forbidden lines such as [OII]3727 and the two lines of [OIII]5007, 4959, [NII]6550, 6585, and [SII]6718, 6733. In addition to the optical lines mentioned above, some UV lines such as Lyα, [Al II]2670, [Mg II]2800, and [He I]3890 lines are also fitted. To accurately measure line parameters,

Gaussian profiles were fitted to the emission lines using the LMFIT package. This method allowed for precise measurements of line intensity, EW, and FWHM. Figures 5.7 and 5.8 show an example of LMFIT line fitting in optical and UV, respectively, of three sources. For the rest of the sample, the fittings are shown in the Appendix.

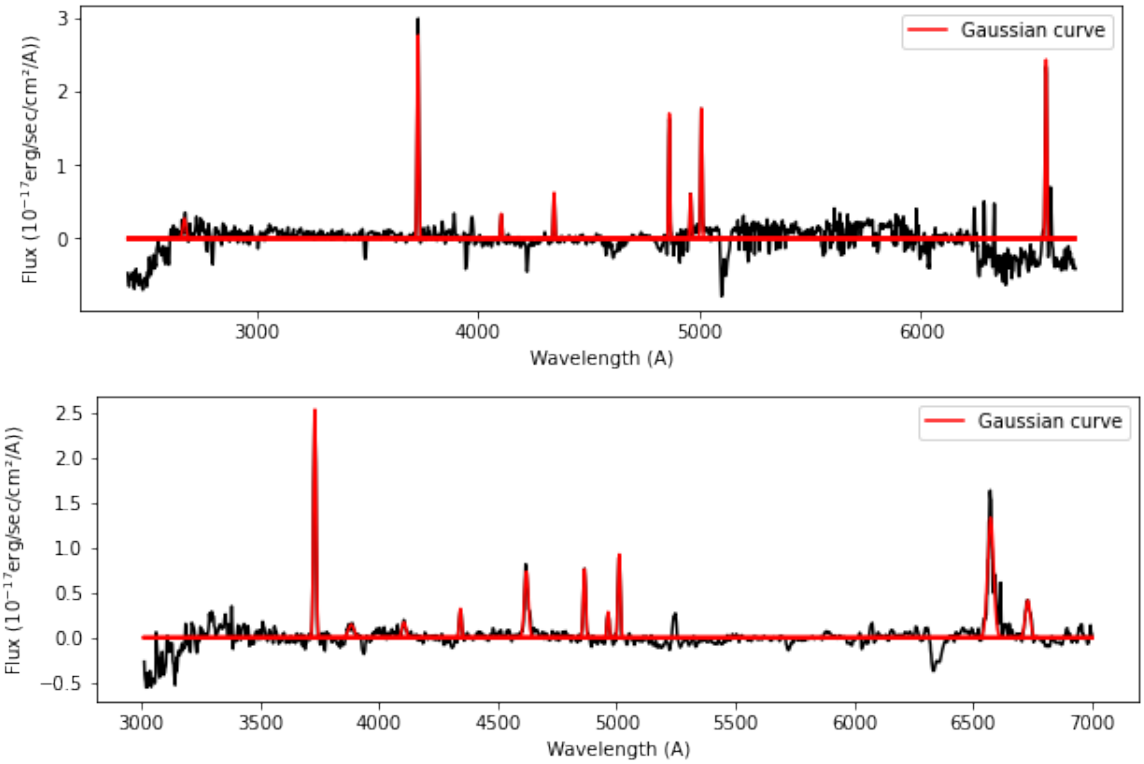

Figure 5.7: Example of the Gaussian fitting for emission line measurement of 123207 (top) and 135313 (bottom) source (in red).

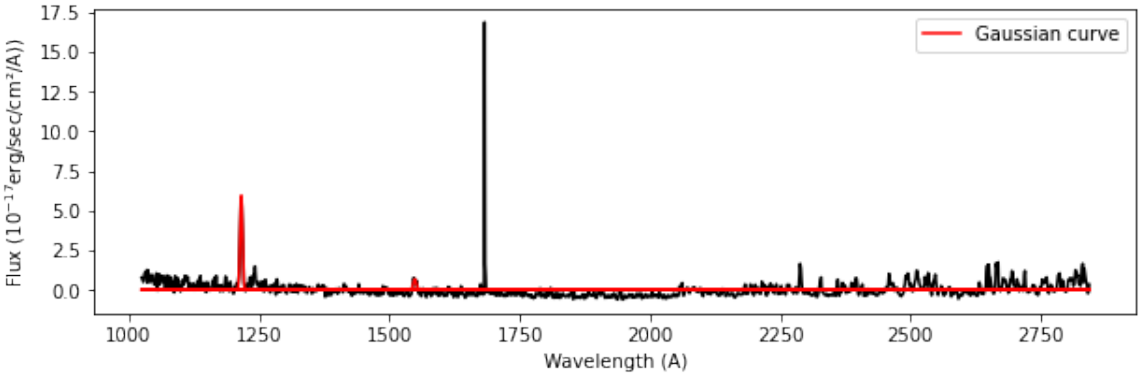

Figure 5.8: An example of UV lines, particularly Lyα, identified in 206603 sources that have also been fitted.

Very often we found difficulties in fitting Hα+[NII] triplet and [SII]6718, 6733 doublet lines using LMFIT. Therefore, we repeated fittings using also IRAF tool fitting the triplet lines and doublet lines simultaneously using the following ranges: 6544-6556 $\AA$ for [NII]6550, 6400-6765 $\AA$ for Hα, 6578-6594 $\AA$ for [NII]6585, 6708-6726 $\AA$ for [SII]6718, 6726-6742 $\AA$ for [SII]6733. Figure 5.9 gives an example of Hα+[NII] and [SII]6718, 6733 fittings using IRAF.

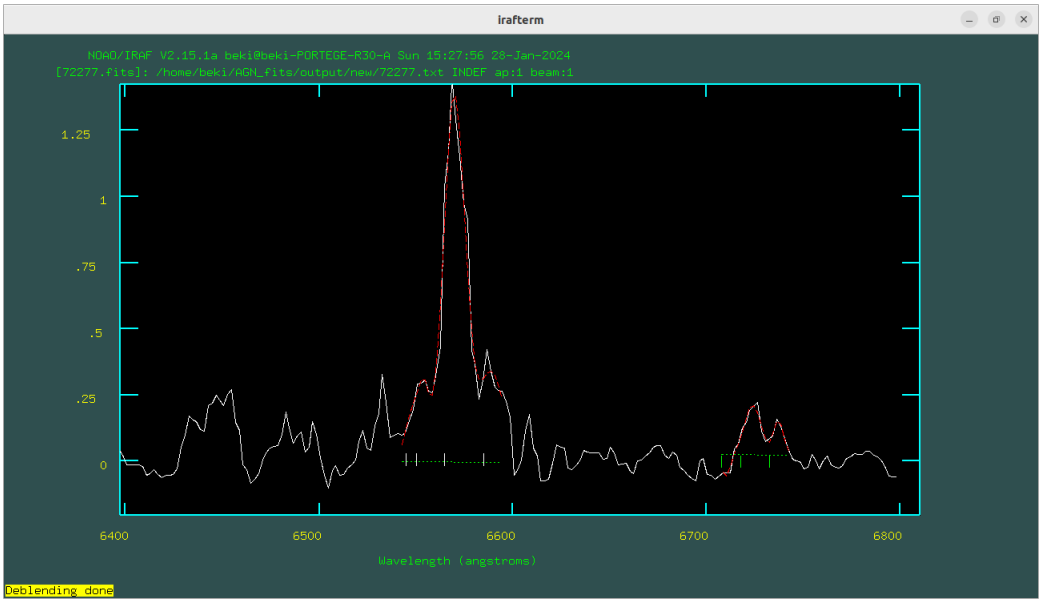

Figure 5.9: Example for measuring Hα+[NII] triplet and [SII] doublet lines for 72277 source using IRAF.

5.4 Catalogue preparation

A comprehensive catalogue summarising all measured parameters for 71 type-2 AGN has been constructed as a result of this work. Line intensity, FWHM, EW and their errors are given for each identified emission line. However, the luminosity measurements are given only for the most common lines such as the Balmer lines (Hα, Hβ, Hγ), [OII]3727, and for the two lines of [OIII]4959, 5007, [NII]6550, 6585, and [SII]6718, 6733. The example of the final catalog is shown in Table 5.1. Parameters such as goodness of fit (adev), S/N, extinction (Av), and various mass estimations such as the total initial mass (Mint_tot), total current mass (Mcor_tot), initial mass processed into stars throughout the galaxies life (M_initial), and present mass in stars (M_current) were derived from STARLIGHT. Luminosity distance (LD) was computed using spectroscopic redshift (z_{spec}), and cosmological parameters of $\Omega_\Lambda = 0.7$, $\Omega_m = 0.3$, and the Hubble constant H0 = $70 kms^{-1} Mpc^{-1}$. Spectroscopic redshift (z_{spec}), right ascension (RA), and declination (DEC) were extracted from (Gonzalez-Otero et al., 2023). The unit of the intensity is expressed in $10^{-17} ergs^{-1} cm^{-1} \AA$, while EW and FWHM are given in ($\AA$). Flux and luminosity are given in $ergs^{-1} cm^{-1}$ and $ergs^{-1}$, respectively.

Table 5.1: Sample of our catalogue with all measured and derived parameters for all type-2 AGN sources.

ID	z_spec	adev	S/N	Av	RAA (deg)	DCC (deg)	LD (cm)	Mini_tot (M⊙)	Mcor_tot (M⊙)	M_initial (M⊙)	M_current (M⊙)
67314	0.6201	13.03	23.32	3.13	162.82	57.26	1.13E+028	3.12E+05	1.57E+05	1.31E+12	6.57E+11
69367	0.4868	5.6	18.37	0.39	162.95	57.27	8.47E+027	1.46E+04	8.60E+03	3.44E+10	2.03E+10
71391	0.5241	8.21	10.09	1.54	162.94	57.29	9.25E+027	2.11E+03	1.66E+03	5.92E+09	4.66E+09
72277	0.3623	9	12.64	0.09	163.38	57.29	5.97E+027	1.95E+03	1.27E+03	2.28E+09	1.48E+09
73205	0.7795	9.52	7.95	0	163.13	57.3	1.5E+028	1.51E+04	7.91E+03	1.11E+11	5.84E+10
105800	0.3412	23.19	13.4	-0.05	163.15	57.49	5.56E+027	4.81E+04	2.40E+04	4.88E+10	2.43E+10
112512	0.4605	4.94	16.53	0	163.25	57.53	7.92E+027	2.36E+04	1.18E+04	4.86E+10	2.42E+10
112822	0.4982	8	10.13	0.18	163.44	57.53	8.7E+027	7.33E+03	4.53E+03	1.82E+10	1.13E+10
115832	0.2026	6.2	18.29	0.25	163.33	57.54	3.07E+027	6.50E+03	3.76E+03	2.01E+09	1.16E+09
116129	0.3403	6.27	21.98	0.81	163.08	57.55	5.55E+027	7.35E+03	4.43E+03	7.43E+09	4.48E+09
116242	1.0324	19.06	4.88	0	163.23	57.55	2.12E+028	9.25E+03	5.22E+03	1.36E+11	7.71E+10
119402	0.3369	15.06	3.11	0.15	162.94	57.56	5.48E+027	3.65E+03	3.27E+03	3.60E+09	3.22E+09

ID	Identified_lines	Intensity	Err_Int (%)	Ew Å	Err_Ew (%)	FWHM Å	Err_FWHM (%)	Flux $ergs^{-1}cm^{-2}$	Luminosity $ergs^{-1}$	Log_L $ergs^{-1}$
69367	[OII]3727	11.77±0.99	8.39	4.78±0.46	9.69	11.25±1.09	9.69	4.39E-13	3.96E44	44.6
	Hγ	2.35±0.83	35.41	3.05±1.25	40.91	7.18±2.94	40.91			
	Hβ	5.93±1.03	17.45	4.82±0.97	20.14	11.35±2.29	20.14	2.88E-13	2.6E44	44.41
	[OIII]4959	2.48±0.93	37.55	3.81±1.65	43.37	8.97±3.89	43.37			
	[OIII]5007	5.81±1.21	20.75	6.49±1.55	23.96	15.28±3.66	23.96	2.9E-13	2.62E44	44.42
	Hα	17.3±1.47	8.48	6.76±9.8	0.66	15.91±9.8	1.56	1.14E-12	1.02E45	45.01
	[NII]6585	3.87±14.87	0.57	3.59±17.99	0.65	8.45±17.99	1.52	2.55E-13	2.3E44	44.36
135313	[OII]3727	33.14±1.22	3.67	5.19±0.2	4.24	12.21±0.52	4.24	1.24E-12	1.45E44	44.16
	Hδ	3.6±1.94	54.05	8.53±5.32	62.34	20.09±12.52	62.34			
	Hγ	3.89±1.47	37.82	4.88±2.13	43.7	11.49±5.02	43.7			
	Hβ	9.72±1.48	15.26	5.1±0.9	17.62	12.01±2.12	17.62	4.73E-13	5.12E43	43.72
	[OIII]4959	3.34±1.44	42.96	4.65±2.31	49.64	10.94±5.43	49.64			
	[OIII]5007	11.69±1.46	12.51	5.04±0.73	14.44	11.87±1.71	14.44	5.85E-13	6.89E43	43.84
	[NII]6550	7.09				29.53		4.64E-13	5.46E43	43.74
	Hα	29.57				17.06		1.94E-12	2.28E44	44.36
	[NII]6585	7.79				10.26		5.13E-13	6.04E43	43.78
	[SII]6733	11.04±2.1	19.03	10.48±2.3	21.96	24.68±21.96	5.42	1.12E-12	1.32E44	44.12

Chapter 6

Results and discussion

In this work, we studied a sample of 71 type-2 FIR AGN in the LH field. We carried out a spectroscopic analysis of their emission line properties using their optical spectra. Our study was carried out in the framework of the Lockman-SpeRSo survey, which is the most comprehensive optical spectroscopic survey for FIR emitters in the LH field, and which provides the deepest up-to-date FIR and spectroscopic optical data (Gonzalez-Otero et al., 2023). In this work, we want to study the properties of type-2 FIR AGN emission lines. We also intend to study the properties of type-2 AGN in terms of SFR and AGN in optical and FIR, to investigate the correlation between the FIR luminosity and the luminosity of strong emission lines. Finally, we aim to compare the properties of FIR and optically selected type-2 AGN. This work will therefore allow us to learn more about type-2 AGN.

This section summarises some of the main analyses carried out after identifying the emission lines and measuring their properties, as explained in section 5. We study the relationship between the luminosity of the strong emission lines and the AGN luminosity, the SFR and the FIR luminosity at 100 and 160 μm. We compare the spectroscopic properties of our sample with the optically selected type-2 AGN sample using the SDSS survey. Finally, we also check where our sources are located in the BPT diagram (Kauffmann et al., 2003; Kewley et al., 2006, 2013). In the following, the main results are briefly presented and discussed.

6.1 Emission line properties of FIR type-2 AGN

In this section we briefly describe the emission line properties of our type-2 AGN. Studying emission lines at different wavelengths provides insight into the physical and chemical composition of galaxies. Diagnostic diagrams that use emission line ratios, such as [OIII]/Hβ, [NII]/Hα, [SII]/Hα, and [OI]/Hα, are effective tools for categorizing galaxies into groups, including star-forming galaxies, LINERs, Seyfert-2, and composite galaxies displaying characteristics from multiple classes. These line ratios also provide information about the physical conditions, such as temperature and density. Since most of our spectra covered a wide wavelength range, we were able to identify a variety of emission lines. The principal permitted lines observed in our spectra are Balmer lines Hα, Hβ, and occasionally Hγ and Hδ. Commonly observed forbidden lines are [OII]3727, and the two lines of [OIII]4959, 5007, [NII]6550, 6585, and [SII]6718, 6733. The presence of these lines confirms the proper identification of sources as type-2, in addition to the lack of the broad component in emission lines, as shown in previous studies (e.g., Netzer, 2015). In some of our spectra, [He I] line, Lyα, and [Fe II] lines are also observed. Due to the wide wavelength range, we often observed sky lines interfering with some of our emission lines, particularly affecting Hα in the red part of the spectrum, making our measurements challenging.

Based on the measured [OIII]/Hβ and [NII]/Hα line ratios, we created the NII-BPT diagram (Kauffmann et al., 2003; Kewley et al., 2006). Figure 6.1 shows the NII-BPT diagram for our type-2 AGN. AGN are expected to appear above the red line, while star-forming galaxies should be below the blue line. The region between the blue and red lines indicates where composite galaxies shall be, that have both star formation and AGN activity. The lines used to separate different types (Kauffmann et al., 2003; Kewley et al., 2006; Schawinski et al., 2007) have been developed for the low redshift of z $<$ 0.1. However, these diagrams evolve with redshift and therefore the limits to separate different types evolve as well (see Kewley et al., 2013). This may affect the location of our sources, which currently occupy mainly the area of star-forming and composite galaxies, instead of the area of Seyfert-2 galaxies, as can be seen in Figure. 6.1. We will test this more in the future.

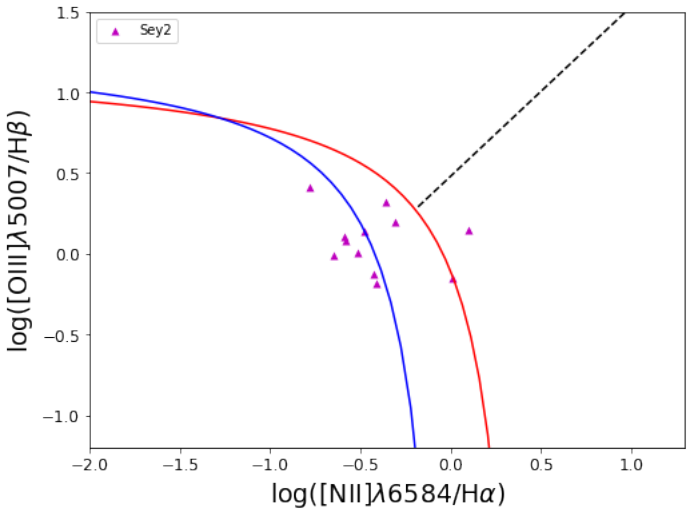

Figure 6.1: NII-BPT diagram for type-2 AGN the blue and black solid lines are from Kewley et al. (2006), and the red line is from Kauffmann et al. (2003), while the dashed line is from Schawinski et al. (2007).

6.2 Luminosity of the strong emission lines in relation to the AGN luminosity and SFR

Understanding the correlation between the luminosity of strong emission lines and the luminosity of AGN is crucial to better understand the properties of AGN and the circumnuclear region, including the obscured regions of AGN. Furthermore, the study of the correlations between the intensity of different emission lines and the AGN luminosity could provide information on the key physical processes taking place in emission line regions and, in particular, in the NLR in the case of type-2 AGN. This could provide a better understanding of the connection between AGN and their host galaxies. On the other hand, comparing the properties of the strong emission lines with SFR measurements could help to understand the interplay between AGN activity and star formation.

In this section we study the correlation between the luminosity of the strong optical emission lines of type-2 AGN detected in FIR and the AGN luminosity and SFR. Both the AGN luminosity and SFR were measured by the Lockman-SpReSo team using the CIGALE code (Boquien et al., 2019) via the SED fittings (Herrera Endoqui et al. 2024, in prep.), using photometric data from UV to FIR (Gonzalez-Otero et al., 2023). We first compare the luminosity of four strong emission lines such as [OII]3727, [OIII]5007, Hβ, and Hα, commonly found in most of our

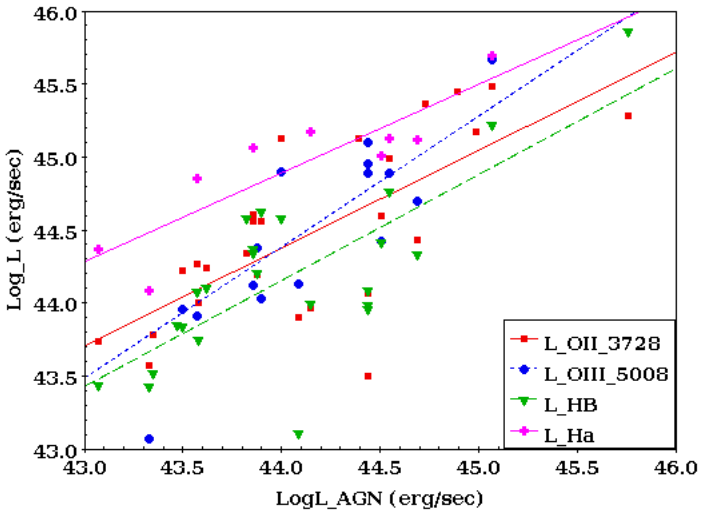

Figure 6.2: Relation between the luminosity of [OII]3727 (red squares), [OIII]5007 (blue circles), Hβ (green triangles), and Hα (pink crosses) and the AGN luminosity.

spectra and the measured AGN luminosity, as shown in Figure 6.1. We observe a linear correlation between the luminosity of the four lines and the AGN luminosity, with correlation factors of 0.71, 0.81, 0.77, and 0.87, for [OII]3727, [OIII]5007, Hβ, and Hα, respectively, thus finding the strongest correlation between the [OIII]5007 and Hα emission with the AGN luminosity. Our result is in line with previous studies by (Matsuoka, 2015), who also studied a large sample of type-2 AGN detected in FIR up to redshift z $<$ 0.22, finding a strong correlation between [OIII]5007 emission and AGN luminosity.

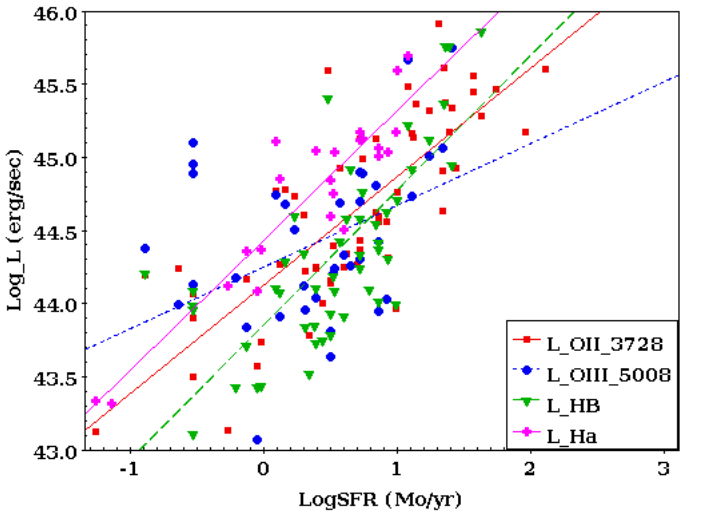

Figure 6.3: Relation between the luminosity of [OII]3727 (red squares), [OIII]5007 (blue circles), Hβ (green triangles), and Hα (pink crosses) and the SFR.

This positive trend suggests that there is a link between AGN activity and surrounding gas properties, as suggested previously (e.g., Netzer, 2009, 2015). Previous studies also suggested that a strong correlation between [OIII]5007 and AGN activity can provide information to study the evolution of type-2 AGN (e.g. (Bongiorno et al., 2010)). However, this result may suffer from different biases (e.g., Malmquist bias) due to the wide range of redshifts in our sample and the limited number of sources, which will be studied in the near future. Figure 6.3 shows the relation between the [OII]3727, [OIII]5007, Hβ, and Hα luminosities and the SFR. We observe a positive linear correlation between the SFR and the luminosity of three emission lines [OII]3727,

Hβ, and Hα with correlation coefficients of 0.8, 0.79, and 0.92, respectively. Our results therefore indicate the strongest correlation of SFR with the Hα luminosity, followed by the [OII]3727 and Hβ lines. For [OIII]5007 we found no correlation with SFR. The observed correlations may suggest the connection between the activity of AGN and the star formation properties of their host galaxies, as already suggested in some of the previous studies (e.g. Mahoro et al., 2017, and references therein).

6.3 Luminosity of the strong emission lines in relation to the IR luminosity

In this section we examine the relation between the intensity of the strong emission lines and the overall IR emission properties in FIR and MIR within a galaxy. The connection between the overall IR luminosity and the specific emission lines can provide information on the amount of dust in the galaxy, the current rate of star formation and the presence of clouds of cold molecular gas. It can also help to distinguish between objects that are primarily influenced by star formation, such as starburst galaxies, and those that are powered by AGN. Most of the AGN activity is usually hidden by dust, but some of the IR bands, in particular at 90, 140, and 160 μm, cover crucial FIR wavelengths, allowing to see through the dust obstruction (e.g. Goto et al., 2011). For our study, we measured luminosities at FIR and MIR. In the FIR, we measured the luminosities in the 100 and 160 μm wavelength bands using data from the Herschel telescope (see section 3.2), while in MIR we considered the 24 μm band measured by the Spitzer telescope. In all cases, the emission intensities in these three bands are taken from (Gonzalez-Otero et al., 2023) First, we studied the relation between the FIR luminosity in the

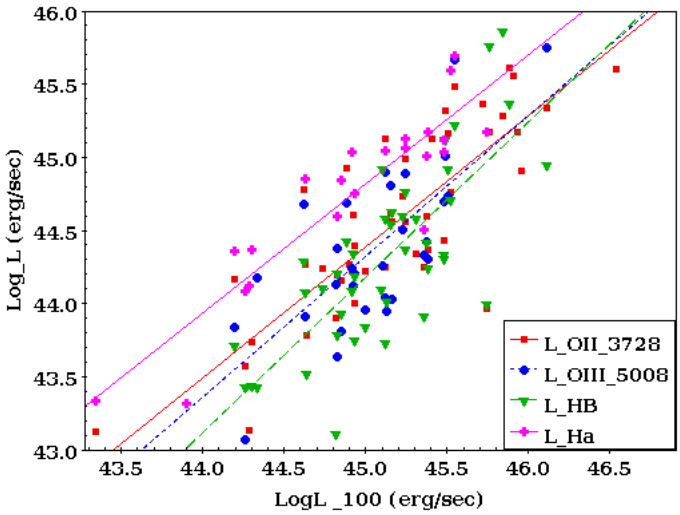

Figure 6.4: Relation between the luminosity of [OII]3727 (red squares), [OIII]5007 (blue circles), Hβ (green triangles), and Hα (pink crosses) and the FIR luminosity at 100 μm.

100 μm and 160 μm bands and the luminosity of four strong emission lines, as can be seen in Figures 6.4 and 6.5, respectively. In both cases we find a strong linear correlation between the FIR luminosity and the luminosity of the [OII]3727, [OIII]5007, Hβ, and Hα lines with correlation coefficients of 0.82, 0.79, 0.82, and 0.9, respectively, in the 100 μm case, and 0.75, 0.65, 0.75, and 0.71, respectively, in the 160 μm case. Therefore, a stronger correlation is found between the properties of strong emission lines in optical and FIR luminosity at 100 μm than in the 160 μm band, in particular for the Hα line. Our results are in line with some of the previous studies (e.g., Netzer, 2015; Matsuoka, 2015) that found a positive trend between FIR

luminosity (e.g., at 90 and 100 μm) with type-2 AGN luminosity, which correlates in our case with the luminosity of strong emission lines as shown in the previous section.

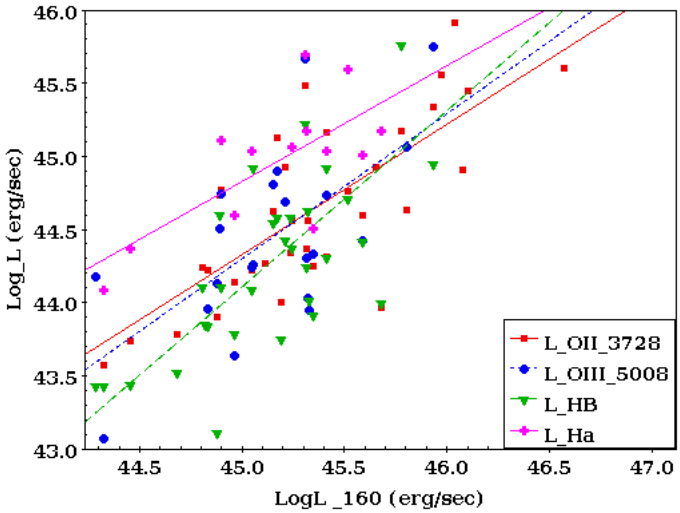

Figure 6.5: Relation between the luminosity of [OII]3727 (red squares), [OIII]5007 (blue circles), Hβ (green triangles), and Hα (pink crosses) and the FIR luminosity at 160 μm.

Second, in addition to the FIR comparison, we compared the luminosity of the strong emission lines with the MIR luminosity at 24 μm, as shown in Figure 6.6 Again, we obtained a positive trend between the MIR luminosity and the luminosity of the four emission lines, with linear correlation coefficients of 0.81, 0.74, 0.83 and 0.9, in the case of [OII]3727, [OIII]5007, Hβ and Hα, respectively. As in the case of FIR luminosity, the Hα line shows the strongest correlation with the 24 μm luminosity compared to other lines, and [OIII]5007 is the weakest. Overall, our results are in agreement with previous studies that showed a correlation between MIR and FIR luminosity with both star formation and AGN activity (e.g. Pérez-González et al., 2006; Calzetti et al., 2007; Zhu et al., 2008; Rodighiero et al., 2010; Netzer, 2015; Matsuoka, 2015), since in our work, as shown above, we found for type-2 AGN a strong correlation between strong optical emission lines and AGN luminosity, SFR, and MIR and FIR luminosity.

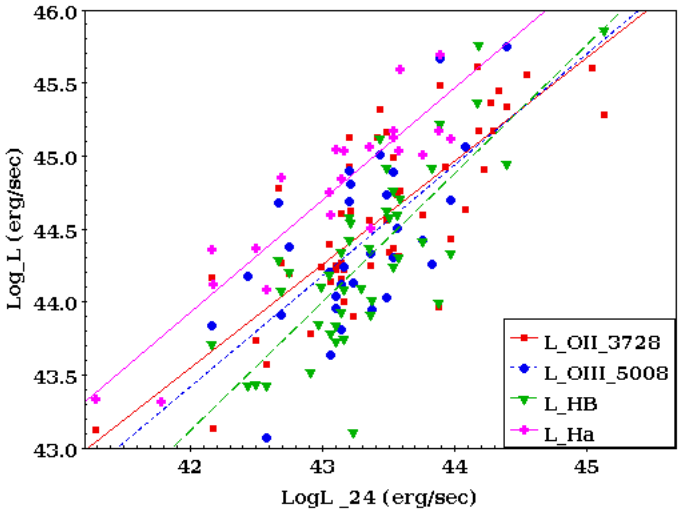

Figure 6.6: Relation between the luminosity of [OII]3727 (red squares), [OIII]5007 (blue circles), Hβ (green triangles), and Hα (pink crosses) and the MIR luminosity at 24 μm.

6.4 Comparison of FIR and optically selected type-2 AGN

In this section, we compare the emission line properties of the FIR-selected type-2 AGN analysed in this work with the optically-selected type-2 AGN from the SDSS DR7 survey at redshift $z < 0.4$. The type-2 AGN from the SDSS survey has been selected using the NII-BPT diagram and emission line measurements from the MPA-JHU catalogue (DR8, Aihara et al., 2011). In all plots, we observe that the FIR-selected type-2 AGN show higher luminosities of all four emission lines compared to the optically-selected sample. This result may be affected by the difference in the range of redshifts covered by the two samples, where in FIR we are representing a sample at higher redshift, as can be seen in Figure 6.7 having a small number of sources with $z < 0.4$ as in the SDSS case. This will be analysed in the future using a larger sample of AGN to fully understand the physical properties of the optically- and FIR-selected type-2 AGN.

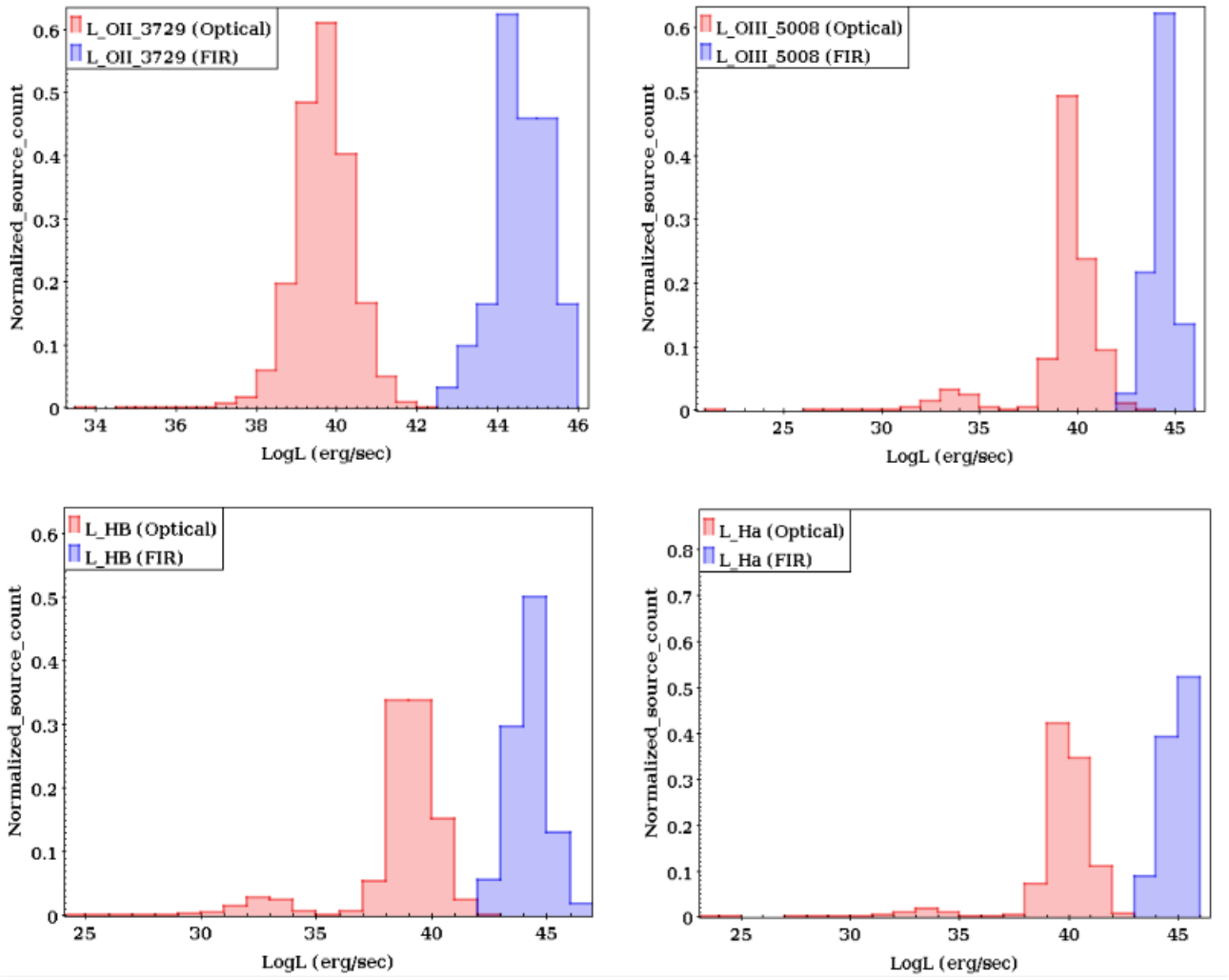

Figure 6.7: Luminosity distribution of the [OII]3727 (top left), [OIII]5007 (top right), Hβ (bottom left), and Hα (bottom right) emission lines of our FIR- (blue) and optically- (red) selected type-2 AGN samples.

Chapter 7

Conclusions

In this work we study the properties of emission lines from FIR-selected type-2 AGN detected in the Lockman Hole field using the Lockman-SpeRSo, the deepest spectroscopic survey (using the 10 m GTC telescope) of the deepest FIR-detected sources (using the Herschel telescope). We identified all emission lines and measured their properties, in particular their intensity, EW, FWHM, and calculated the luminosity of four strong emission lines commonly found in type-2 AGN, such as [OII]3727, [OIII]5007, Hβ and Hα. This was done after extracting the blue and red spectra for each source, combining them, running STARLIGHT, extracting the emission line spectra and fitting the lines using a single Gaussian function. The analysis was performed for a total of 71 detected type-2 AGN. We compared the luminosity of the strong emission lines with other properties of the AGN and its host galaxy, such as the AGN luminosity, the SFR, and the IR luminosity in FIR and MIR. Finally, we compare the luminosity of the strong emission lines for our type-2 AGN selected in FIR and those optically selected in SDSS. This is to date the most comprehensive study of the spectroscopic properties of type-2 AGN detected in FIR. Our main conclusions are the following:

- FIR-detected type-2 AGN show various properties in terms of optical/UV detected emission lines, such as Balmer lines (Hα, Hβ, Hγ, Hδ), and commonly observed forbidden lines, [OII]3727, the two lines of [OIII]4959, 5007, [NII]6550, 6585, and [SII]6718, 6733. In some of our sources, some UV lines such as [He I]3890, Lyα, Fe II, [Al II]2670, and [Mg II]2800 have been detected. As in the case of optically-detected type-2 AGN, FIR-detected type-2 AGN have [OII]3727, [OIII]5007, Hβ and Hα as their strongest emission lines.
- We constructed a catalogue of all emission line measurements from 71 sources. This is currently the largest optical spectroscopic catalogue of type-2 AGN detected in FIR. This catalogue will be made public to the entire scientific community.
- We found a positive trend between the luminosity of four strong emission lines and the AGN luminosity, showing the connection between the AGN and the surrounding gas, and between the luminosity of the emission lines and the SFR, suggesting the connection between the AGN and the star-forming properties of its host galaxy.
- We found a linear correlation between the luminosity of strong emission lines and the IR luminosity (in FIR and MIR) at 100 μm, 160 μm, and 24 μm, suggesting the connection between AGN activity and the emission of dust particles of different size and mass.
- We observed higher luminosities of type-2 AGN detected in FIR compared to the optically-selected sources. Further studies are needed to see if there are real physical differences and/or if the observed differences are due to a bias introduced by covering different redshift ranges.

7.1 Future work

This work will be published in the A&A journal, and we are currently working on the development of the manuscript. The analysis in the paper will be expanded to include the following: revision of the BPT diagrams at higher redshift, more detailed analysis taking into account stellar mass, redshift and galaxy type (in terms of morphology), and analysis of AGN luminosity and SFR versus IR properties of type-2 AGN detected in FIR. We will also make a more detailed comparison with previous studies and further develop the section explaining the relevance of our study. In the future, metallicity properties can be measured using our emission line properties and the HCm code (Pérez-Montero et al., 2021). Finally, the Lockman Hole field has been observed with LOFAR in radio, and we are planning to compare our analysis with the radio properties of type-2 AGN detected in FIR.

References

Abdulrahman M. A., et al., 2023, MNRAS, 519, 861

Abraham R. G., et al., 1996, ApJS, 107, 1

Abraham R. G., et al., 2003, ApJ, 588, 218

Abramowicz M. A. & Fragile P. C., 2013, LRR, 16, 1

Abramowicz M. A., et al., 1988, ApJ, 332, 646

Aihara H., et al., 2011, ApJS, 193, 29

Ajay Y., et al., 2022, Research Notes of the AAS, 6, 274

Albán M. & Wylezalek D., 2023, A&A, 674, A85

Amado Z. B., et al., 2019, MNRAS, 485, 1528

Andika I., 2016, PhD thesis, doi:10.13140/RG.2.2.23303.80809

Andrews B. & Martini P., 2013, ApJ, 765, 140

Antonucci R. J. & Miller J. S., 1985, ApJ, 297, 621

Antonucci R., 1993, ARA&A, 31, 473

Arcones A. & Thielemann F.-K., 2023, A&A Rev., 31, 1

Armah M., et al., 2023, MNRAS, 520, 1687

Assef R. J., et al., 2013, ApJ, 772, 26

Baes M. & Gentile G., 2011, A&A, 525, A136

Baker W. M., et al., 2023, MNRAS, 519, 1149

Baldwin J. A., et al., 1981, PASP, 93, 5

Ball N. M., et al., 2004, MNRAS, 348, 1038

Ballantyne D. R., 2020, MNRAS, 491, 3553

Balmaverde B. & Capetti A., 2014, A&A, 563, A119

Balogh M. L., et al., 2004, ApJL, 615, L101

Bamford S. P., et al., 2008, MNRAS, 391, 607

Barchi P. H., et al., 2020, Astronomy and Computing, 30, 100334

Barvainis R., et al., 2005, ApJ, 618, 108

Bastian N. & Lardo C., 2018, ARA&A, 56, 83

Beckmann V. & Shrader C. R., 2012, Active Galactic Nuclei

Belvedersky M. I., et al., 2022, Astronomy Letters, 48, 109

Bennert N., et al., 2006, A&A, 446, 919

Bershady M. A., et al., 2000, AJ, 119, 2645

Best P. N. & Heckman T. M., 2012, MNRAS, 421, 1569

Bianchi S., et al., 2012, Advances in Astronomy, 2012, 782030

Bickley R. W., et al., 2023, MNRAS, 519, 6149

Birchall K. L., et al., 2022, MNRAS, 510, 4556

Blandford R., et al., 2019, ARA&A, 57, 467

Bonato M., et al., 2021, A&A, 656, A48

Bongiorno A., et al., 2010, A&A, 510, A56

Boquien M., et al., 2019, A&A, 622, A103

Bornancini C. G., et al., 2022, A&A, 664, A110

Bowles M., et al., 2021, MNRAS, 501, 4579

Brandt W. N., et al., 2015, A&AR, 23, 1

Brinchmann J. & Ellis R. S., 2000, ApJ, 536, L77

Burke C. J., et al., 2021, Science, 373, 789

Buta R. J., 2013, Galaxy Morphology, doi:10.48550/arXiv.1304.3529.

Calzetti D., et al., 1994, ApJ, 429, 582

Calzetti D., et al., 2007, ApJ, 666, 870

Carrasco E. R., et al., 2021, ApJ, 918, 61

Casasola V., et al., 2004, A&A, 422, 941

Castro-Neves Margarida & Draper P. W., 2014, SPLAT-VO: Spectral Analysis Tool for the Virtual Observatory, Astrophysics Source Code Library, record ascl:1402.008

Cautun M., et al., 2020, MNRAS, 494, 4291

Cavanagh M. K., et al., 2021, MNRAS, 506, 659

Cazzoli S., et al., 2018, MNRAS, 480, 1106

Cepa J., et al., 2008, A&A, 490, 1

Chang X., et al., 2023, MNRAS, 520, 4118

Cheng T.-Y., et al., 2021, MNRAS, 507, 4425

Chiaberge M., et al., 2015, ApJ, 806, 147

Cho H., et al., 2020, ApJ, 892, 93

Cid Fernandes R., et al., 2005, MNRAS, 358, 363

Cid Fernandes R., et al., 2011, MNRAS, 413, 1687

Coatman L., et al., 2016, MNRAS, 461, 647

Conselice C. J., 2006, MNRAS, 373, 1389

Conselice C. J., 2014, ARA&A, 52, 291

Conselice C. J., et al., 2000, ApJ, 529, 886

Curti M., et al., 2023, MNRAS, 518, 425

D'Ammando F., 2019, Galaxies, 7, 87

Dai Y. s., et al., 2018, MNRAS, 478, 4238

Dale D. A., et al., 2014, ApJ, 784, 83

De Vis P., et al., 2019, A&A, 623, A5

Dermer C. D. & Giebels B., 2016, Comptes Rendus Physique, 17, 594

Dey B., et al., 2022, MNRAS, 515, 5285

Dicken D., et al., 2023, MNRAS, 519, 5807

Dieleman S., et al., 2015, MNRAS, 450, 1441

Domínguez Sánchez H., et al., 2018, MNRAS, 476, 3661

Donley J. L., et al., 2012, ApJ, 748, 142

Draper P. W., 2014, SPLAT: Spectral Analysis Tool, Astrophysics Source Code Library, record ascl:1402.007

Draper P. W., et al., 2013, Starlink User Note, 243

Egami E., et al., 2008, Ultra-Deep MIPS Imaging of the Lockman Hole, Spitzer Proposal ID 50249

Elitzur M., 2006, New Astron. Rev., 50, 728

Elitzur M., 2012, ApJL, 747, L33

Fabj G., et al., 2020, MNRAS, 499, 2608

Feltre A., et al., 2012, MNRAS, 426, 120

Feltre A., et al., 2017, Frontiers in Astronomy and Space Sciences, 4, 32

Ferrarese L. & Merritt D., 2000, ApJL, 539, L9

Ferrari F., et al., 2015, ApJ, 814, 55

Fontanot F., et al., 2023, MNRAS, 520, 740

Forster K., et al., 2001, ApJS, 134, 35

Fotopoulou S., et al., 2012, ApJS, 198, 1

Fraix-Burnet D., 2023, MNRAS, 523, 3974

García-Lorenzo B., et al., 2015, A&A, 573, A59

Garcia A. M., et al., 2023, MNRAS, 519, 4716

Garilli B., et al., 2010, PASP, 122, 827

Ge X., et al., 2020, ApJ, 889, 132

Genzel R. & Cesarsky C. J., 2000, ARA&A, 38, 761

Getachew-Woreta T., et al., 2022, MNRAS, 514, 607

Getman K. V., et al., 2014, ApJ, 787, 108

Ghisellini G., 2013, Radiative Processes in High Energy Astrophysics. Vol. 873, Springer

Gonzalez-Otero M., et al., 2023, A&A, 669, A85

González-Otero M., et al., 2024, A&A, 684, A31

Goto T., et al., 2011, MNRAS, 410, 573

Granato G. L., et al., 2004, ApJ, 600, 580

Greene Jenny E. & Ho L. C., 2006, ApJ, 641, 117

Greene J. E., et al., 2011, ApJ, 732, 9

Griffin M. J., et al., 2010, A&A, 518, L3

Guseva N. G., et al., 2009, A&A, 505, 63

Haas M., et al., 2011, A&A, 535, A73

Hada K., 2019, Galaxies, 8, 1

Hainline K. N., et al., 2016, ApJ, 823, 42

Hardcastle M. J. & Croston J. H., 2020, New Astron. Rev., 88, 101539

Hardcastle M. J., et al., 2019, A&A, 622, A12

Harrison C., 2014, PhD thesis, Durham University, UK

Hartmann L., et al., 2016, ARA&A, 54, 135

He Z., et al., 2018, MNRAS, 478, 3614

Heckman T. M., Best P. N., 2014, ARA&A, 52, 589

Hirashita H., et al., 2003, A&A, 410, 83

Ho L. C., 2008, ARA&A, 46, 475

Hogg David W. & Fruchter A. S., 1999, ApJ, 520, 54

Huang W., et al., 2023, ApJS, 264, 52

Hubble E. P., 1926, ApJ, 64, 321

Hubble E., 1936, ApJ, 84, 158

Huertas-Company M., et al., 2008, A&A, 478, 971

Iwasawa K., et al., 2011, A&A, 529, A106

Ji Z., et al., 2022, ApJ, 925, 74

Jiang J., et al., 2023, Research in Astronomy and Astrophysics, 23, 115019

Juodžbalis I., et al., 2023, MNRAS, 525, 1353

Jurlin N., et al., 2021, Galaxies, 9, 122

Kartaltepe J. S., et al., 2023, ApJL, 946, L15

Kaspi S., et al.,, 2005, ApJ, 629, 61

Kauffmann Guinevere & Maraston C., 2019, MNRAS, 489, 1973

Kauffmann G., et al., 2003, MNRAS, 341, 33

Kayal A & Singh V., 2024, MNRAS, 531, 830

Kellermann K. I., et al., 2016, ApJ, 831, 168

Kelly Brandon C. & McKay T. A., 2004, AJ, 127, 625

Kewley L. J., et al., 2001, ApJ, 556, 121

Kewley L. J., et al., 2006, MNRAS, 372, 961

Kewley L. J., et al., 2013, ApJ, 774, 100

Khochfar S. & Burkert A., 2005, MNRAS, 359, 1379

Khosroshahi H. G., et al., 2000, ApJL, 531, L103

Kim Minbae & Choi Y.-Y., 2020, ApJL, 901, L38

Kim A. G., et al., 2015, Astroparticle Physics, 62, 195

Kormendy John & Bender R., 1996, ApJ, 464, L119

Kormendy J. & Ĥo L. C., 2013, ARA&A, 51, 511

Kramarenko I. G., et al., 2022, MNRAS, 510, 469

Krezinger M., et al., 2024, MNRAS, 530, 4614

Kuraszkiewicz J. K., et al., 2004, ApJS, 150, 165

Lacerna I., et al., 2020, A&A, 644, A117

Laughlin G., et al., 2004, ApJL, 612, L73

Le Fèvre O., et al., 2013, A&A, 559, A14

Lee S., et al., 2010, ApJ, 725, 1644

Leroy A. K., et al., 2021, ApJS, 257, 43

Li J., et al., 2020, ApJ, 903, 49

Li Y., et al., 2022, ApJ, 927, 58

Li W., et al., 2023, ApJ, 944, 168

Lin Y., et al., 2023, MNRAS, 520, 963

Lintott C. J., et al., 2008, MNRAS, 389, 1179

Lintott C., et al., 2011, MNRAS, 410, 166

Lister M. L., et al., 2016, AJ, 152, 12

Liu G., et al., 2013, MNRAS, 436, 2576

Liu C., et al., 2022, ApJ, 940, 40

Lombardi G., et al., 2022, MNRAS, 517, 201

Lotz J. M., et al., 2004, AJ, 128, 163

Lusso E., et al., 2010, A&A, 512, A34

Lutz D., 2014, ARA&A, 52, 373

Lutz D., et al., 2011, A&A, 532, A90

Lyu J., et al., 2022, ApJ, 941, 191

Madau P. & Dickinson M., 2014, ARA&A, 52, 415

Mahony E. K., et al., 2016, MNRAS, 463, 2997

Mahoro A., et al., 2017, MNRAS, 471, 3226

Mahoro A., et al., 2019, MNRAS, 485, 452

Mahoro A., et al., 2022, MNRAS, 513, 4494

Matsuoka Kenta & Woo J.-H., 2015, ApJ, 807, 28

McConnell N. J. & Ma C.-P., 2013, ApJ, 764, 184

Meléndez M. et al., 2008, ApJ, 689, 95

Melia Fulvio & Falcke H., 2001, ARA&A, 39, 309

Mendez A J., et al., 2013, ApJ, 770, 40

Mickaelian A. M., 2015, Iranian Journal of Astronomy and Astrophysics, 2, 1

Mignoli M., et al., 2013, A&A, 556, A29

Miller A. A., et al., 2017, AJ, 153, 73

Milone A. P., et al., 2012, ApJ, 744, 58

Miraghaei H., 2020, AJ, 160, 227

Mobasher B., et al., 2015, ApJ, 808, 101

Molero M., et al., 2023, MNRAS, 518, 987

Morales-Vargas A., et al., 2023, MNRAS, 526, 2863

Mościbrodzka M., 2019, A&A, 623, A152

Mountrichas G., et al., 2021, A&A, 653, A70

Mushotzky R., 2004, Progress of Theoretical Physics Supplement, 155, 27

Nair P. B., Abraham R. G., 2010, ApJS, 186, 427

Nenkova M., et al., 2008, ApJ, 685, 160

Nersesian A., et al., 2023, A&A, 673, A63

Netzer H., 2009, MNRAS, 399, 1907

Netzer H., 2015, ARA&A, 53, 365

Newville M., et al., 2016, Lmfit: Non-Linear Least-Square Minimization and Curve-Fitting for Python, Astrophysics Source Code Library, record ascl:1606.014

Noda H., et al., 2023, ApJ, 943, 63

Nour D. & Sriram K., 2023, Journal of High Energy Astrophysics, 37, 34

Ogawa S., et al., 2021, ApJ, 906, 84

Paczynski B., et al., 1996, in Unsolved Problems of the Milky Way. p. 93

Padovani P., et al., 2017, A&AR, 25, 2

Pak M., et al., 2021, ApJ, 906, 43

Paliya V. S., et al., 2019, ApJ, 881, 154

Pancoast A., et al., 2012, ApJ, 754, 49

Papovich C., et al., 2019, BAAS, 51, 266

Parikh T., et al., 2021, MNRAS, 502, 5508

Pâris I., et al., 2017, A&A, 597, A79

Park S. Q., et al., 2008, ApJ, 678, 744

Peña-Herazo H. A., et al., 2022, A&A, 659, A32

Peluso G., et al., 2023, ApJ, 958, 147

Pérez-González P. G., et al., 2006, ApJ, 648, 987

Pérez-Montero E., et al., 2019, MNRAS, 489, 2652

Pérez-Montero E., et al., 2021, MNRAS, 504, 1237

Peterson B. M., 2006, The Broad-Line Region in Active Galactic Nuclei. Vol. 693, Springer, doi:10.1007/3-540-34621-X˙3

Pfeffer J., et al., 2023, MNRAS, 518, 5260

Pilbratt G. L., et al., 2010, A&A, 518, L1

Poglitsch A., et al., 2010, A&A, 518, L2

Pollo A., 2015, in "Galaxy properties". Introduction to Cosmology, pp 89–100

Pović M., et al., 2009, ApJ, 706, 810

Pović M., et al., 2012, A&A, 541, A118

Pović M., et al., 2013, MNRAS, 435, 3444

Povic M., et al., 2015, MNRAS, 453, 1644

Pović M., et al., 2016, MNRAS, 462, 2878

Ramos Almeida C., et al., 2009, ApJ, 694, 1379

Ramos Almeida C., et al., 2014, MNRAS, 439, 3847

Ramos Almeida C., et al., 2017, Nature Astronomy, 1, 679

Ramos Padilla A. F., et al., 2020, MNRAS, 499, 4325

Rathore H., et al., 2022, MNRAS, 513, 389

Reza M., 2021, Astronomy and Computing, 37, 100492

Rodighiero G., et al., 2010, A&A, 515, A8

Romero G. E., et al., 2017, Space Sci. Rev., 207, 5

Saha Kanak & Cortesi A., 2018, ApJL, 862, L12

Sánchez-Sáez P., et al., 2019, ApJS, 242, 10

Schawinski K., et al., 2007, MNRAS, 382, 1415

Schawinski K., et al., 2014, MNRAS, 440, 889

Schneider P., 2006, Extragalactic Astronomy and Cosmology. Vol. 146, Springer

Schneider D. P., et al., 2010, AJ, 139, 2360

Sersic J. L., 1968, Atlas de Galaxias Australes

Shakura N. I. & Sunyaev R. A., 1973, AA, 24, 337

Shen Juntai & Zheng X.-W., 2020, Res. Astron. Astrophys., 20, 159

Shen L., et al., 2017, MNRAS, 472, 998

Sil'chenko O. K., et al., 2019, ApJS, 244, 6

Smethurst R. J., et al., 2024, MNRAS, 527, 10855

Smith N., et al., 2008, High Time Resolution Astrophysics, pp 257–279

Soifer B. T., et al., 2008, ARA&A, 46, 201

Sommariva V., et al., 2012, A&A, 539, A136

Sreejith S., et al., 2018, MNRAS, 474, 5232

Stanway E. R. & Eldridge J. J., 2018, MNRAS, 479, 75

Stern D., et al., 2005, ApJ, 631, 163

Stern D., et al., 2012, ApJ, 753, 30

Sturm E., et al., 2002, A&A, 393, 821

Sulentic J. W., et al., 2000, ARA&A, 38, 521

Tadhunter C., 2008, New Astron. Rev., 52, 227

Tarrío P. & Zarattini S., 2020, A&A, 642, A102

Taylor M. B., 2005, in Astronomical Data Analysis Software and Systems XIV. p. 29

Tescari E., et al., 2018, MNRAS, 473, 380

Tody D., 1986, The IRAF data reduction and analysis system. Vol. 627

Trager S. C., et al., 2000, AJ, 120, 165

Urry C. M., Padovani P., 1995, PASP, 107, 803

Van Rossum Guido & Drake F. L., 2009, Python 3 reference manual. CreateSpace

Vanden Berk D. E., et al., 2001, AJ, 122, 549

Vavilova I. B., et al., 2021, A&A, 648, A122

Wang J., et al., 2021, ApJL, 911, L14

Wang J., et al., 2023, ApJ, 956, 137

Wenderoth E., et al., 2022, MNRAS, 515, 1052

Wijesinghe D. B., et al., 2010, MNRAS, 404, 2077

Willett K. W., et al., 2013, MNRAS, 435, 2835

Wuyts S., et al., 2007, ApJ, 655, 51

Wylezalek D., et al., 2020, MNRAS, 492, 4680

Xu D. W., et al., 2003, ApJ, 590, 73

Xu K., et al., 2022, MNRAS, 509, 1237

Xue Y. Q., et al., 2016, ApJS, 224, 15

Yuan F., et al., 2008, ApJ, 679, 984

Zasov A. V., et al., 2017, Physics Uspekhi, 60, 3

Zhang Xue-Guang & Zhao Y., 2022, MNRAS, 516, 2470

Zhong Y., et al., 2022, ApJ, 925, 157

Zhu Y., et al., 2008, ApJ, 686, 155

Zovaro H. R. M., et al., 2024, MNRAS, 527, 8566

de Diego J. A., et al., 2020, A&A, 638, A134

Appendix A

In this section, we present all the fittings and spectra described in the data analysis process in Chapter 5 for 71 type-2 sources. Each page corresponds to one source, with the ID and spectroscopic redshift of the fit presented at the top of each plot. The original spectra are shown in the top left for the blue part and in the middle left for the red part of the spectrum. The combined original and final spectra at each step are presented in the top right plots, while the final spectrum used in fittings after moving to the rest frame, K-correction, and extinction correction are displayed in the central plot. The bottom left plots show the results from STARLIGHT fitting, with the original spectrum in blue, the best fit in red, and the residual with masked regions in violet. The top left plot displays the original spectrum in blue and the best fit in red. The bottom left plot shows the residual with masked regions in violet, while the right plot illustrates the obtained stellar populations. The upper right plot shows the extracted emission spectra in green after subtracting the best fit in red from the input spectra in blue, and the lower right plot displays the measurement of the emission lines, with the red line representing the Gaussian curve to the central wavelength. In addition to these, for source 206490 (pg. 121), there are three different grisms (R300B, R316R, and R600R), and therefore without combining them we performed fitting and line measurements. For source 206501 (pg 122), there is a strong sky line that makes it difficult to identify and measure other emission lines. To work around this, we divided the measurement into parts before and after the strong sky line. As for sources 206545 (pg. 125), 206586 (pg. 128), and 206603 (pg. 131), the wavelength range is too small to be fitted with STARLIGHT, so we measured the emission line properties without running STARLIGHT.

67314 (z_{spec} = 0.6201)

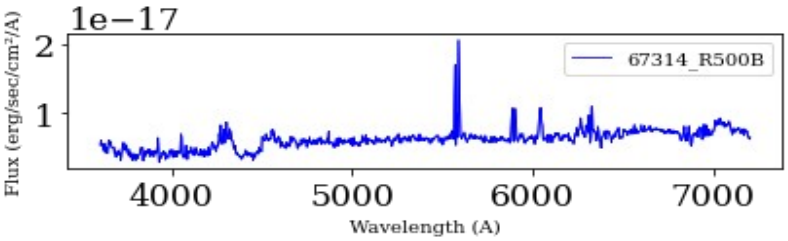

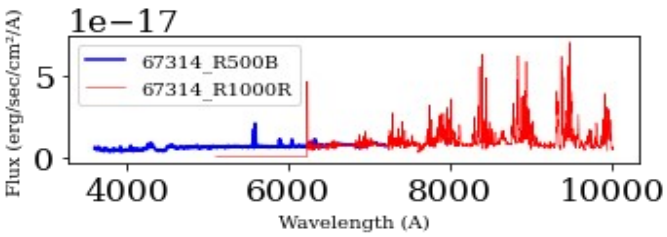

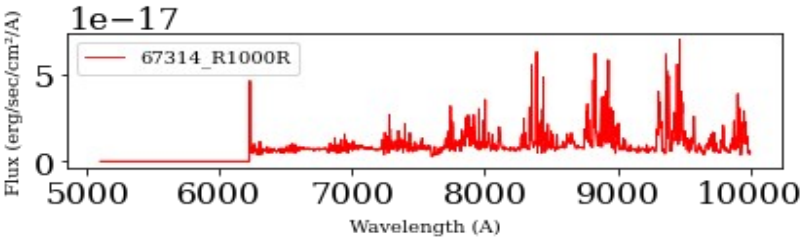

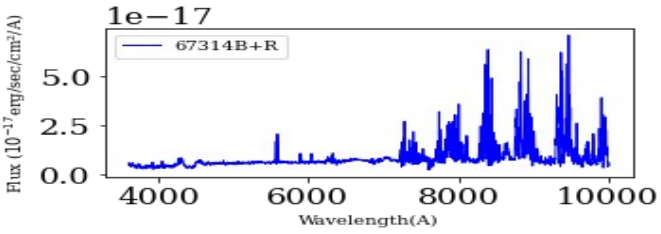

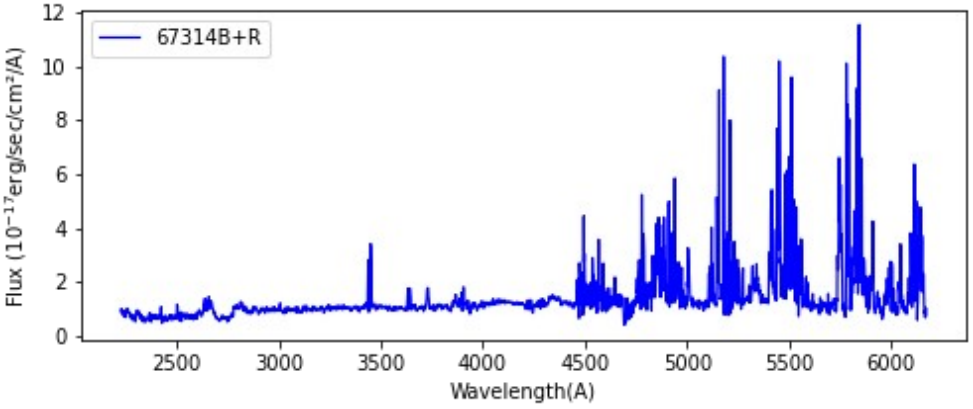

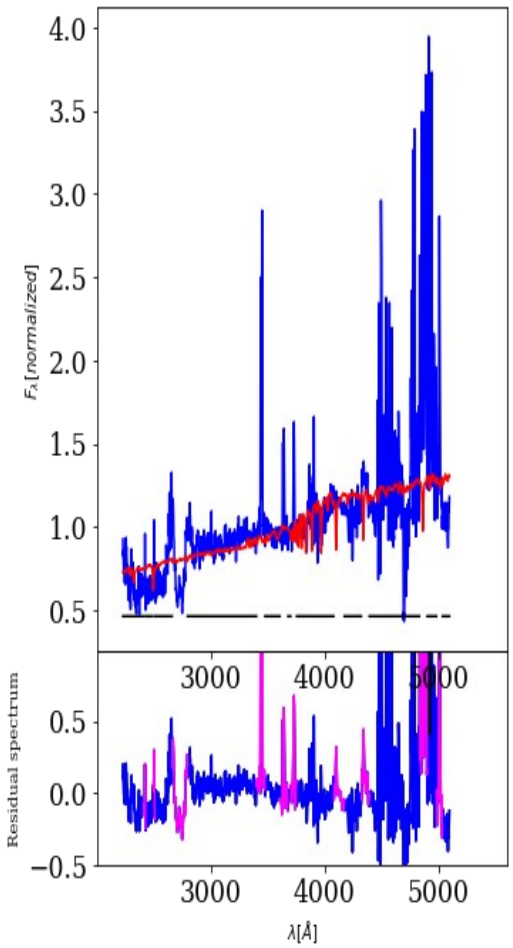

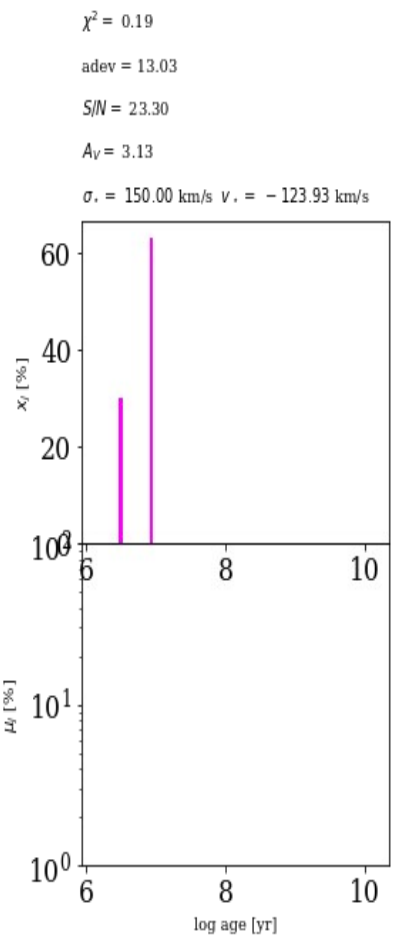

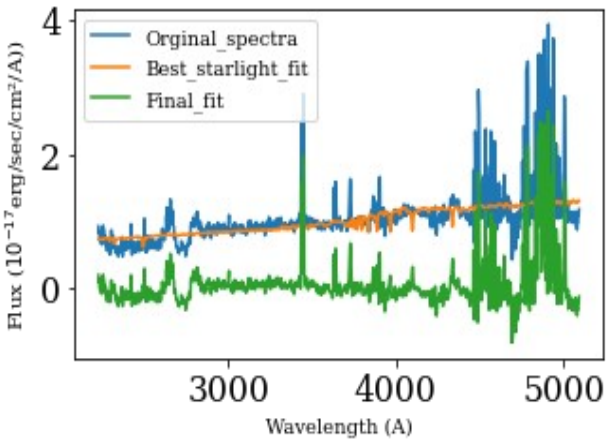

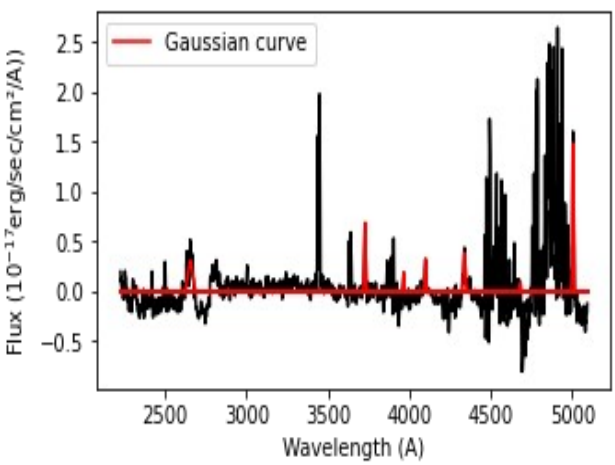

69367 (z_{spec} = 0.4868)

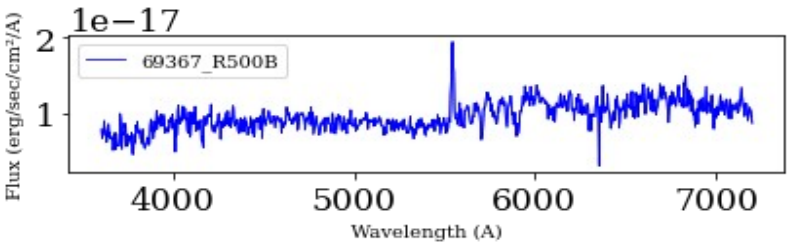

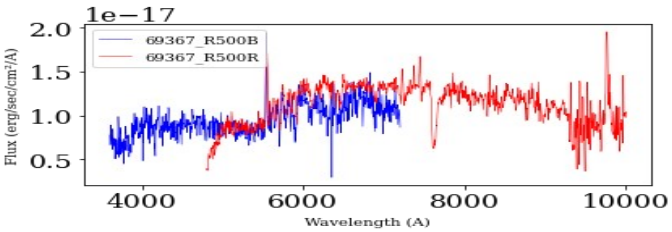

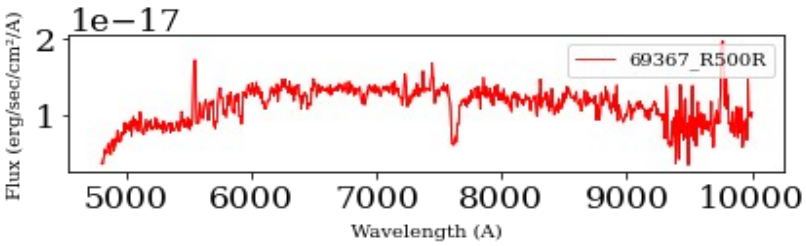

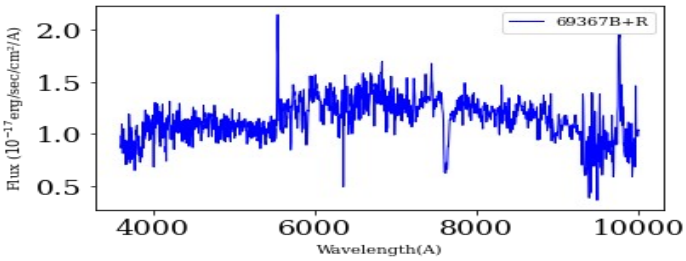

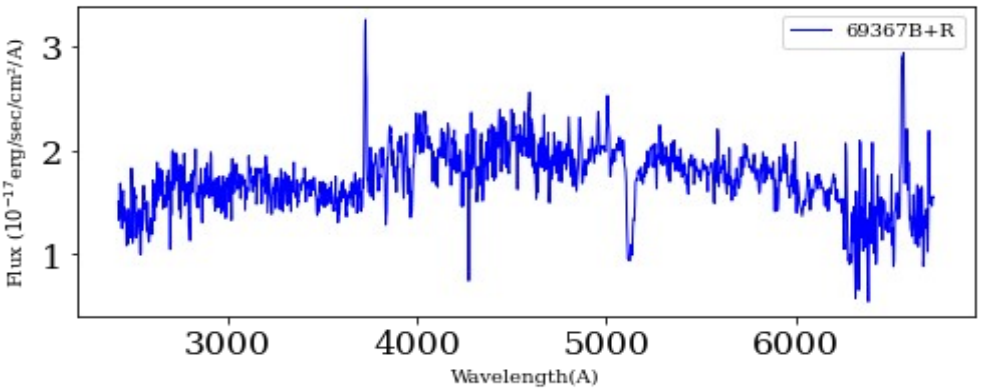

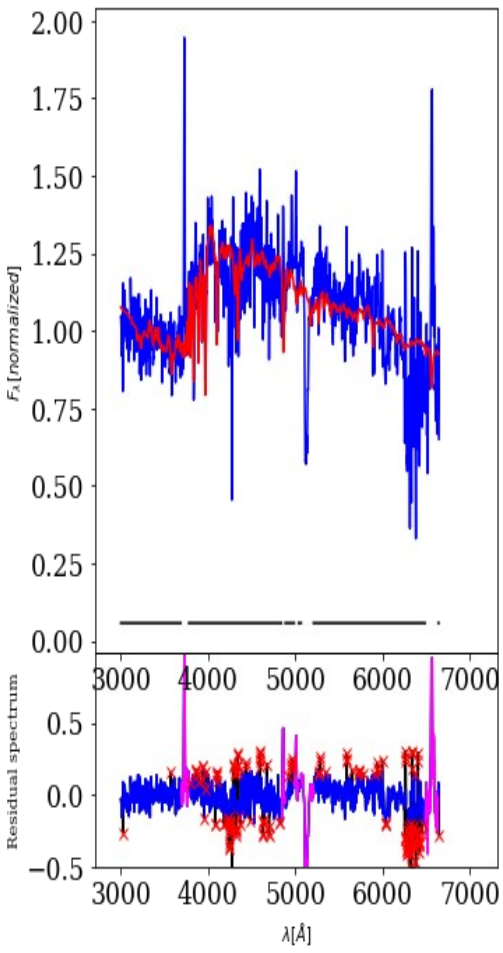

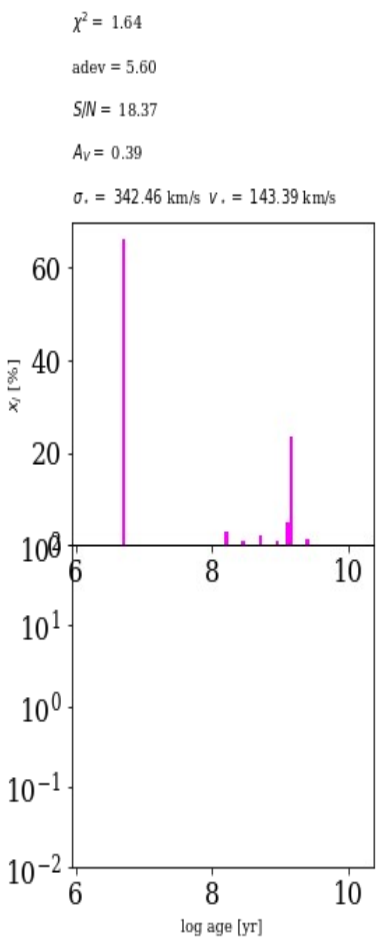

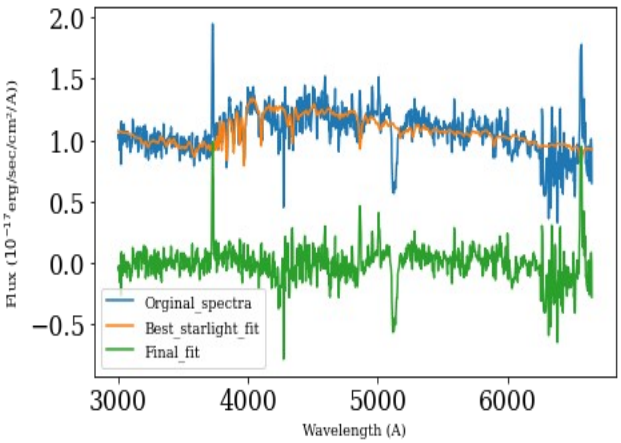

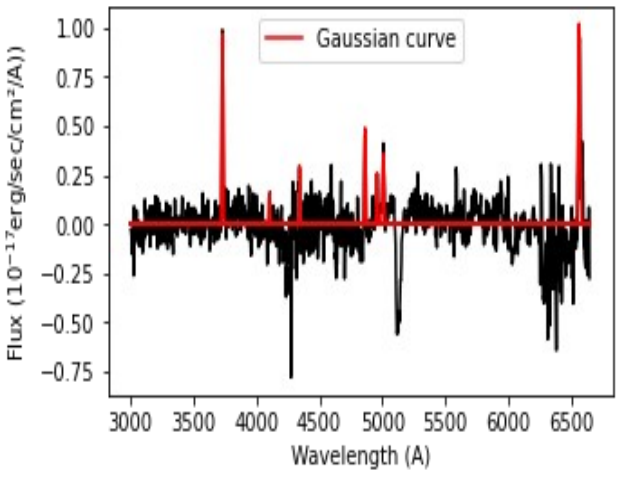

71391 (z_{spec} = 0.5241)

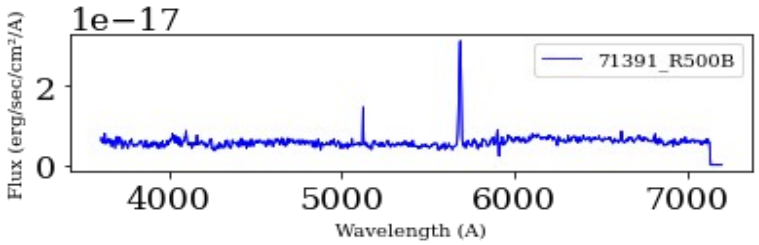

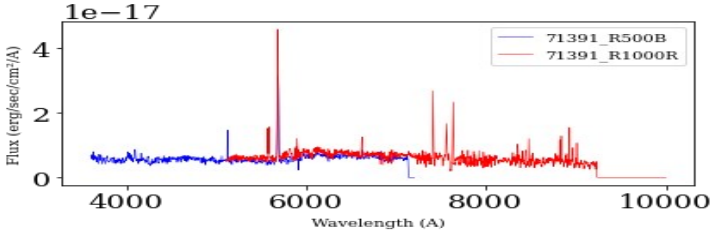

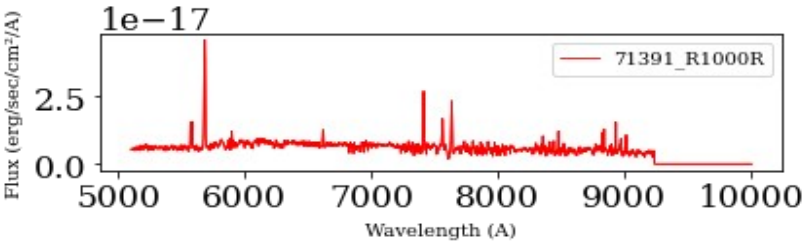

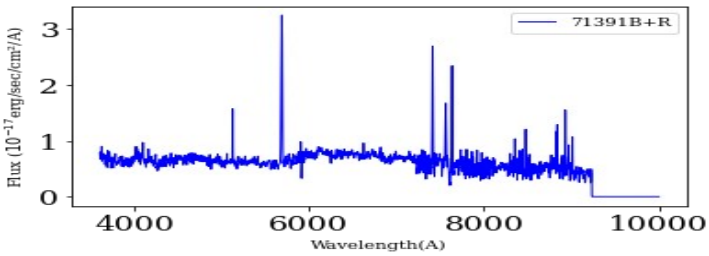

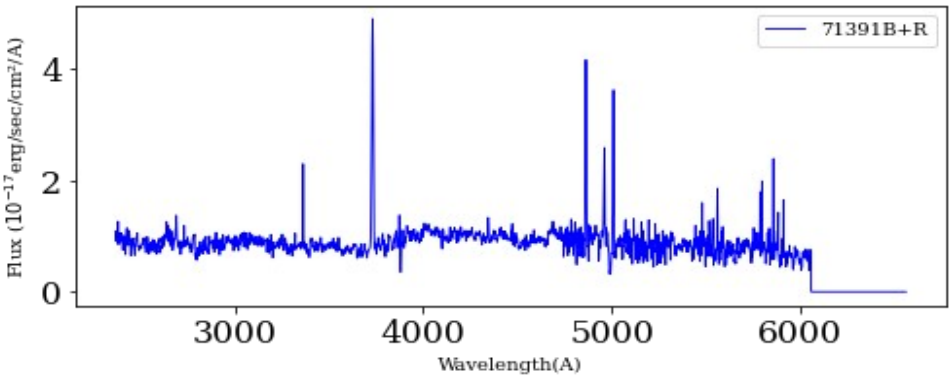

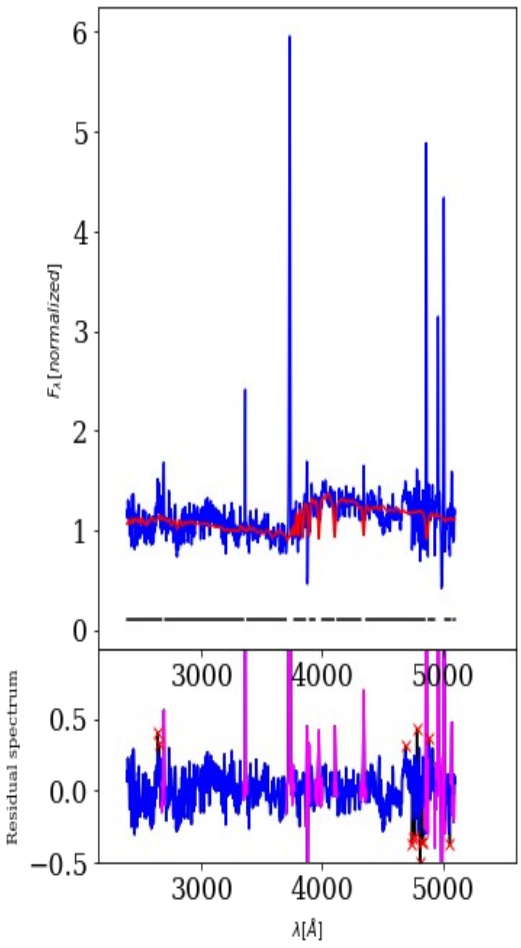

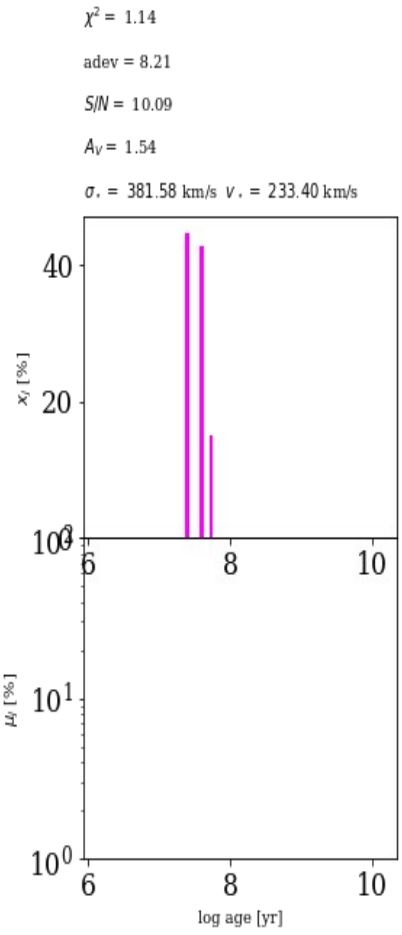

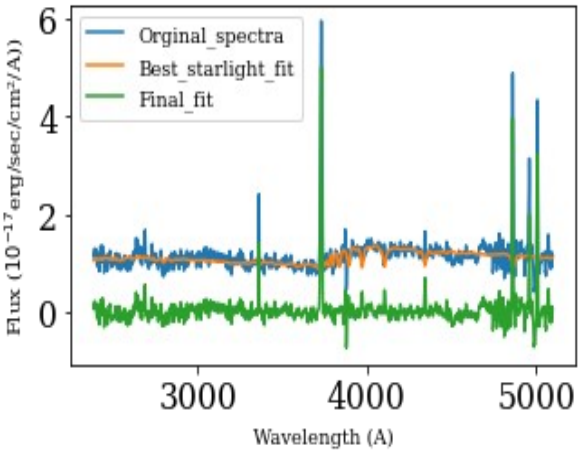

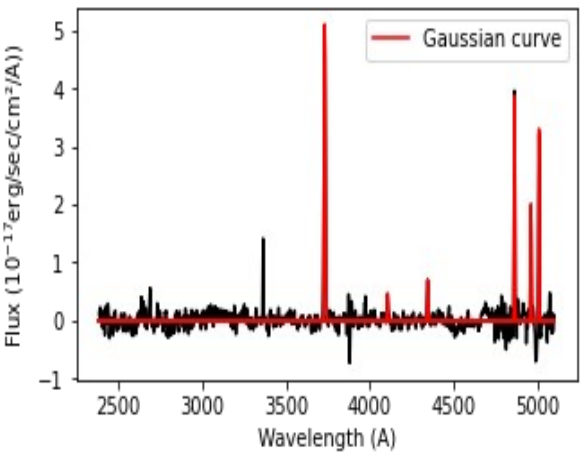

72277 (z_{spec} = 0.3623)

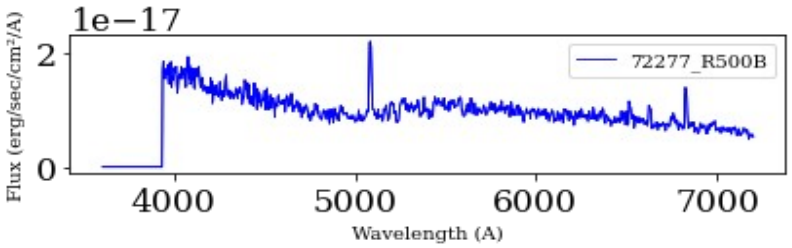

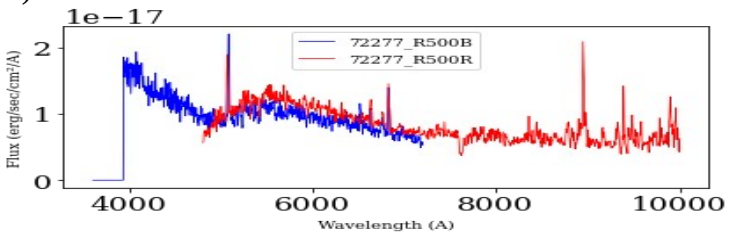

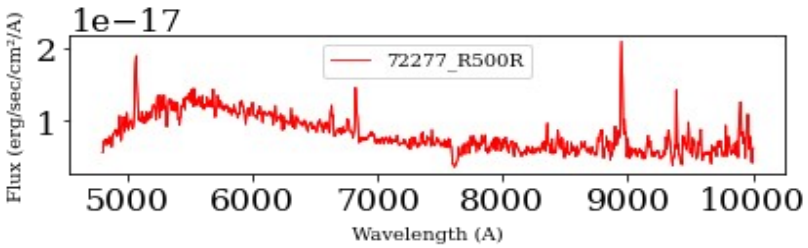

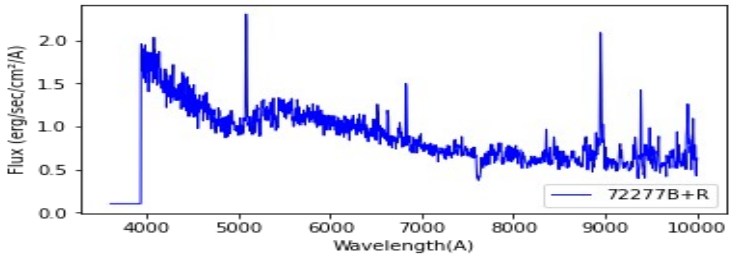

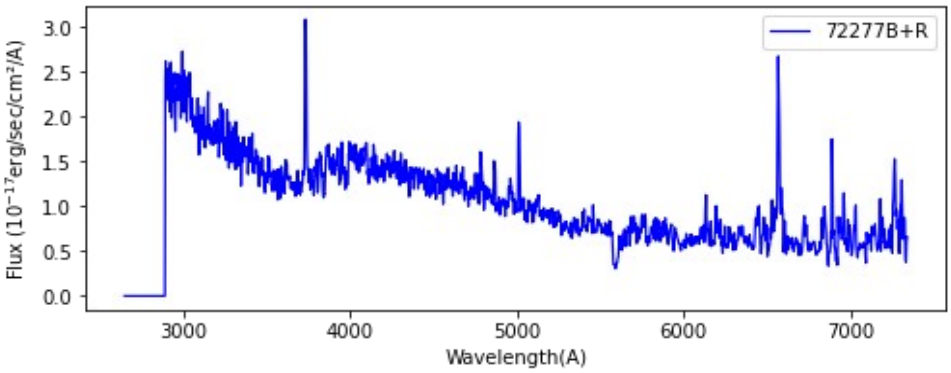

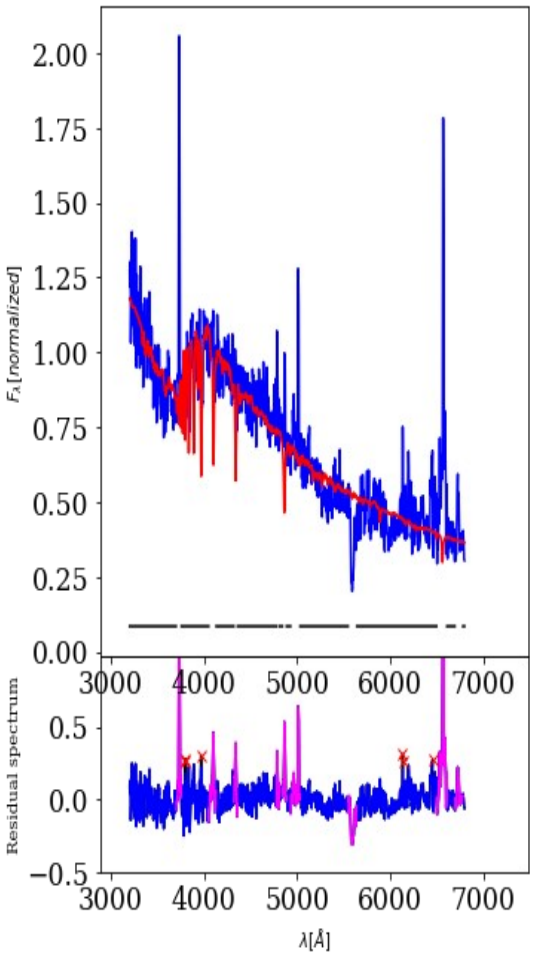

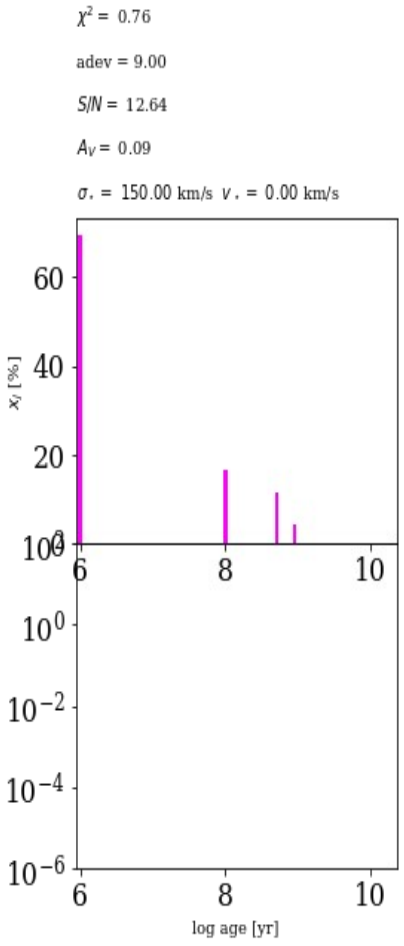

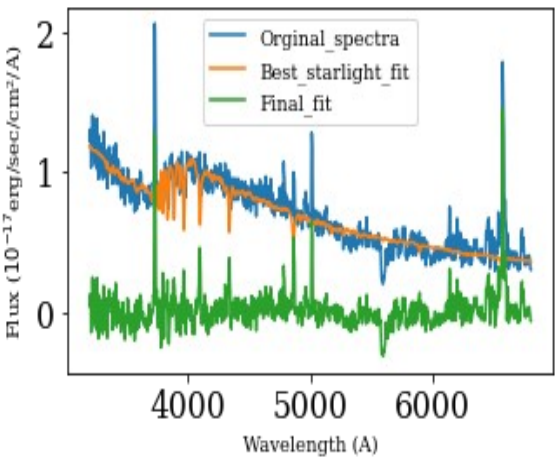

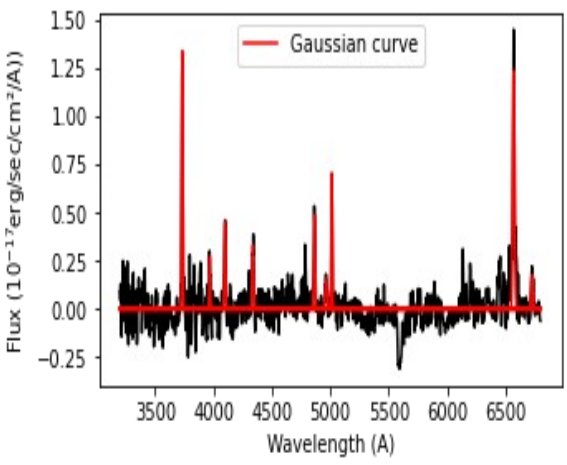

73205 (z_{spec}= 0.7795)

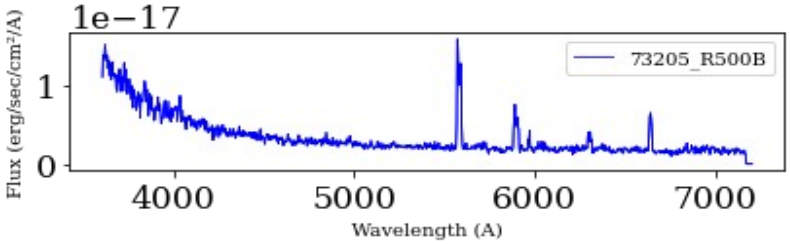

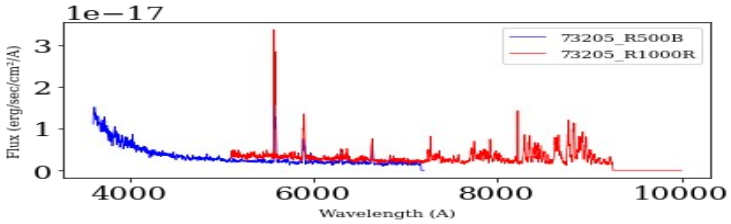

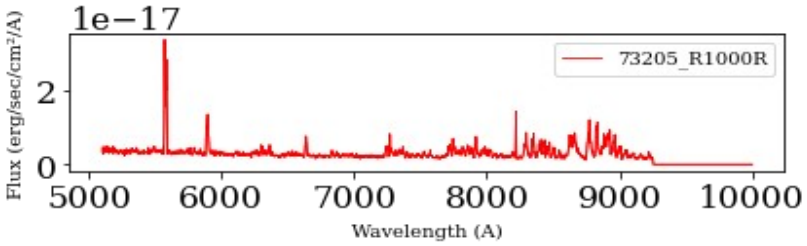

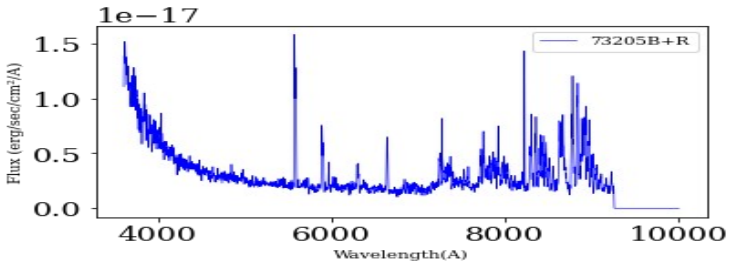

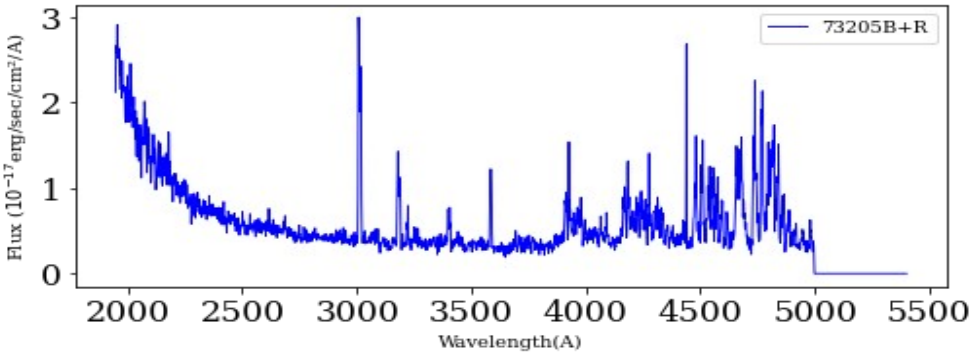

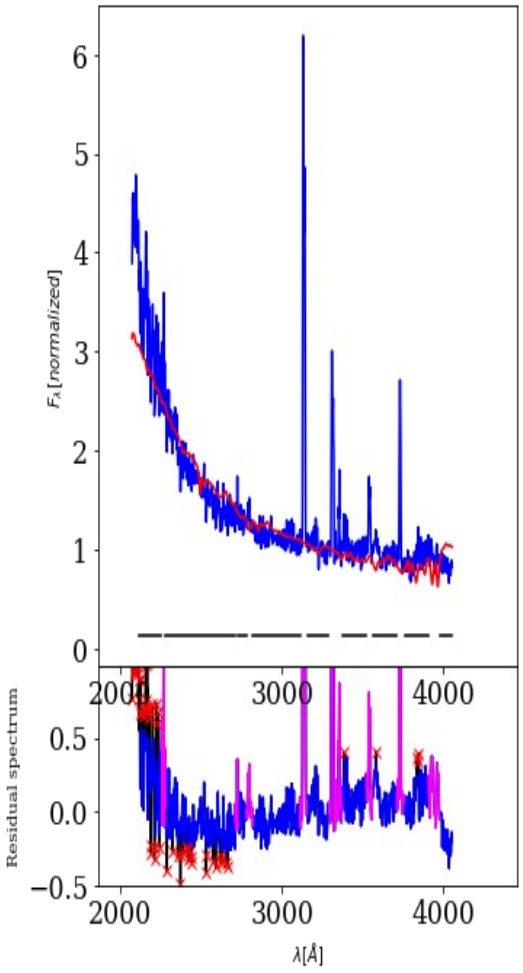

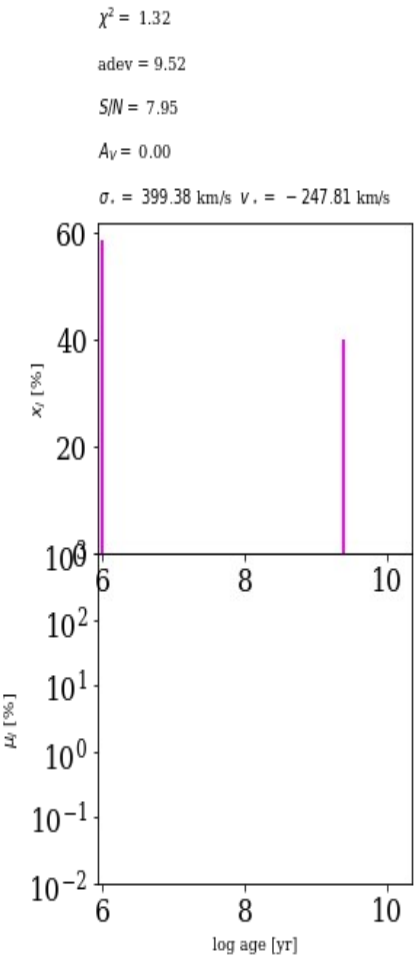

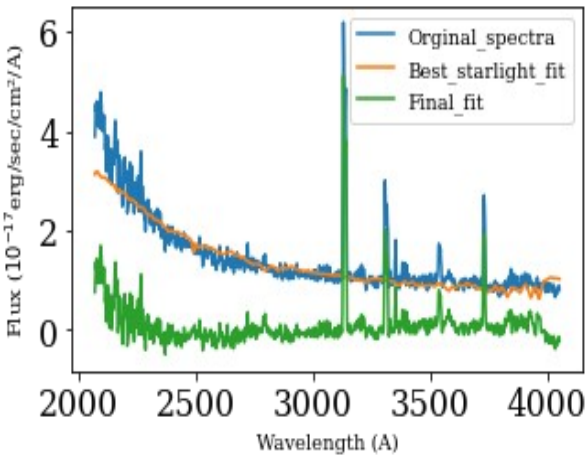

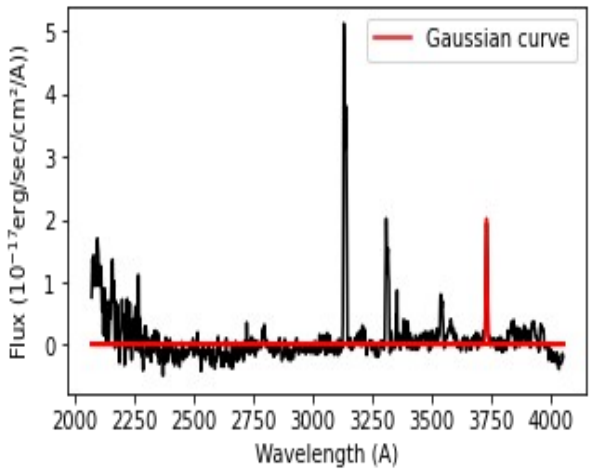

76168 (z_{spec} = 0.41067)

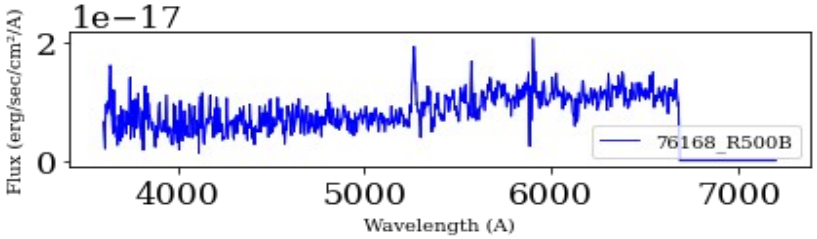

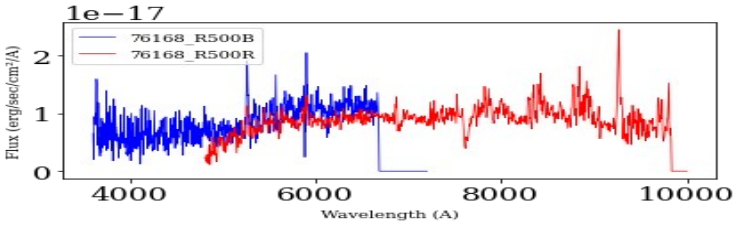

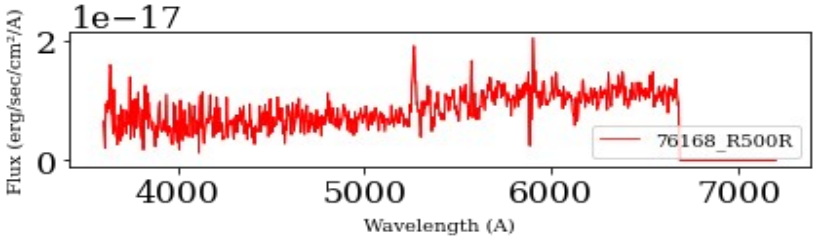

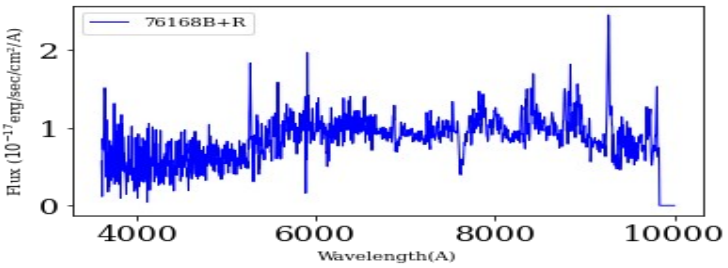

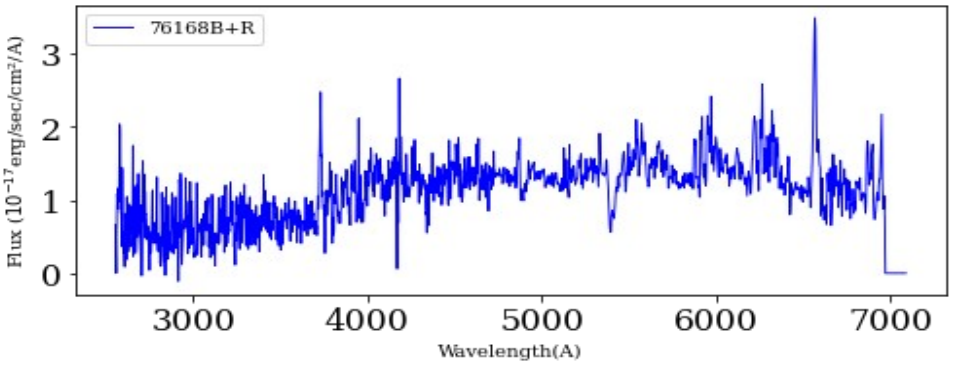

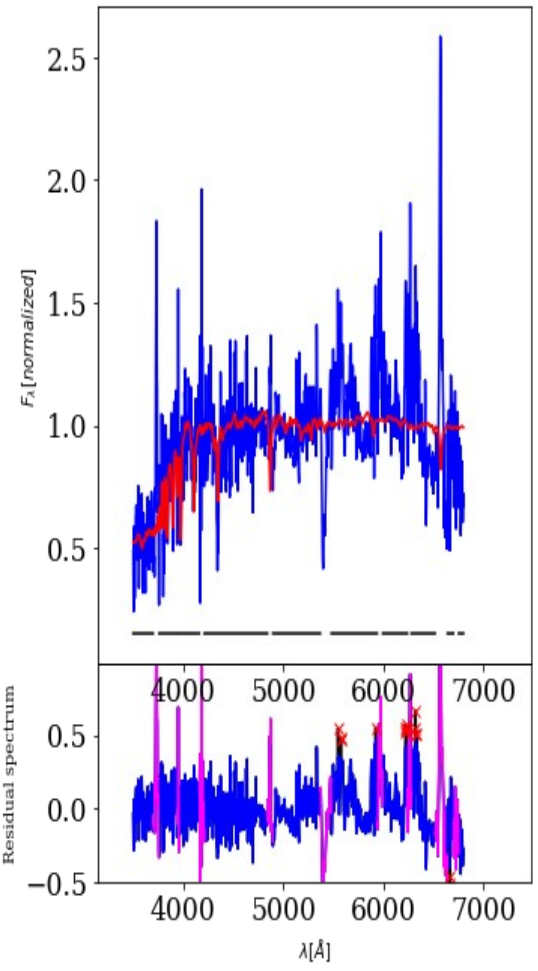

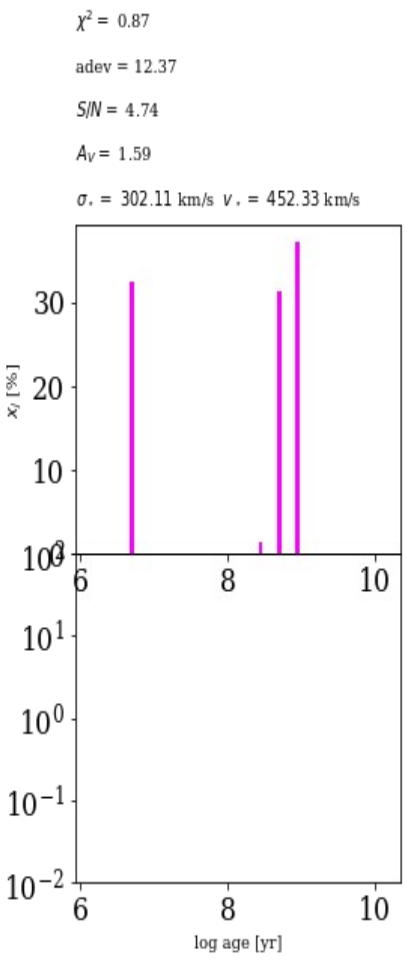

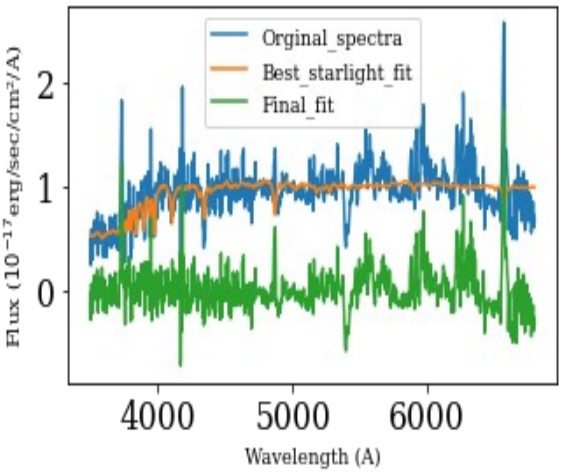

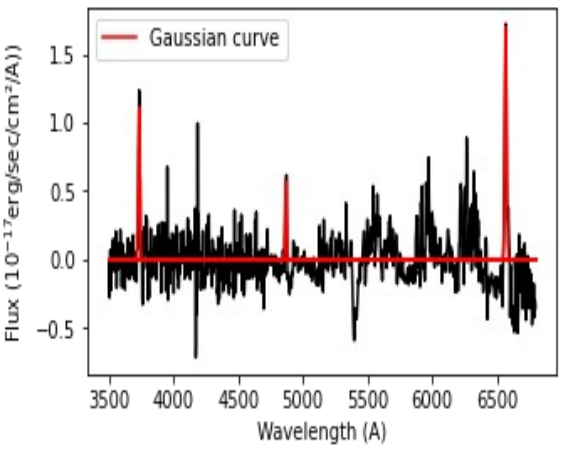

76375 (z_{spec} = 0.3621)

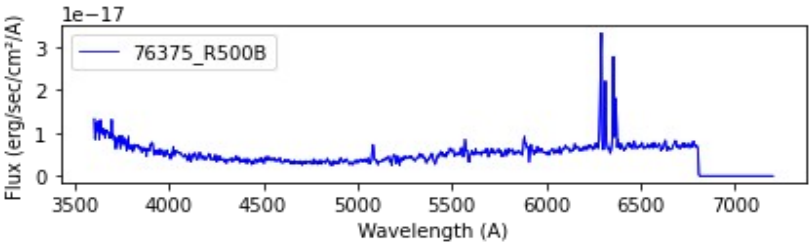

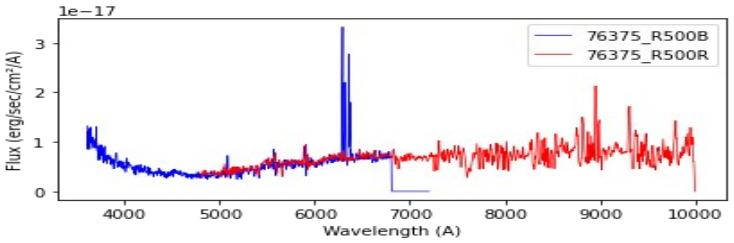

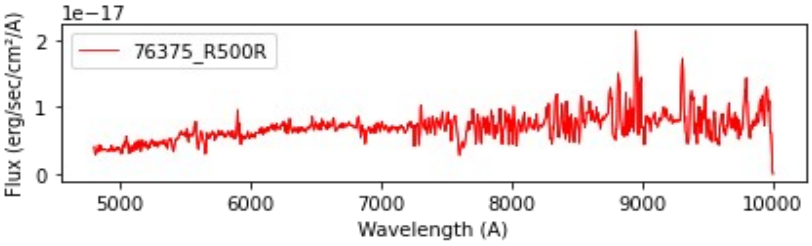

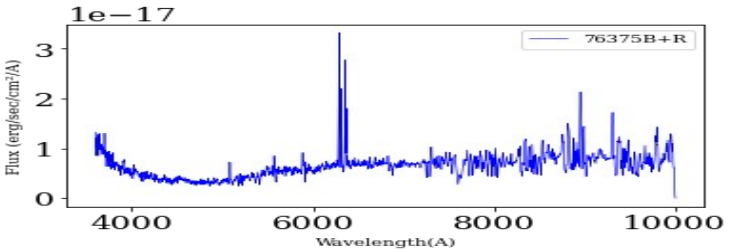

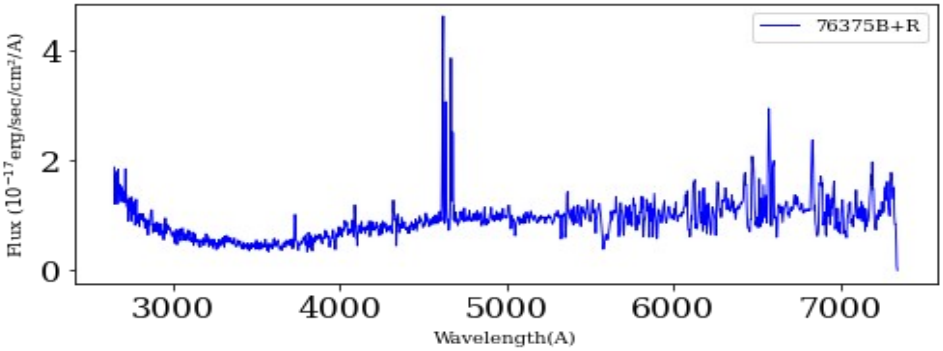

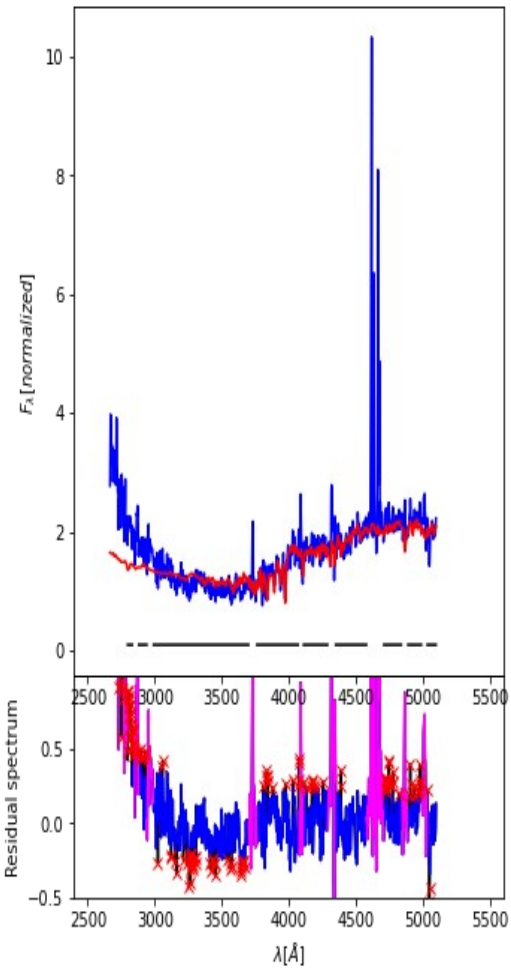

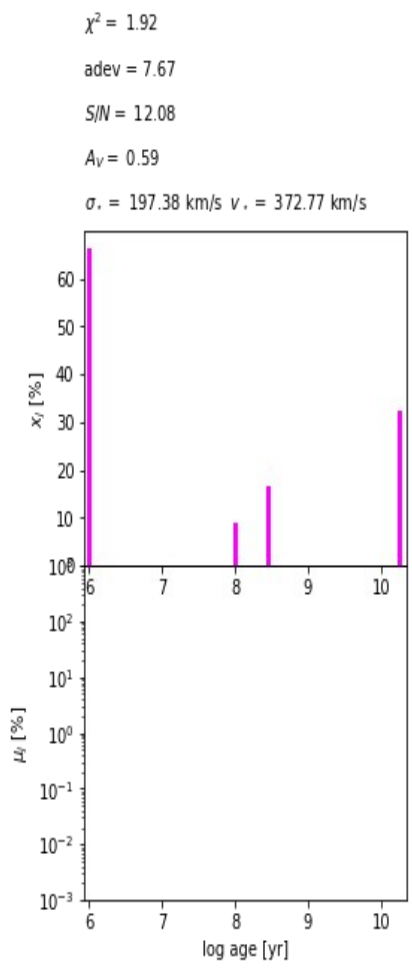

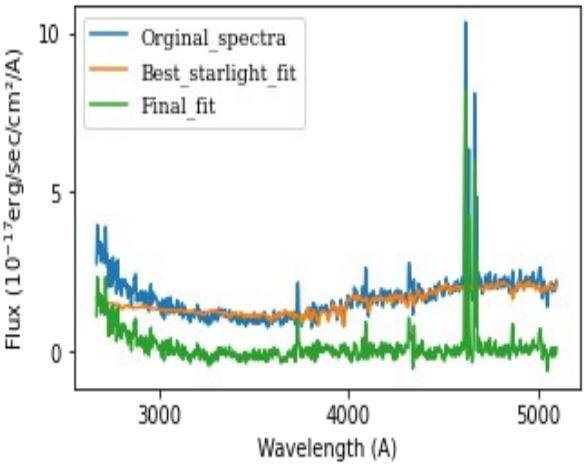

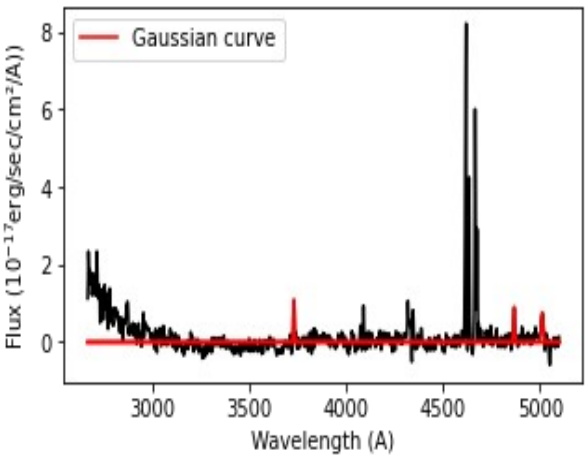

78620 (z_{spec}=0.4497)

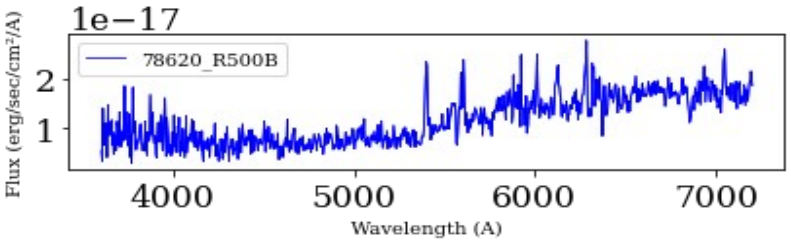

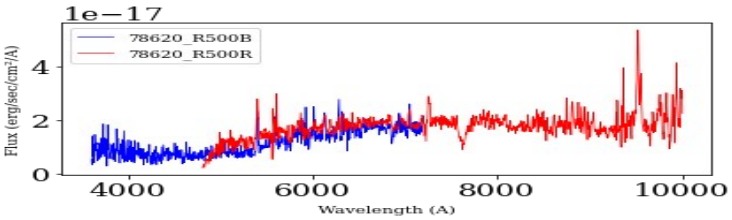

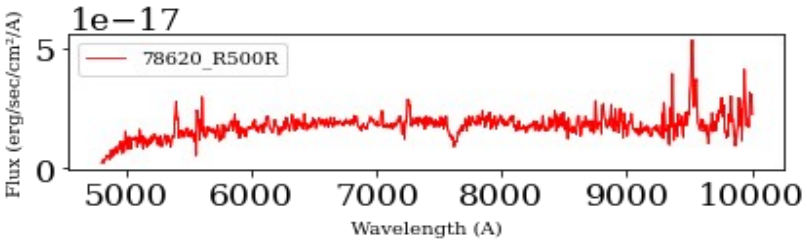

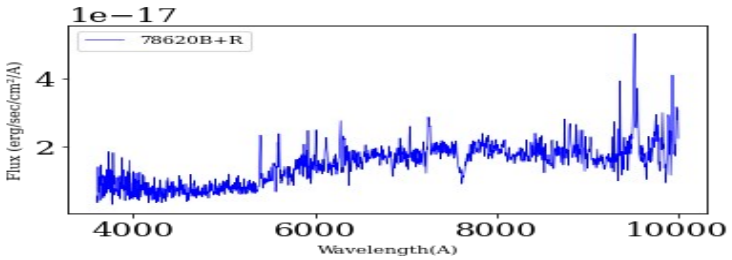

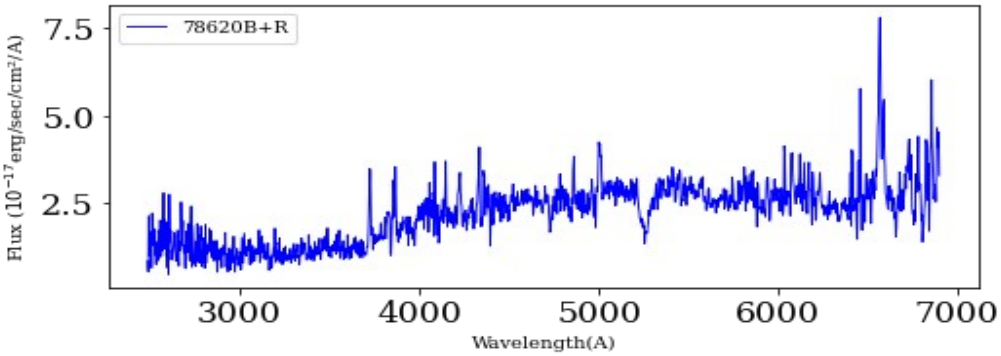

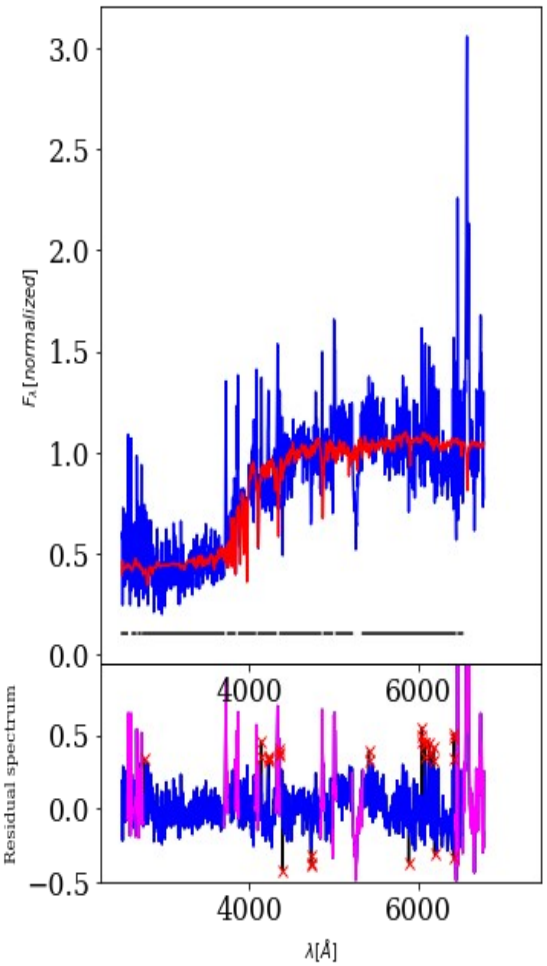

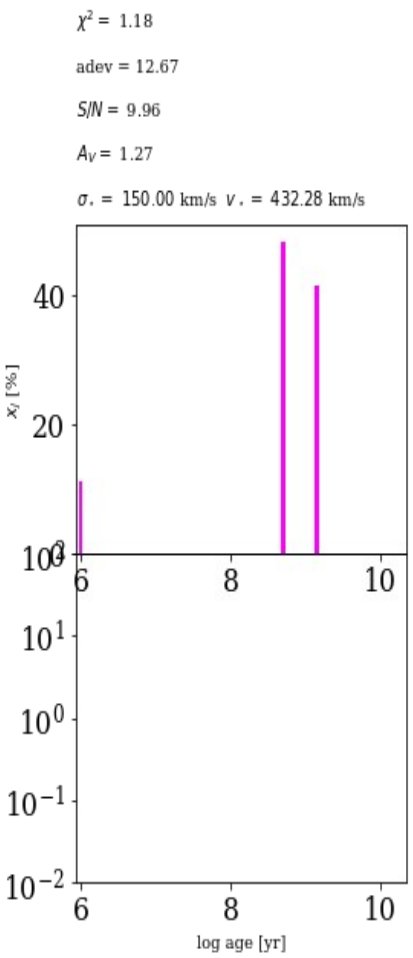

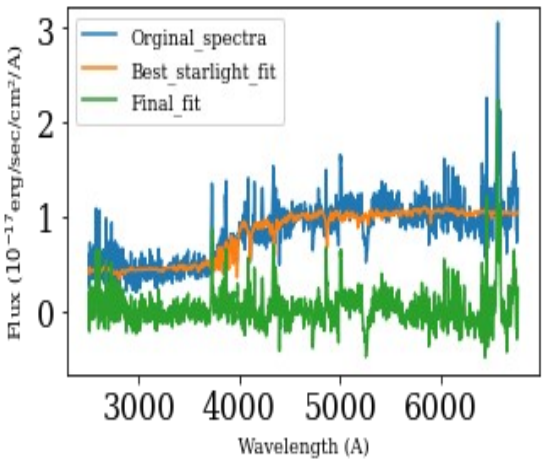

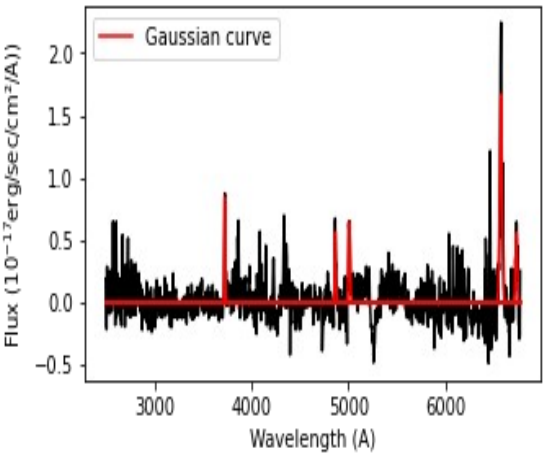

82204 (z_{spec}=0.4029)

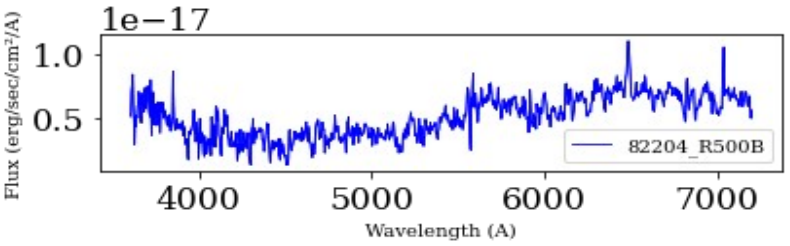

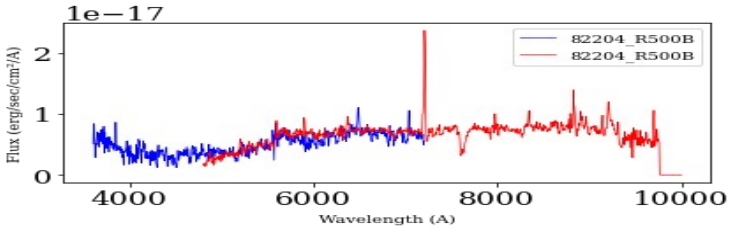

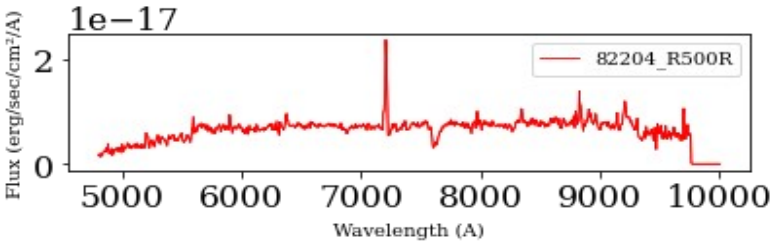

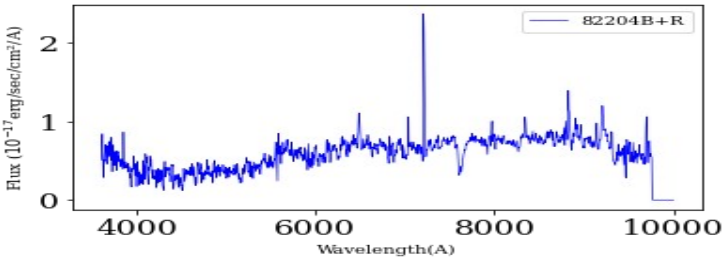

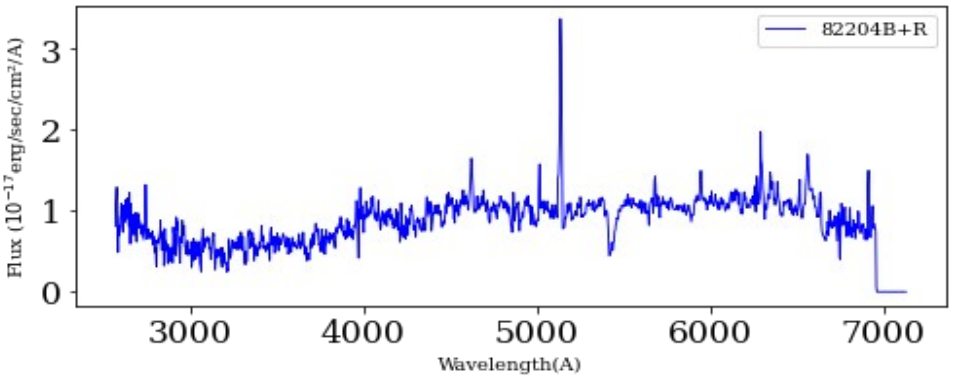

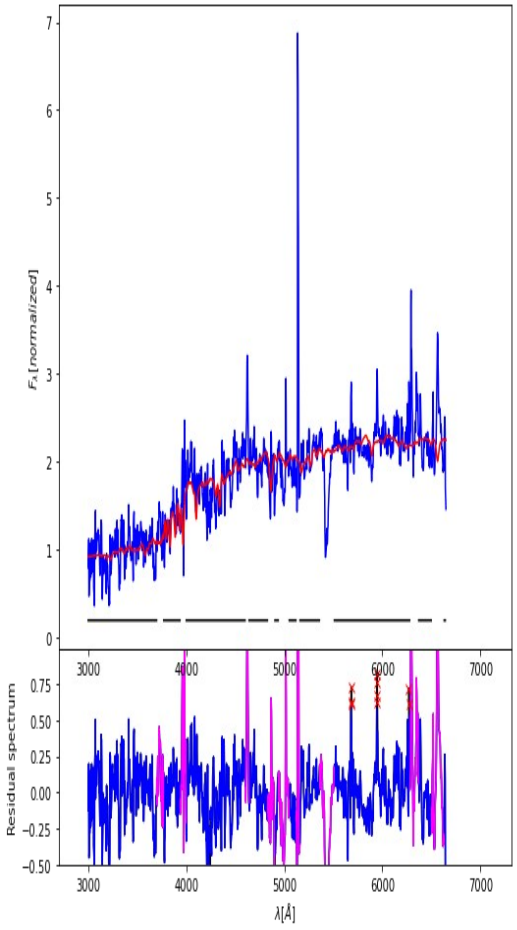

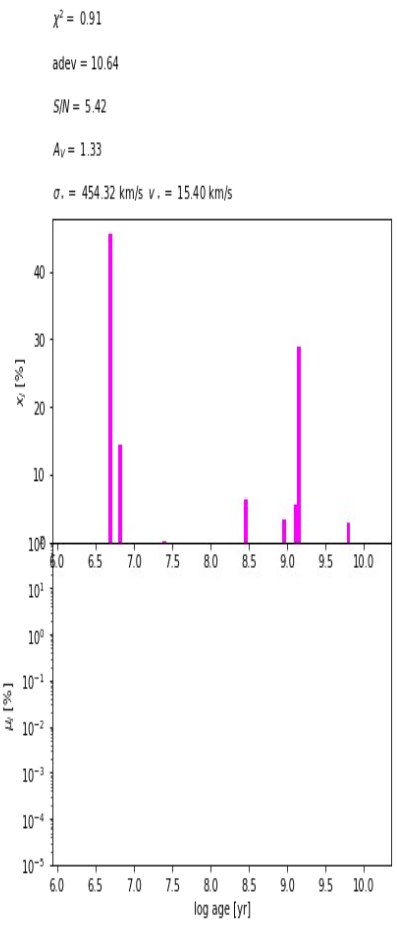

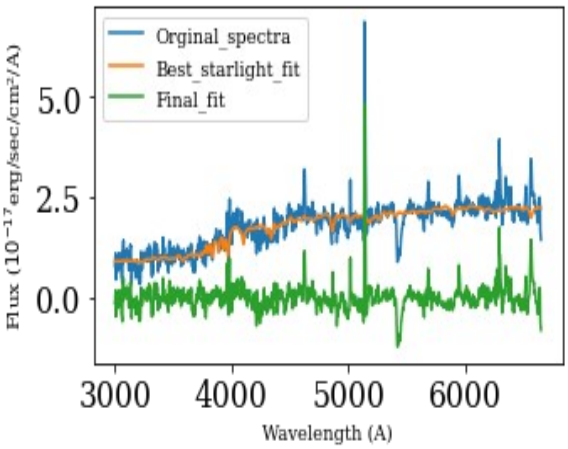

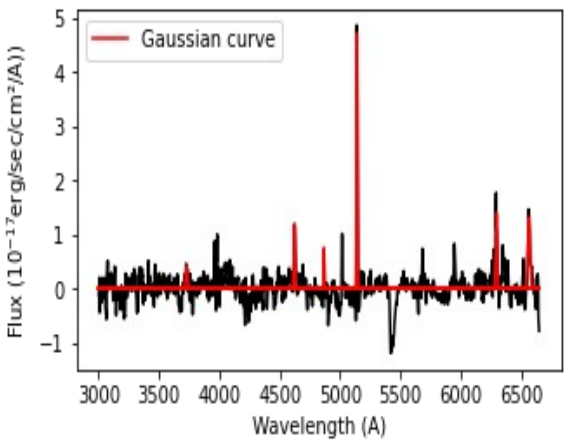

82297 (z_{spec}=0.207)

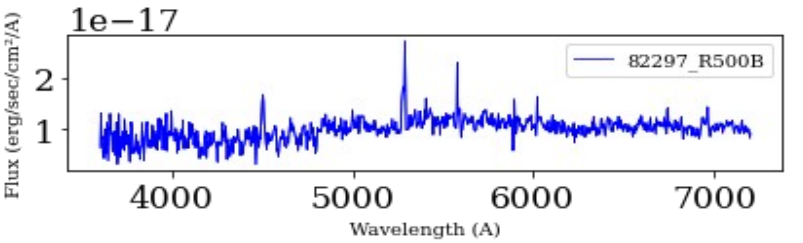

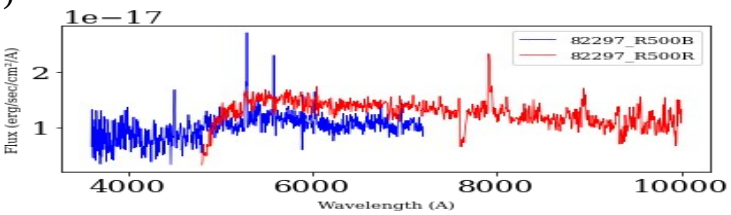

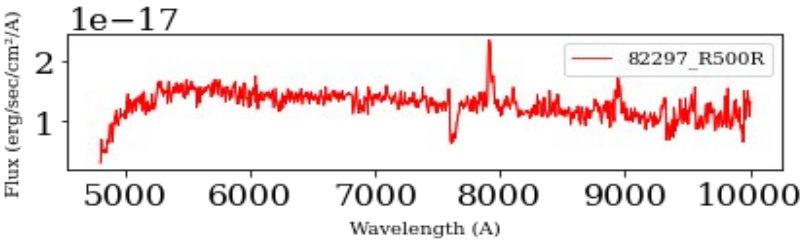

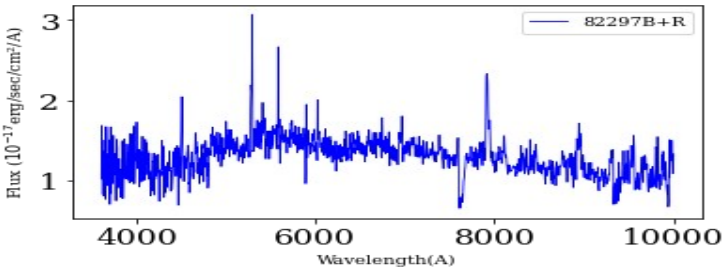

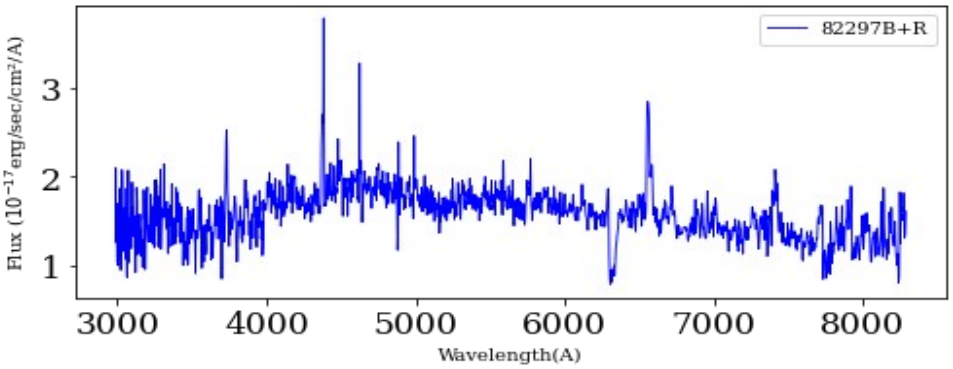

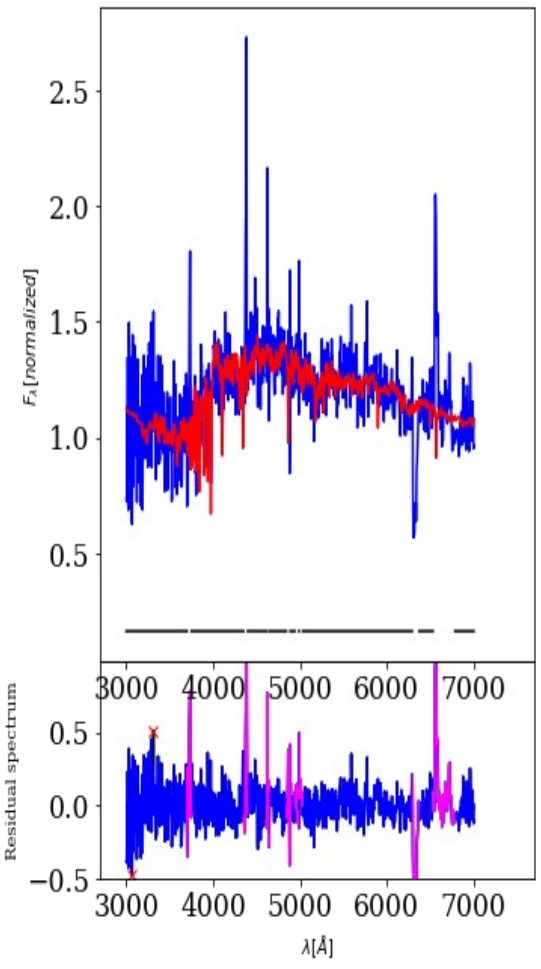

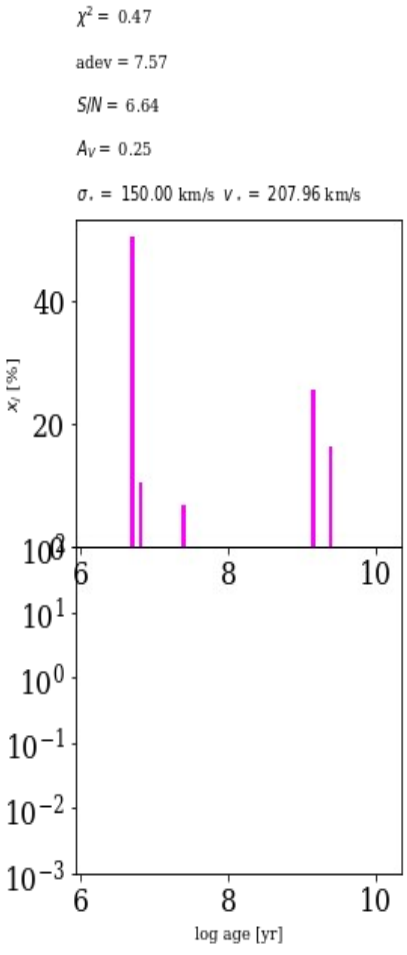

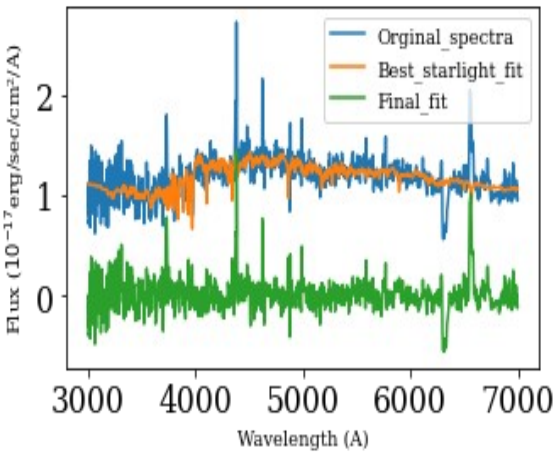

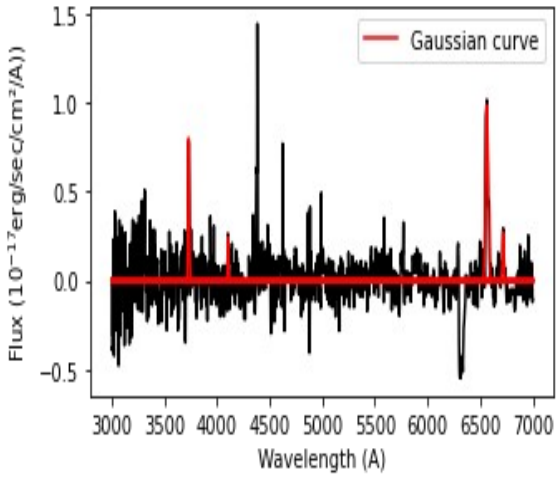

82506 (z_{spec}=0.4249)

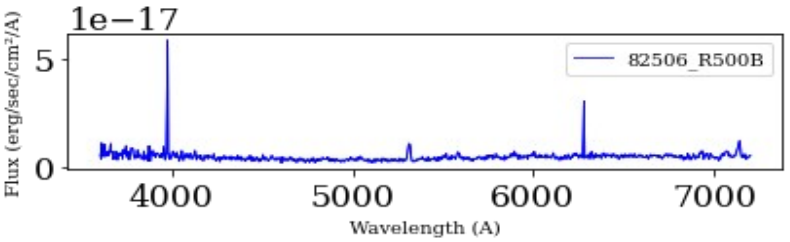

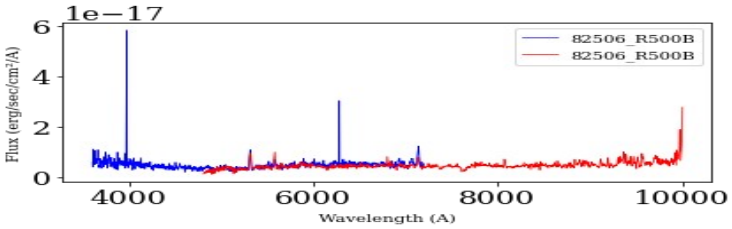

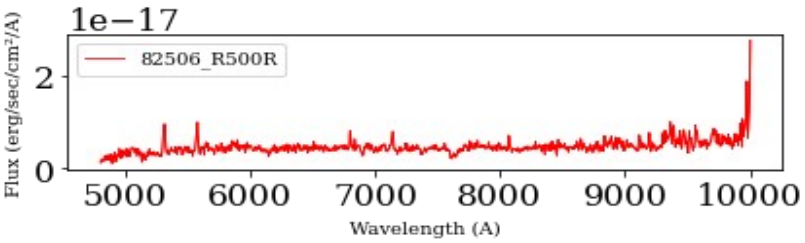

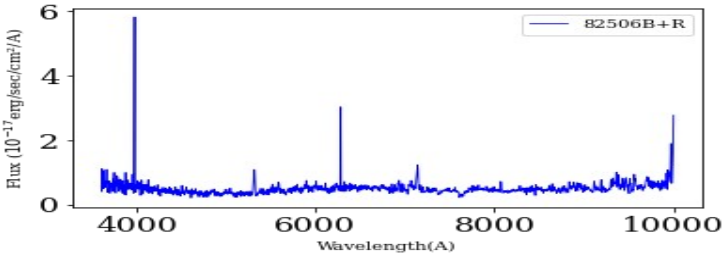

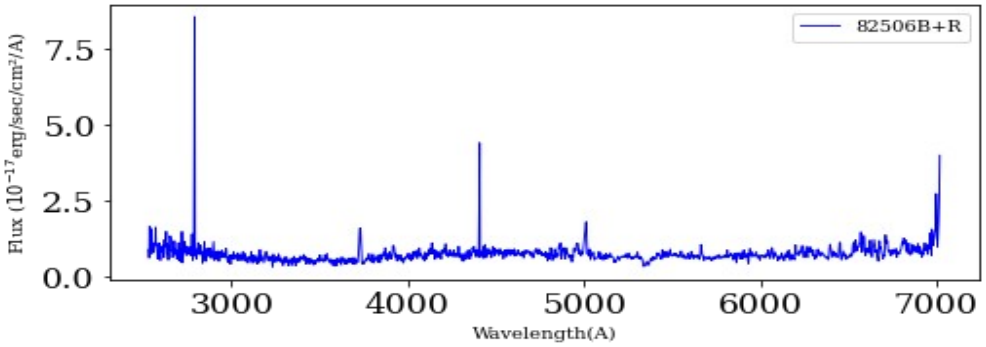

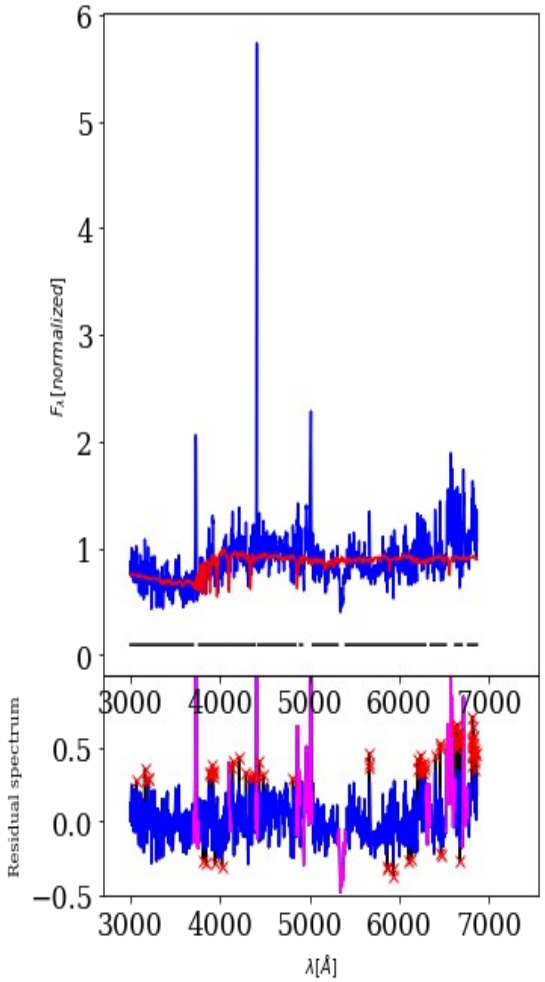

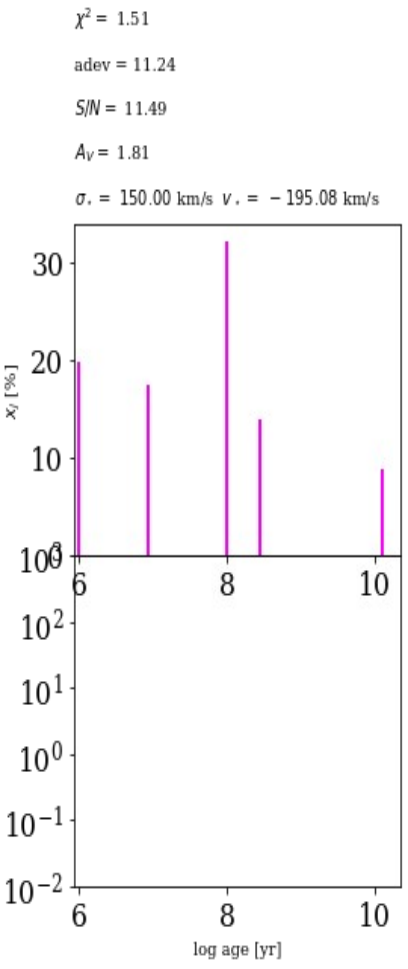

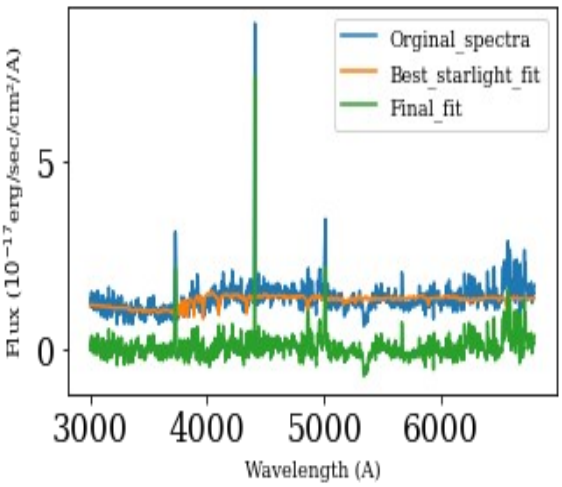

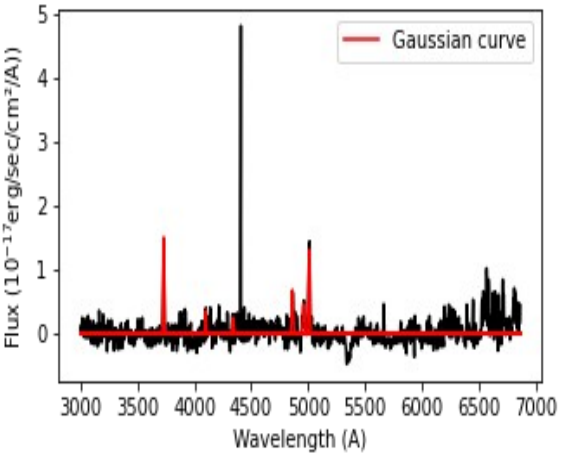

82584 (z_{spec} =0.4913)

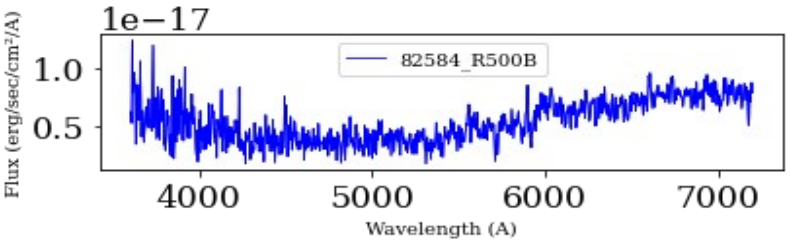

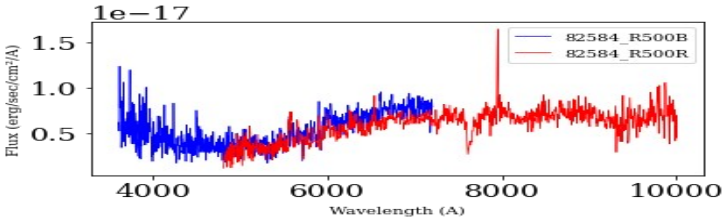

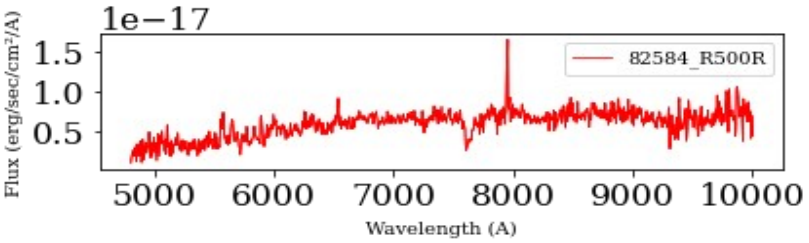

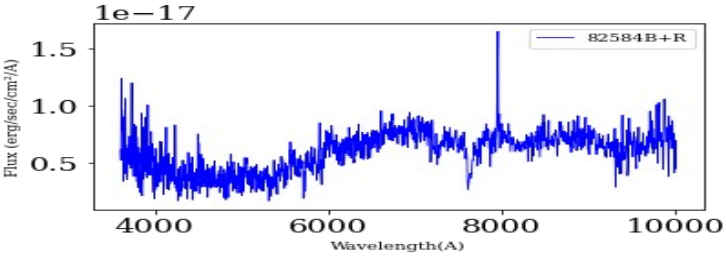

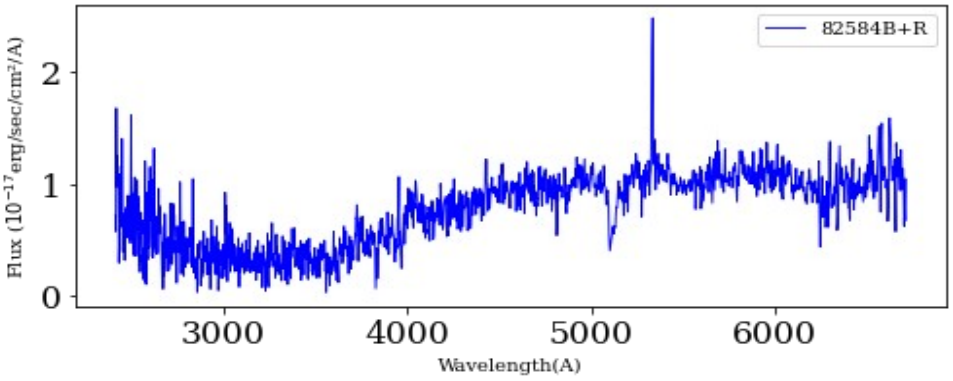

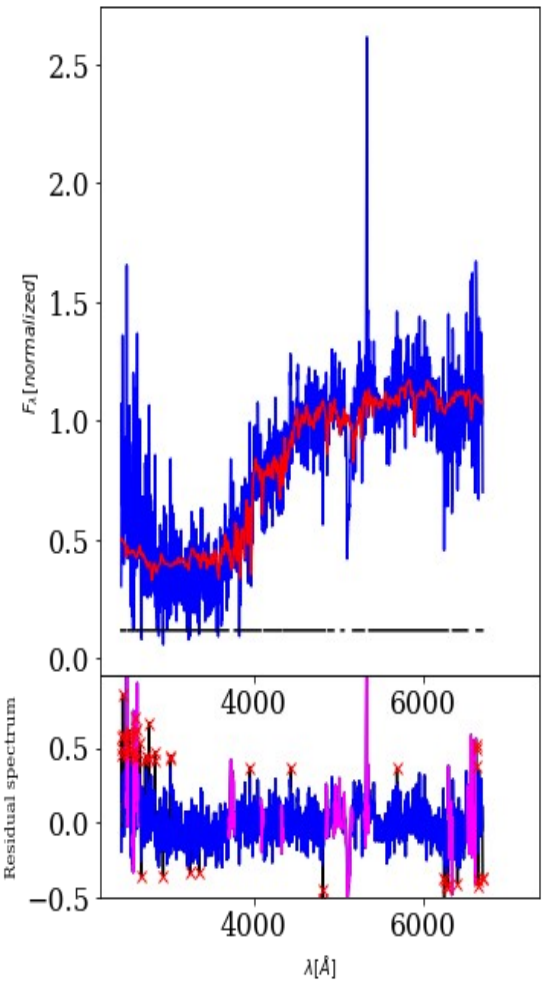

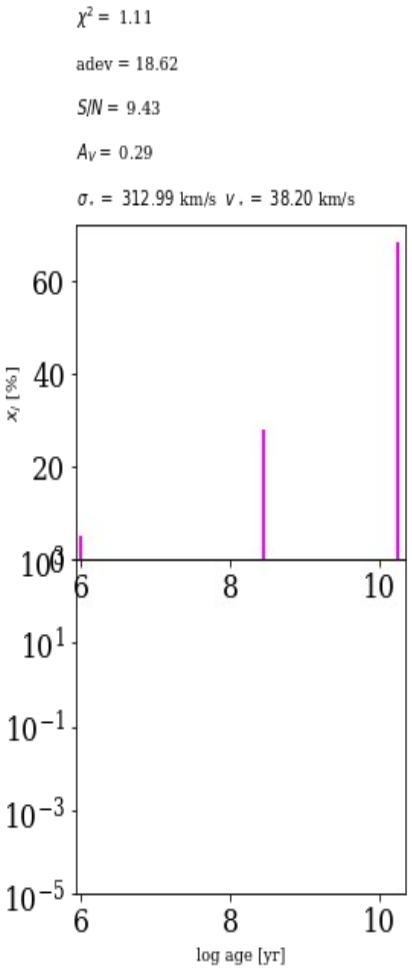

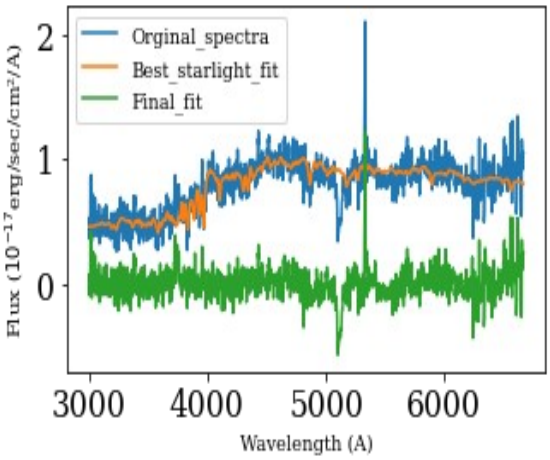

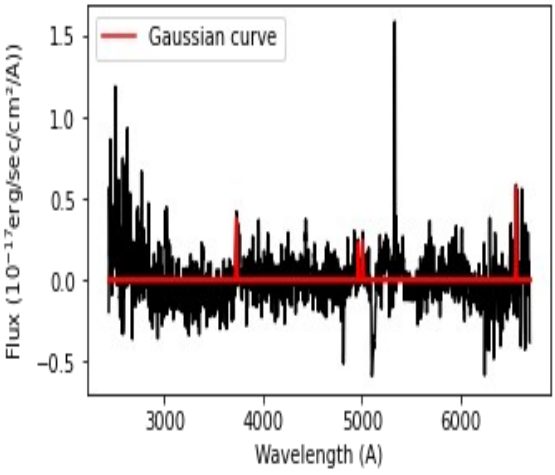

83268 (z_{spec} =0.38)

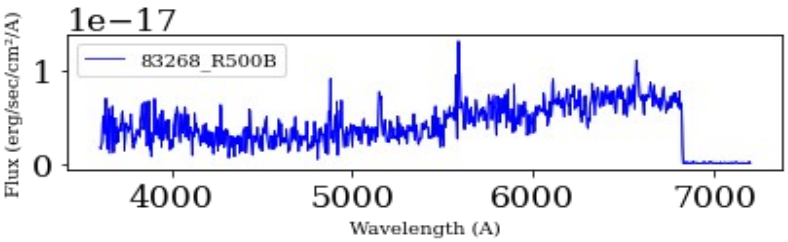

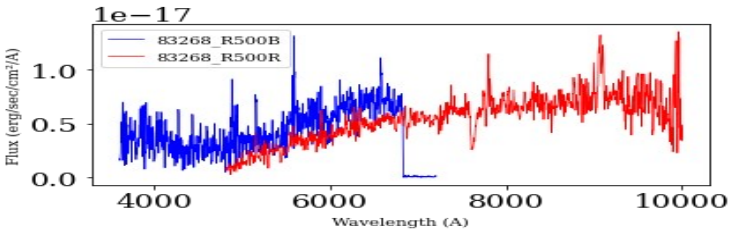

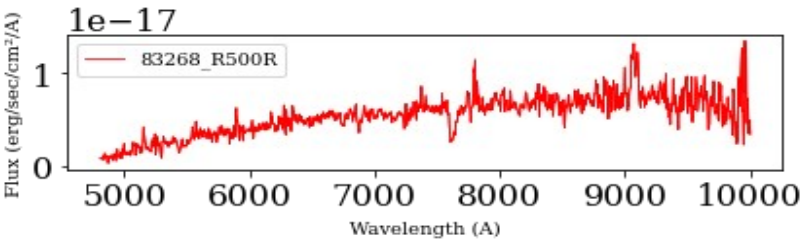

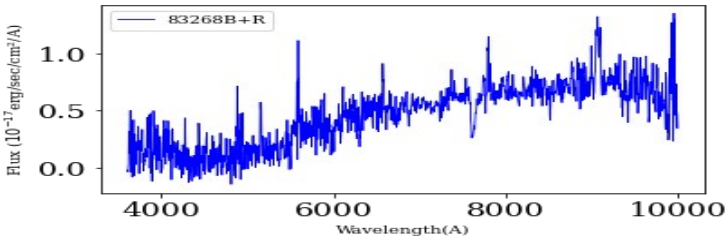

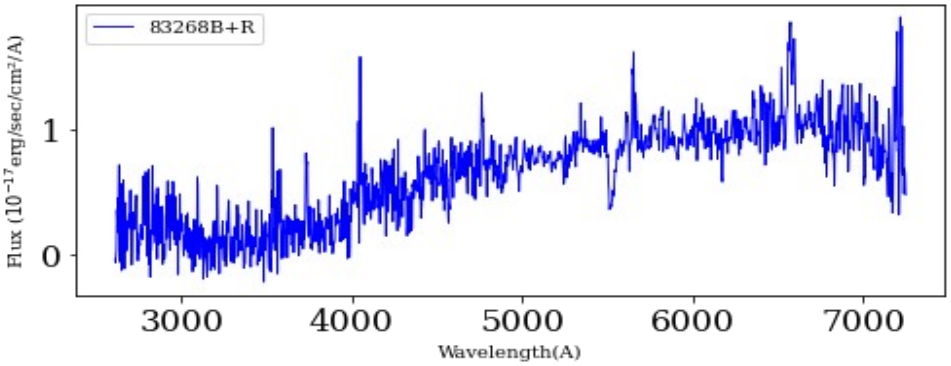

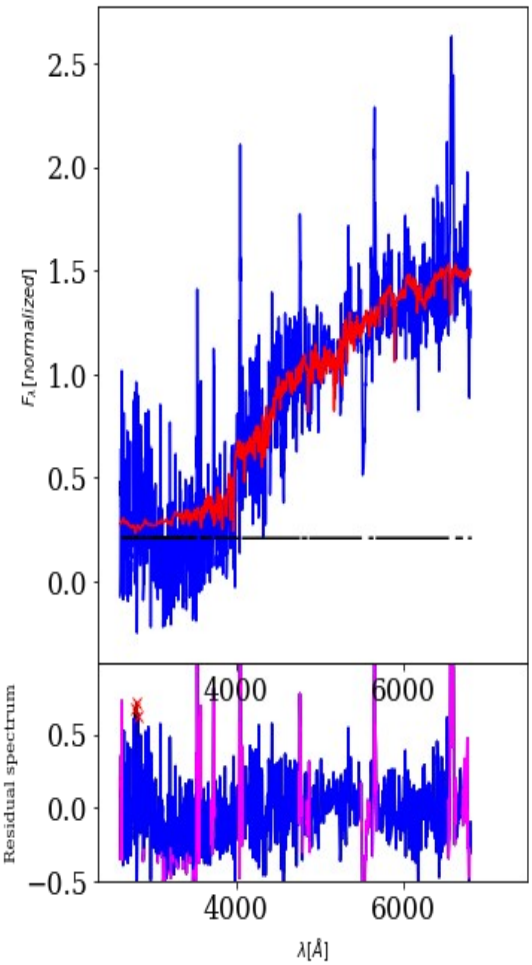

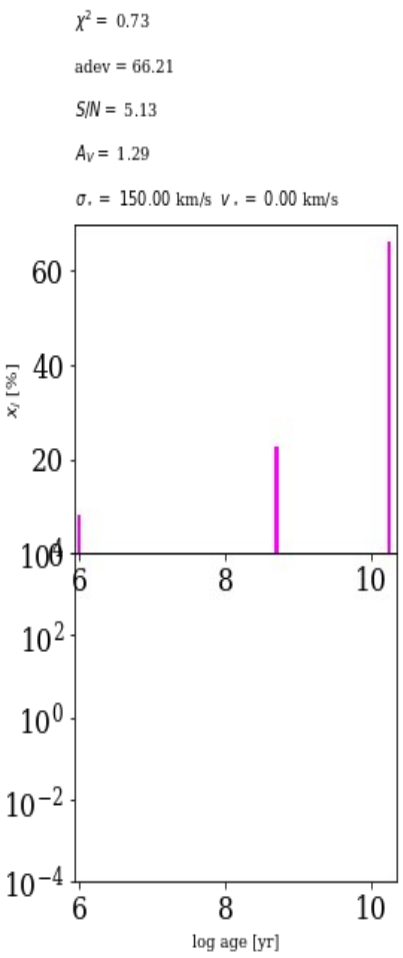

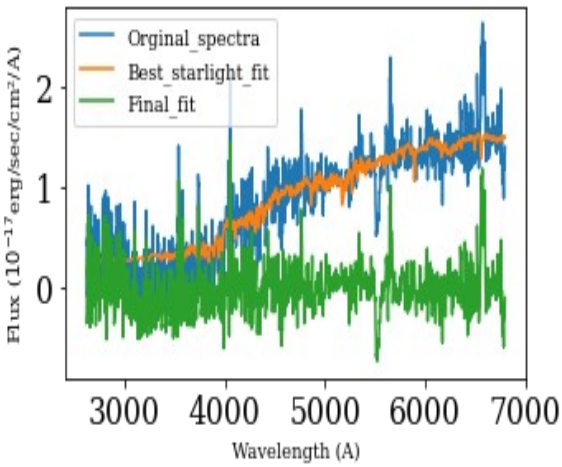

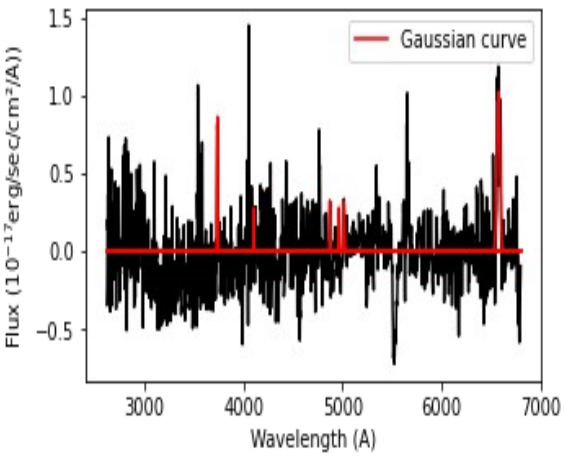

88430 (z_{spec} =0.5144)

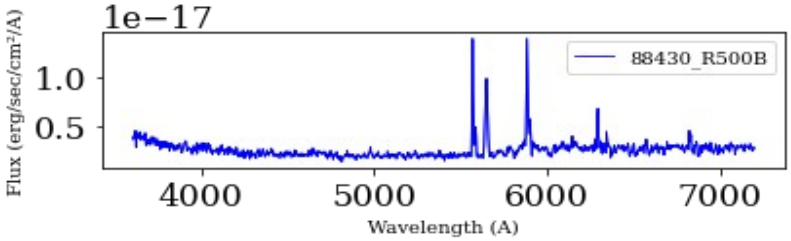

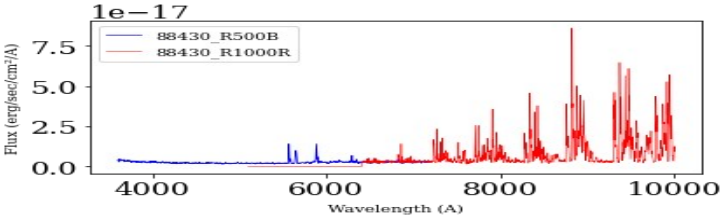

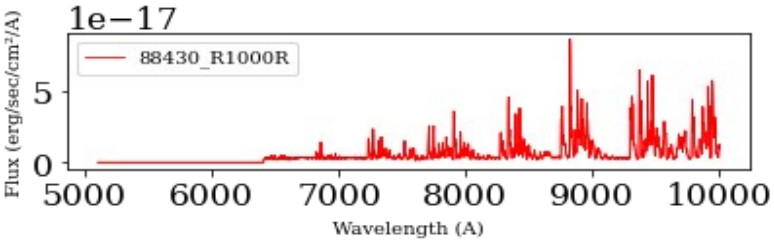

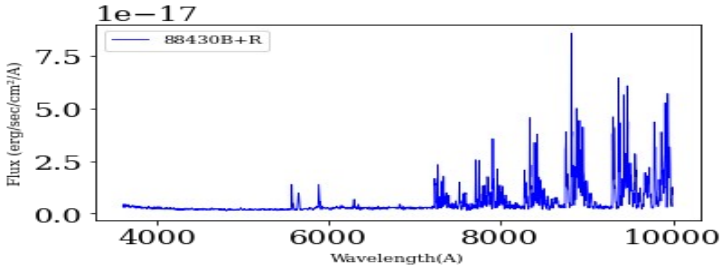

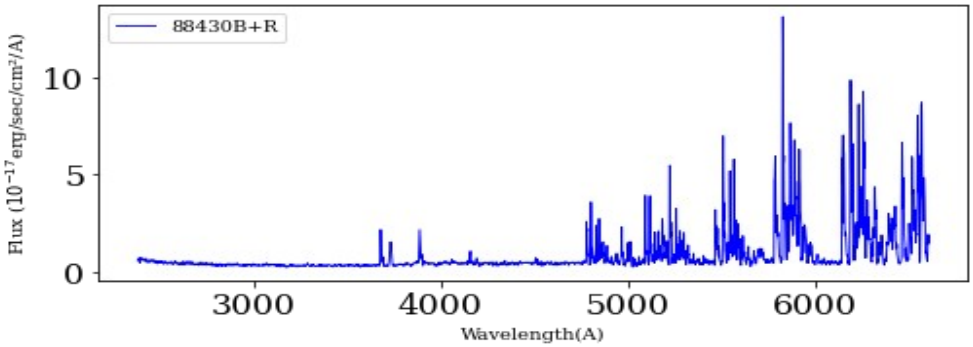

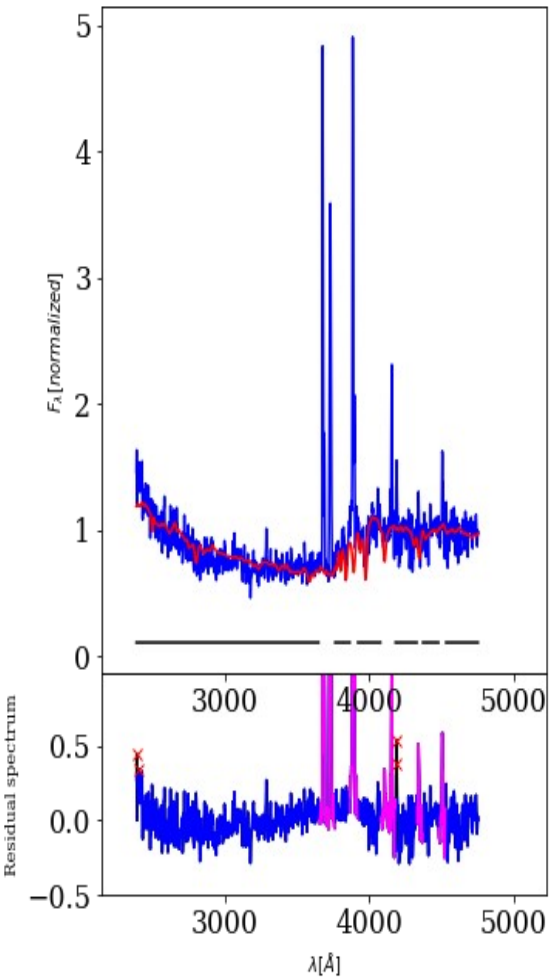

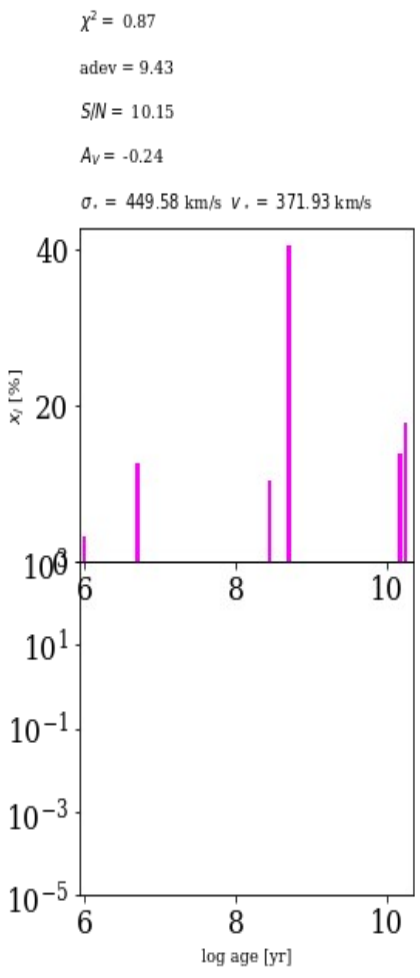

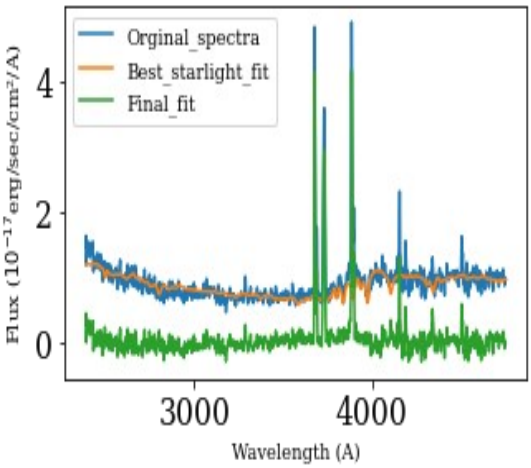

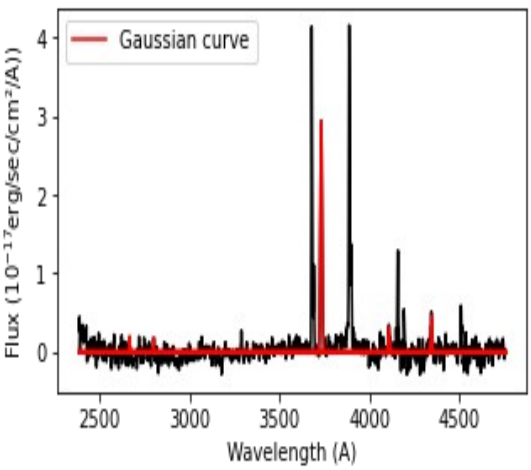

88890 (z_{spec} =0.4568)

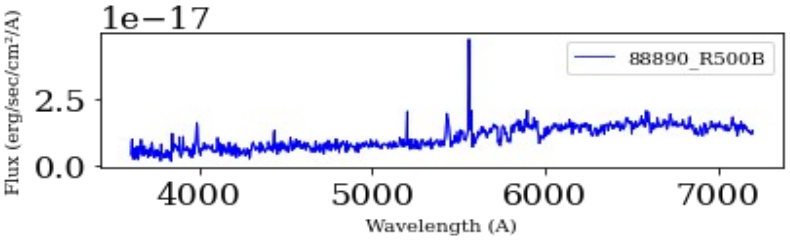

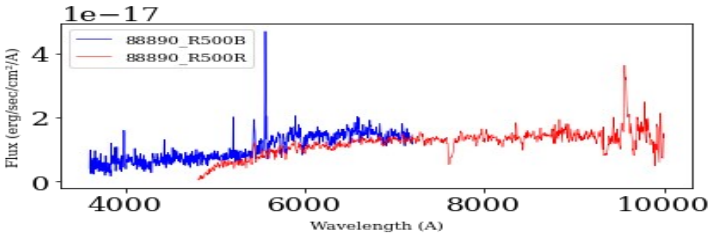

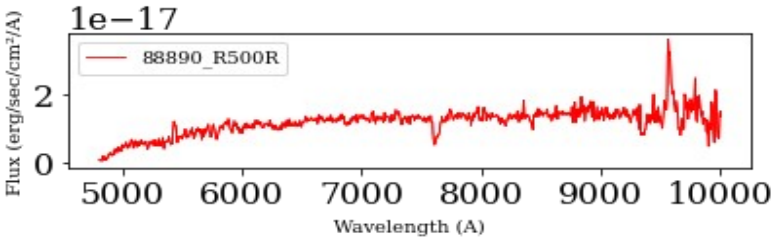

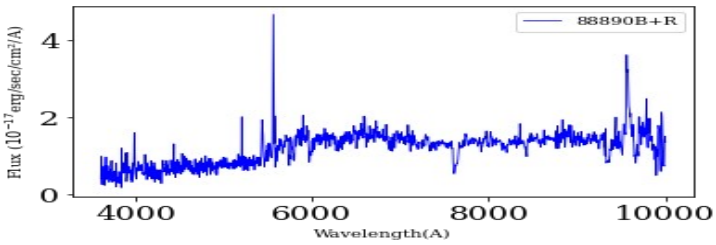

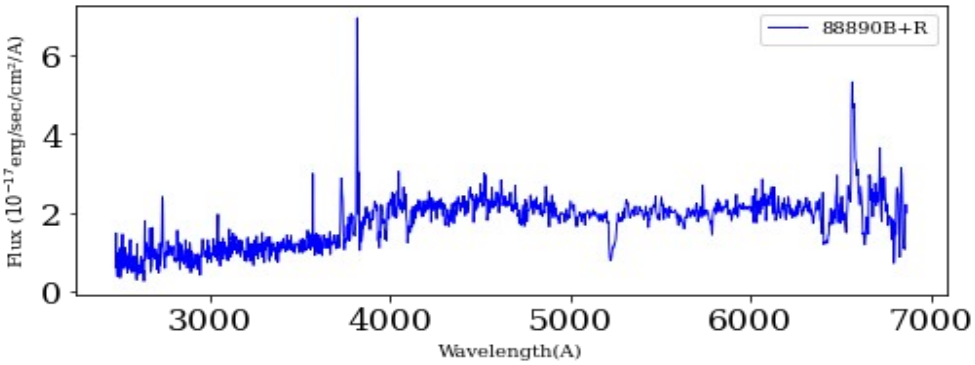

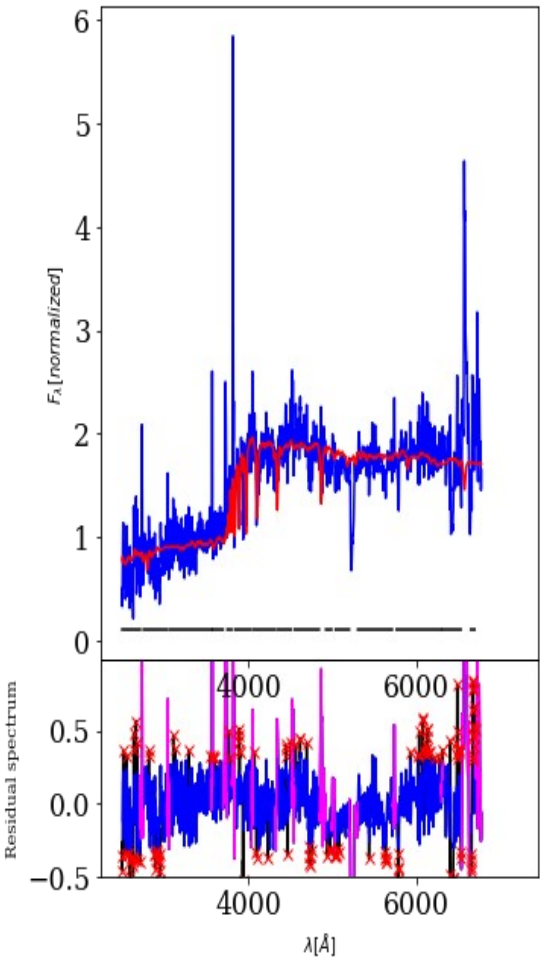

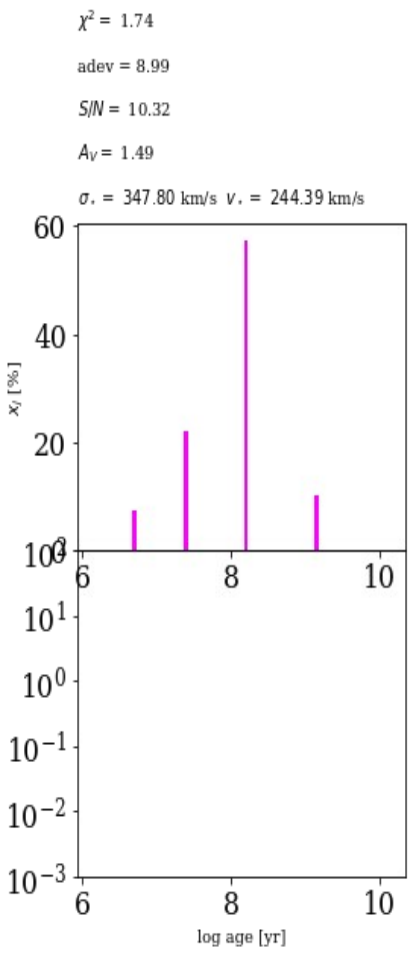

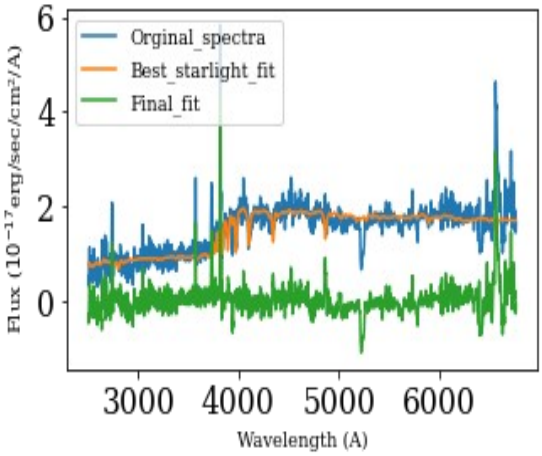

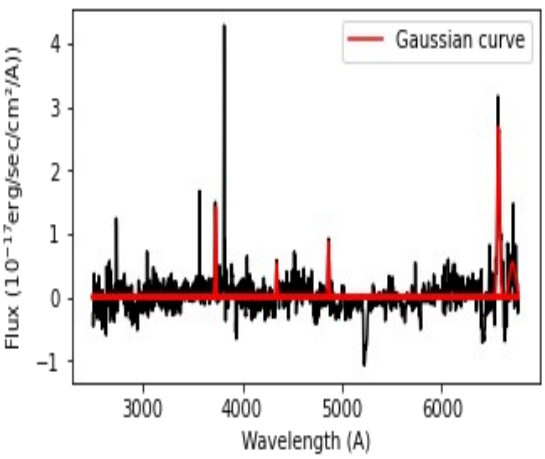

88957 (z_{spec} =0.4082)

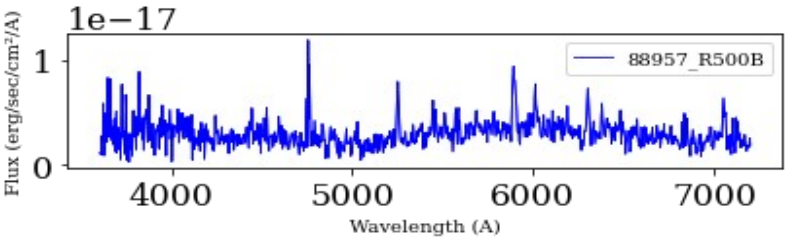

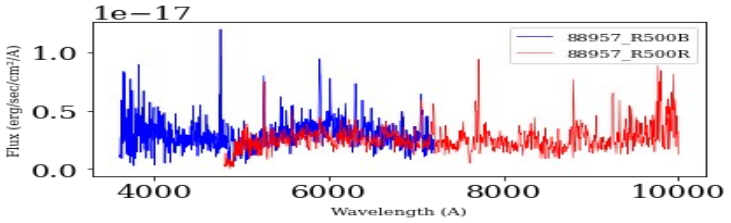

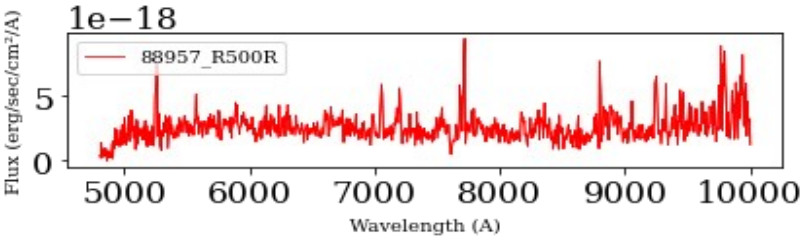

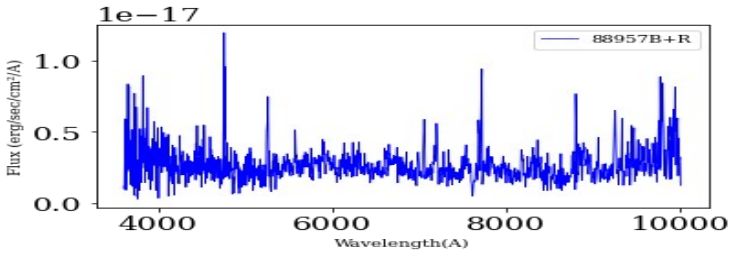

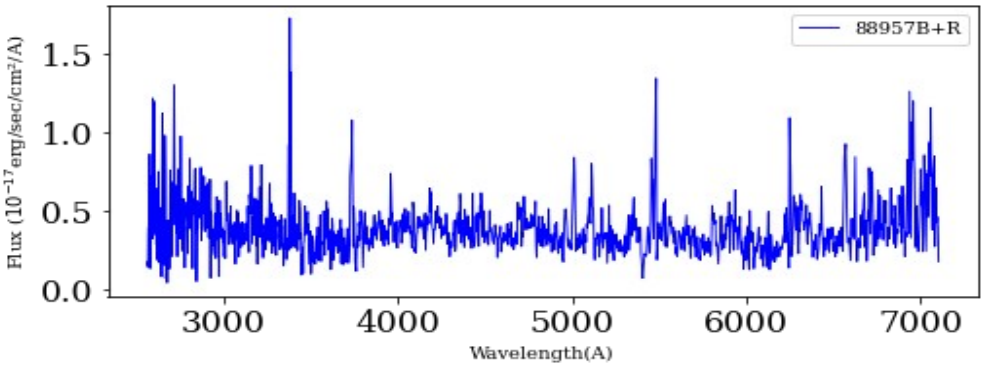

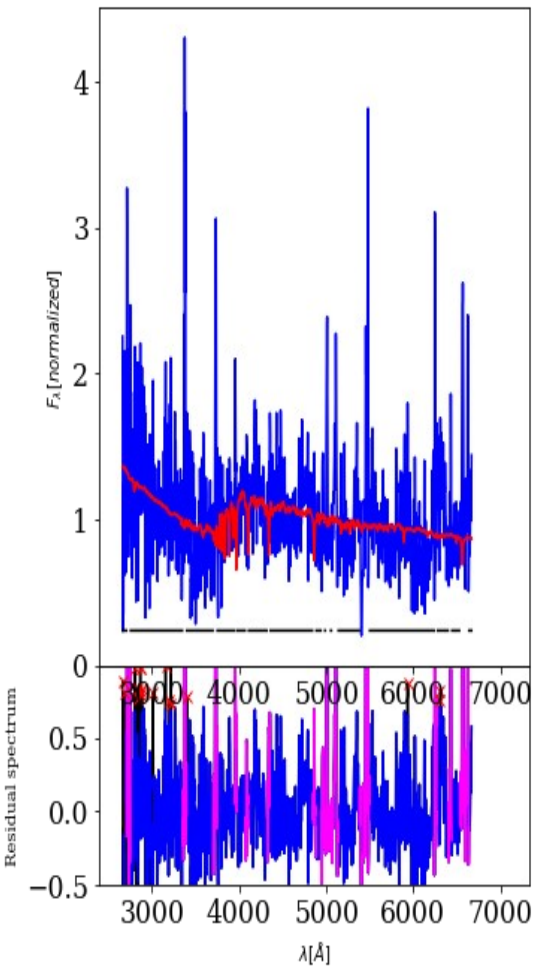

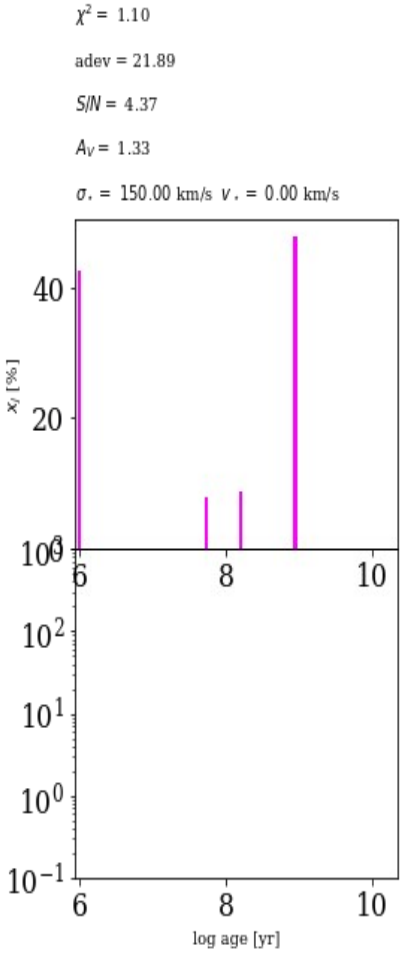

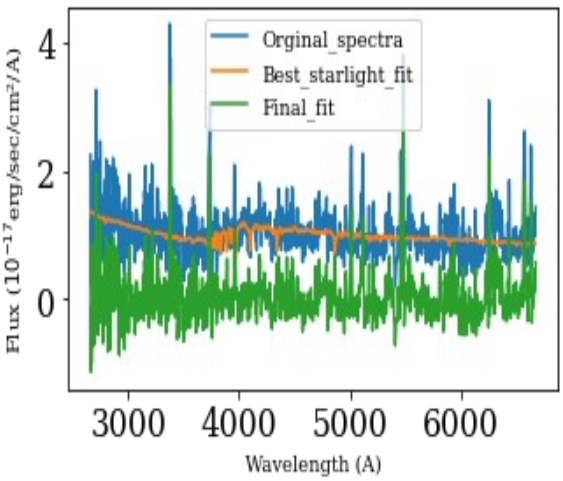

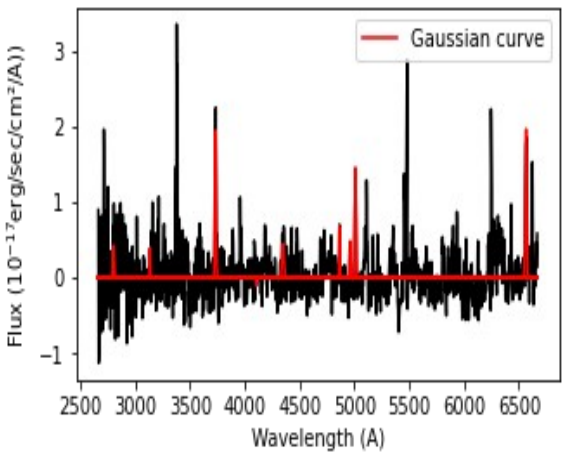

94606 (z_{spec} =0.3334)

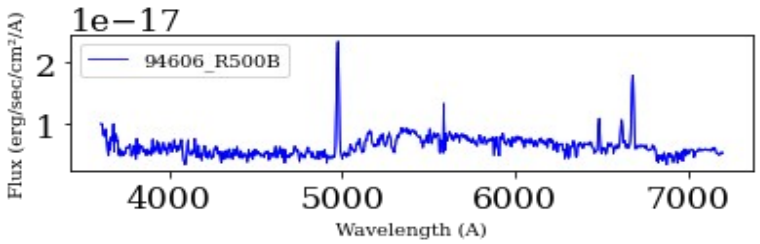

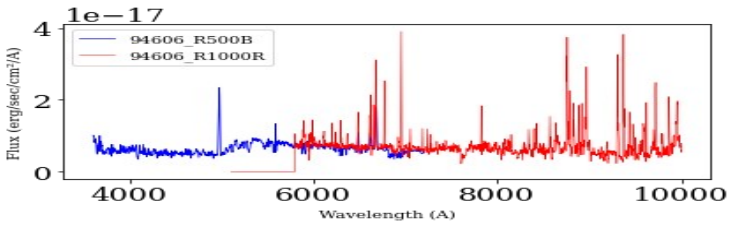

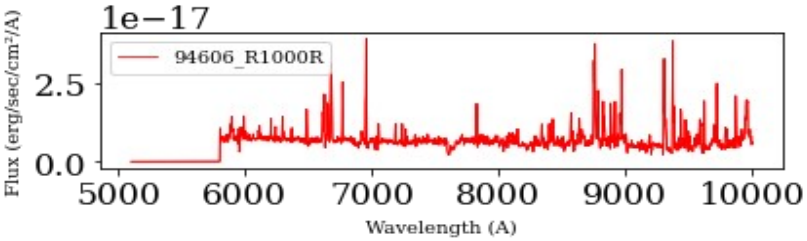

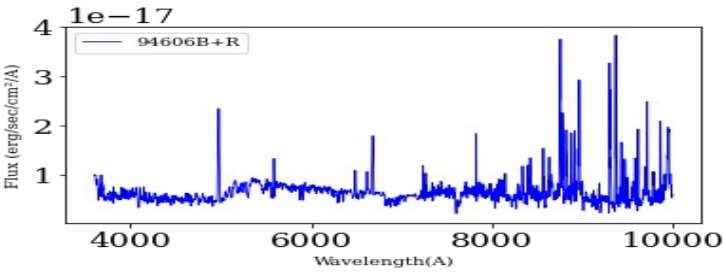

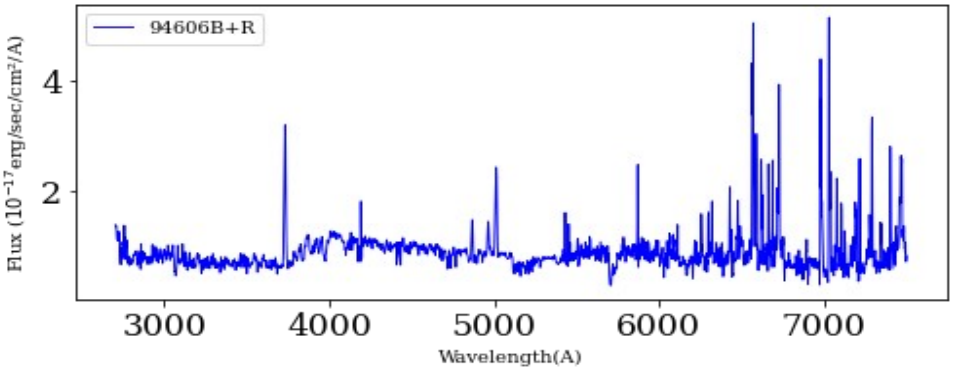

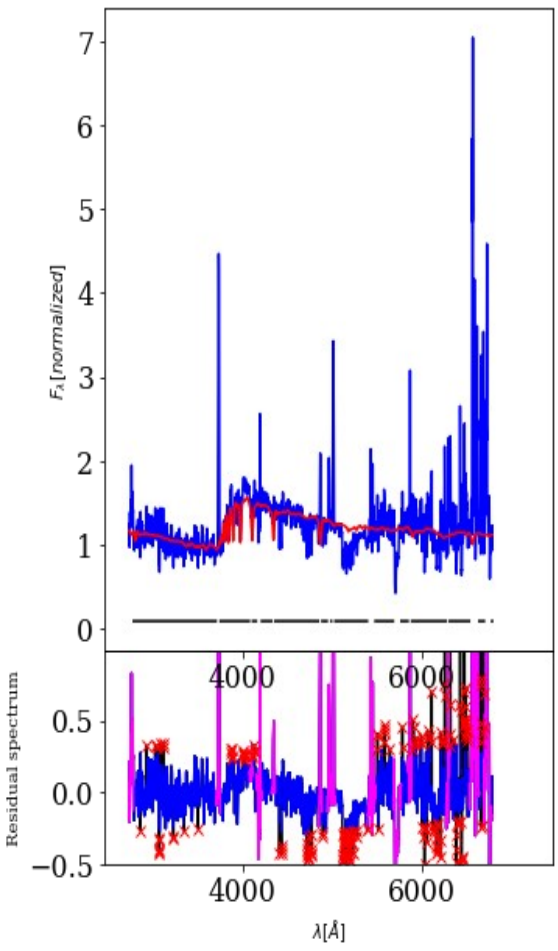

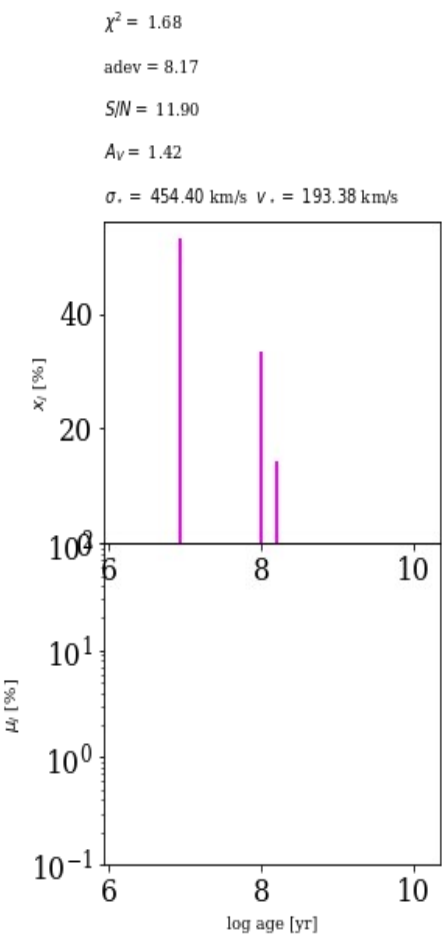

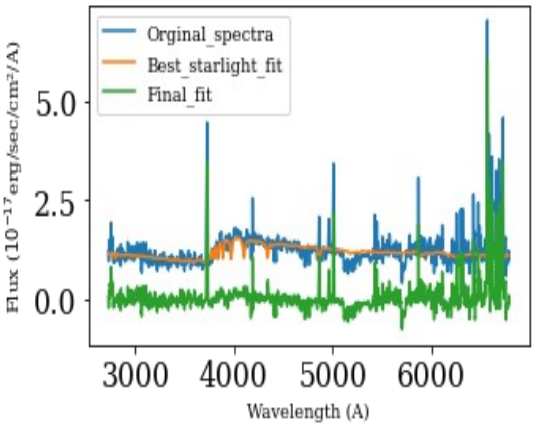

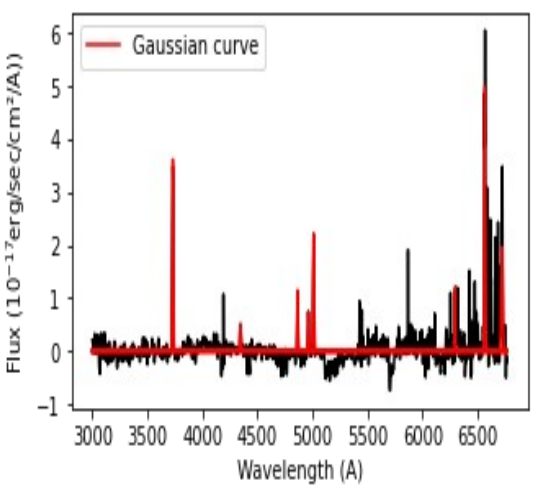

102234 (z_{spec} =0.7888)

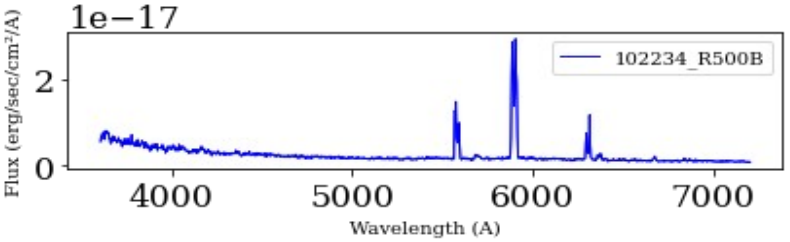

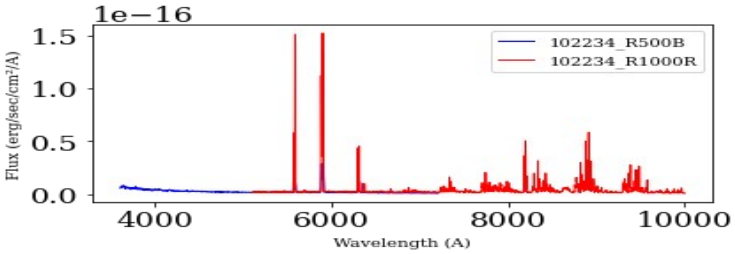

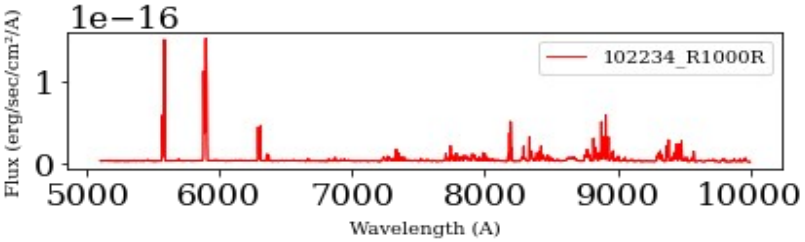

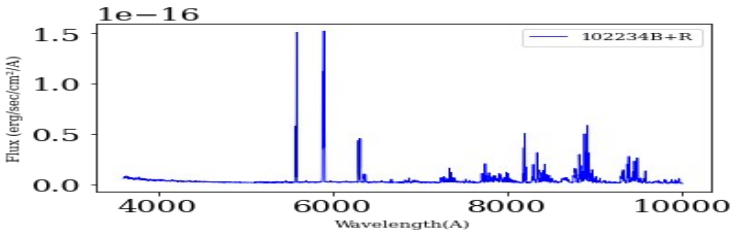

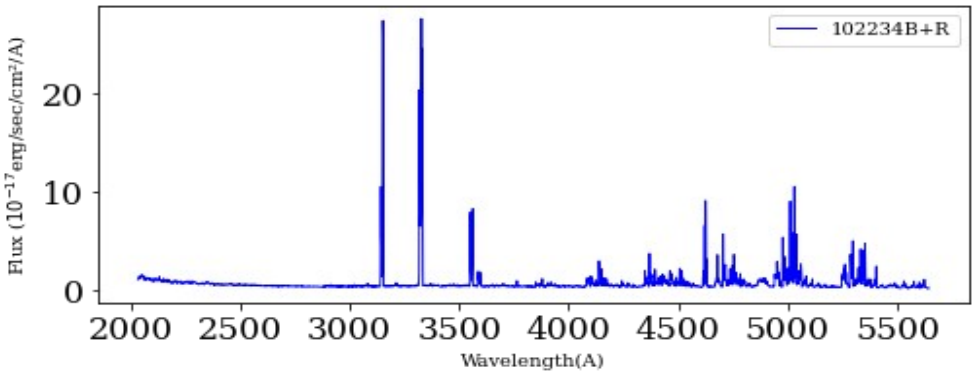

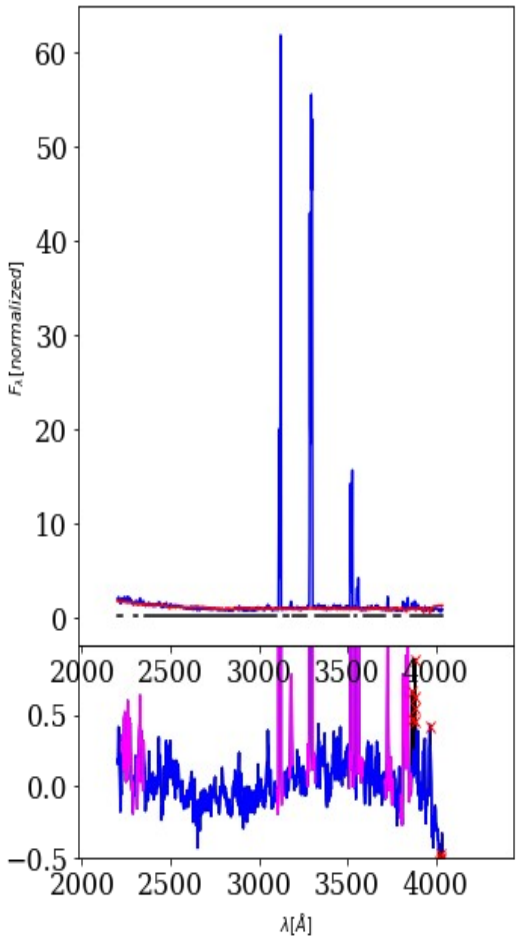

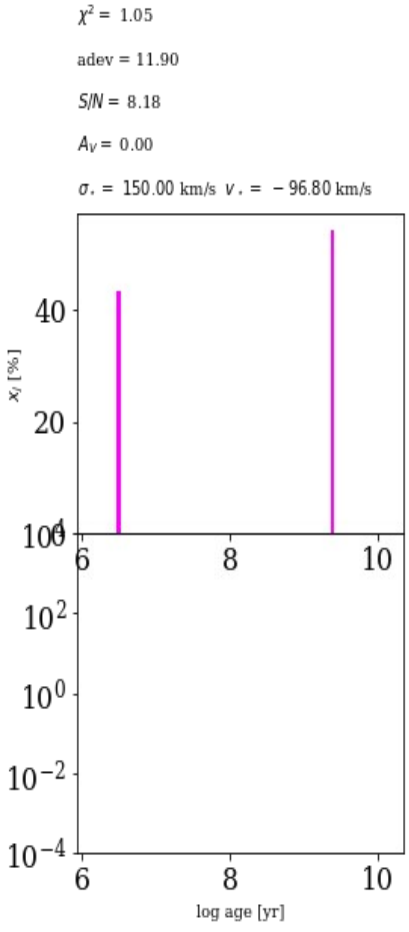

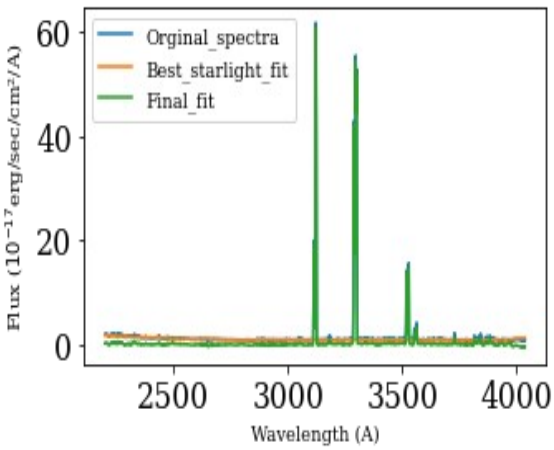

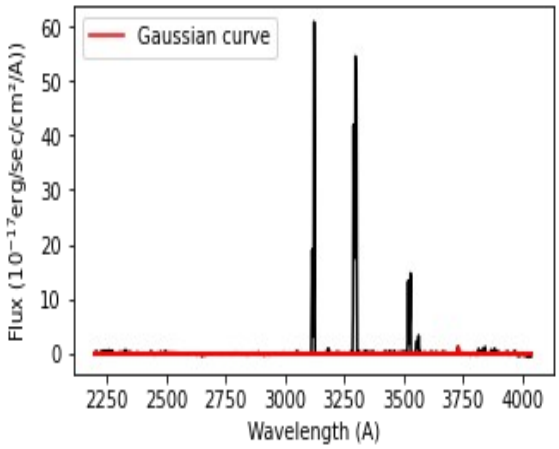

102976 (z_{spec} =0.3433)

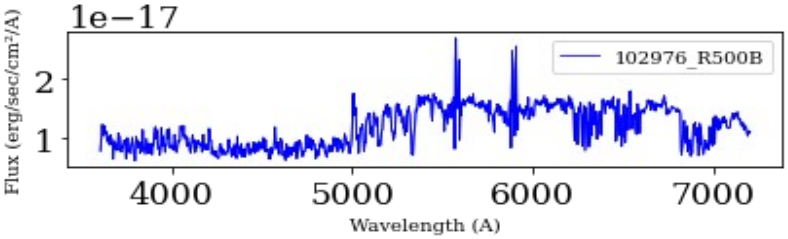

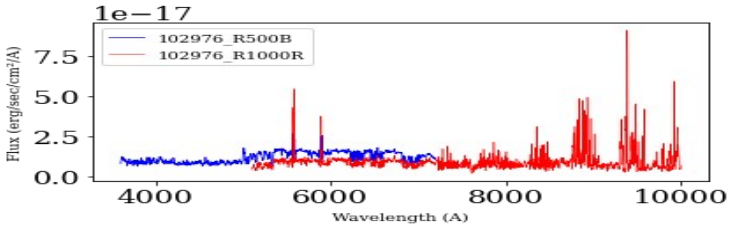

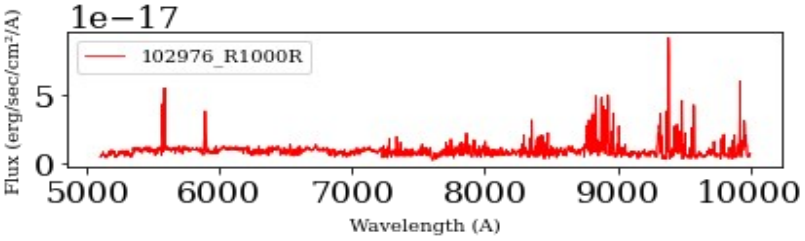

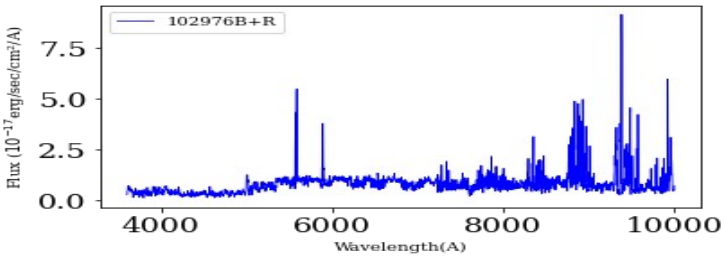

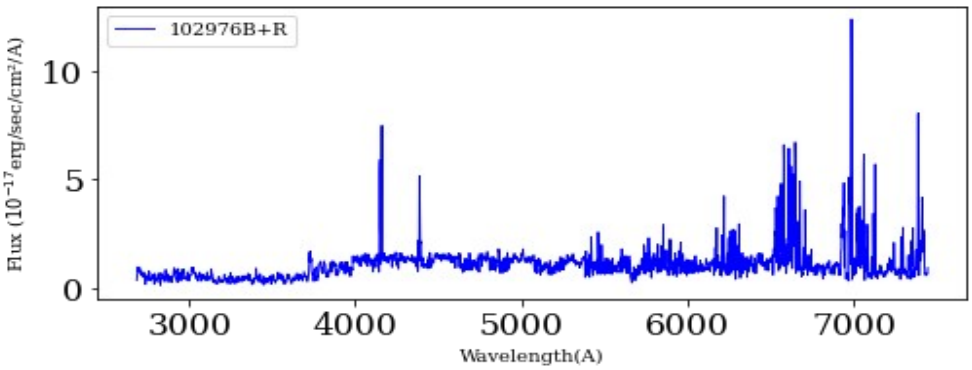

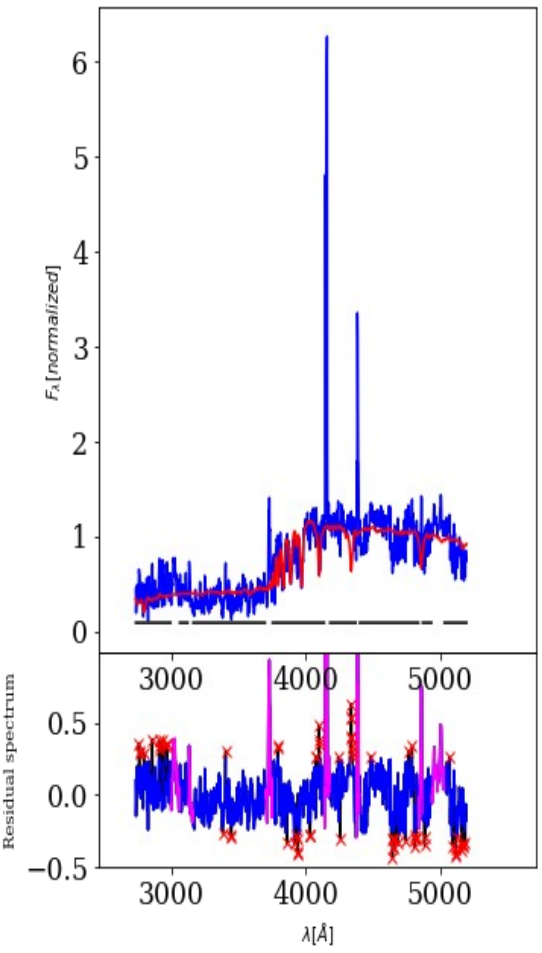

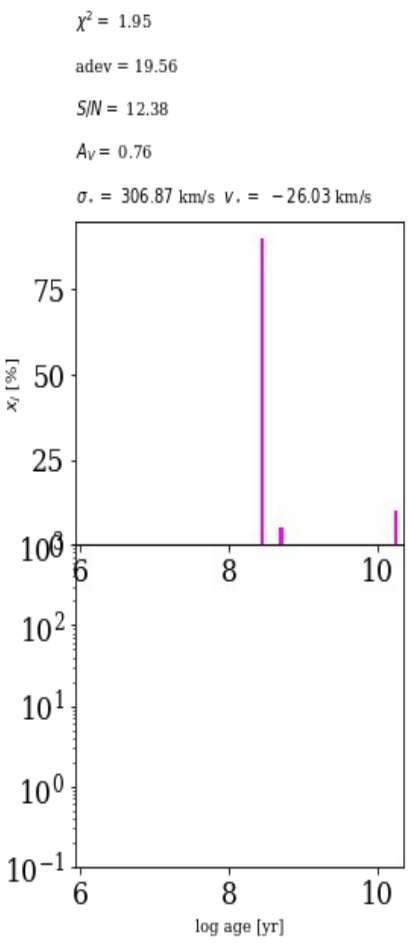

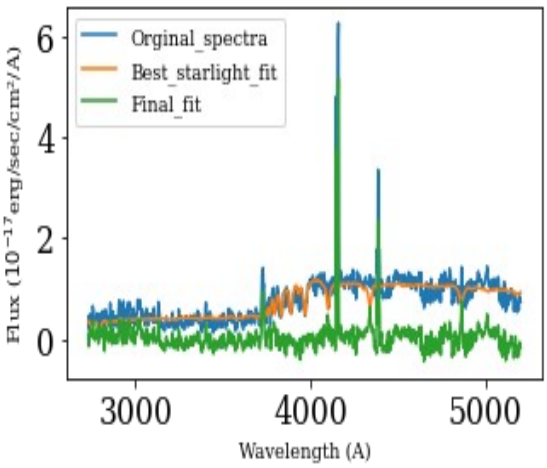

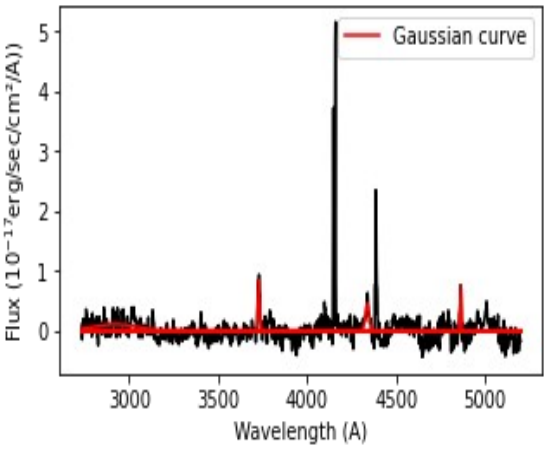

105507 (z_{spec} =0.0791)

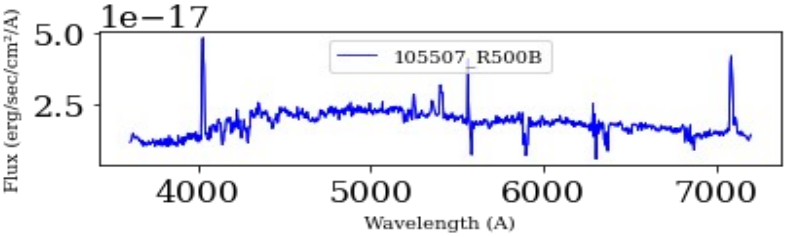

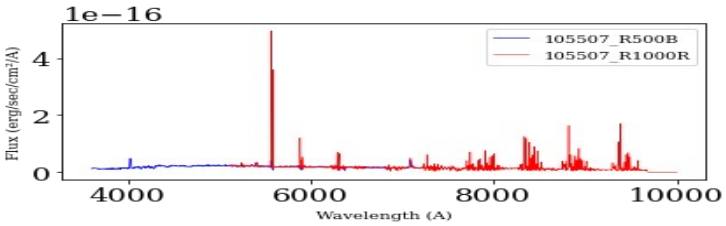

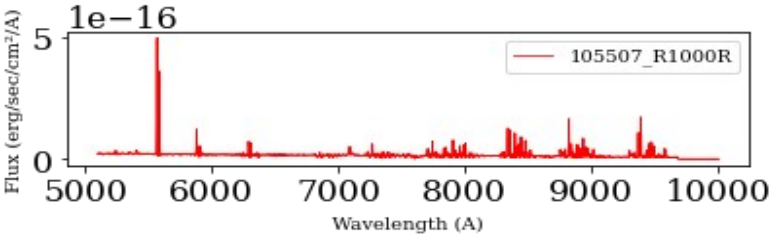

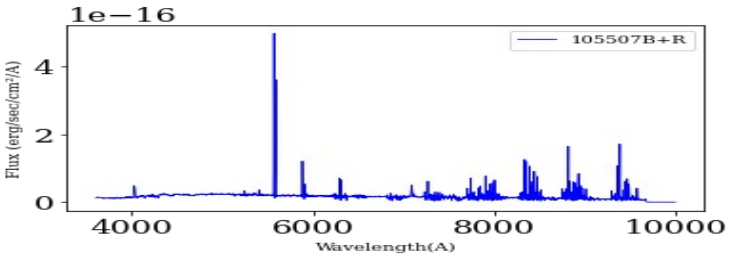

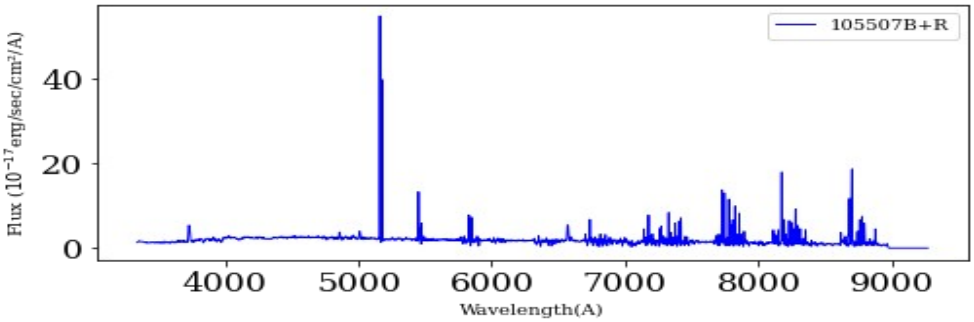

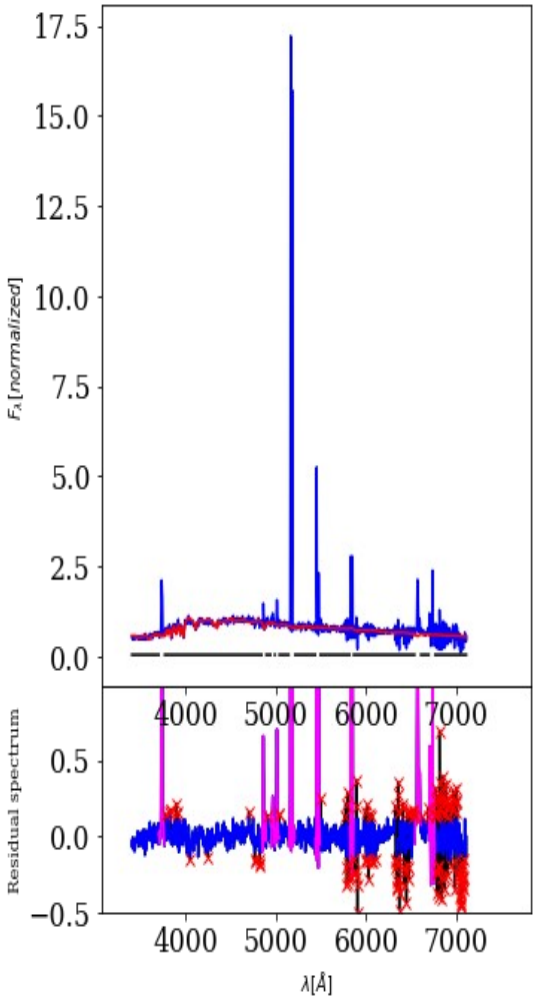

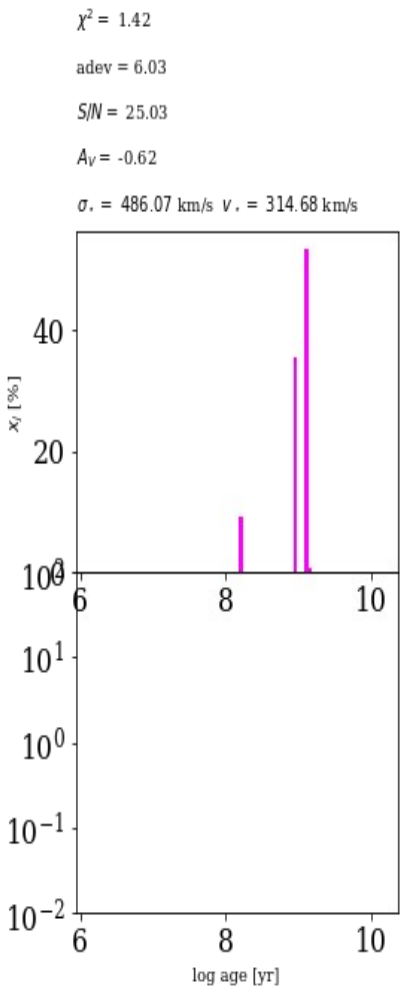

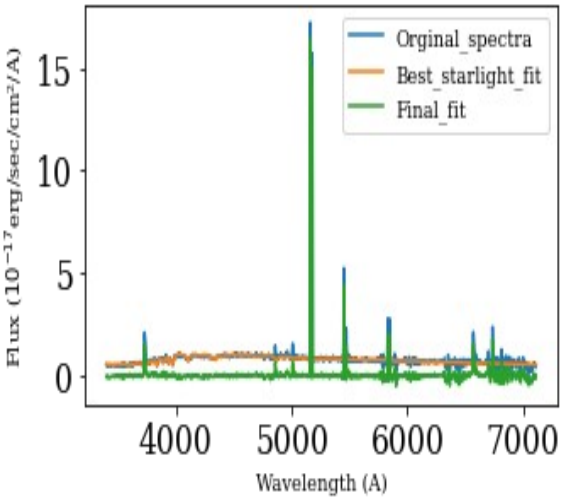

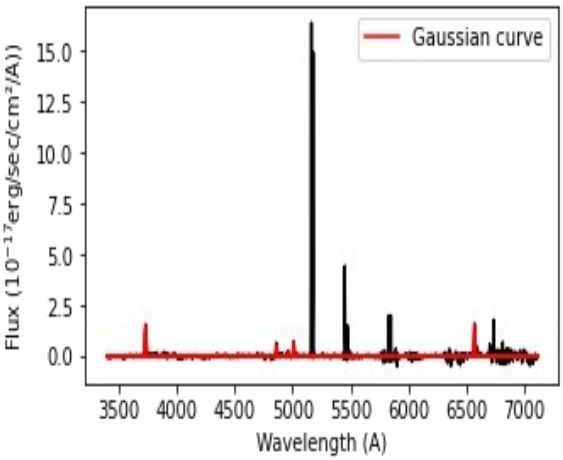

105800 (z_{spec} =0.3412)

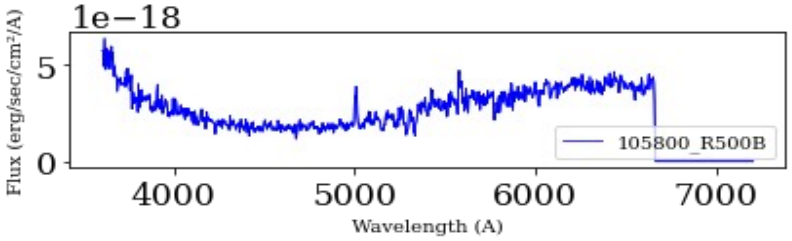

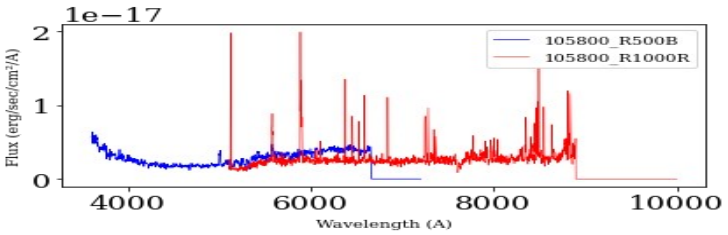

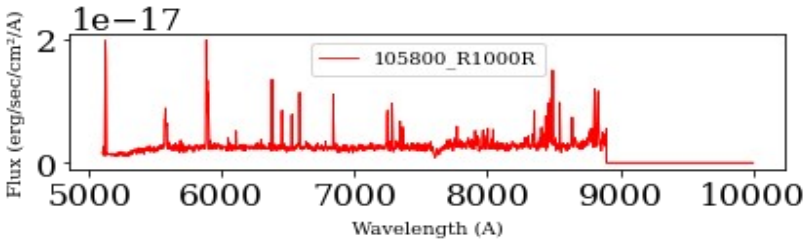

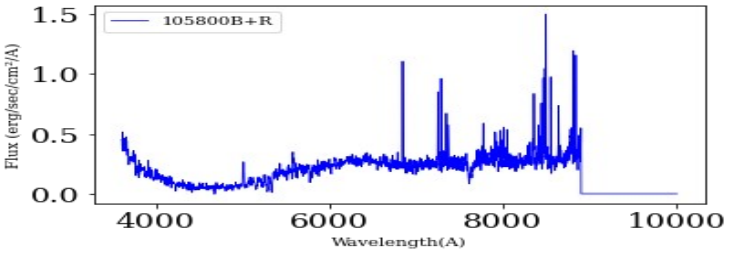

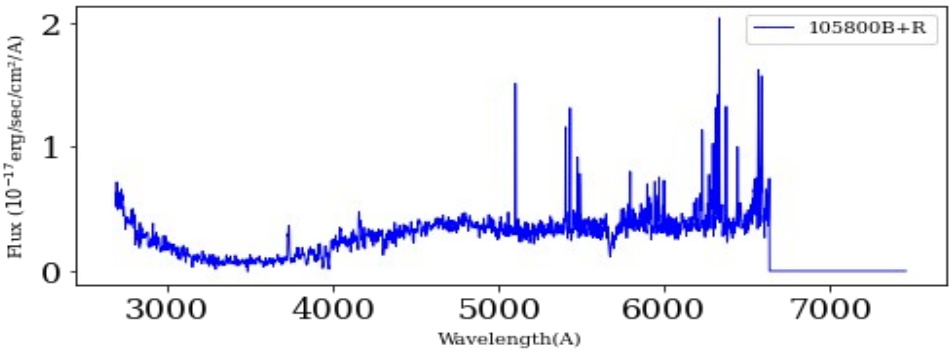

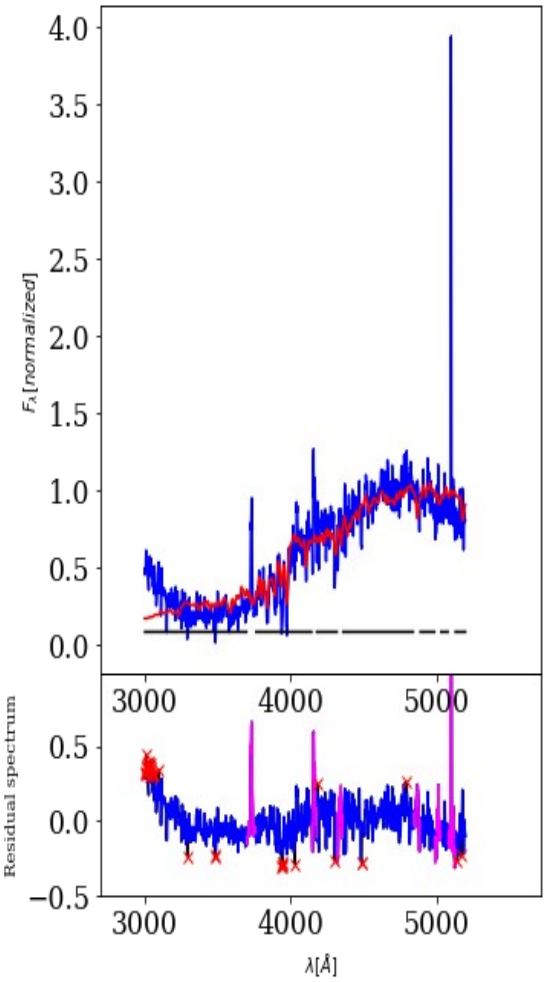

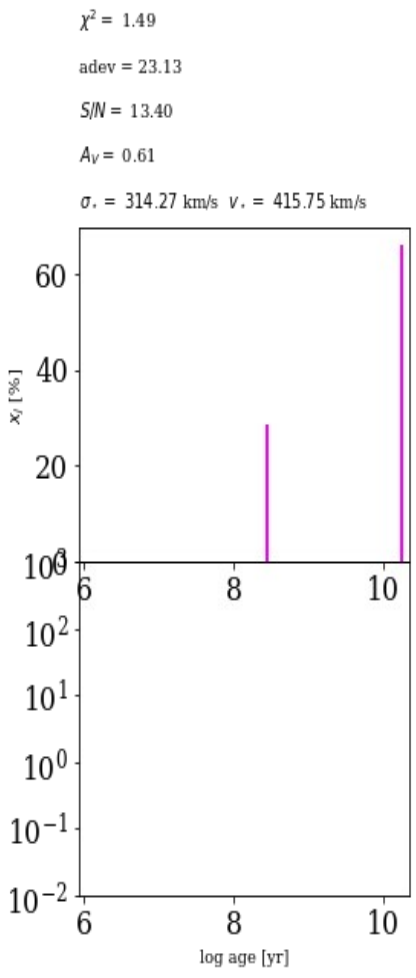

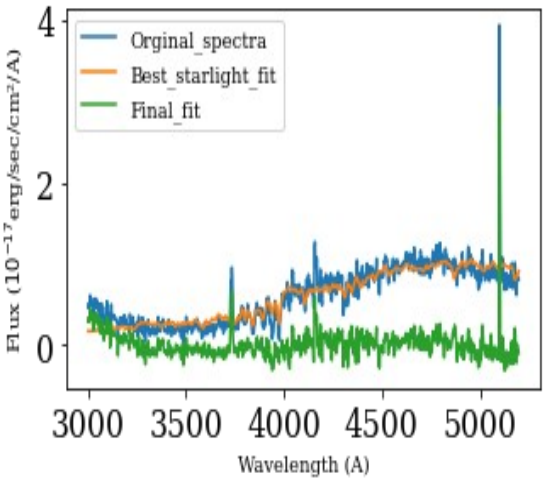

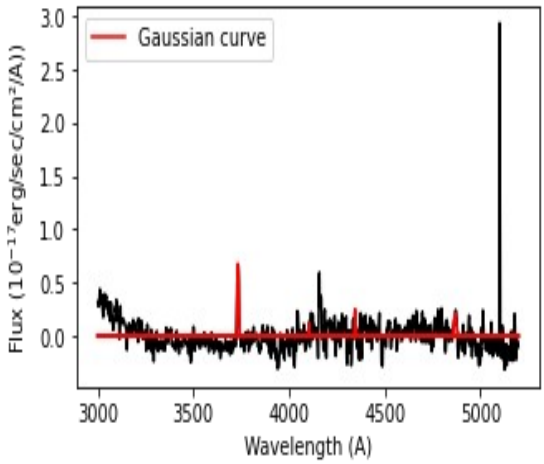

107406 (z_{spec} =0.4656)

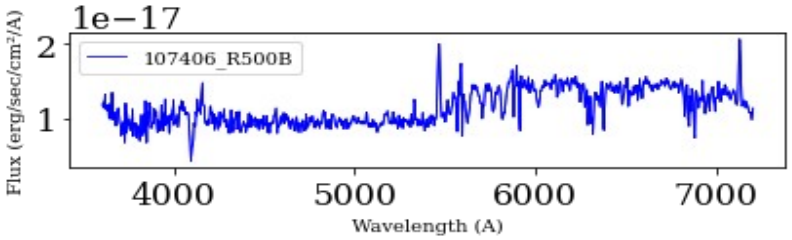

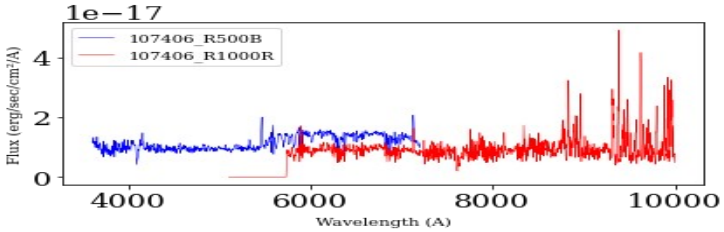

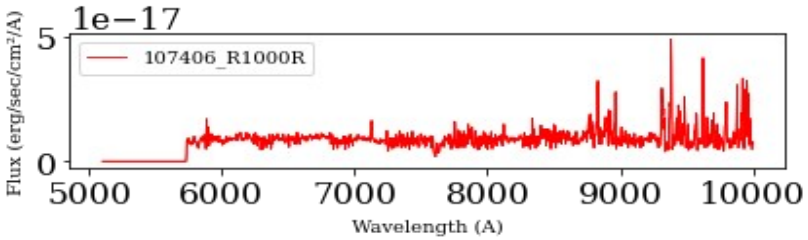

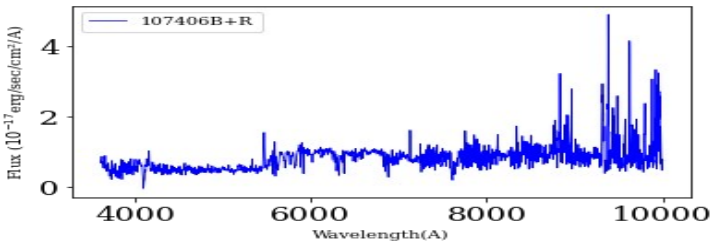

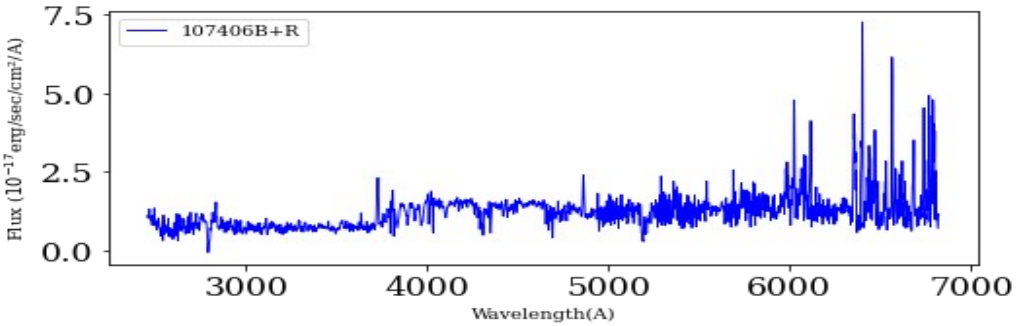

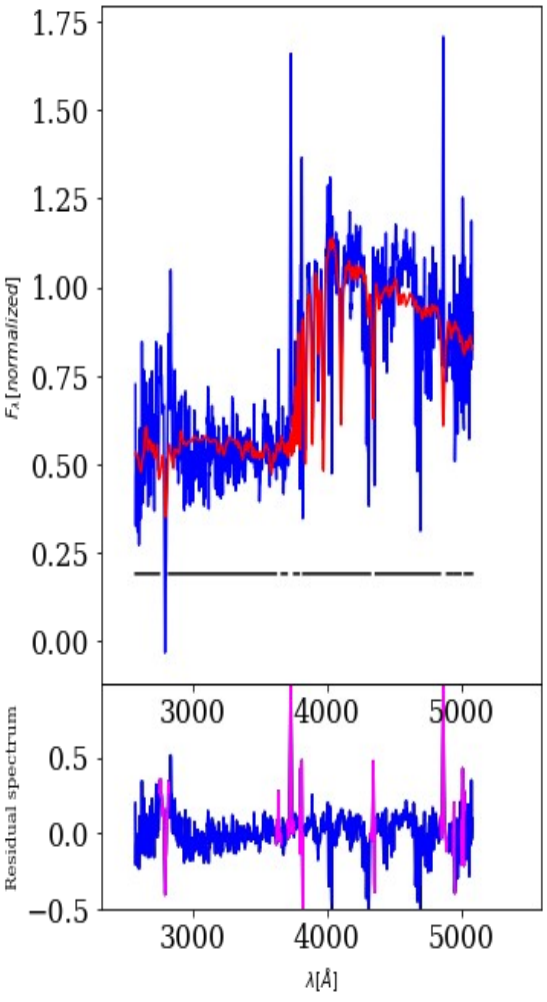

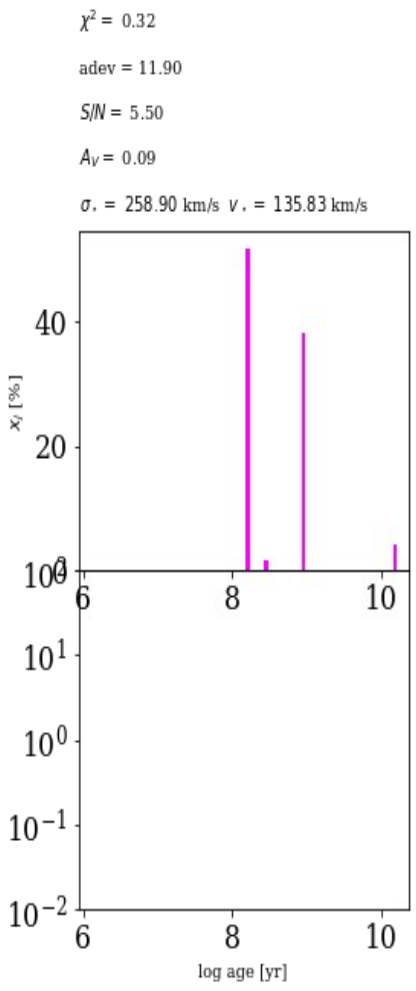

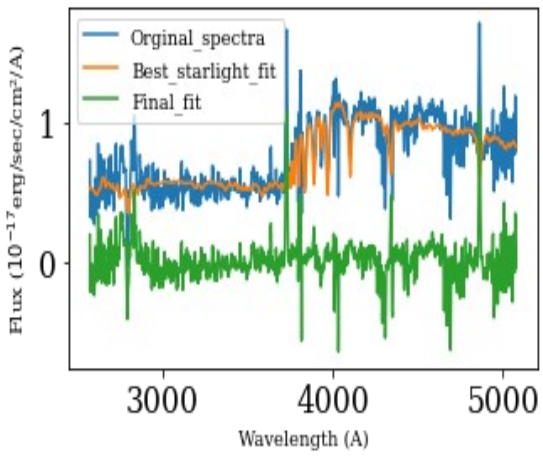

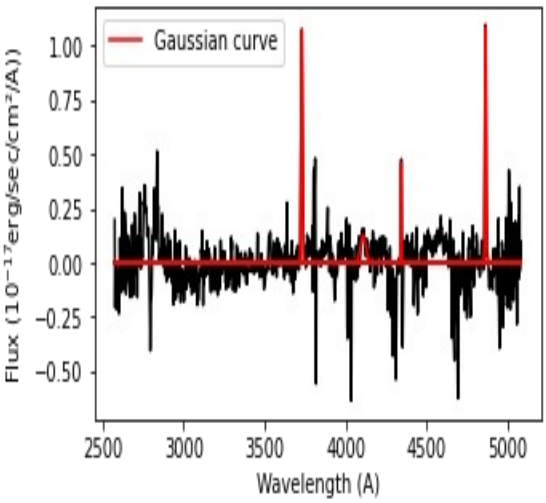

108626 (z_{spec} =0.3342)

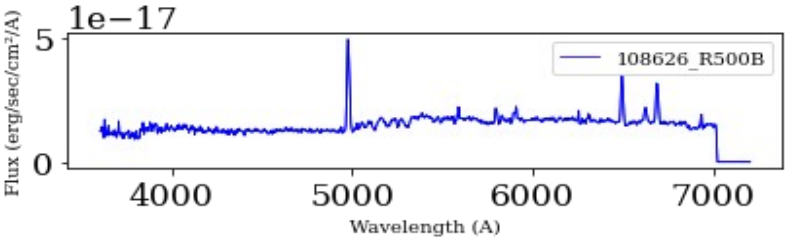

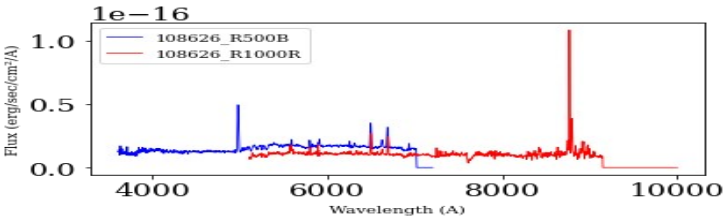

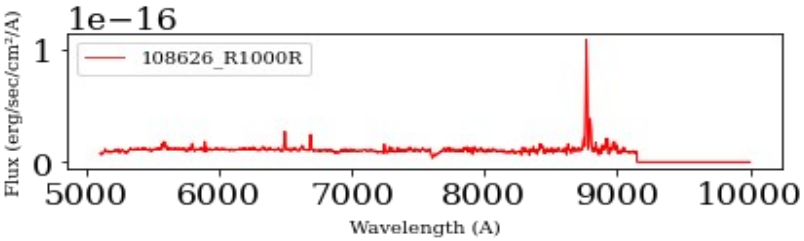

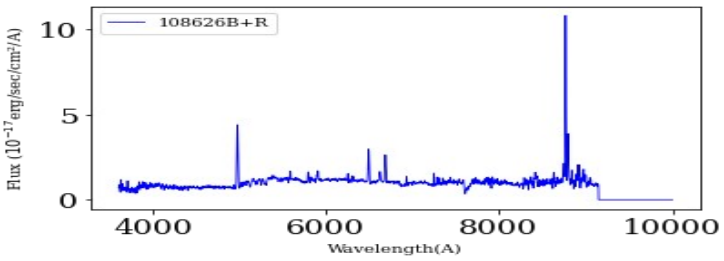

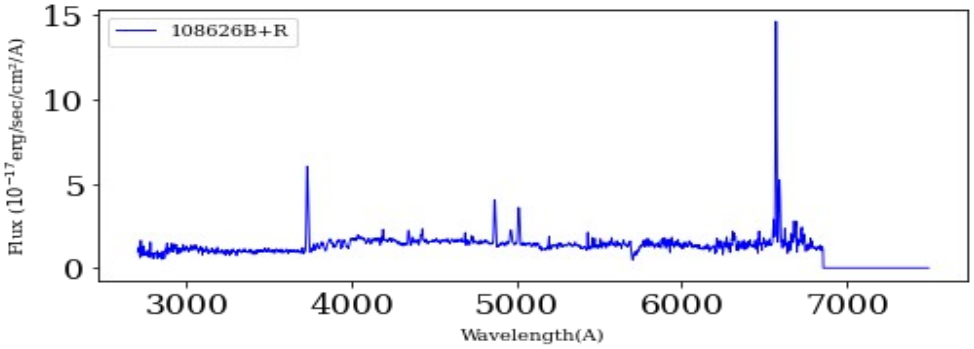

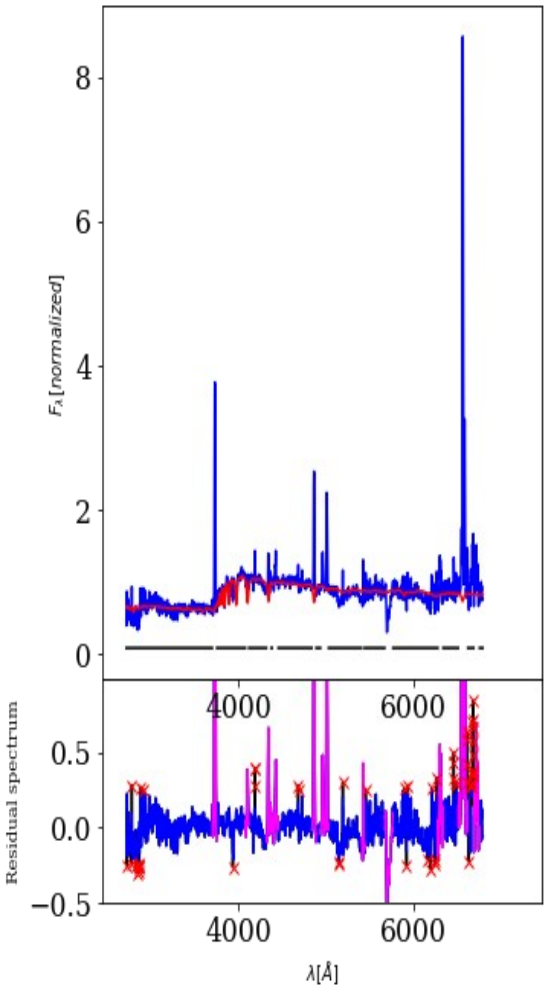

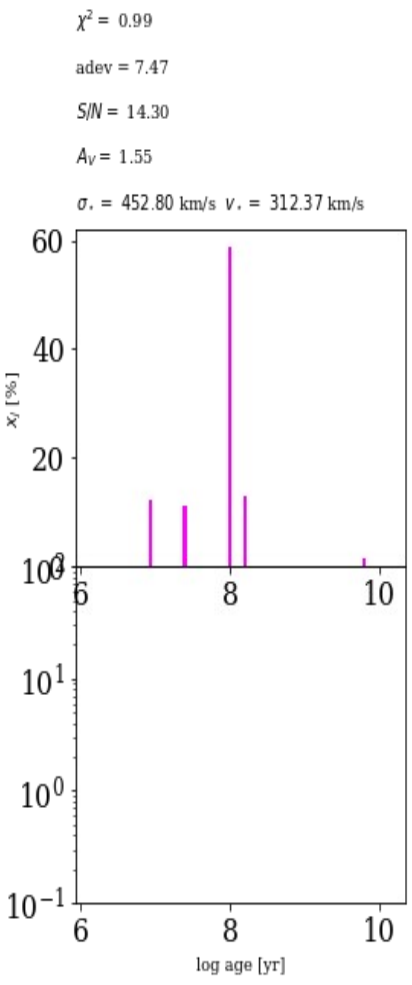

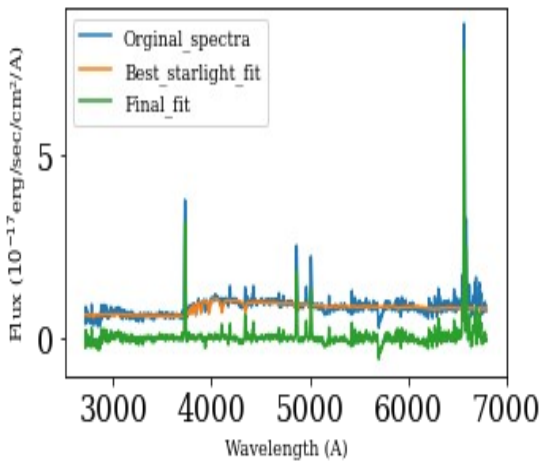

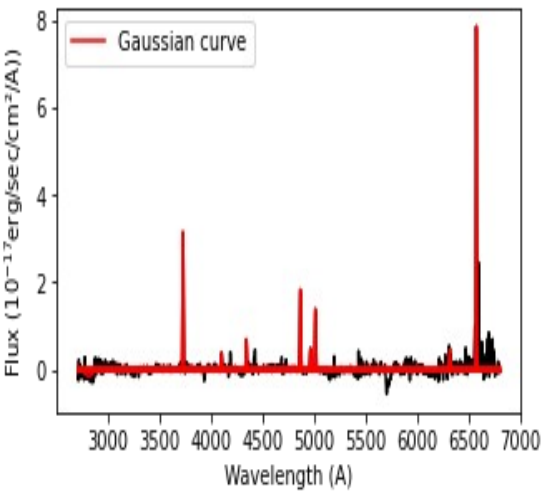

109723 (z_{spec} =0.1957)

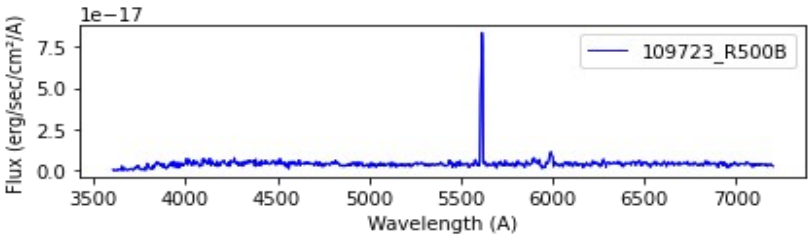

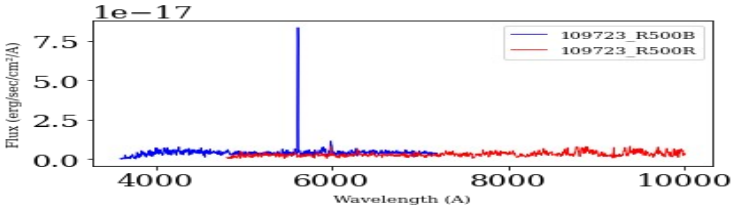

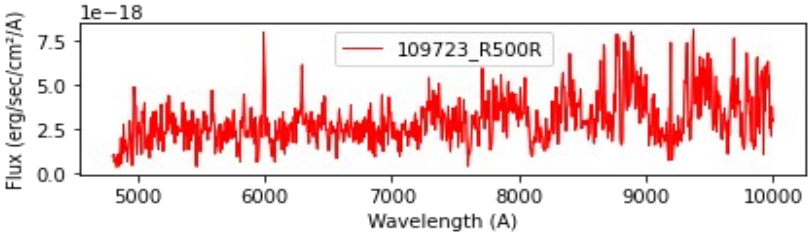

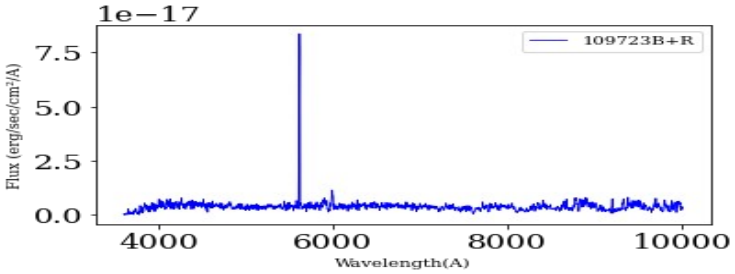

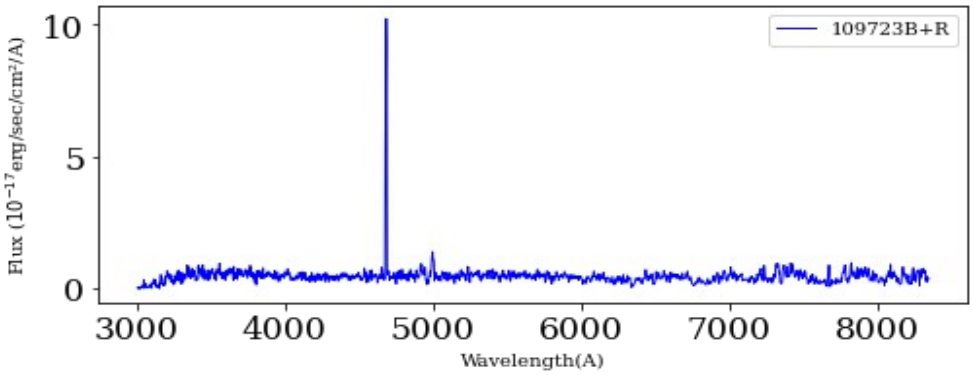

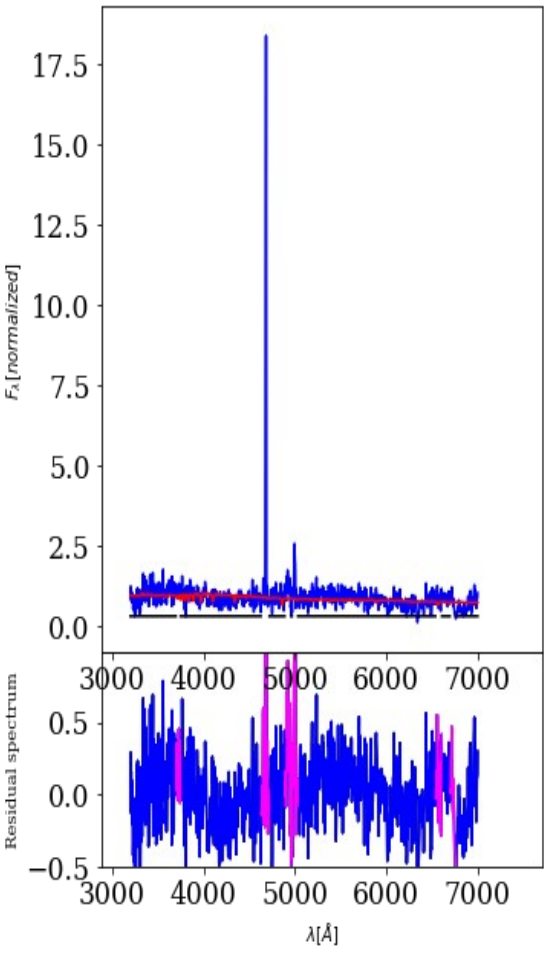

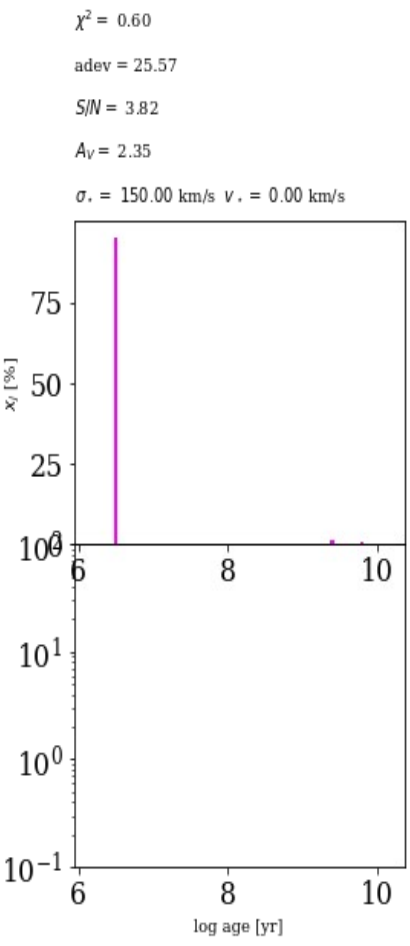

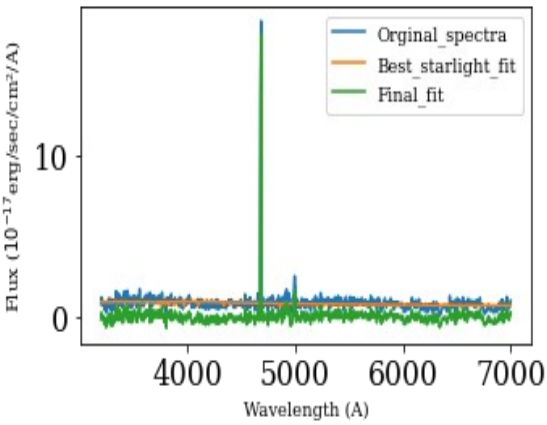

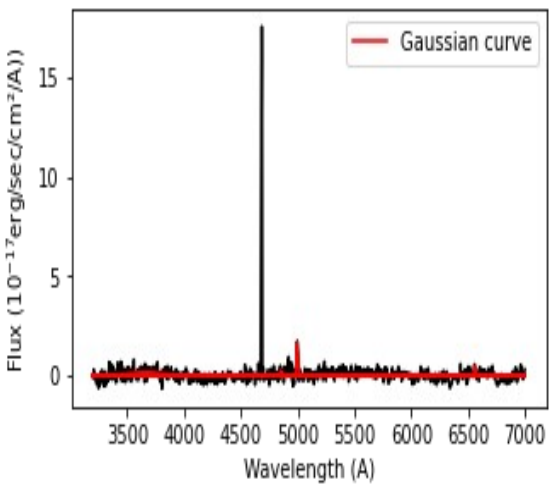

109862 (z_{spec} =0.3195)

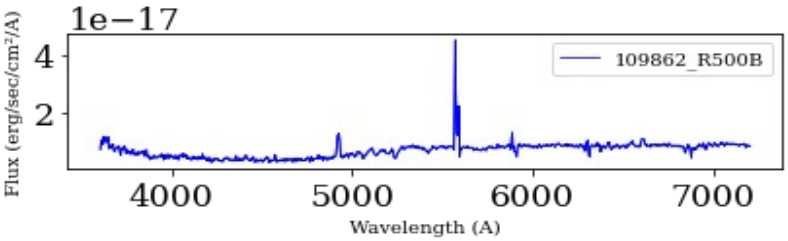

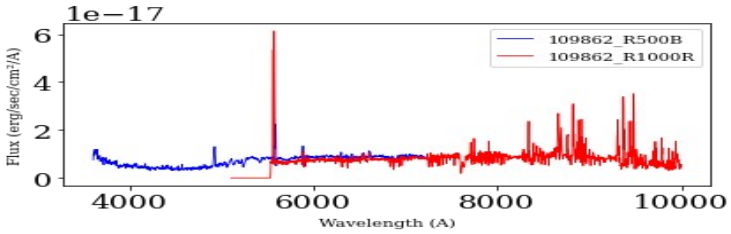

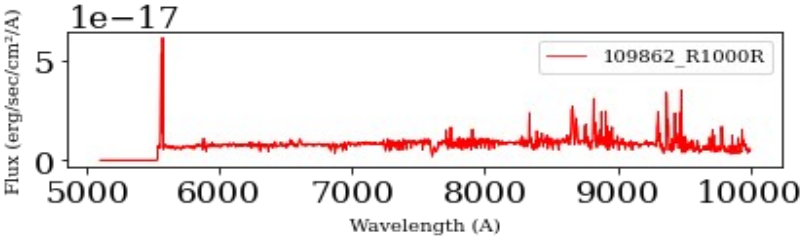

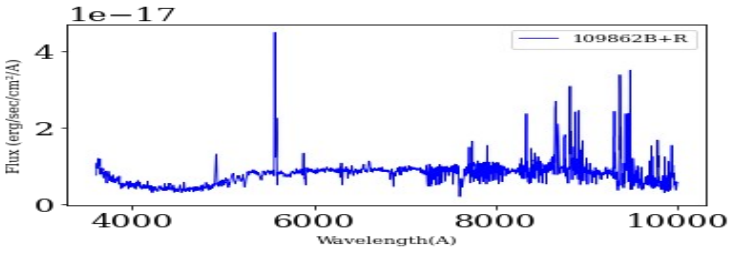

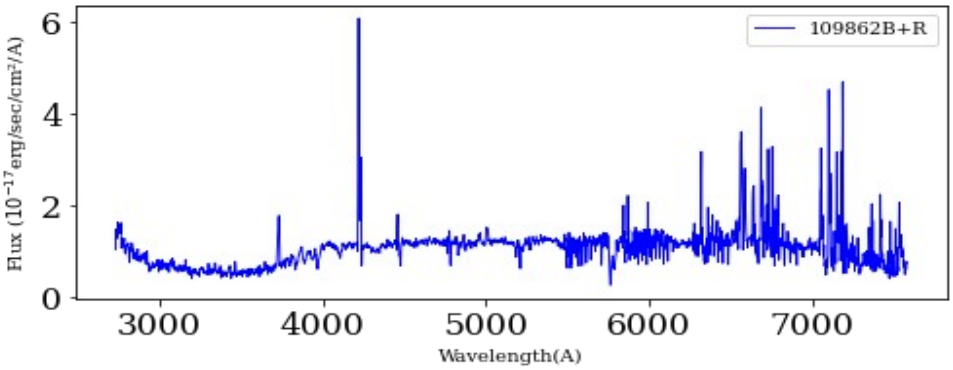

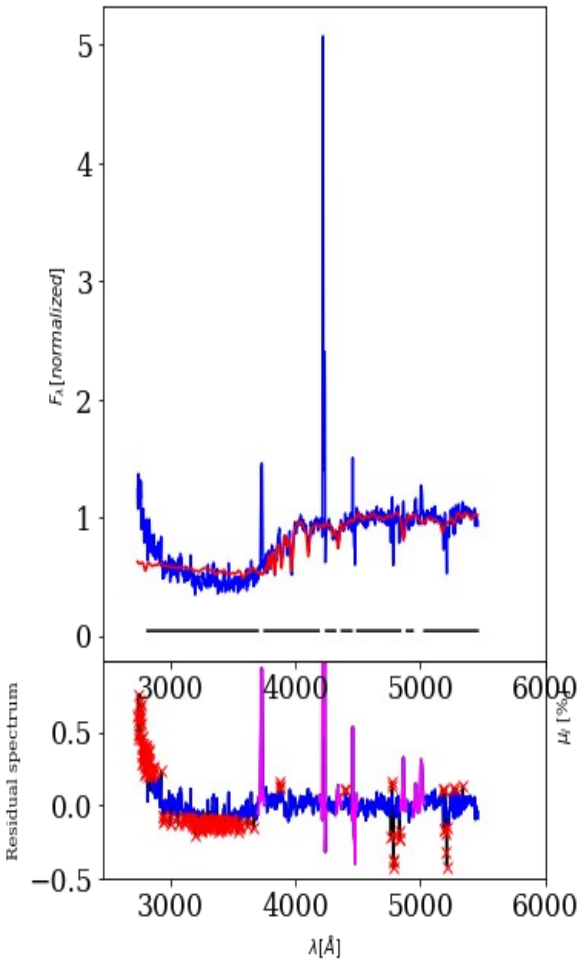

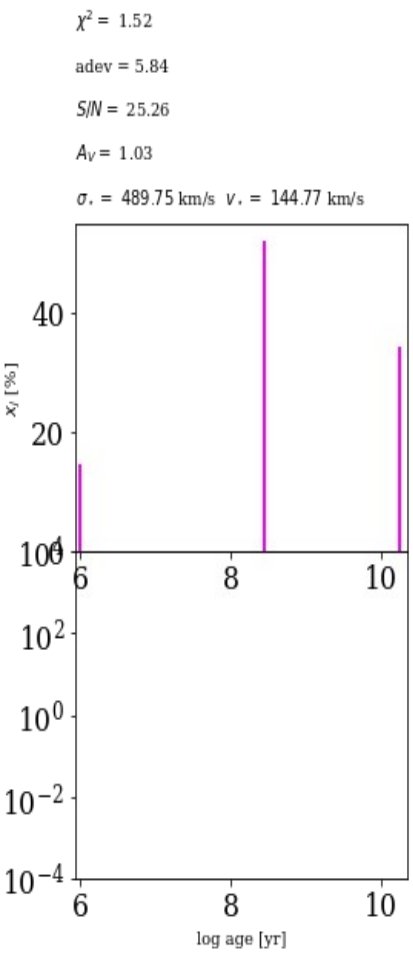

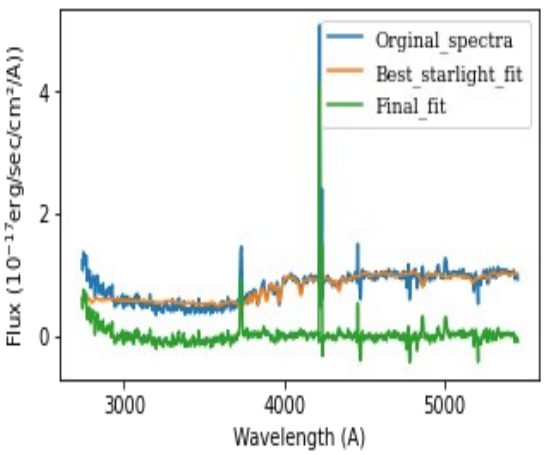

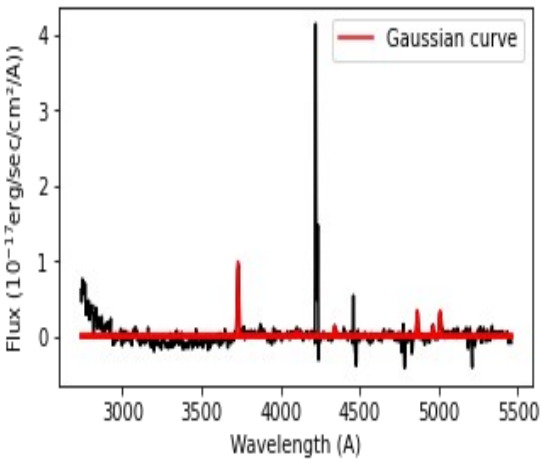

112488 (z_{spec} =0.4647)

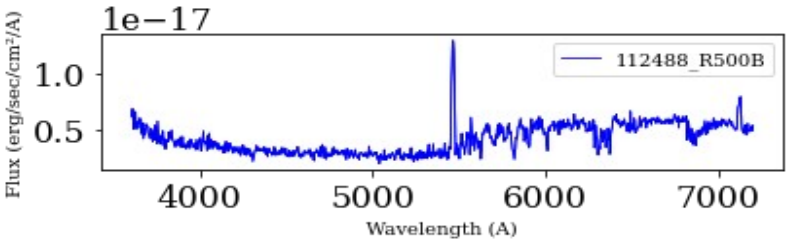

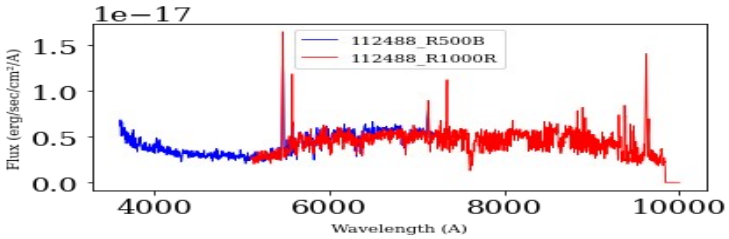

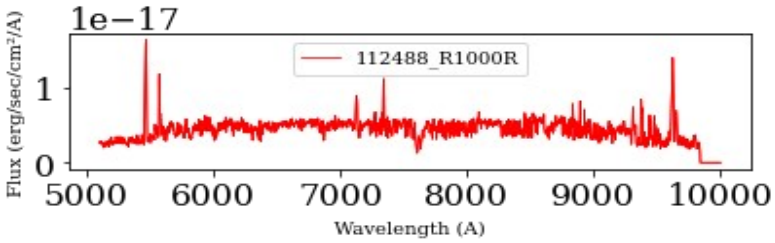

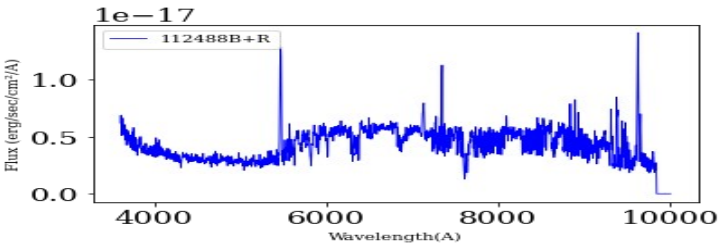

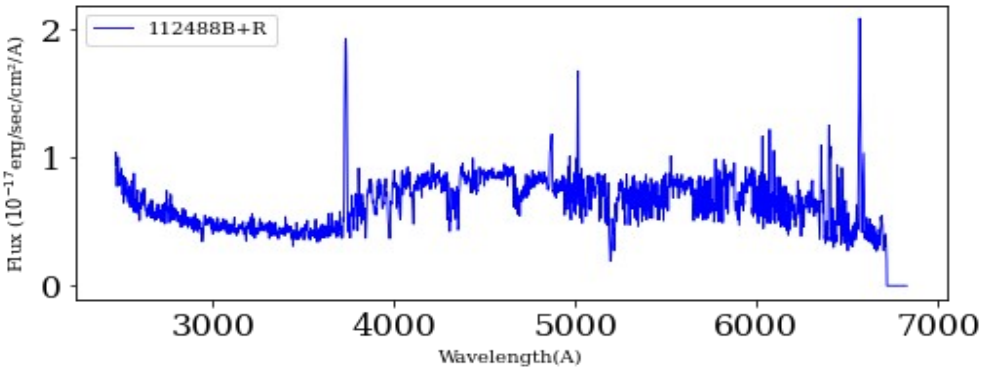

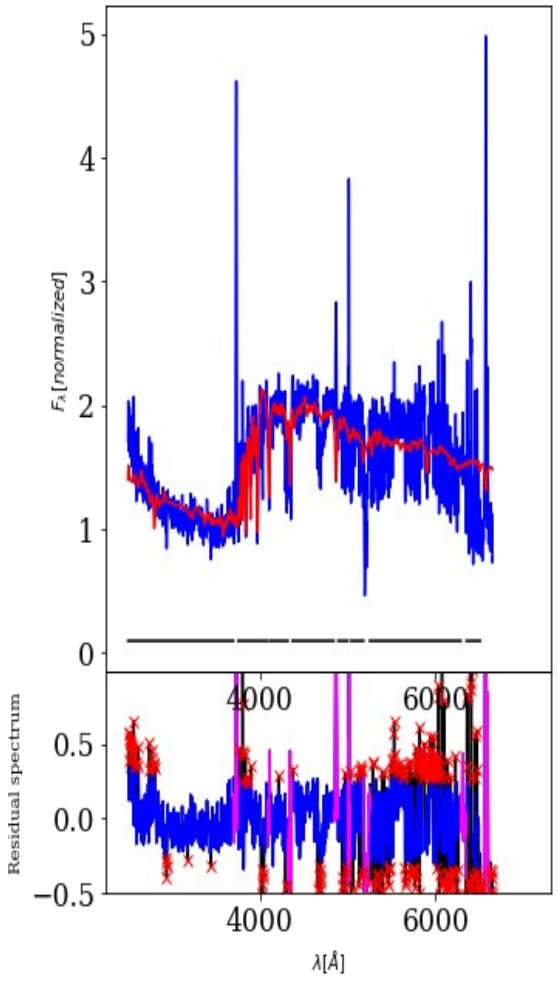

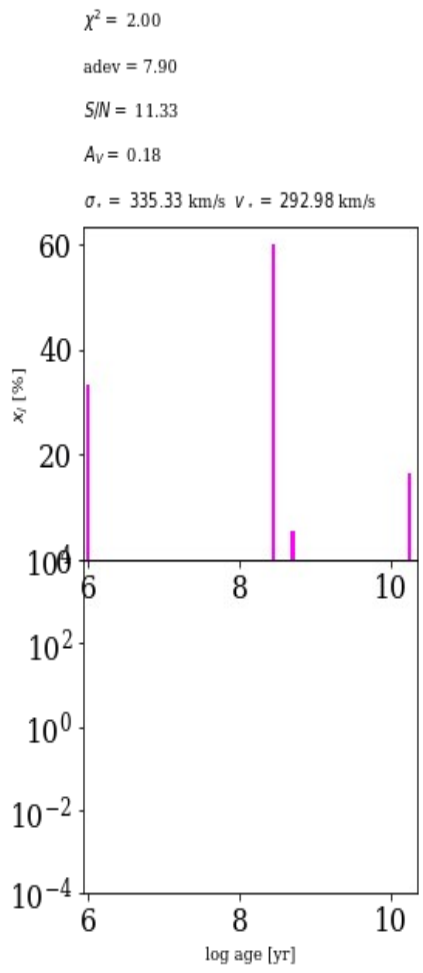

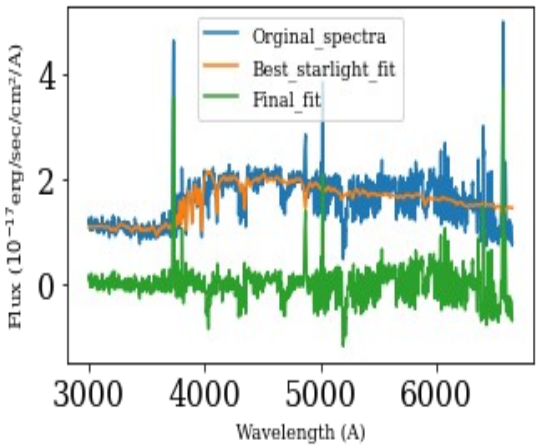

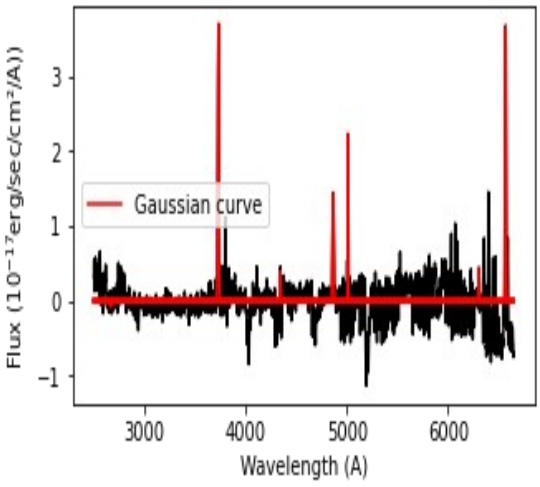

112512 (z_{spec} =0.4605)

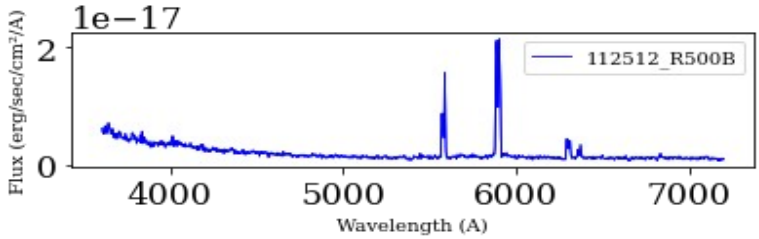

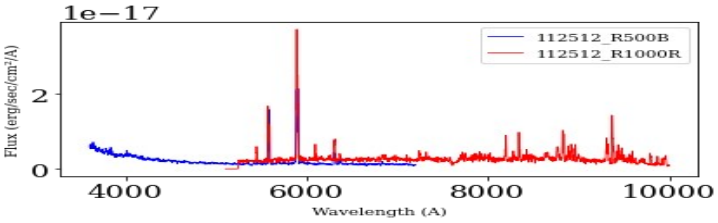

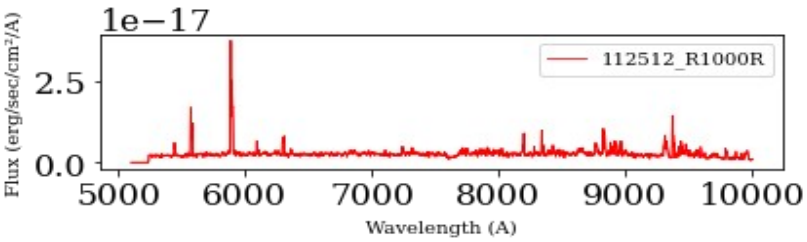

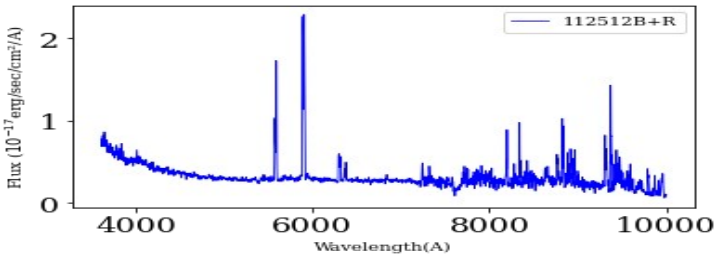

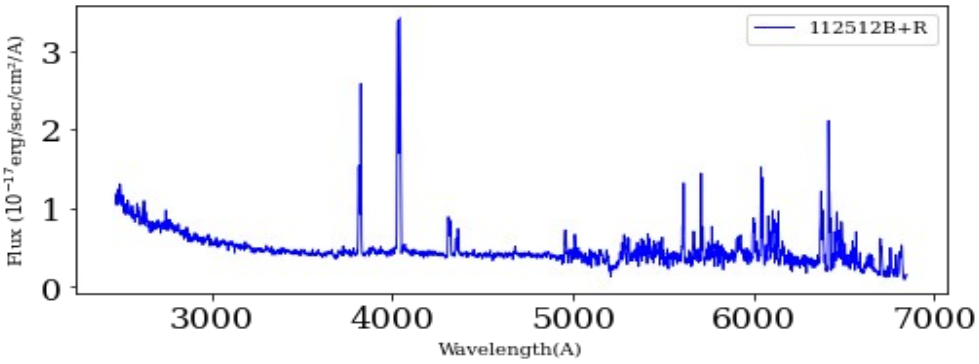

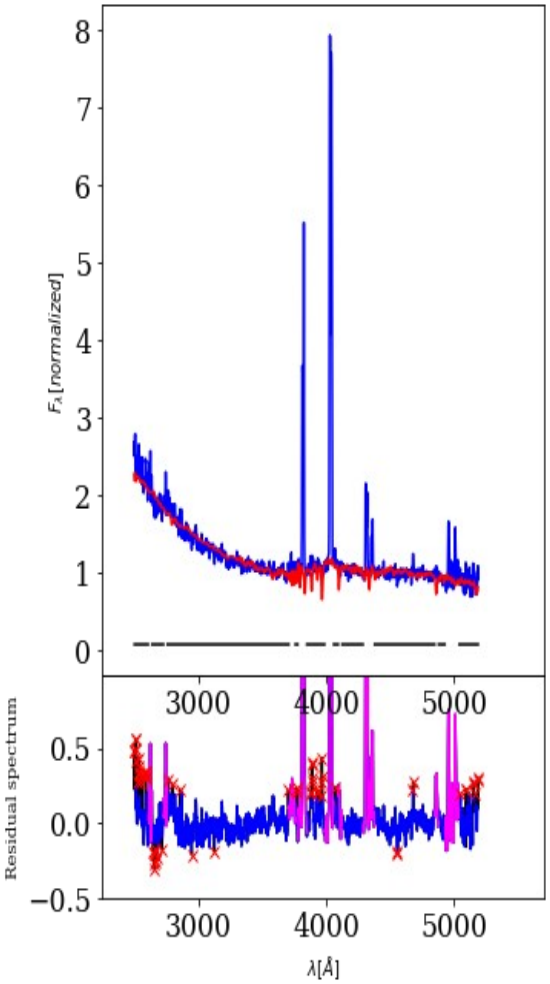

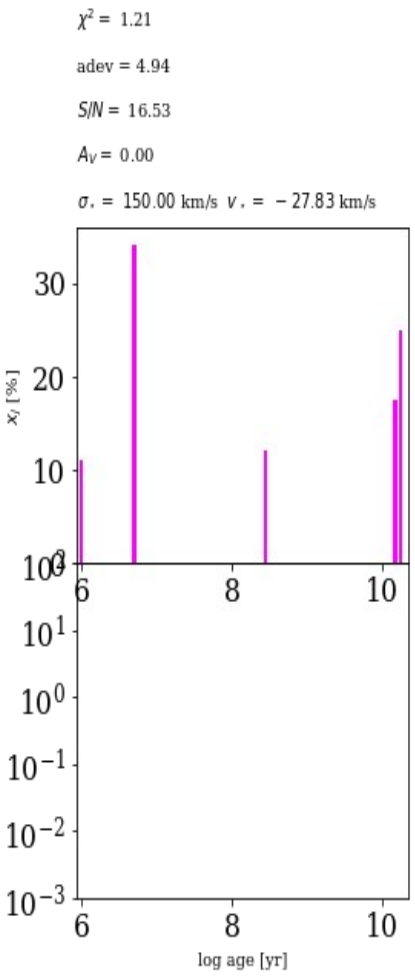

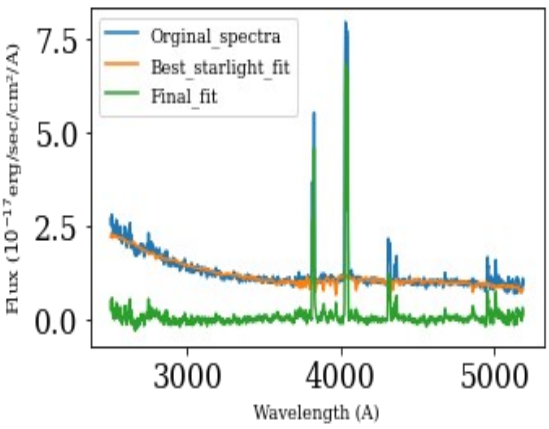

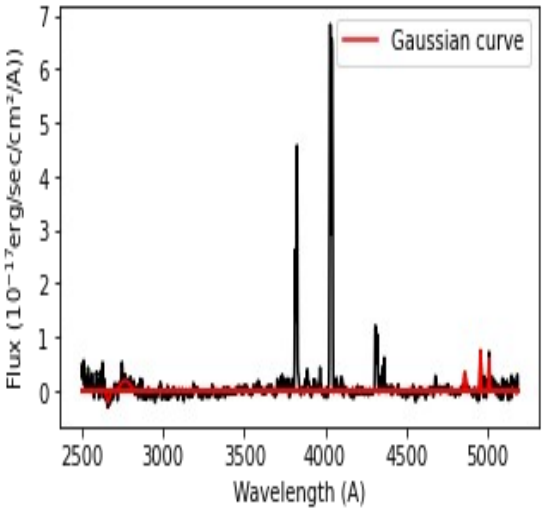

112822 (z_{spec} =0.4982)

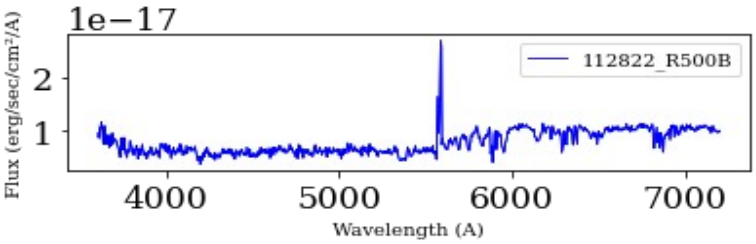

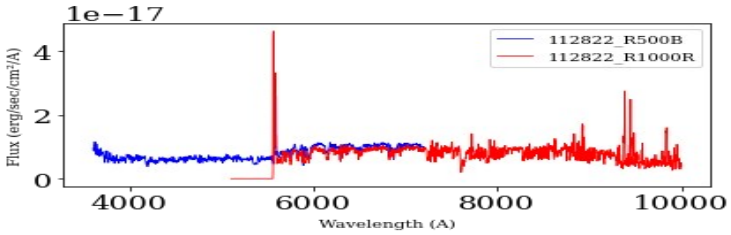

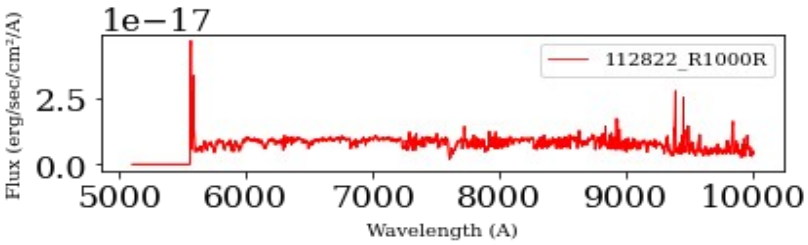

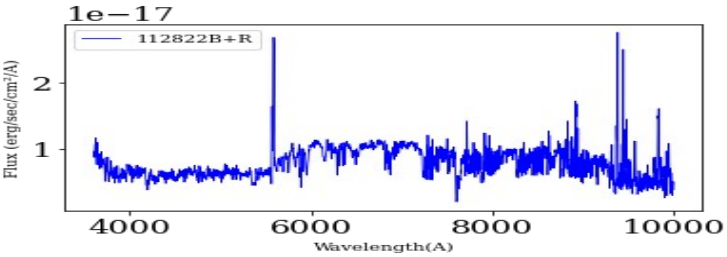

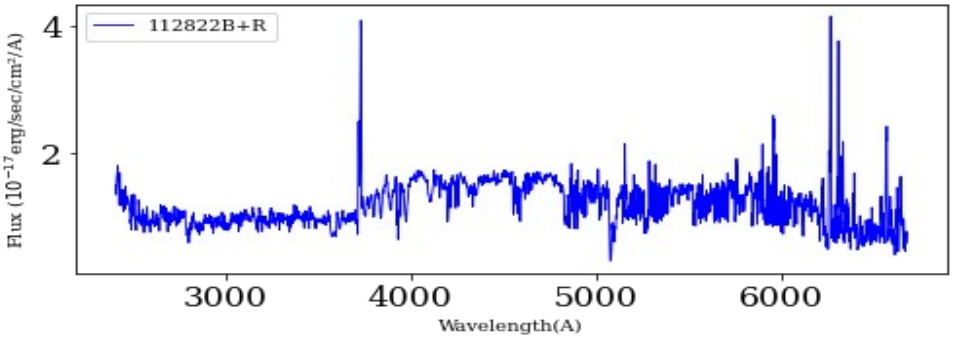

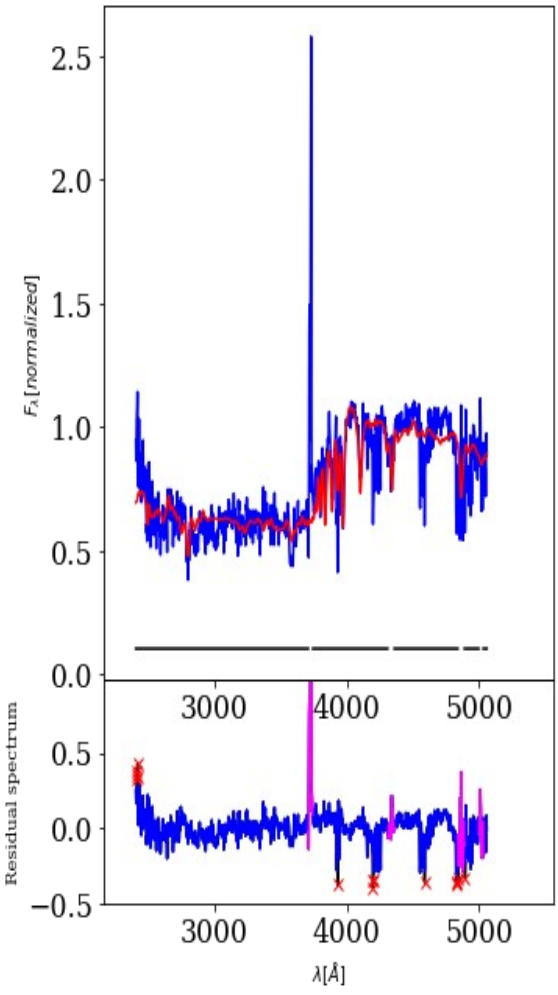

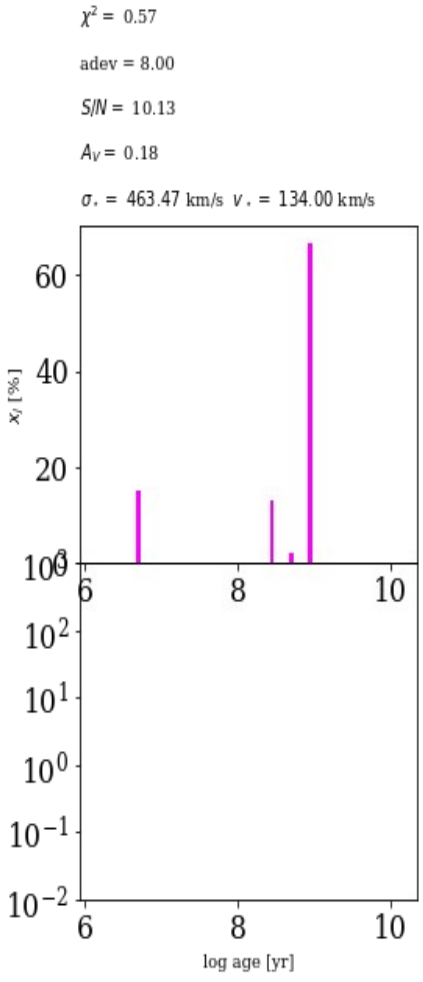

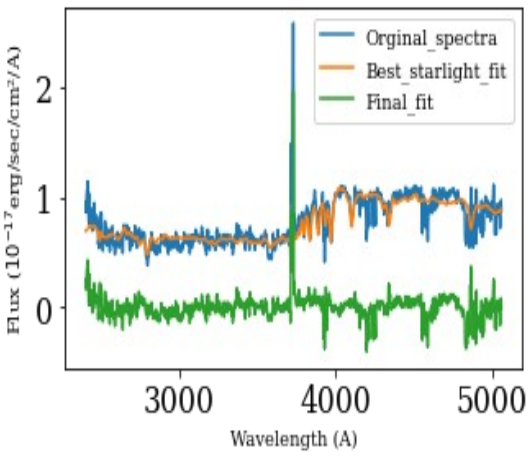

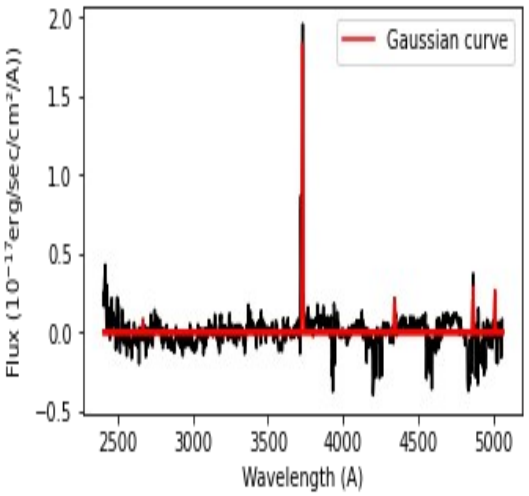

115832 (z_{spec} =0.2026)

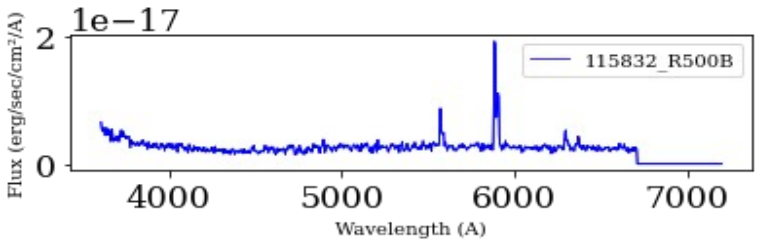

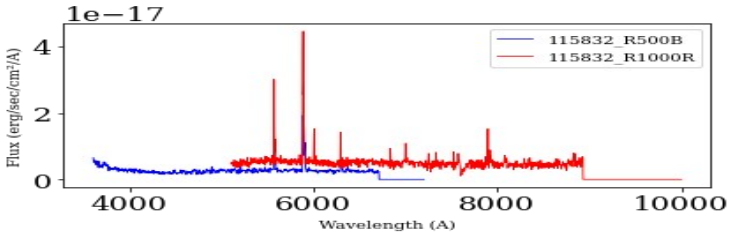

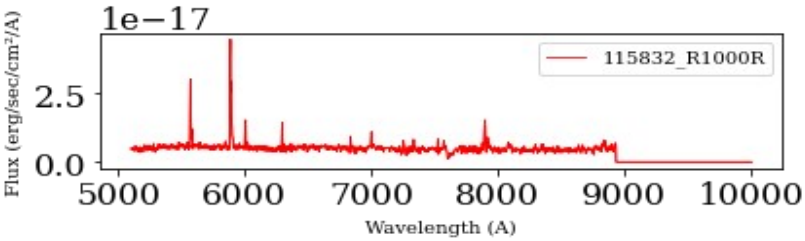

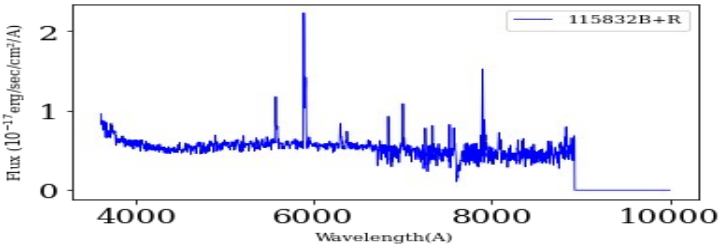

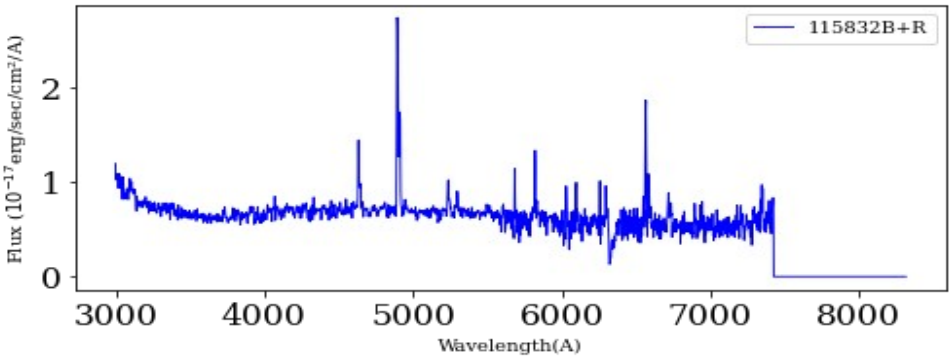

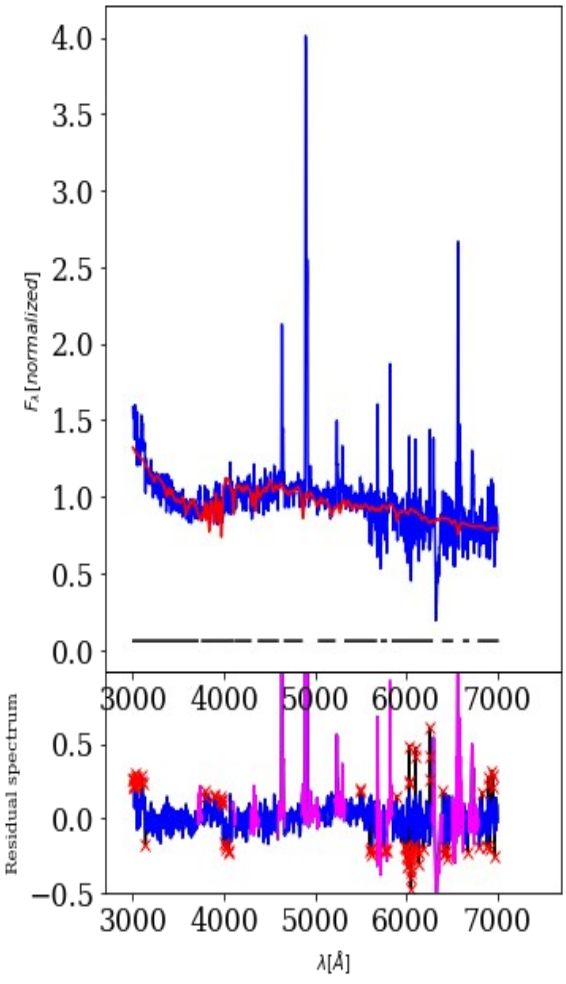

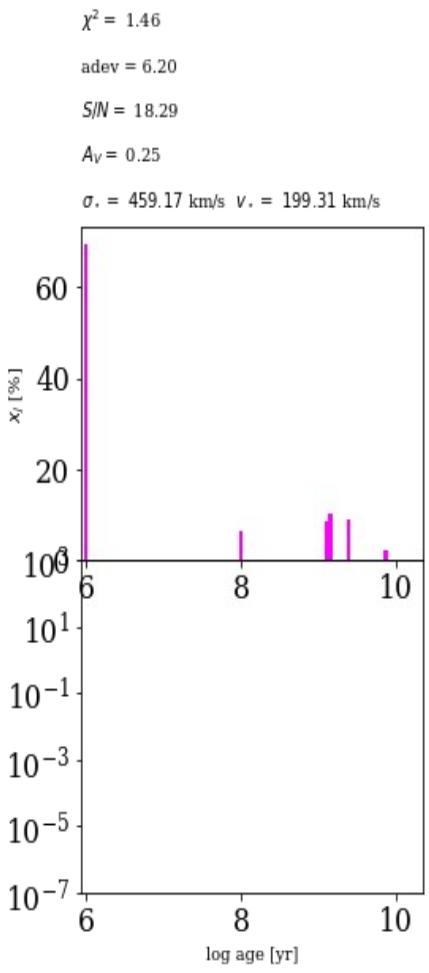

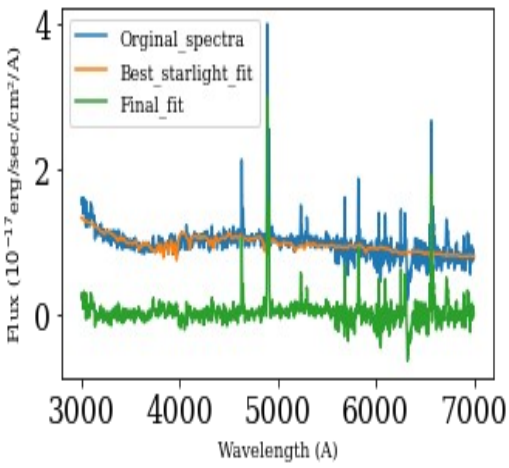

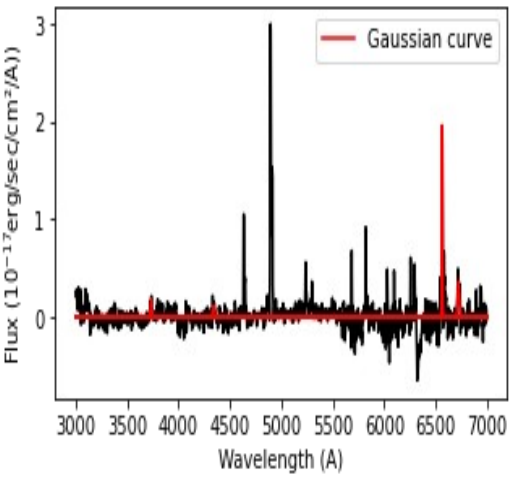

116129 (z_{spec} =0.3403)

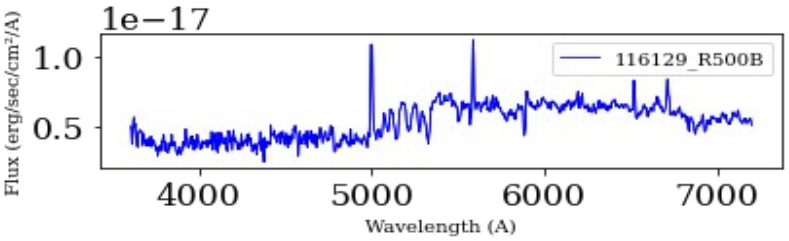

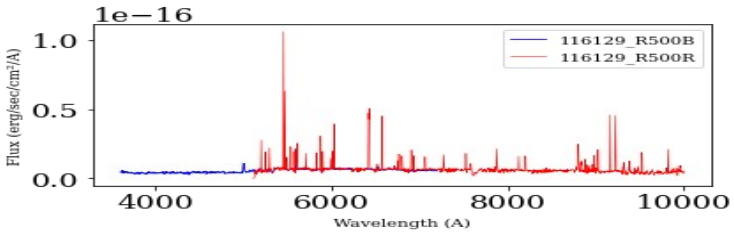

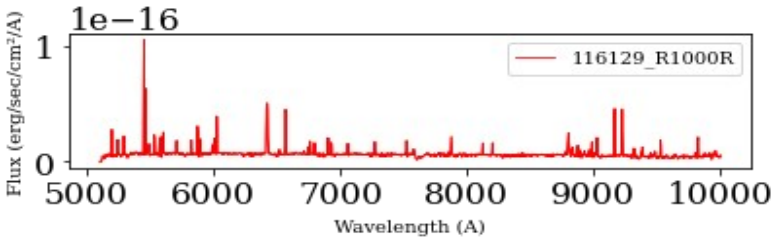

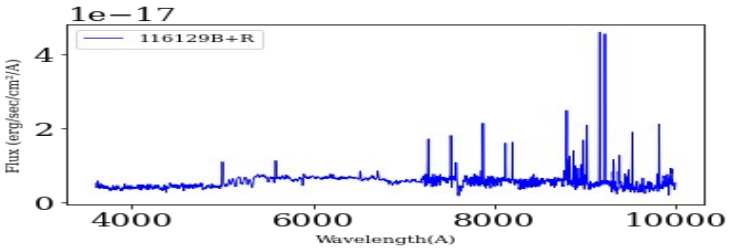

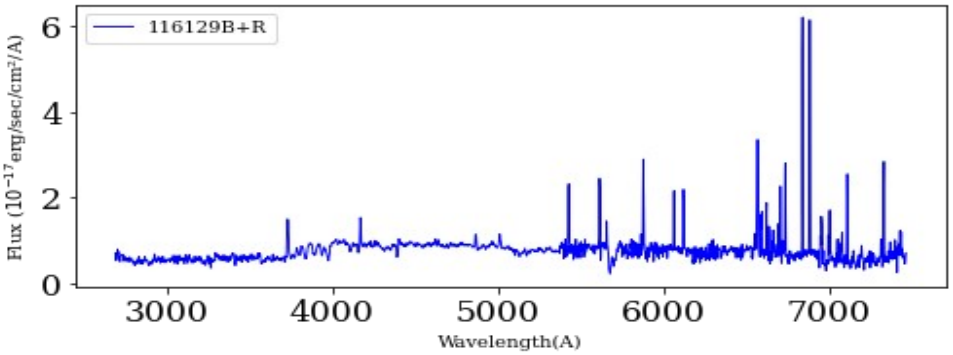

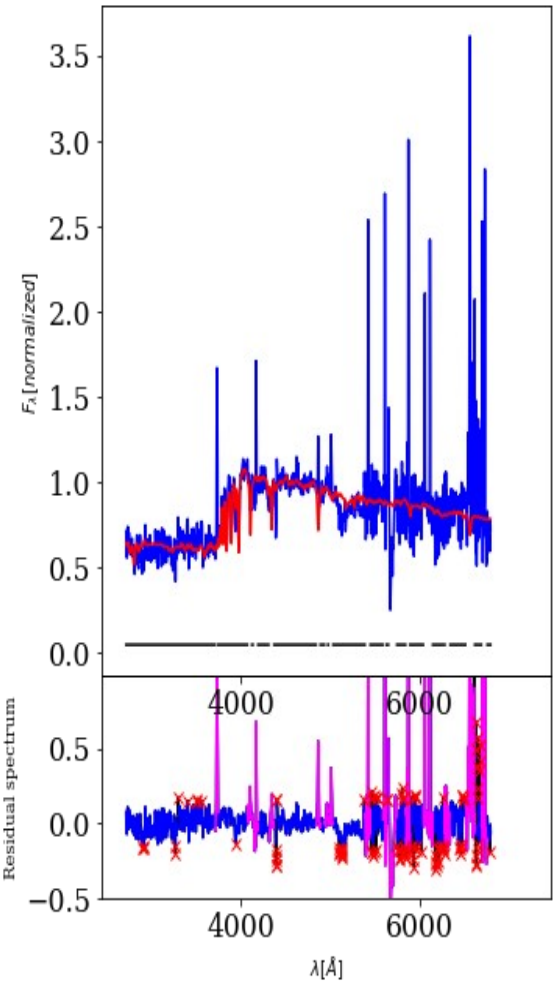

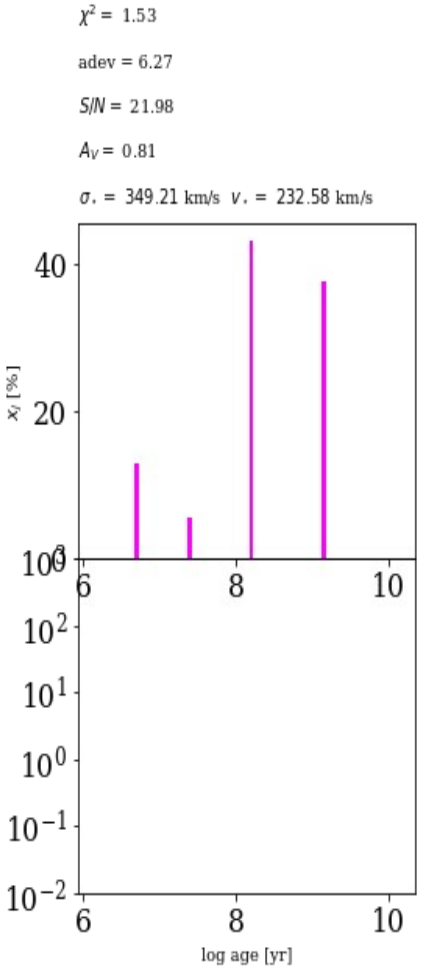

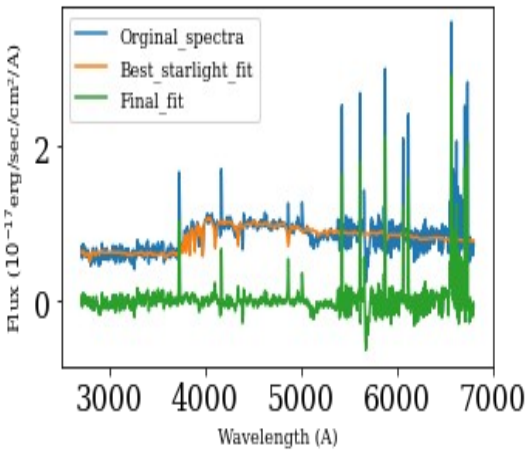

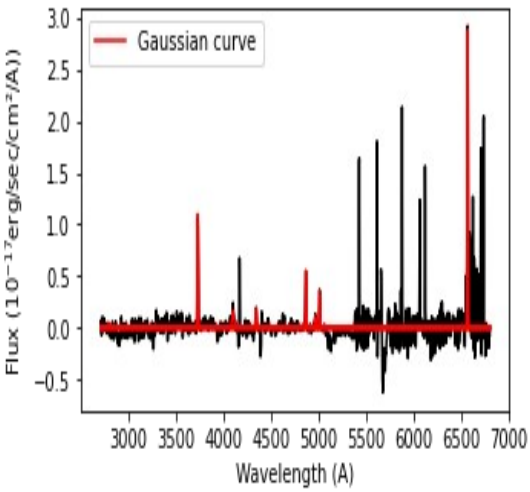

116242 (z_{spec} =1.0324)

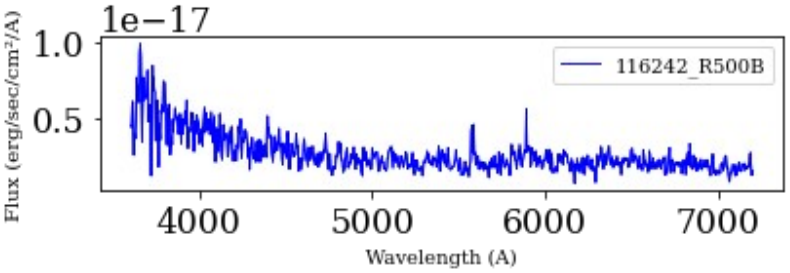

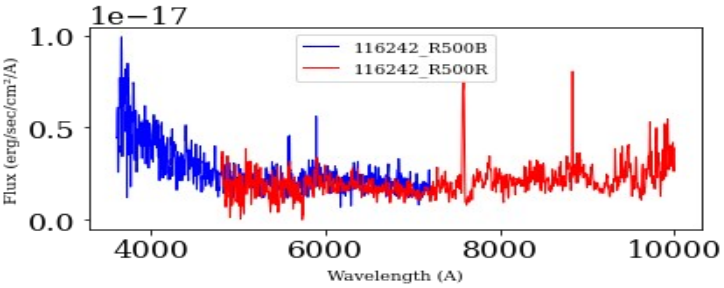

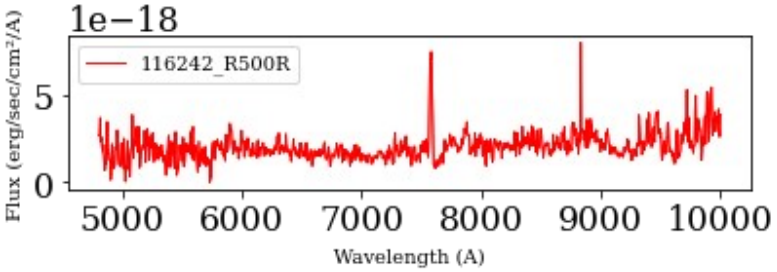

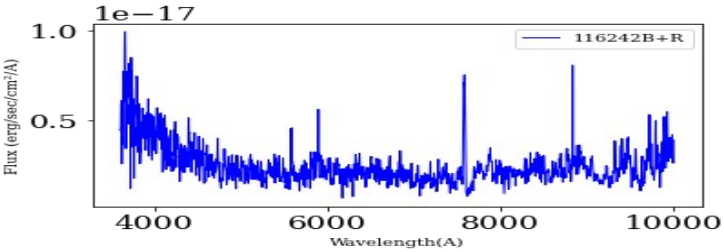

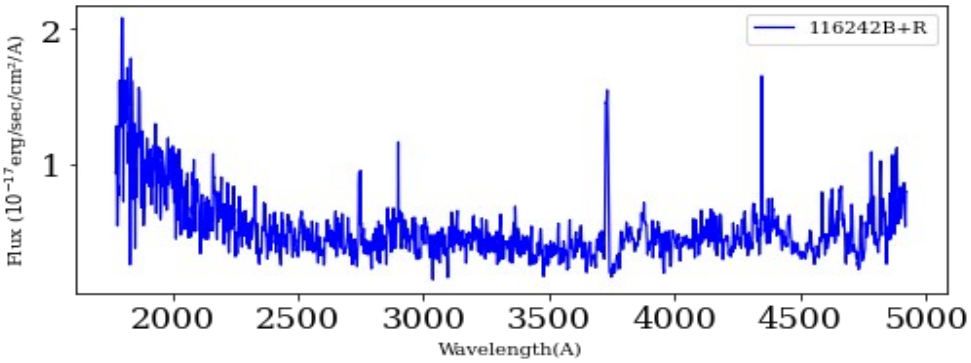

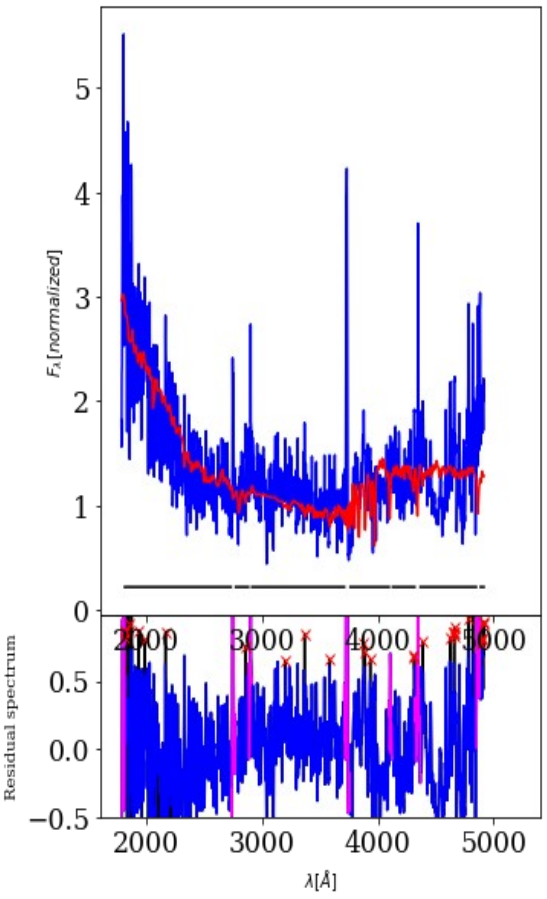

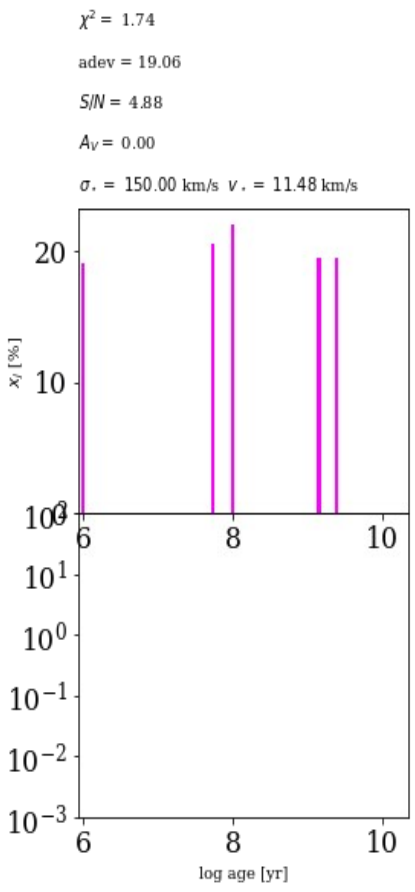

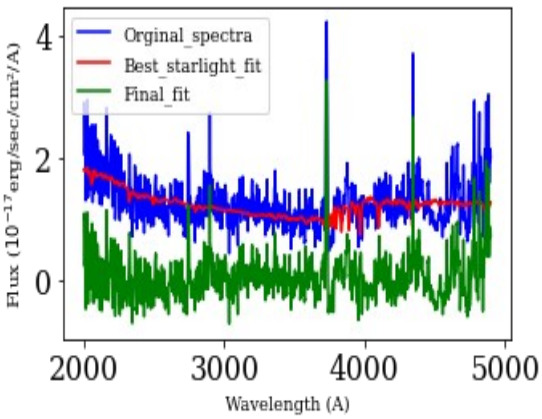

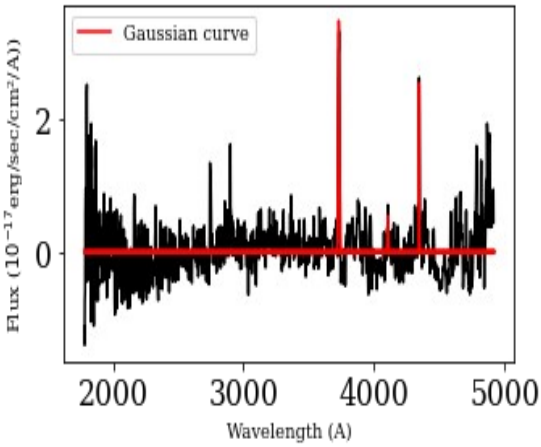

119402 (z_{spec} =0.3369)

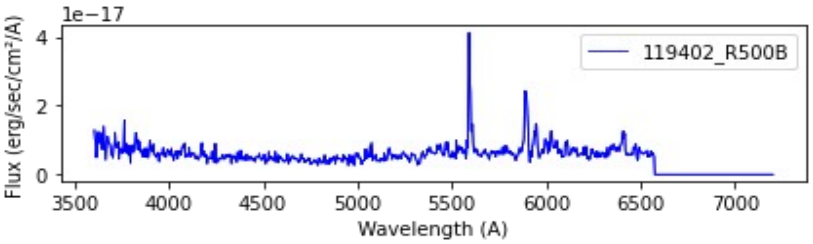

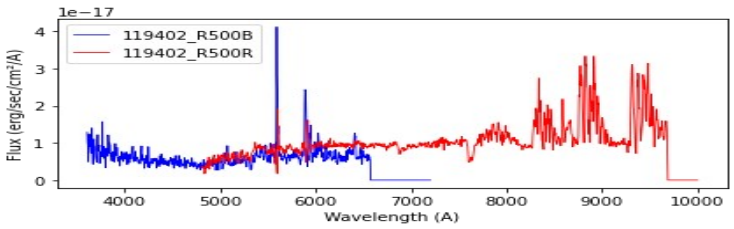

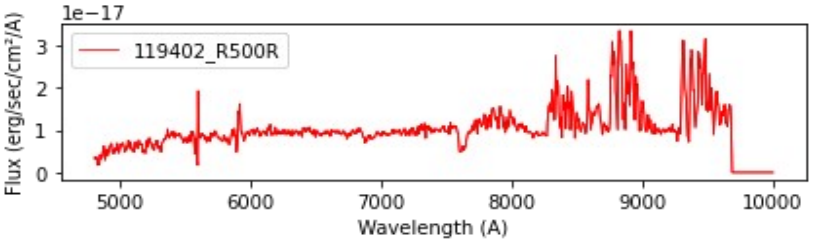

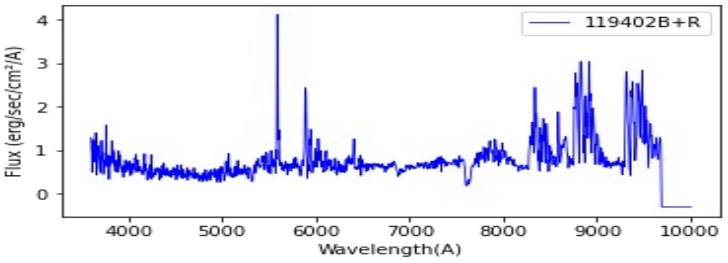

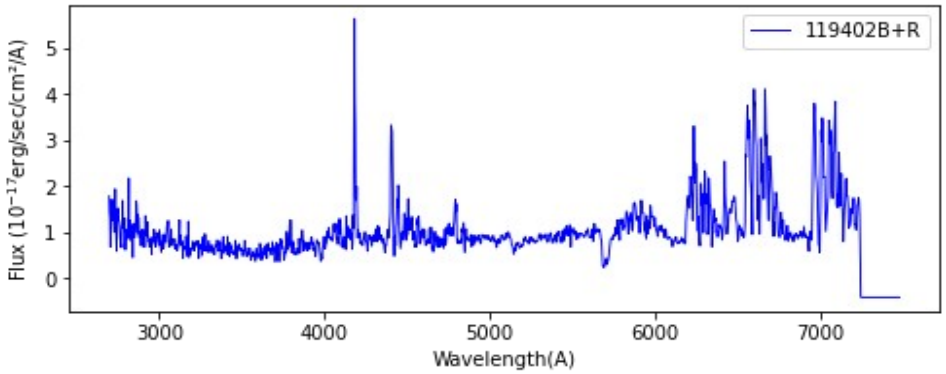

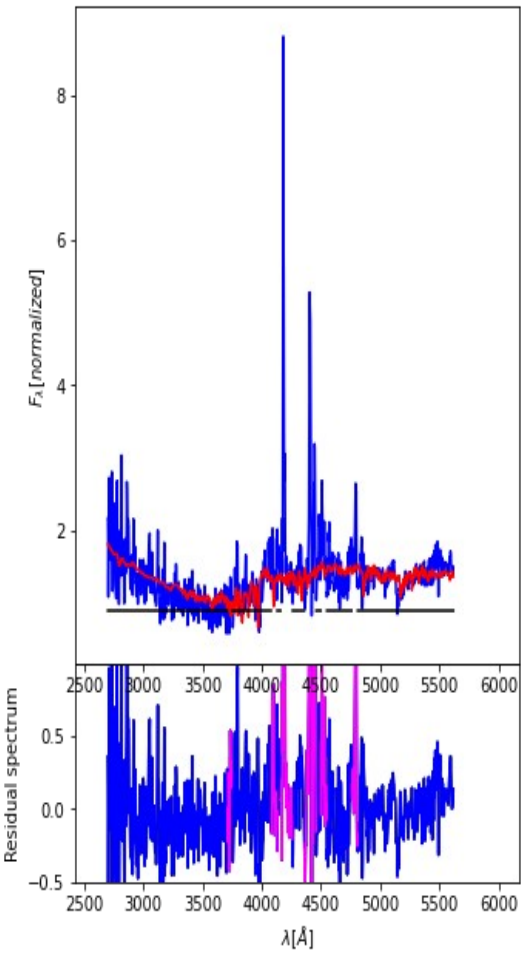

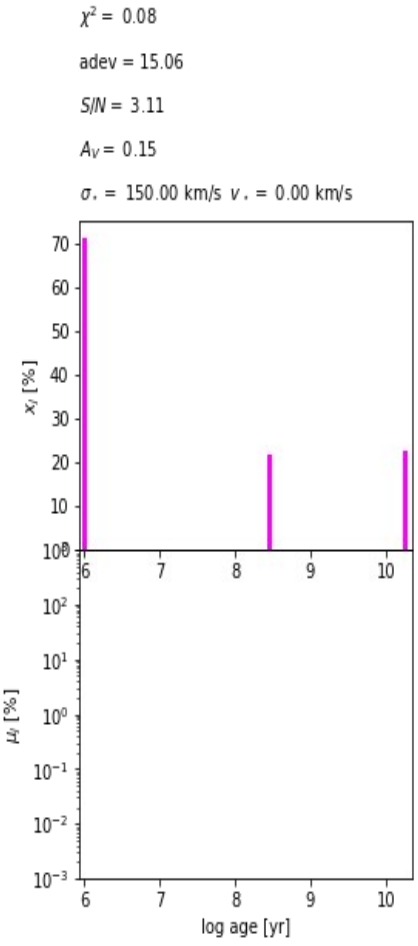

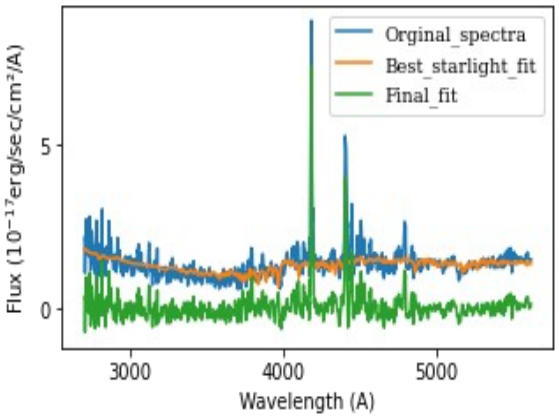

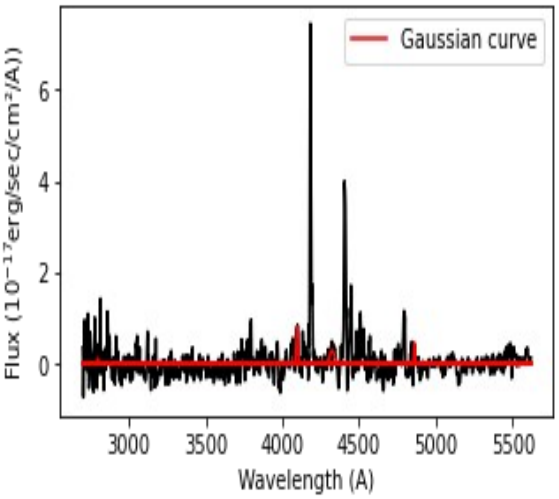

120205 (z_{spec} =0.3953)

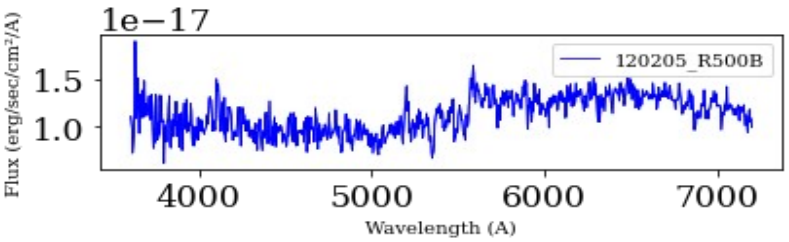

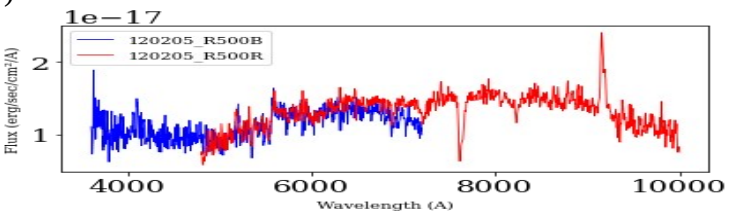

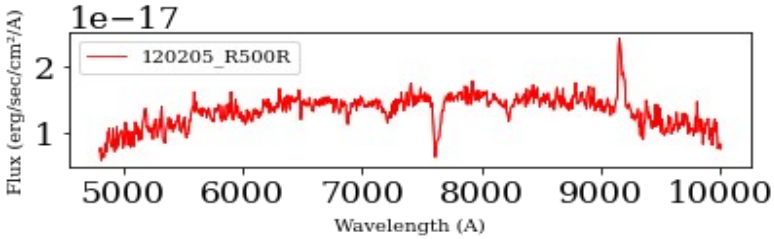

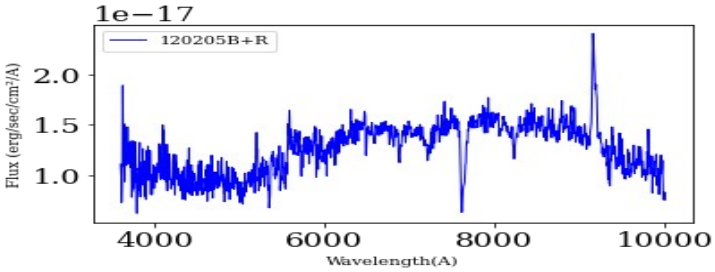

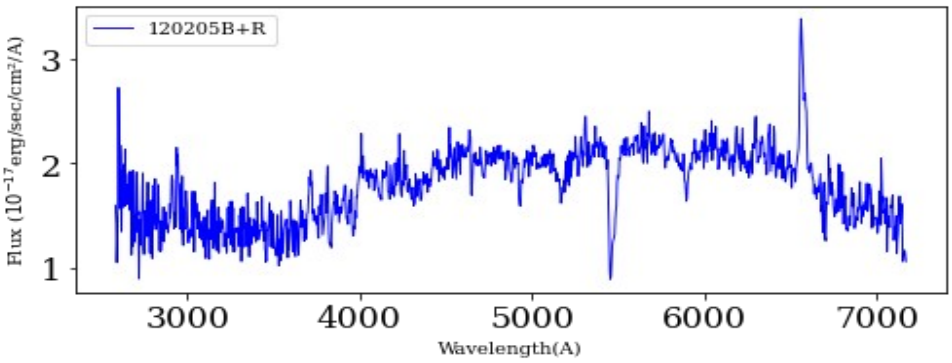

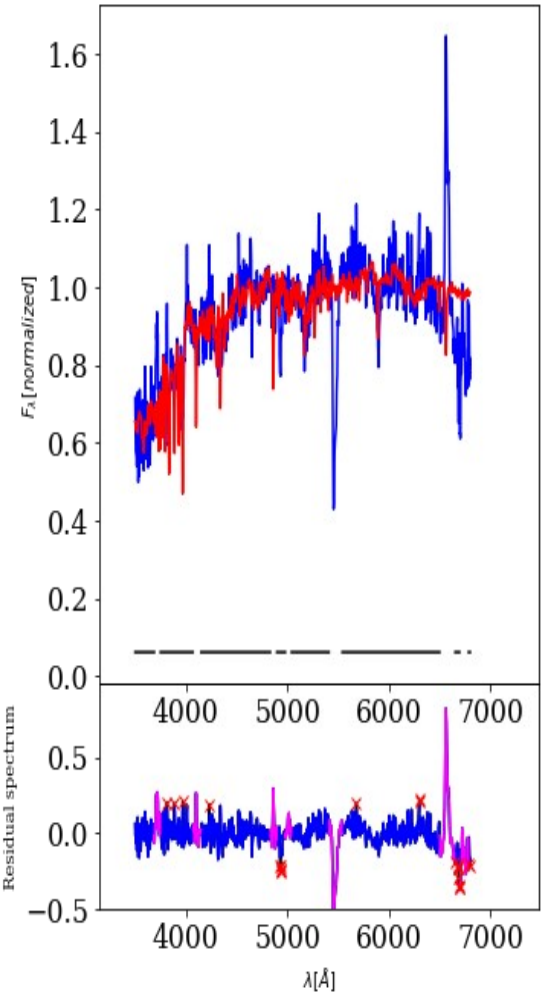

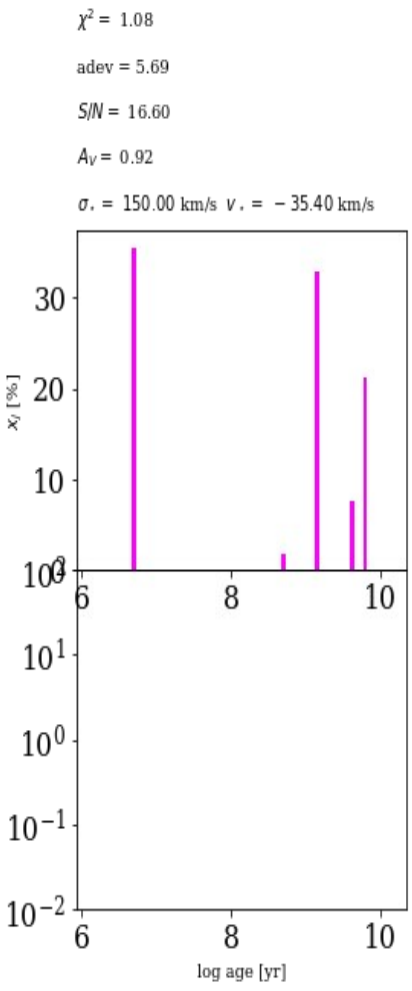

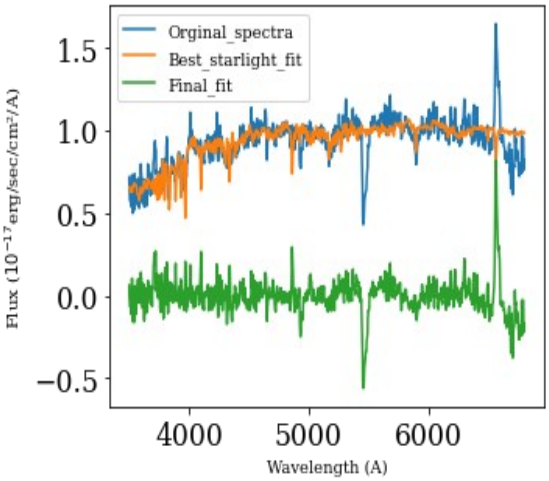

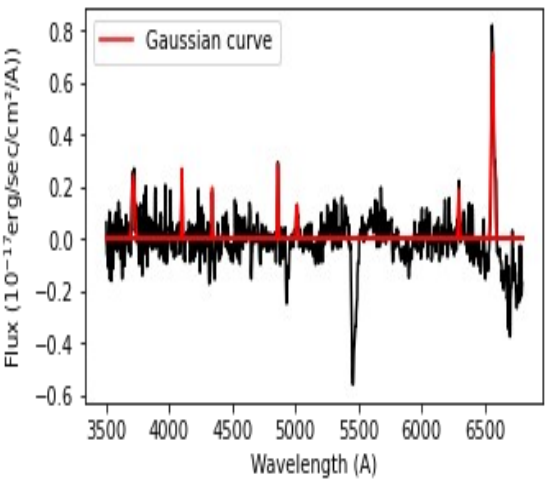

121206 (z_{spec} =1.3371)

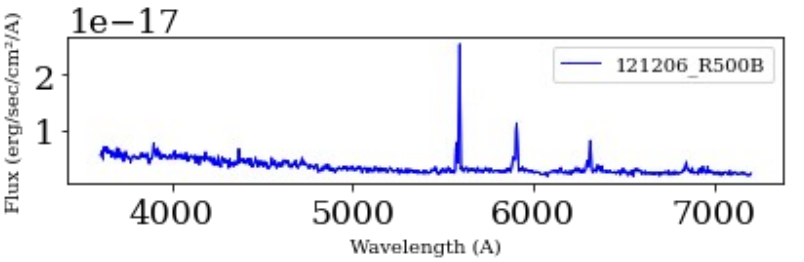

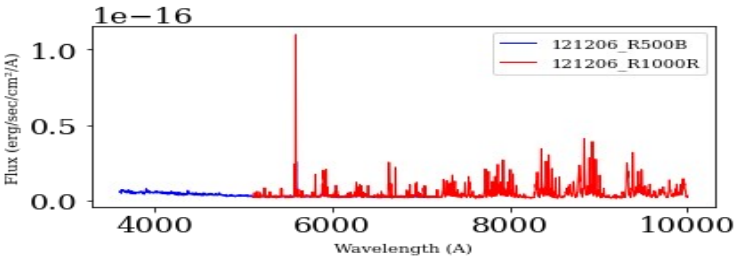

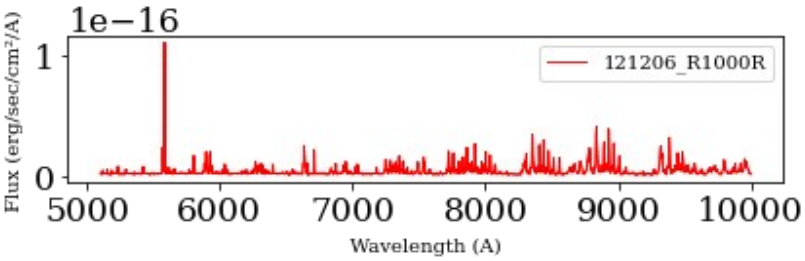

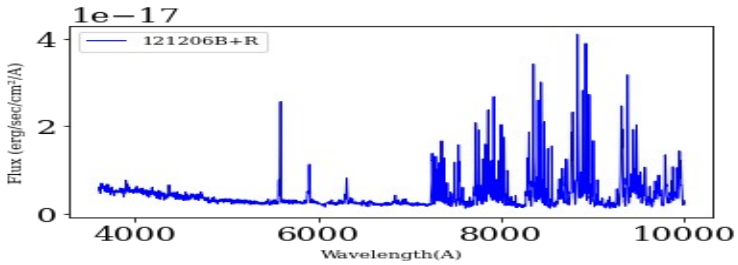

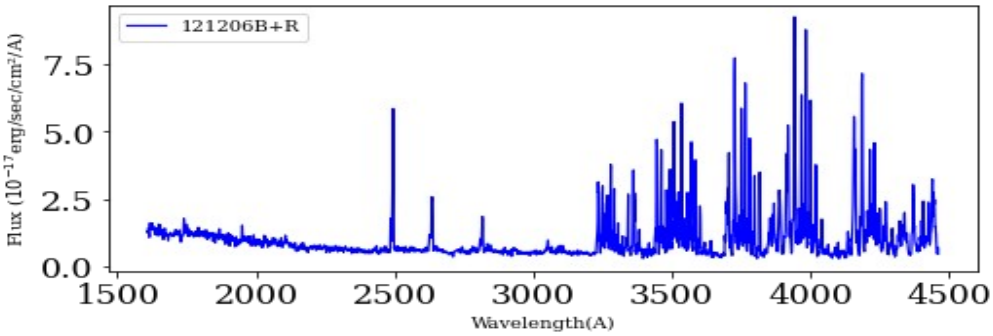

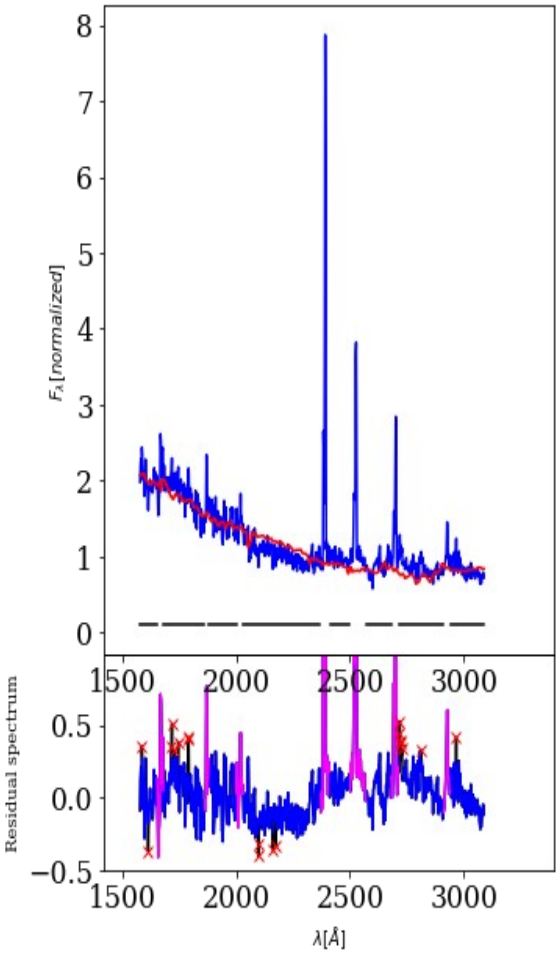

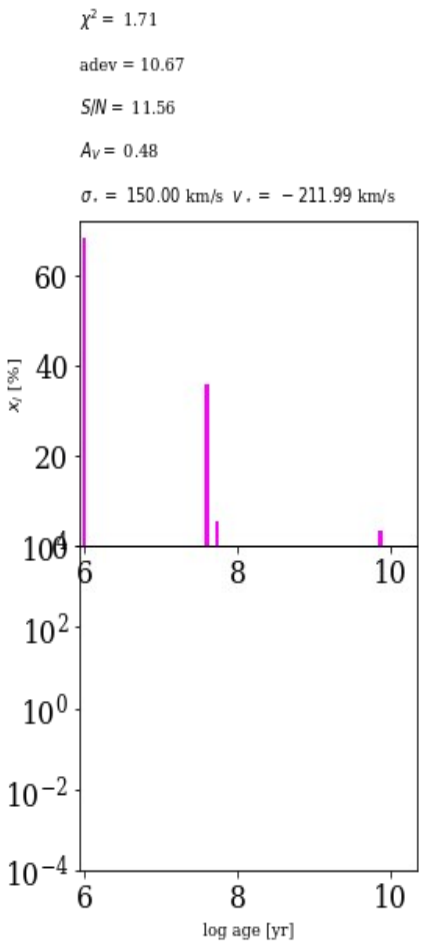

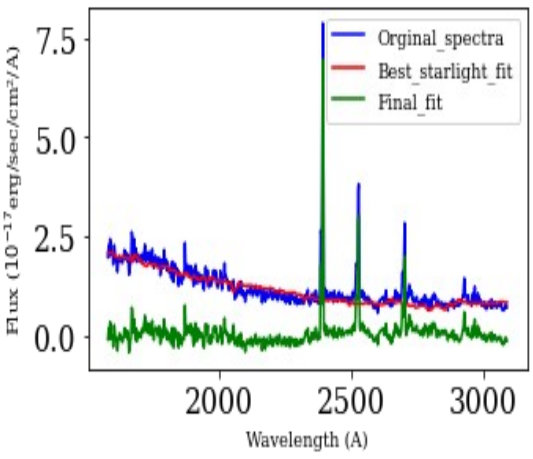

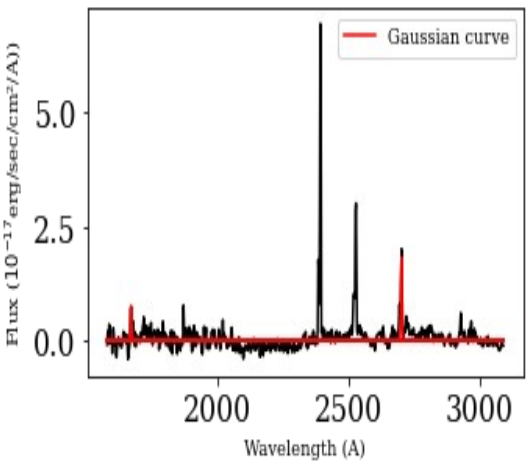

123207 (z_{spec} =0.4914)

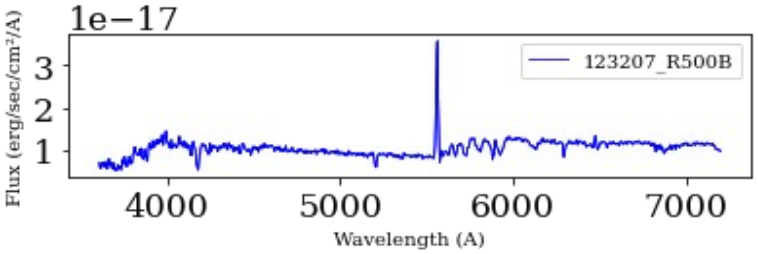

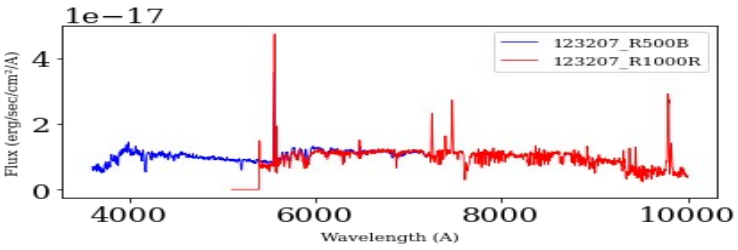

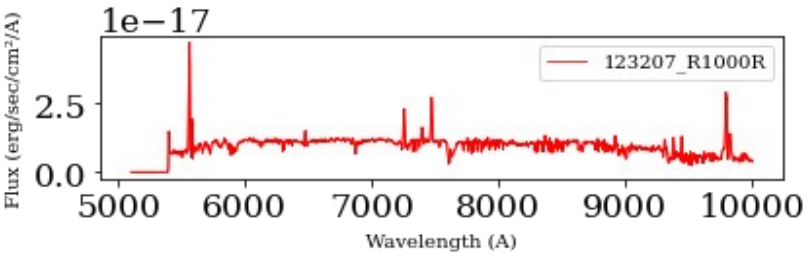

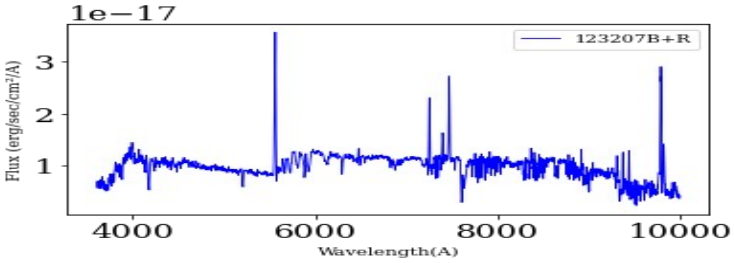

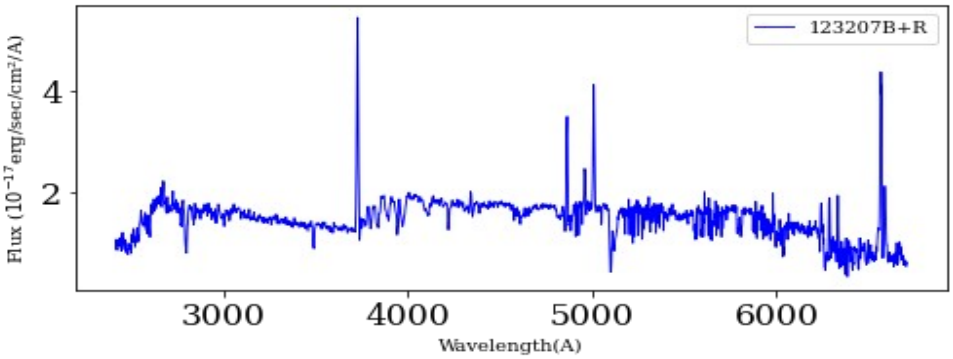

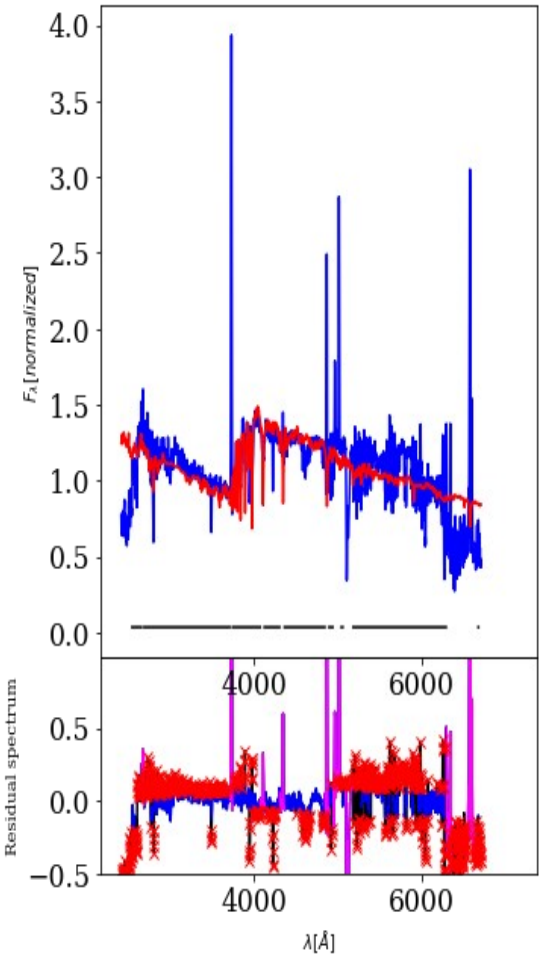

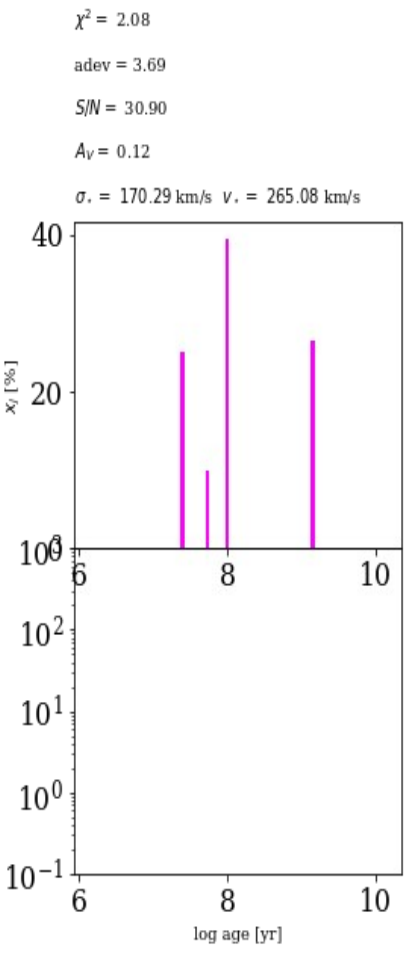

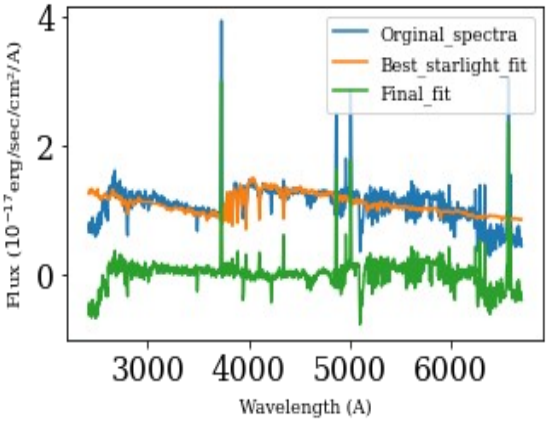

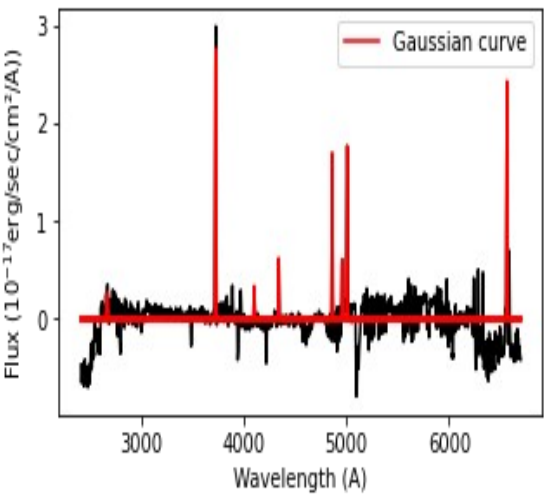

123268 (z_{spec} =0.4203)

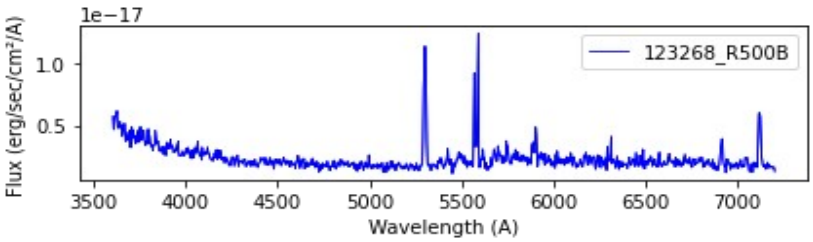

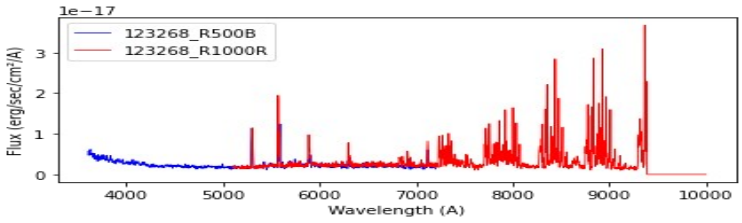

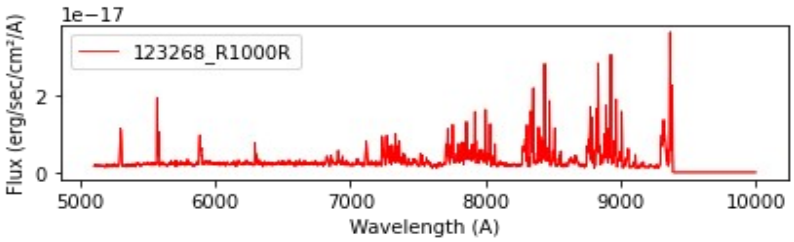

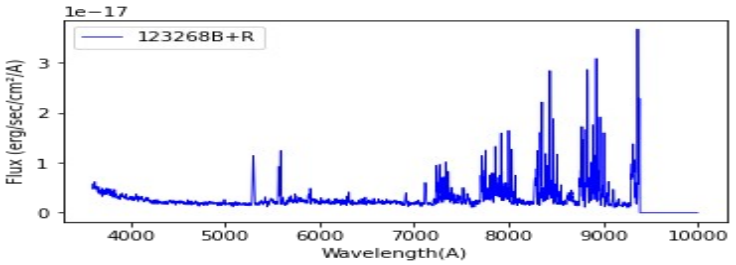

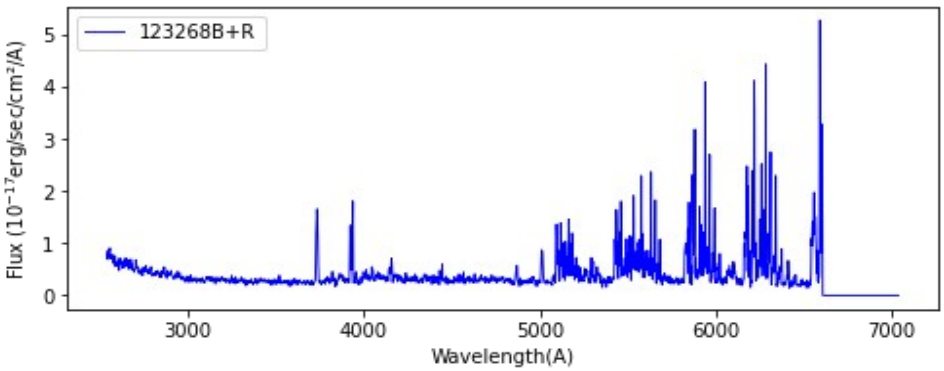

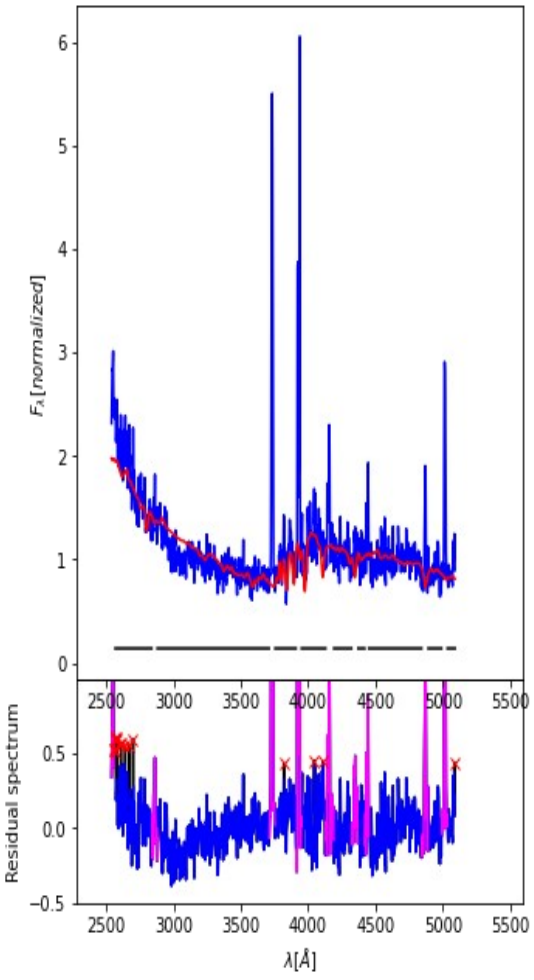

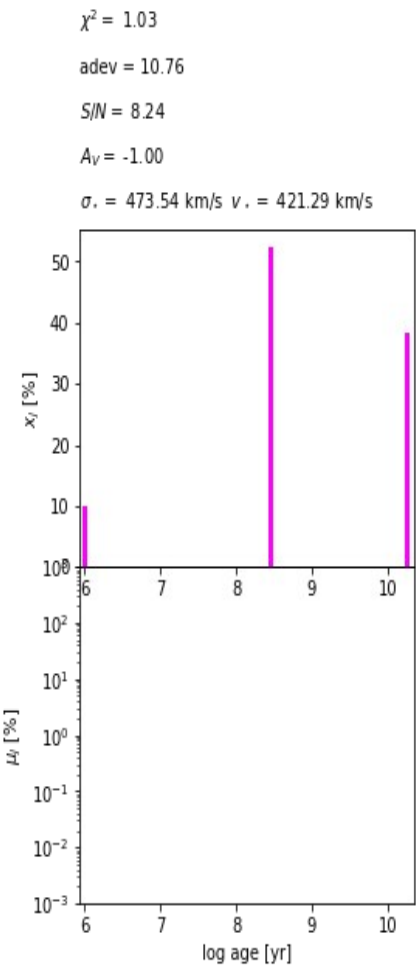

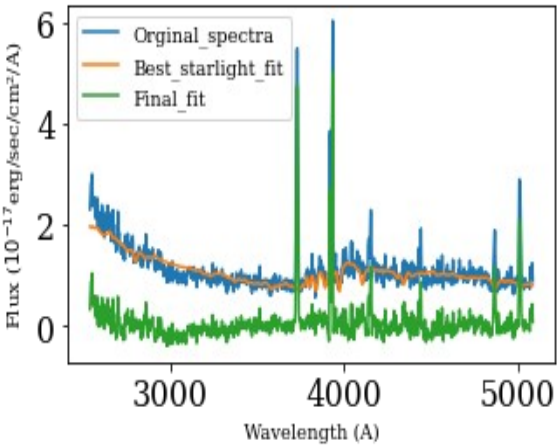

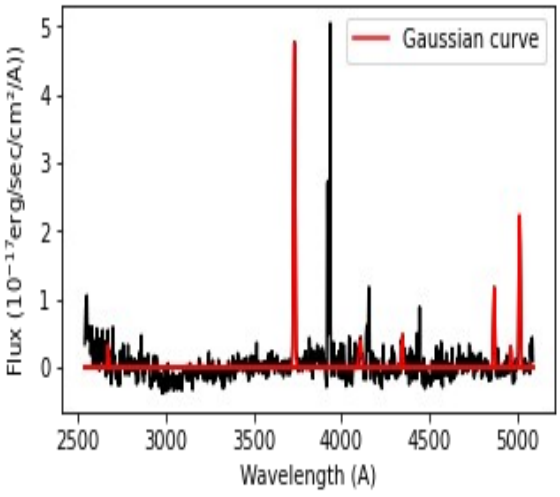

124614 (z_{spec} =0.3068)

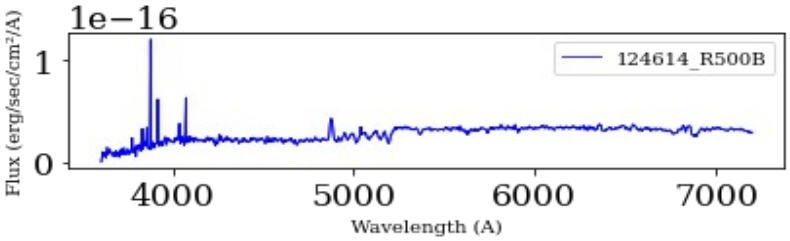

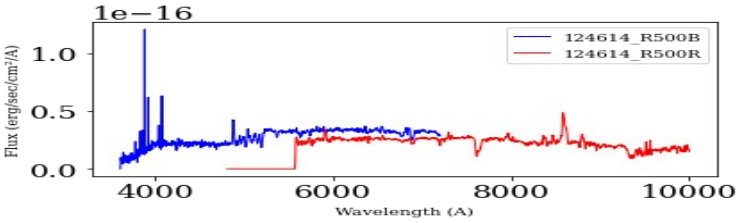

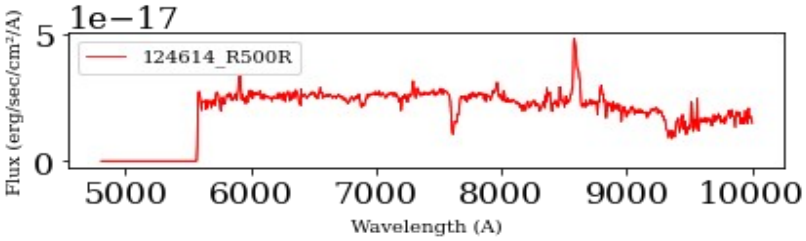

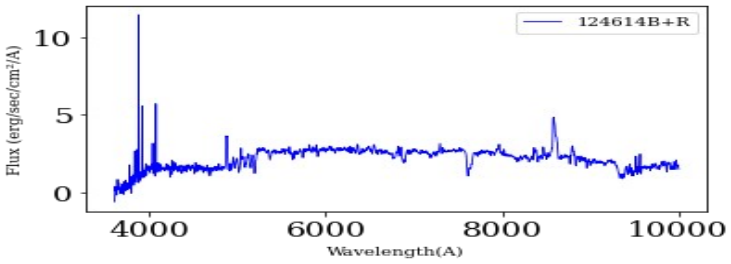

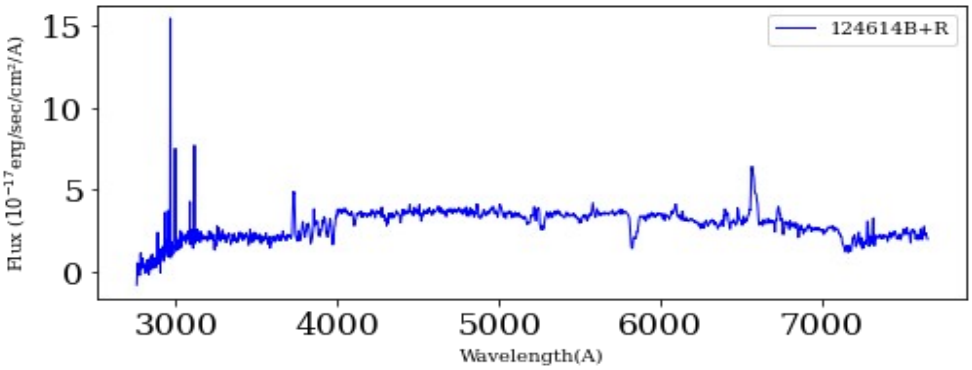

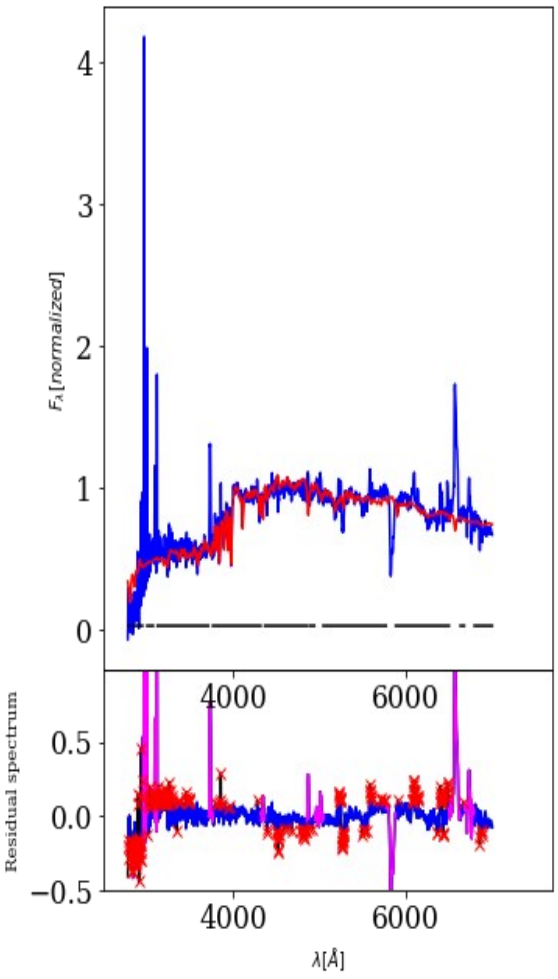

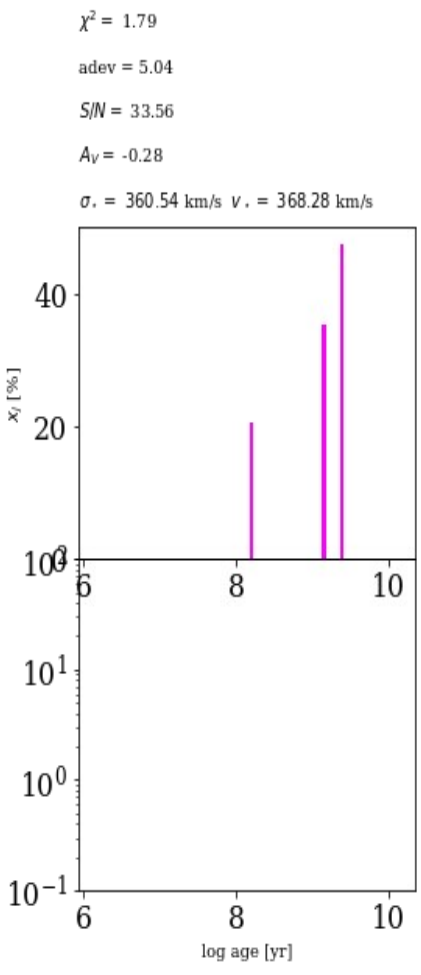

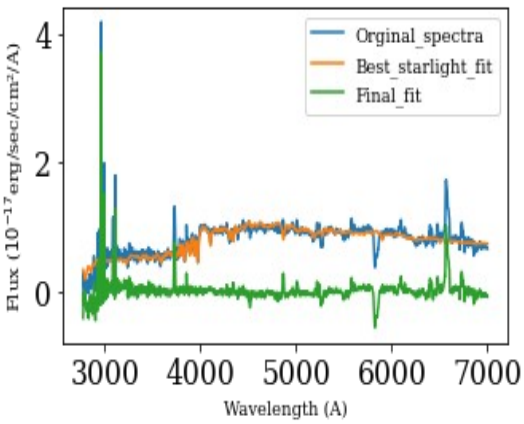

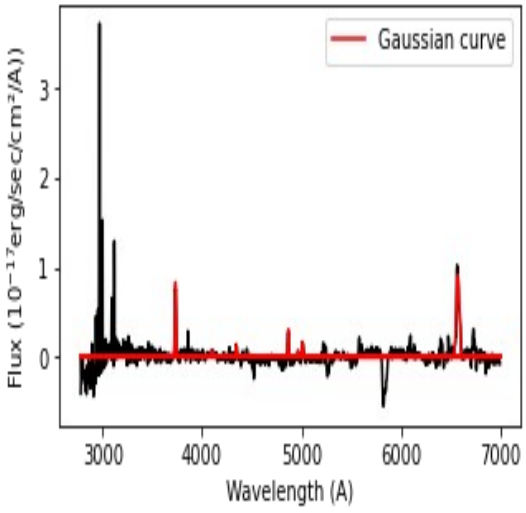

125150 (z_{spec} =0.3161)

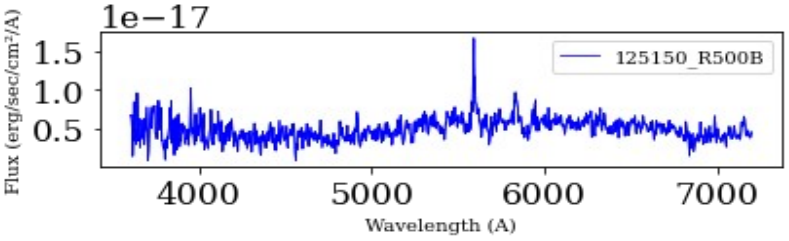

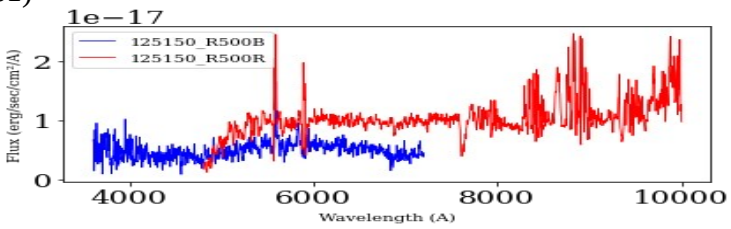

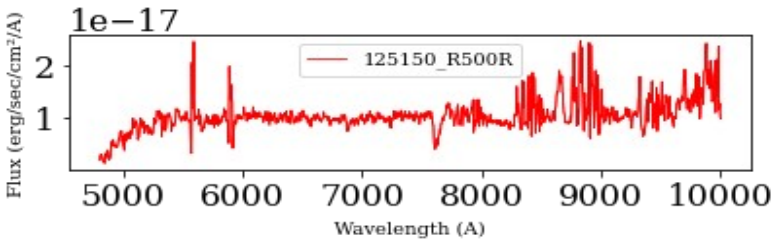

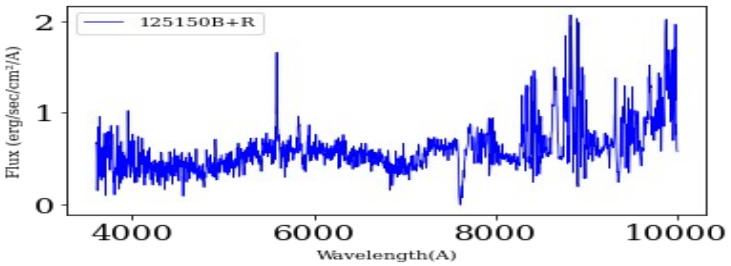

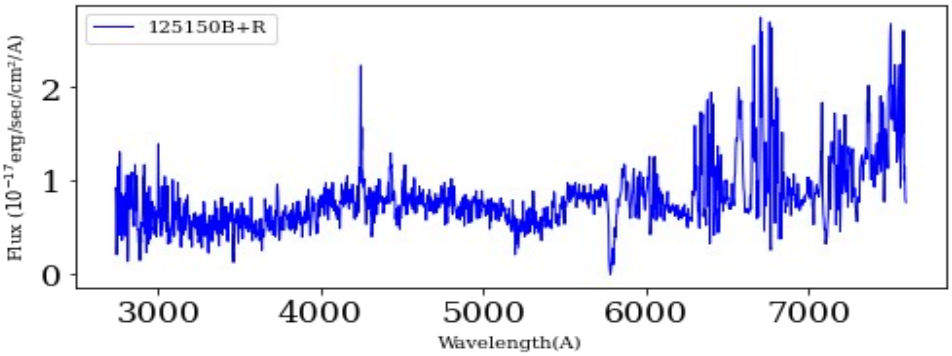

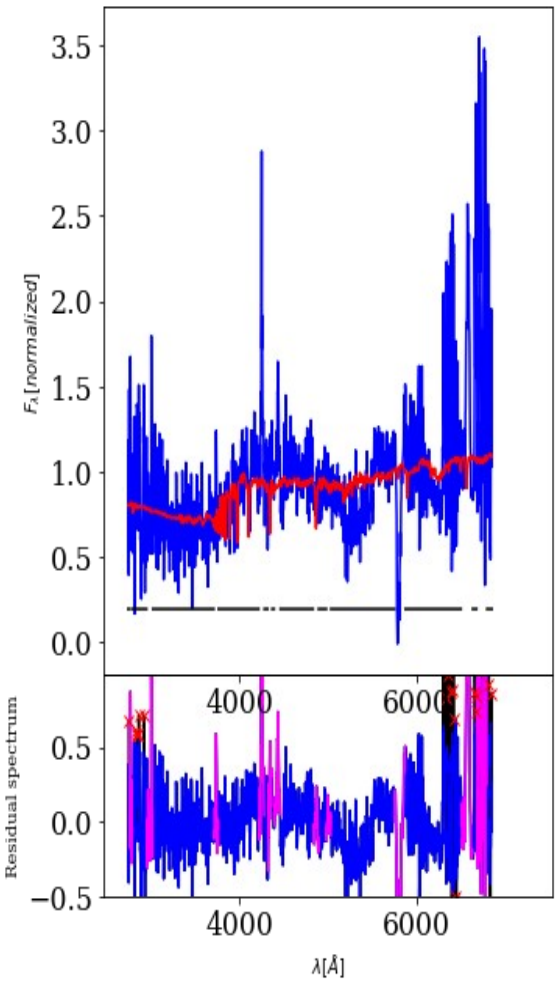

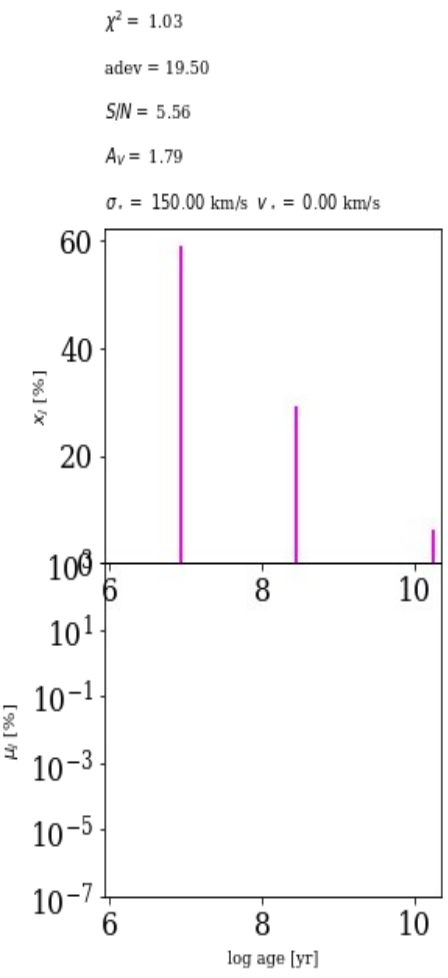

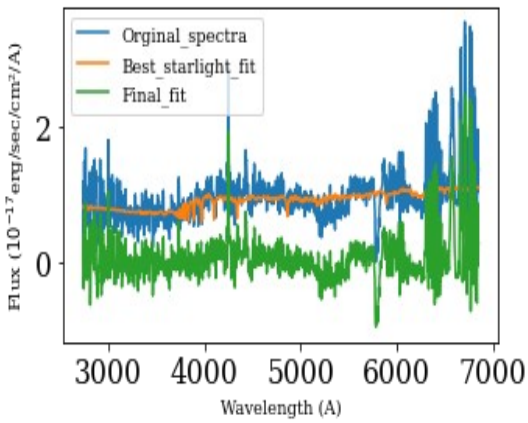

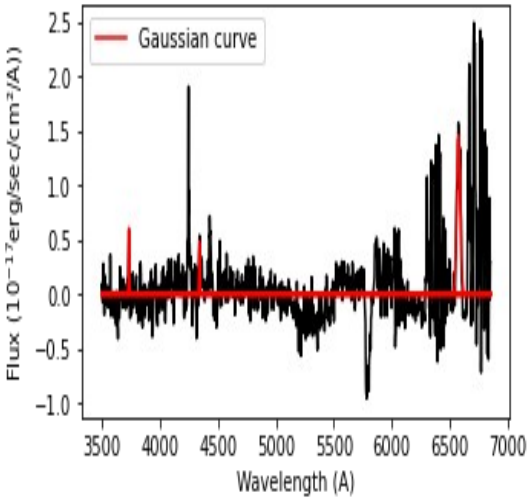

128229 (z_{spec} =0.4826)

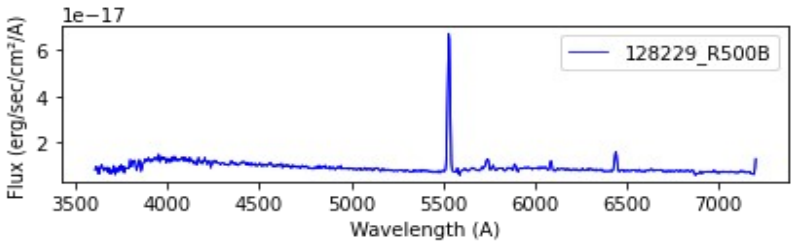

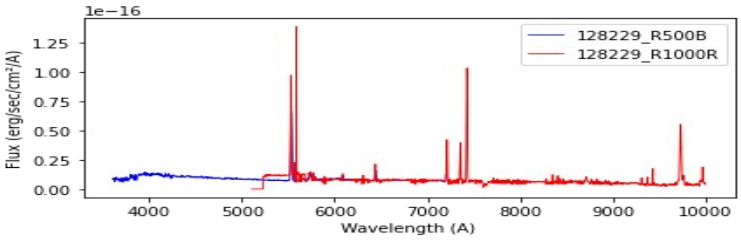

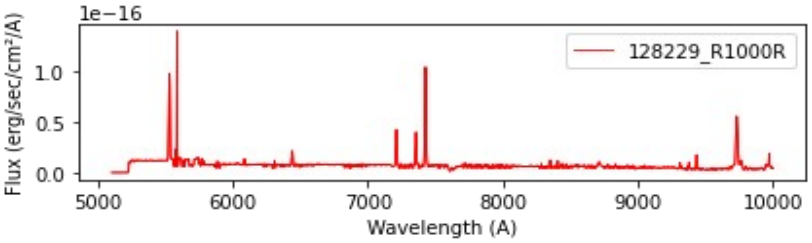

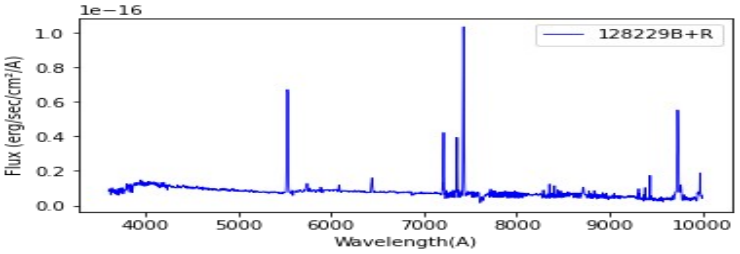

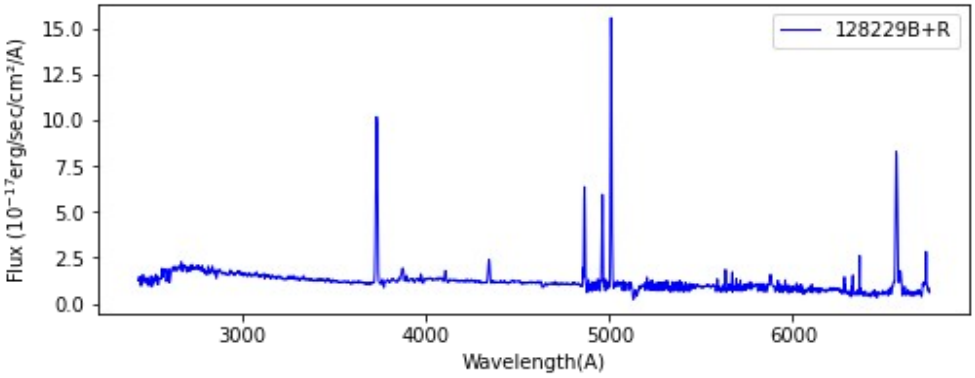

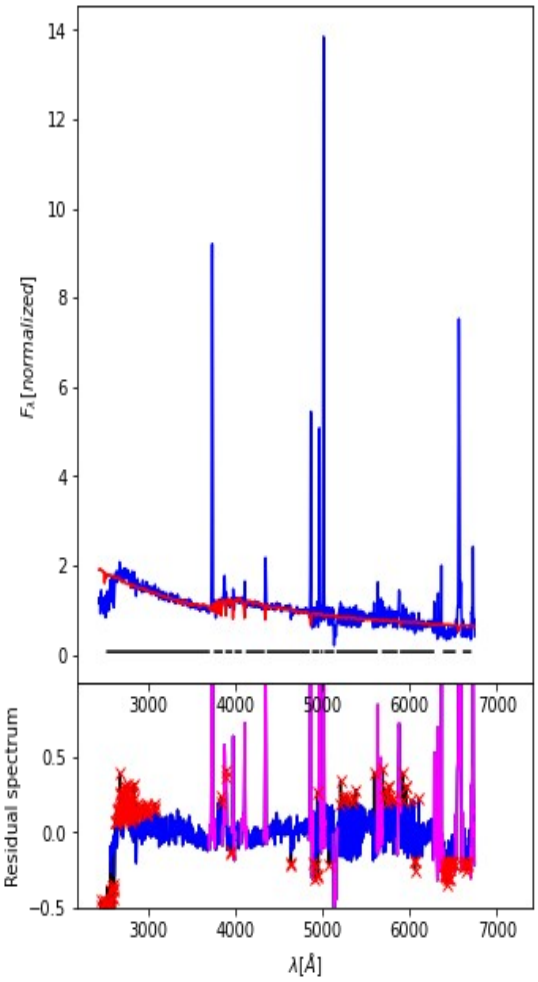

χ^2 = 1.46

adev = 6.95

S/N = 15.99

A_V = 1.38

$\sigma_\star$ = 150.00 km/s $v_\star$ = 20.65 km/s

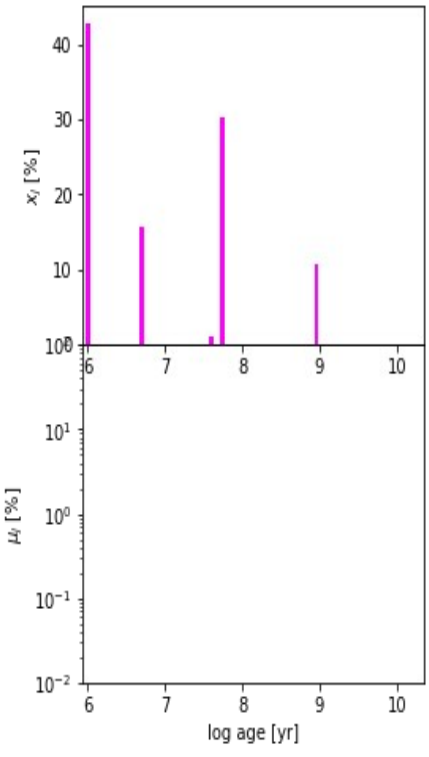

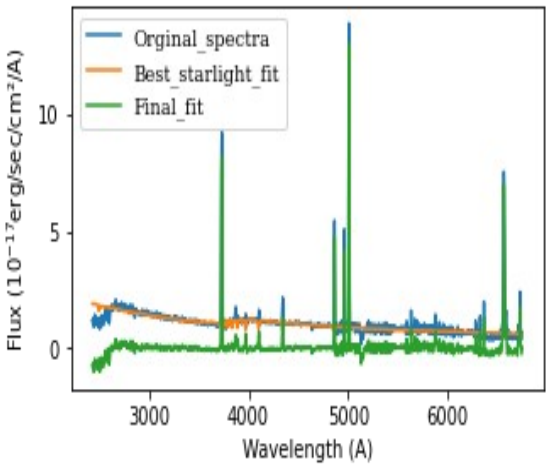

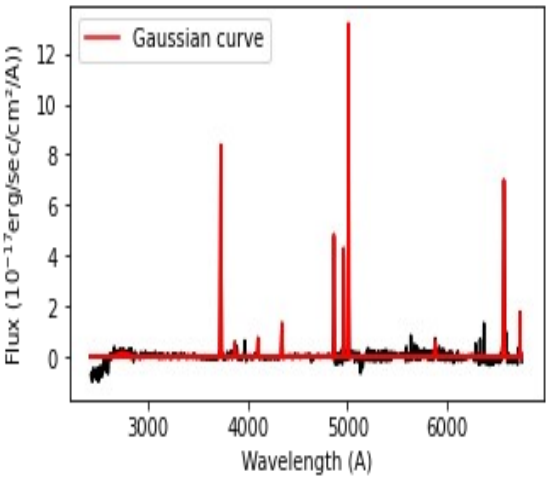

135313 (z_{spec} =0.2022)

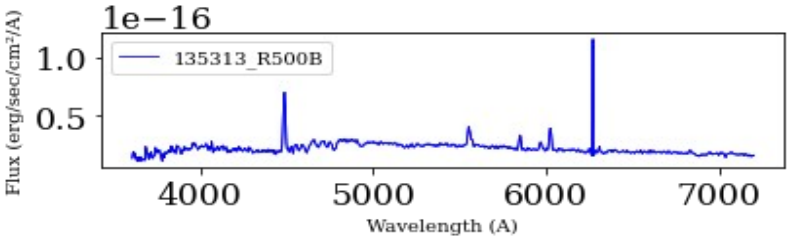

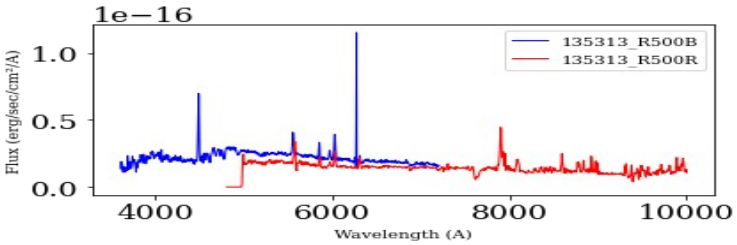

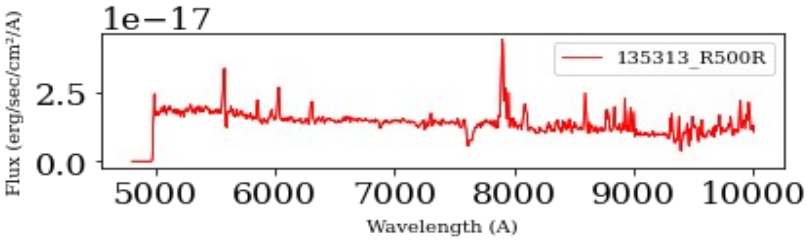

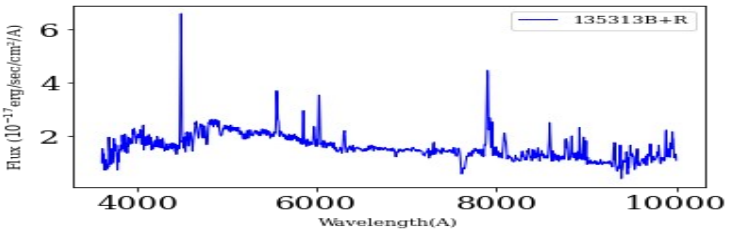

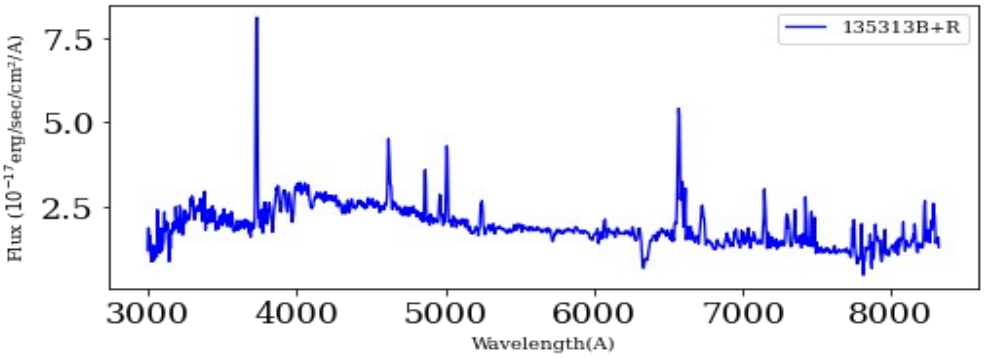

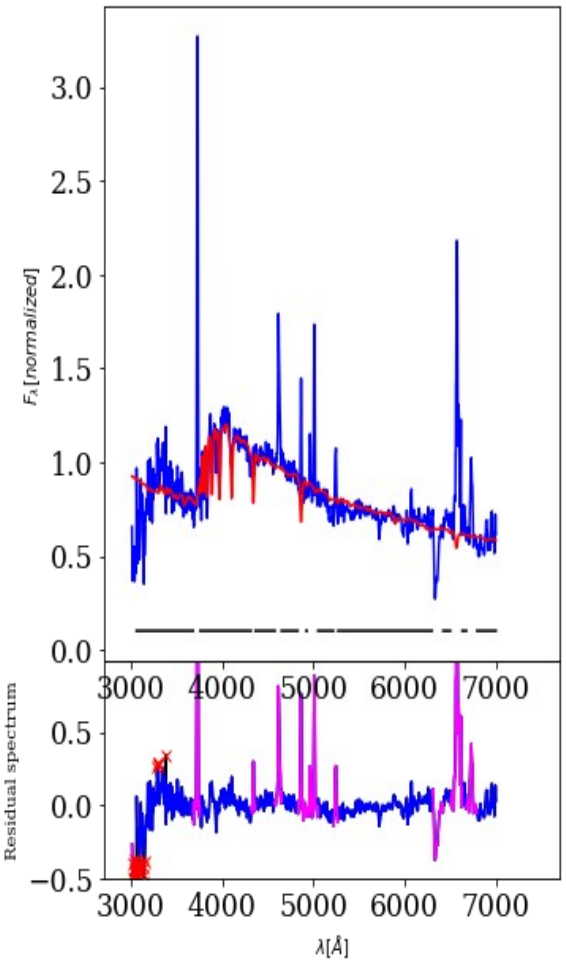

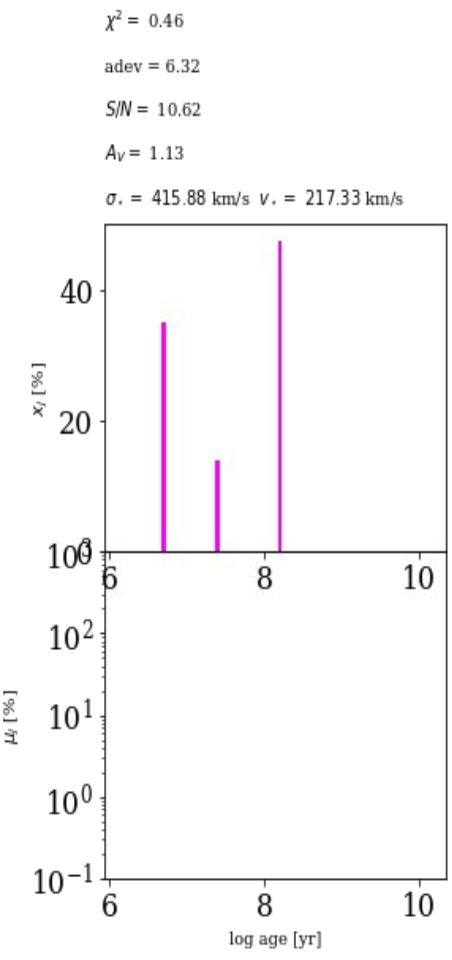

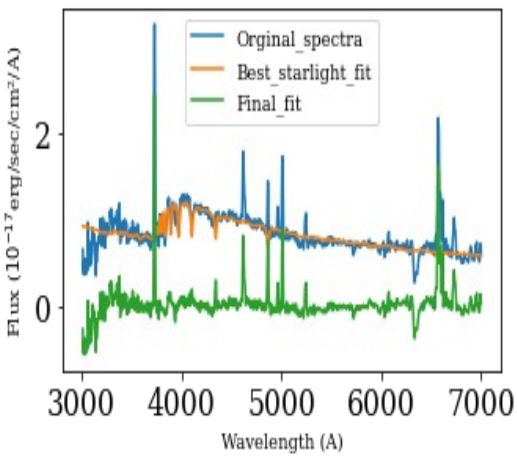

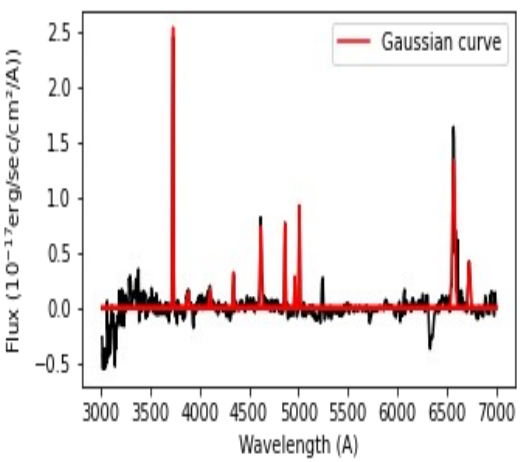

135919 (z_{spec} =0.3948)

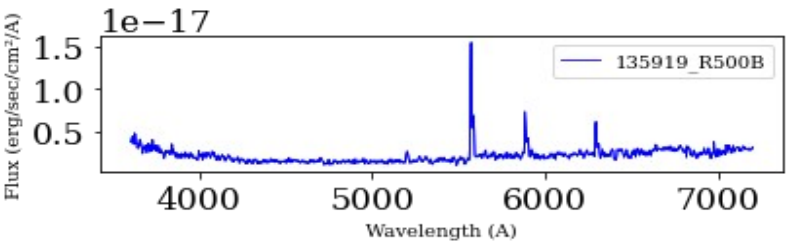

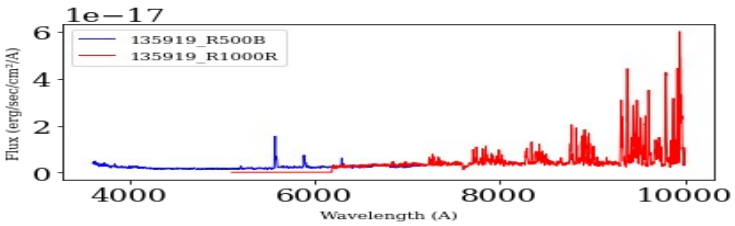

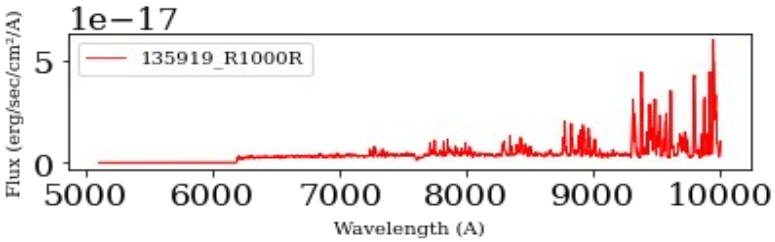

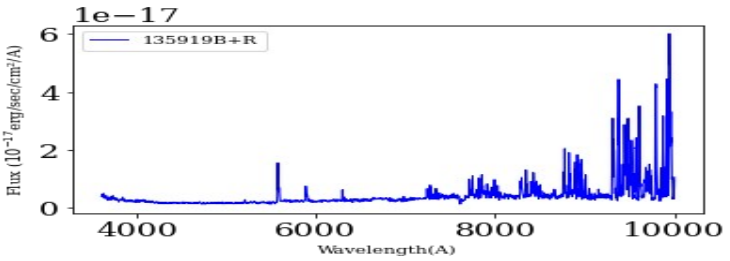

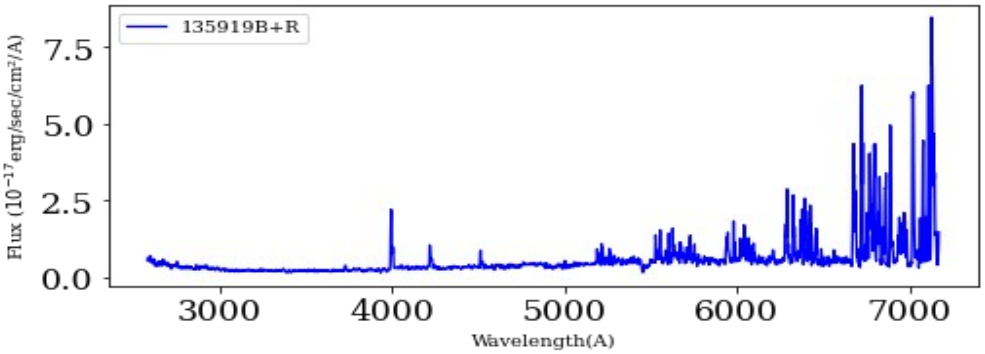

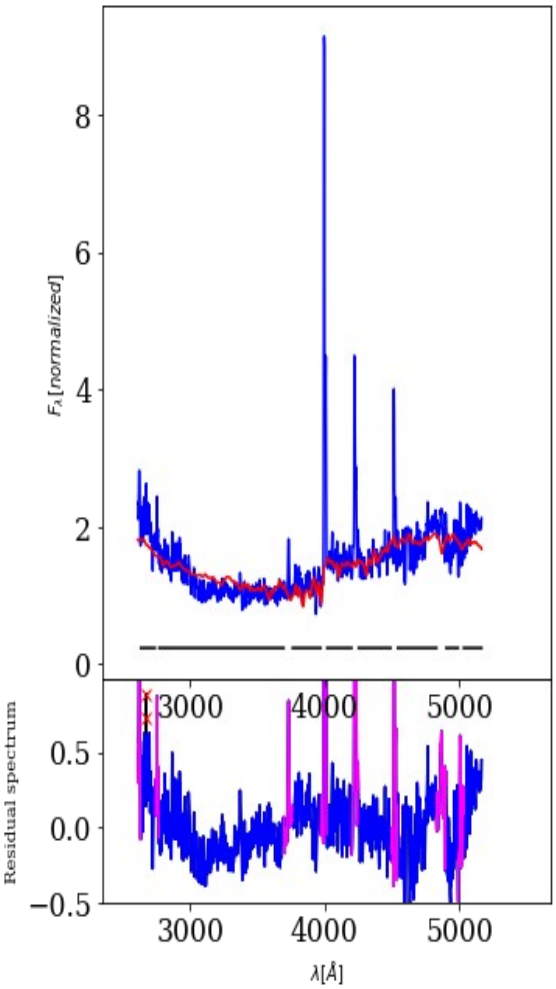

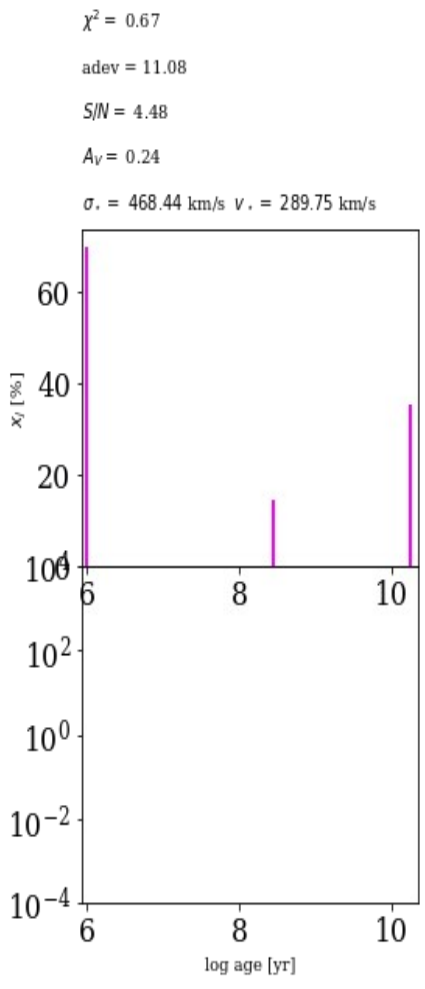

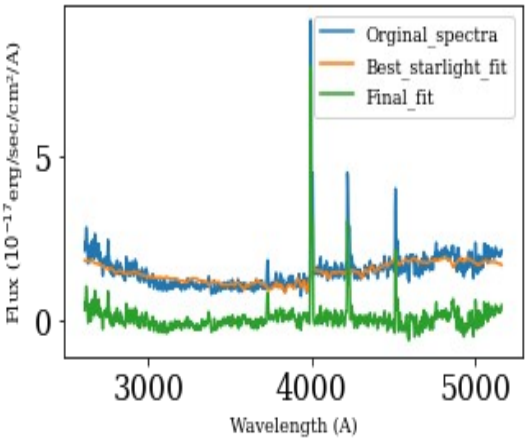

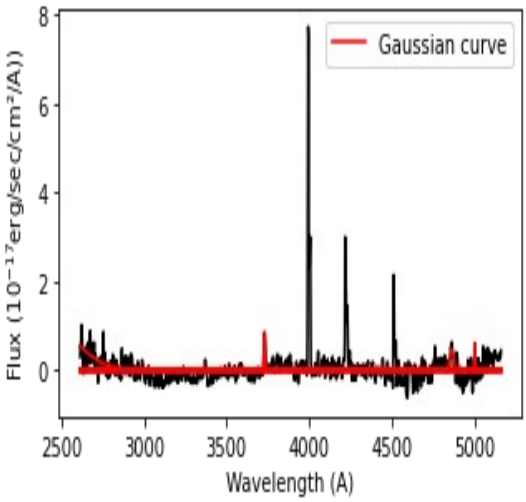

136207 (z_{spec} =1.0362)

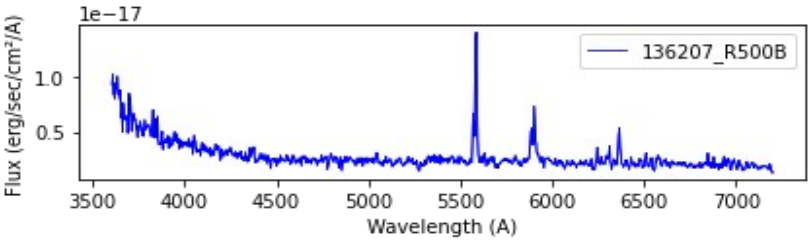

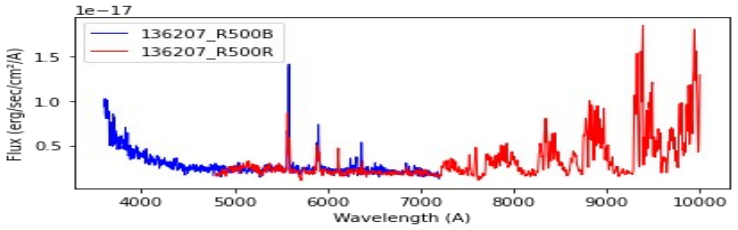

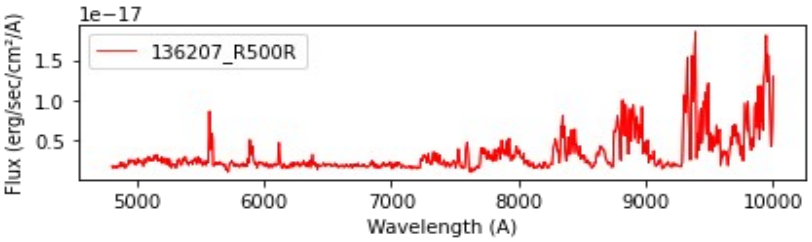

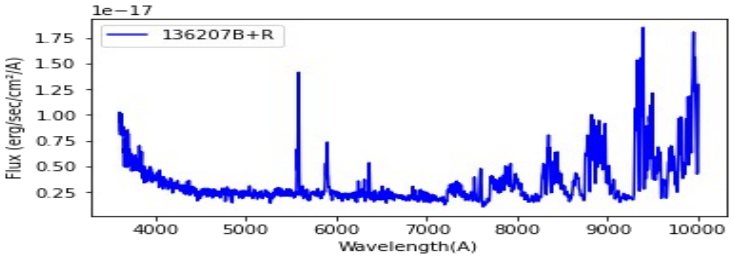

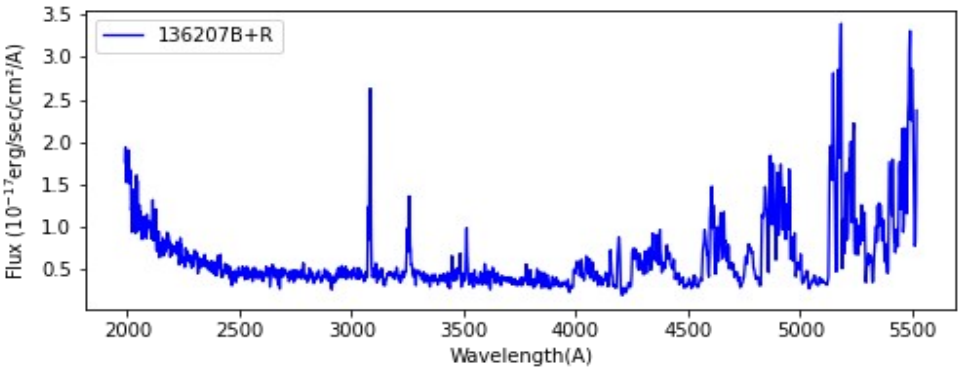

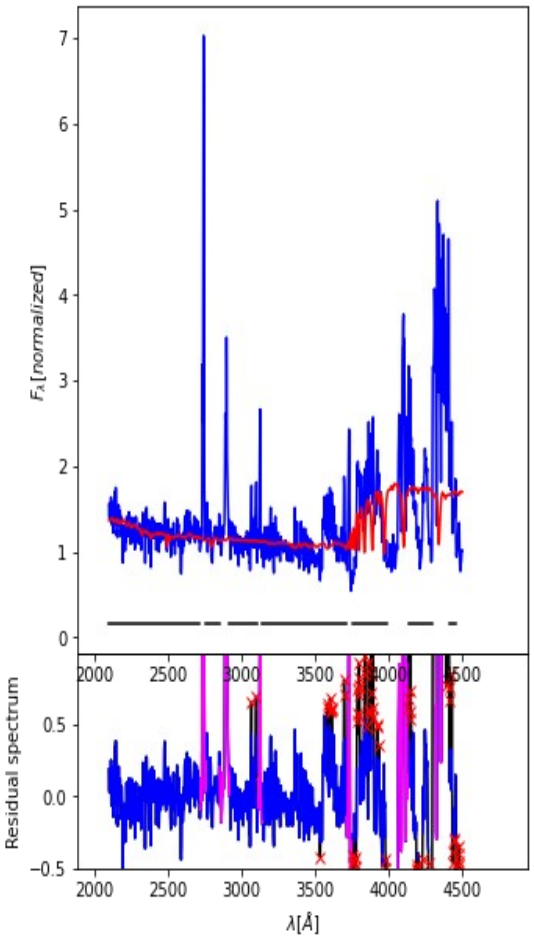

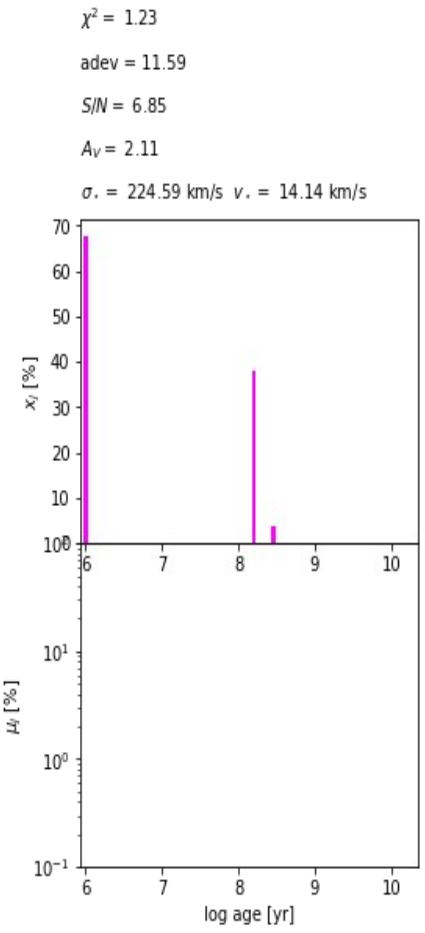

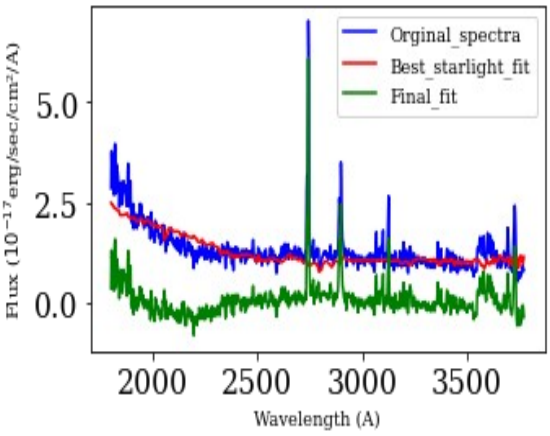

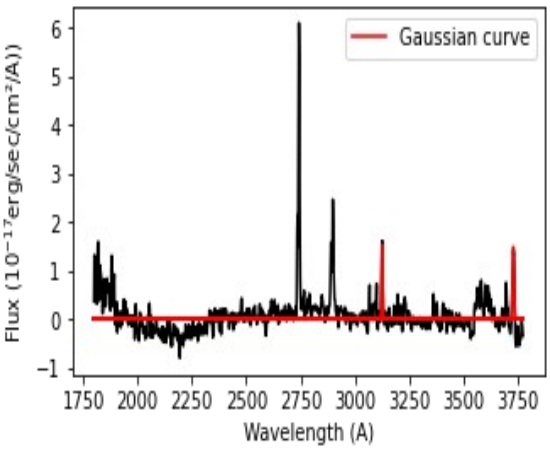

137010 (z_{spec} =0.4192)

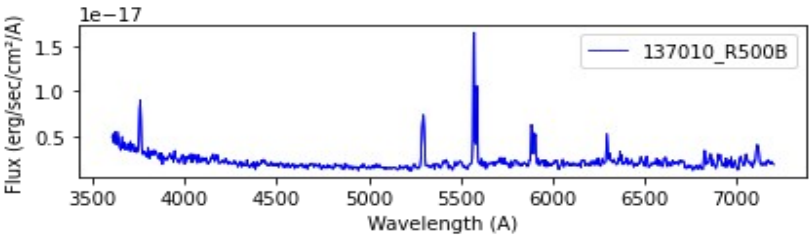

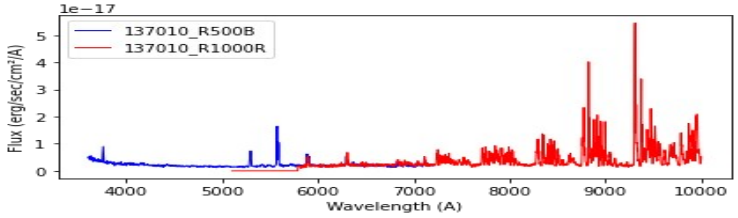

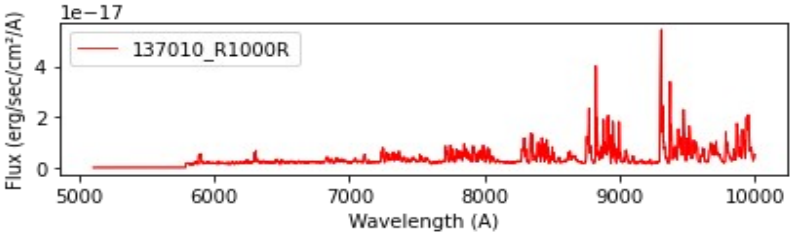

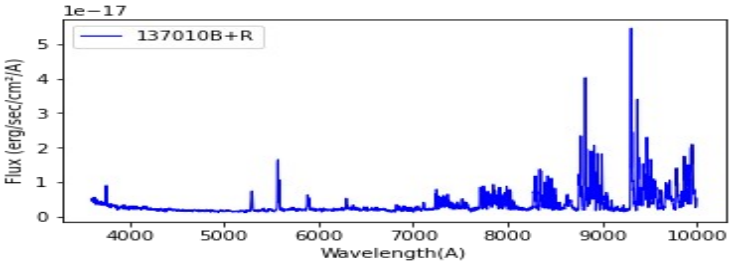

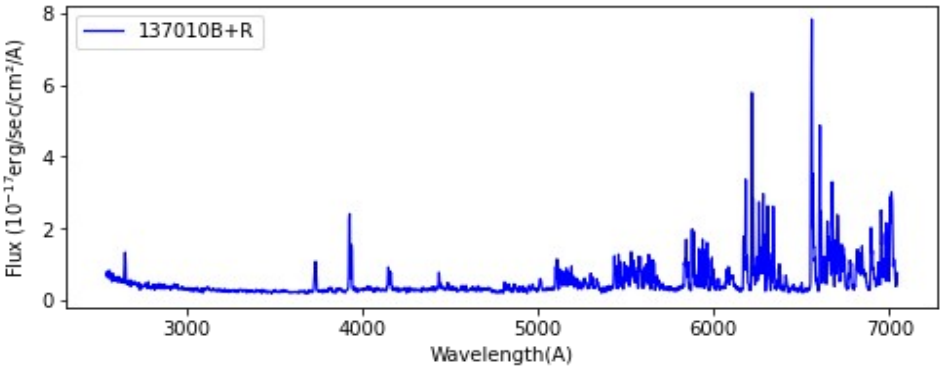

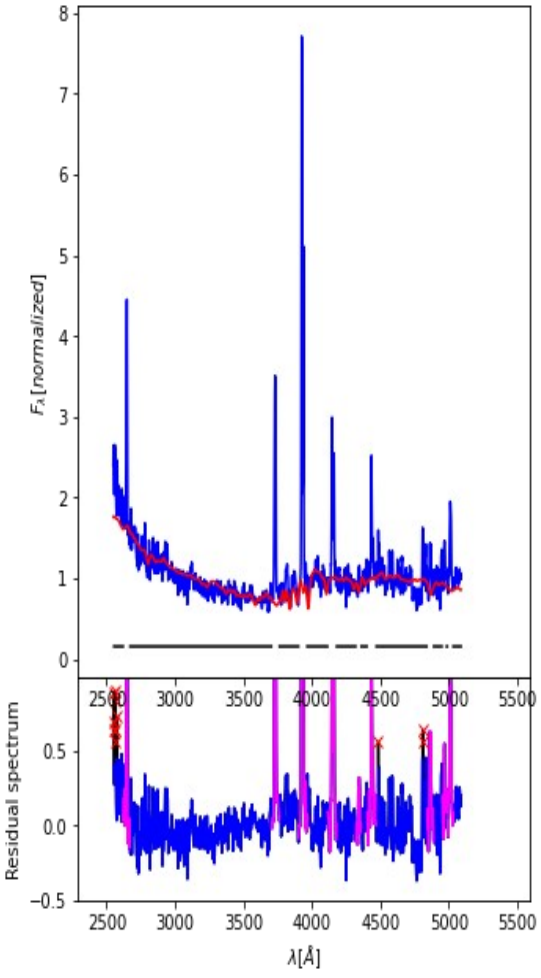

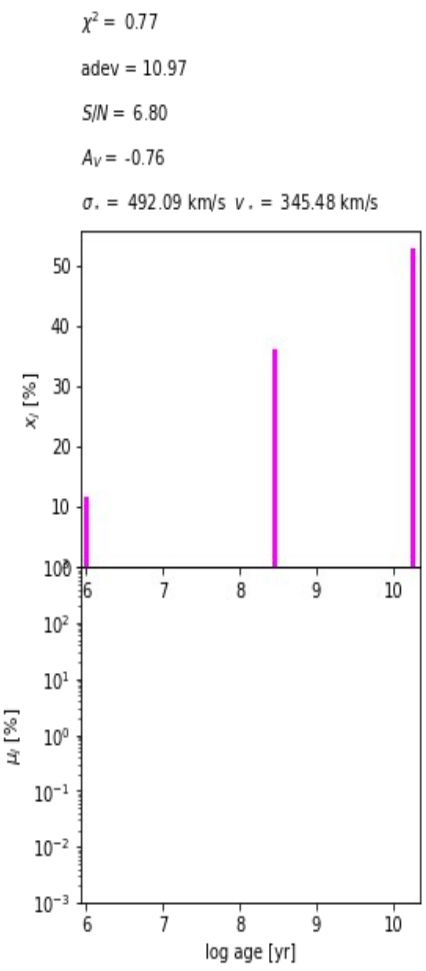

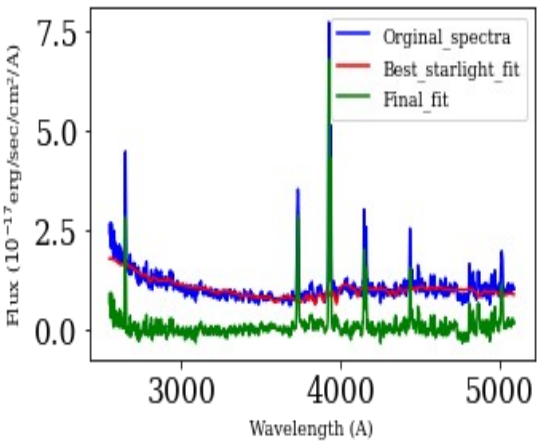

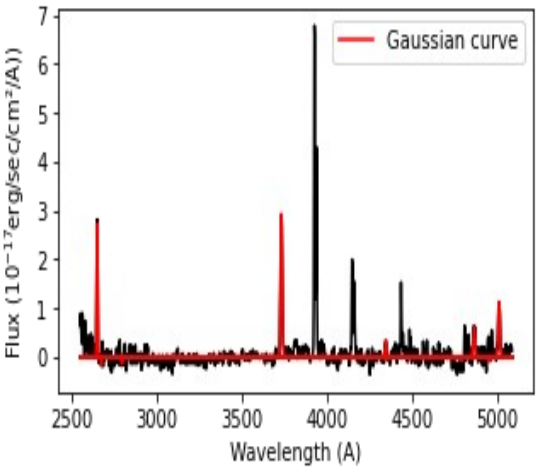

138428 (z_{spec} =0.333)

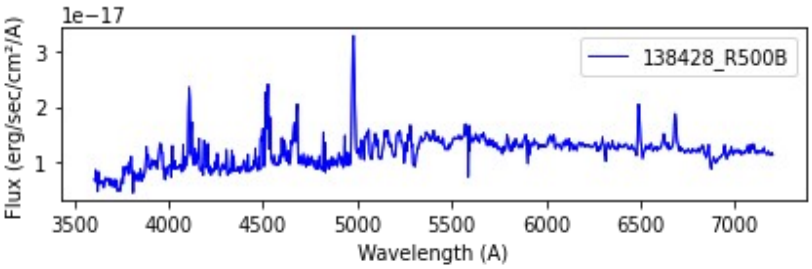

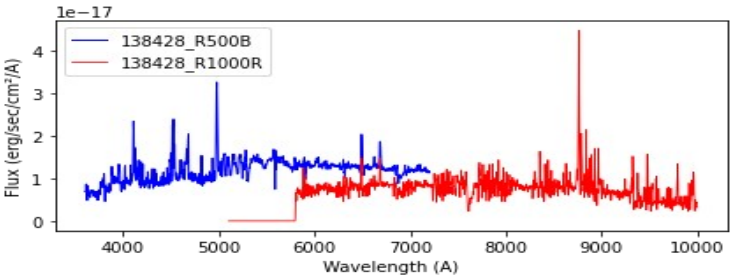

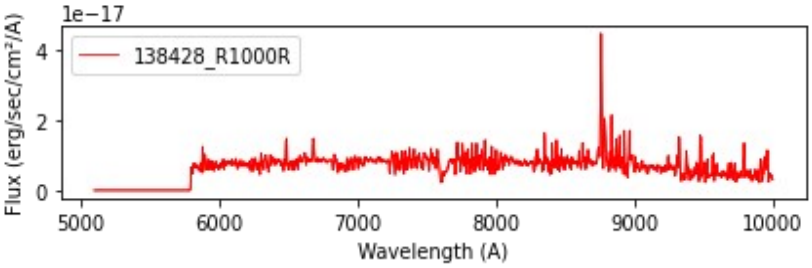

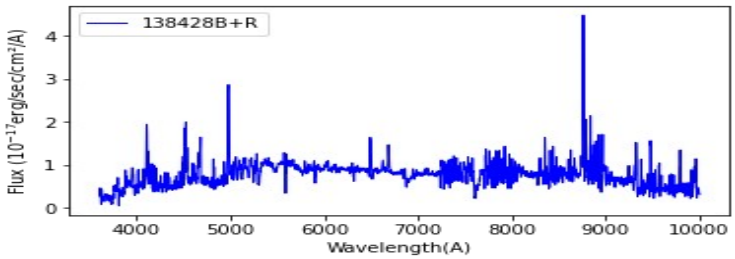

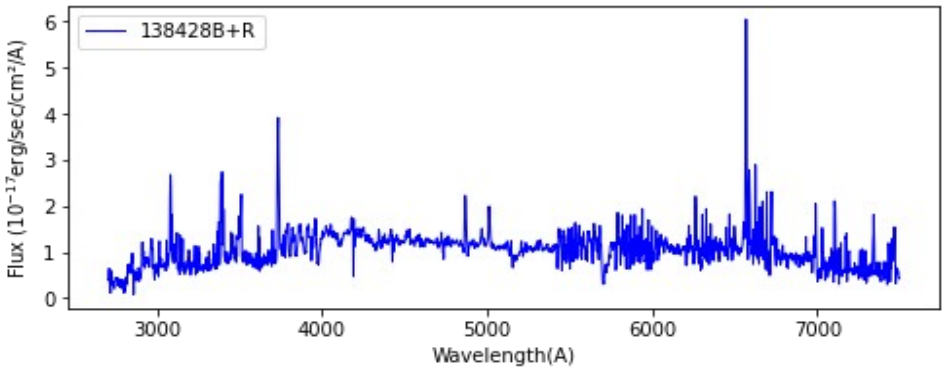

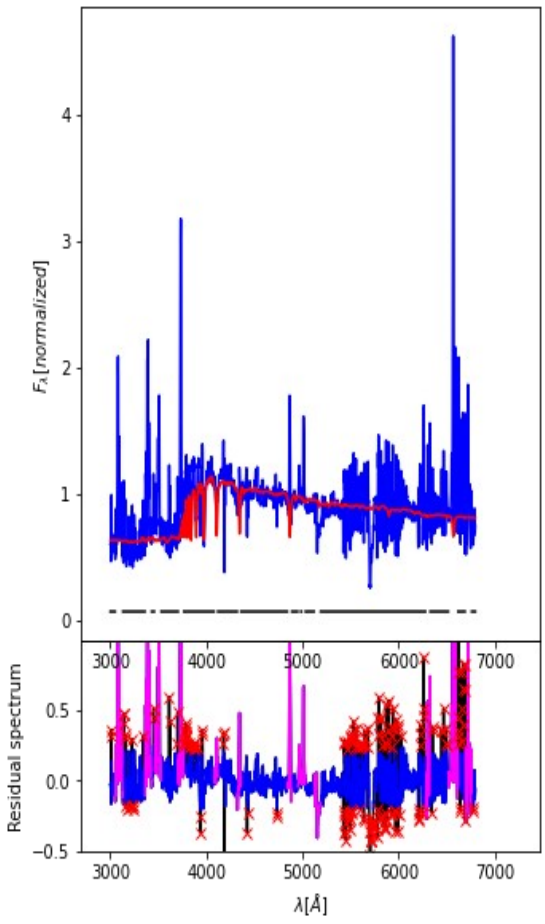

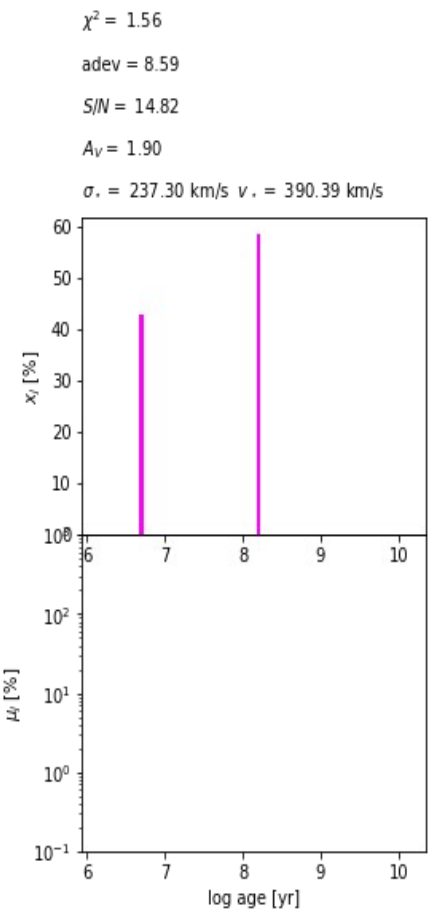

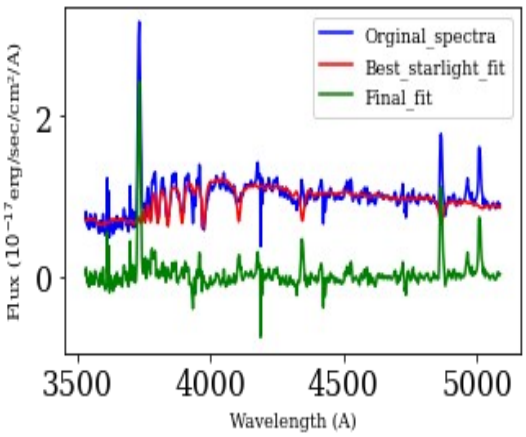

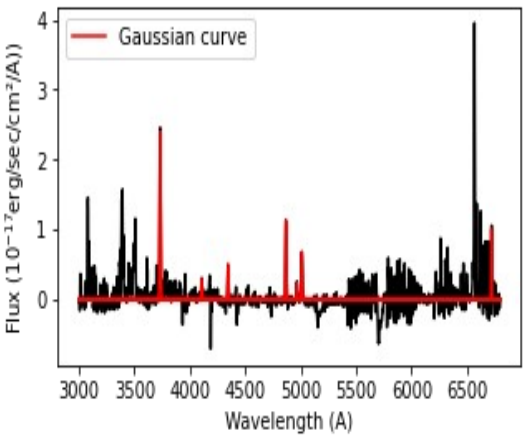

139918 (z_{spec} =0.4884)

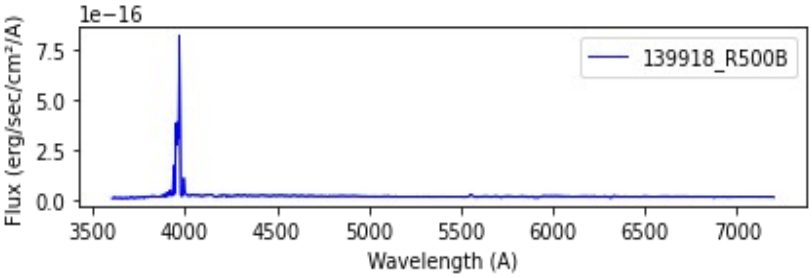

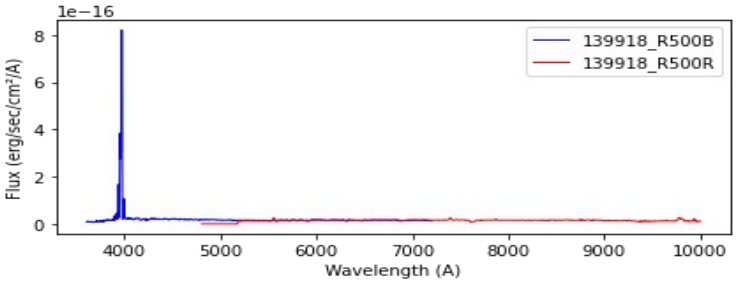

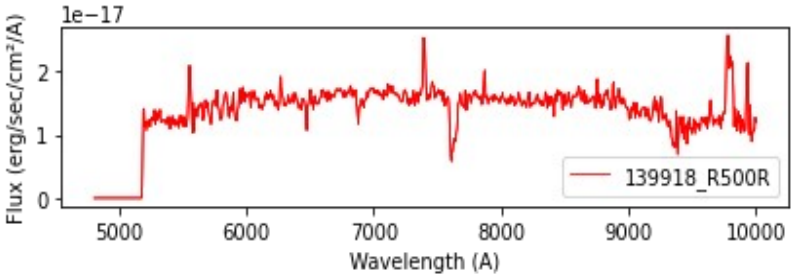

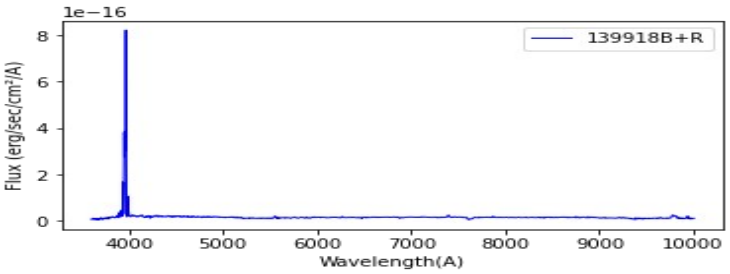

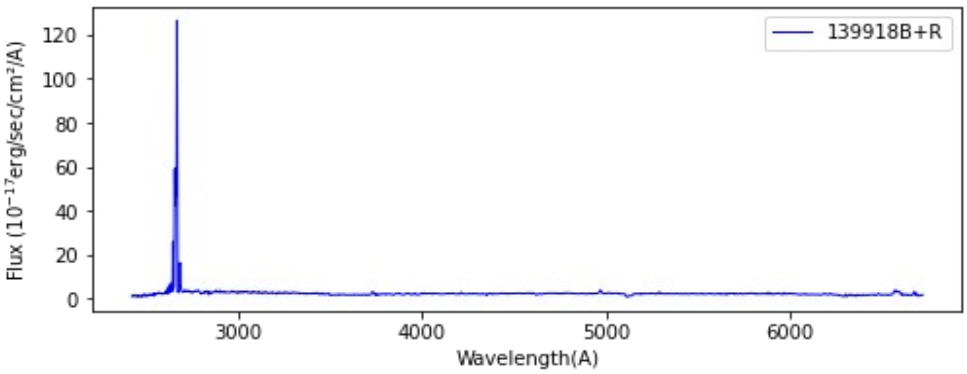

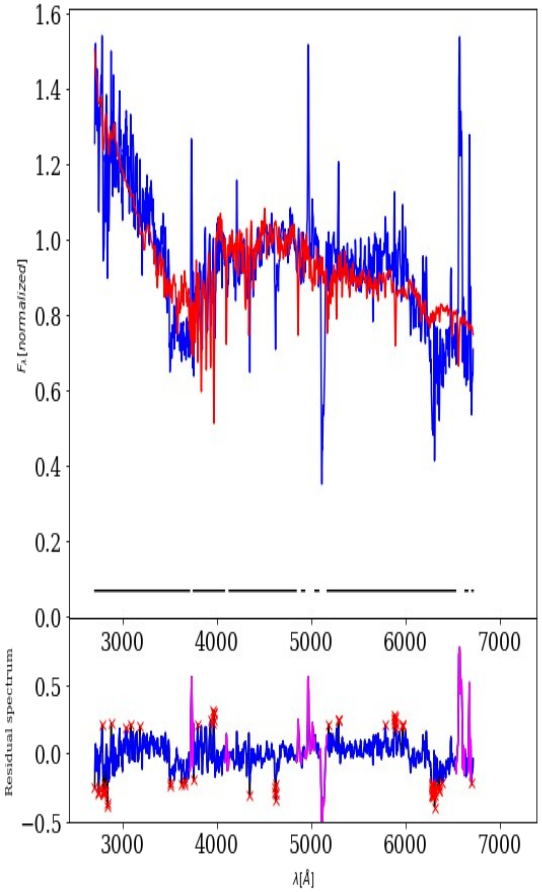

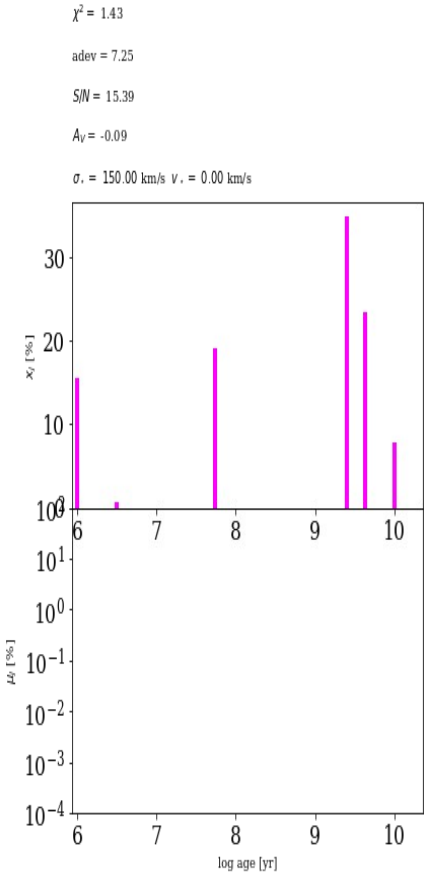

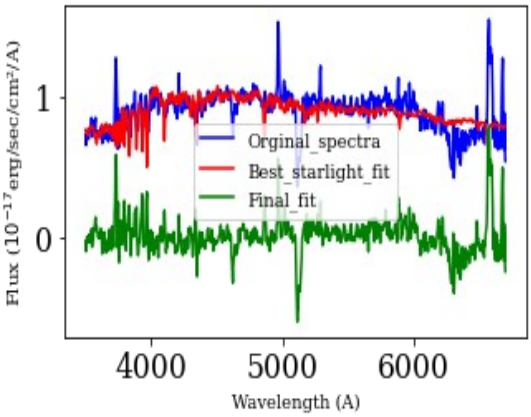

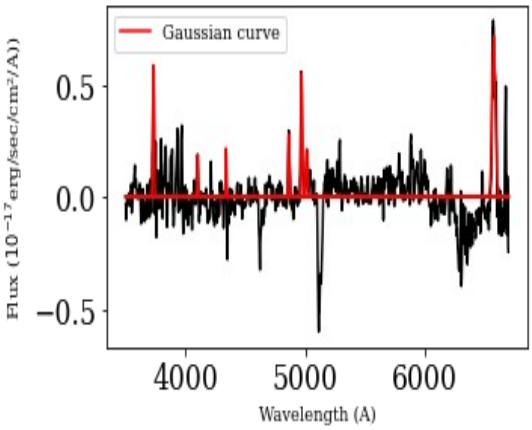

181067 (z_{spec} =0.1341)

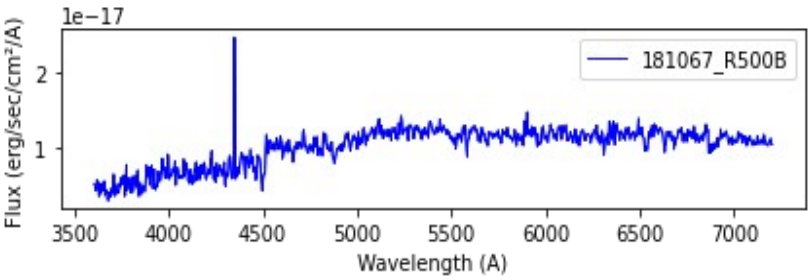

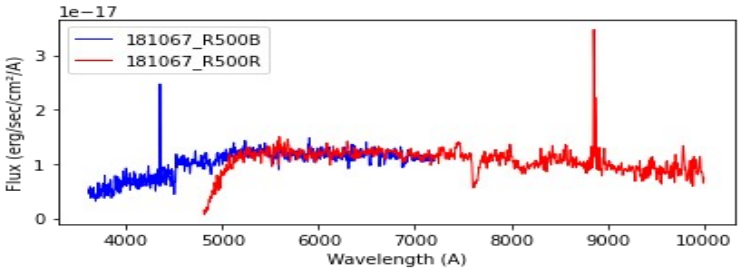

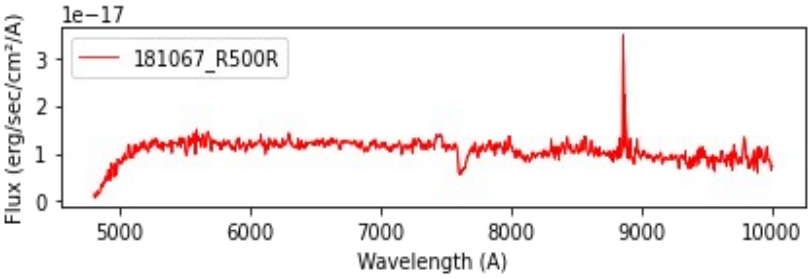

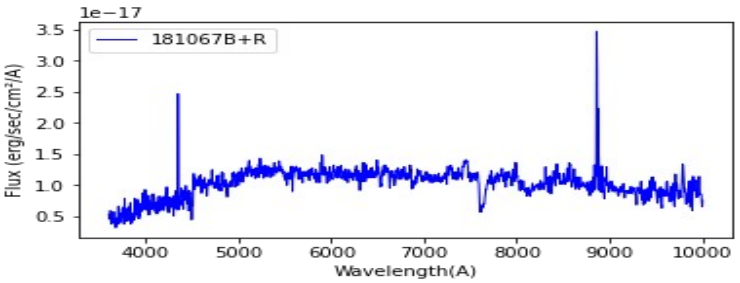

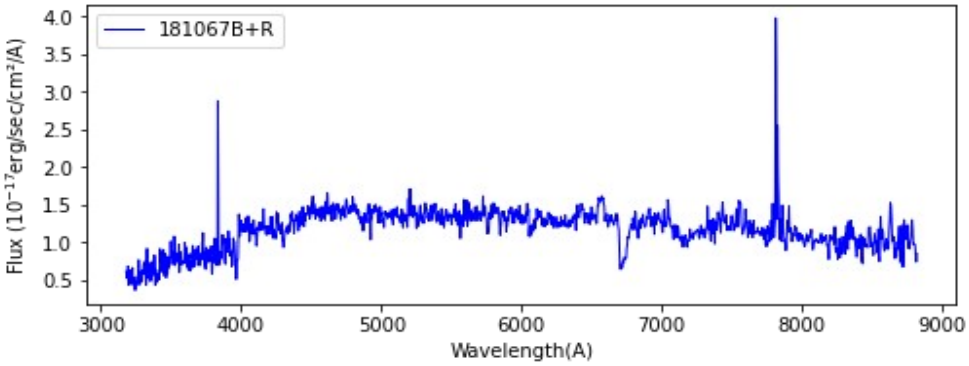

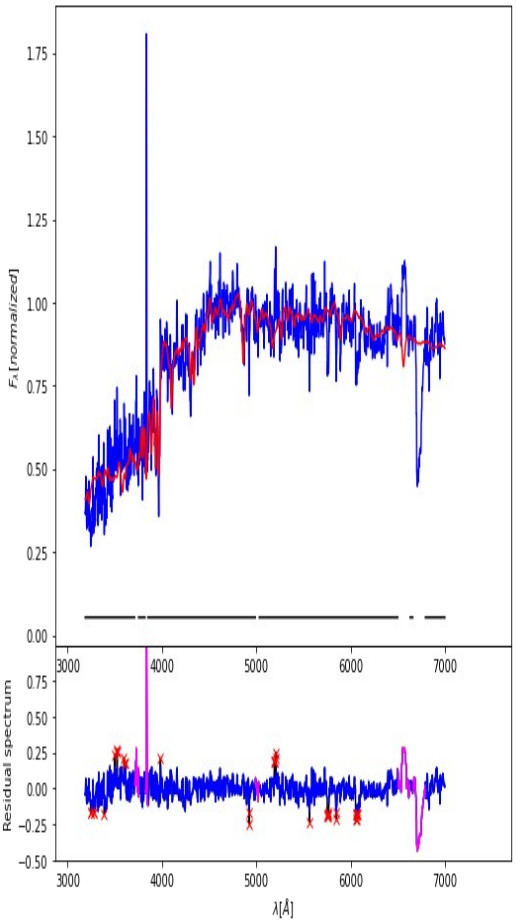

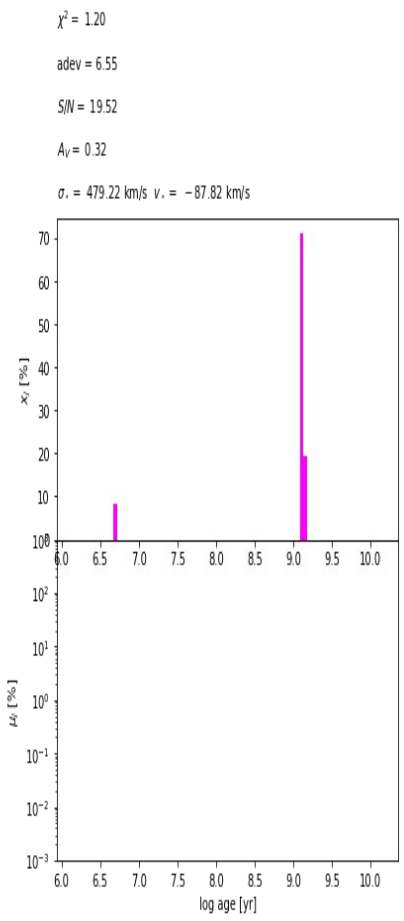

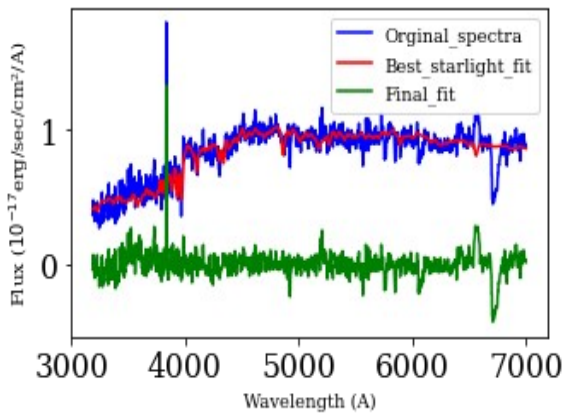

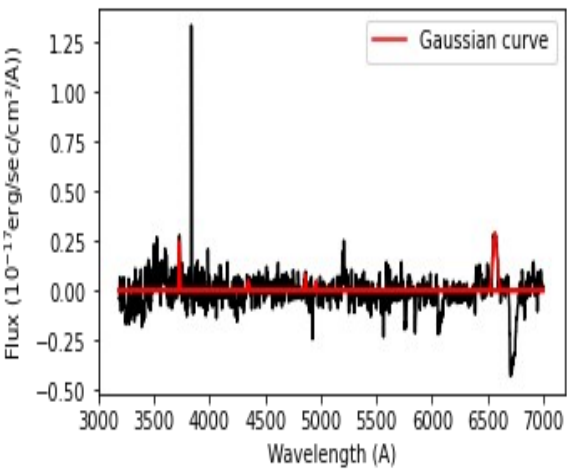

185864 (z_{spec} =0.3942)

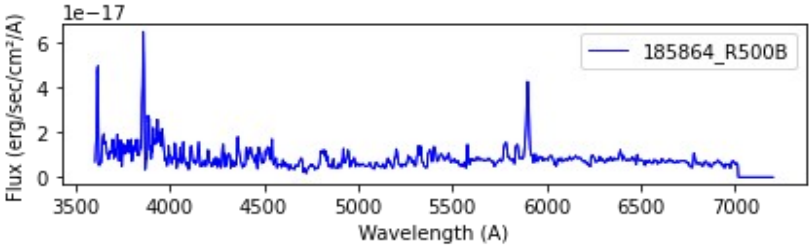

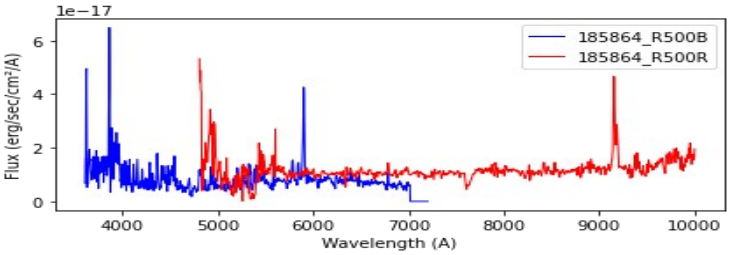

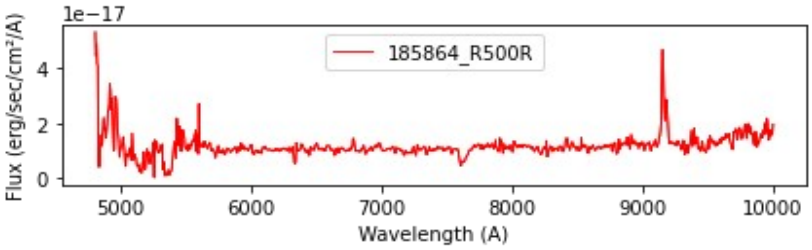

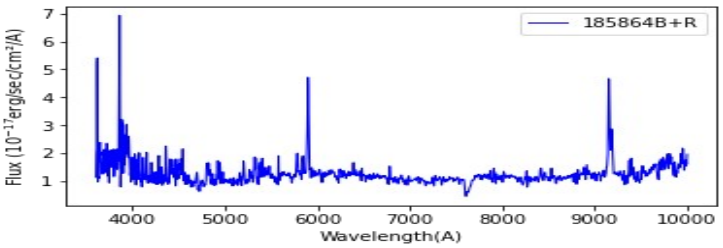

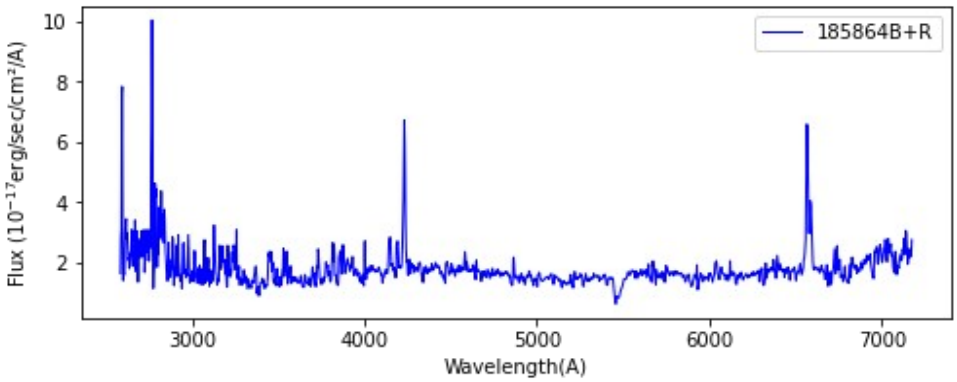

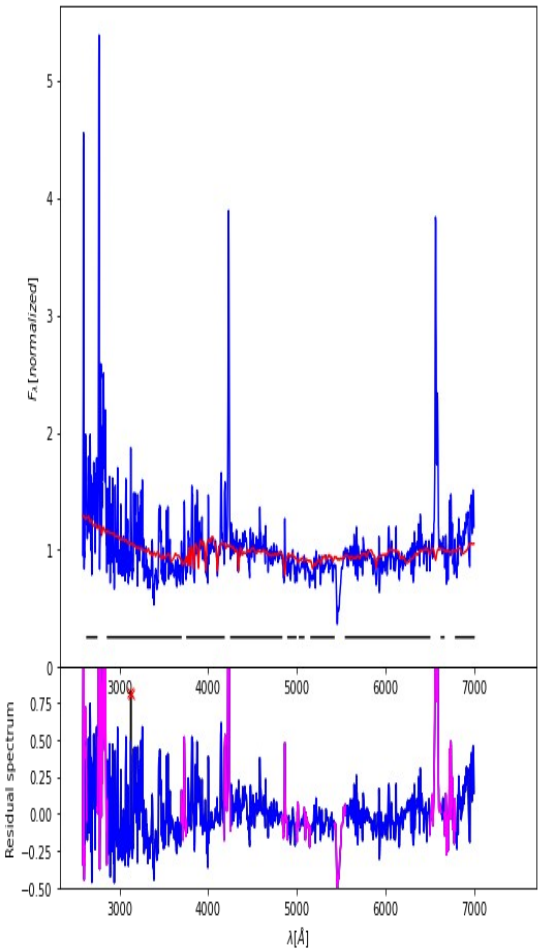

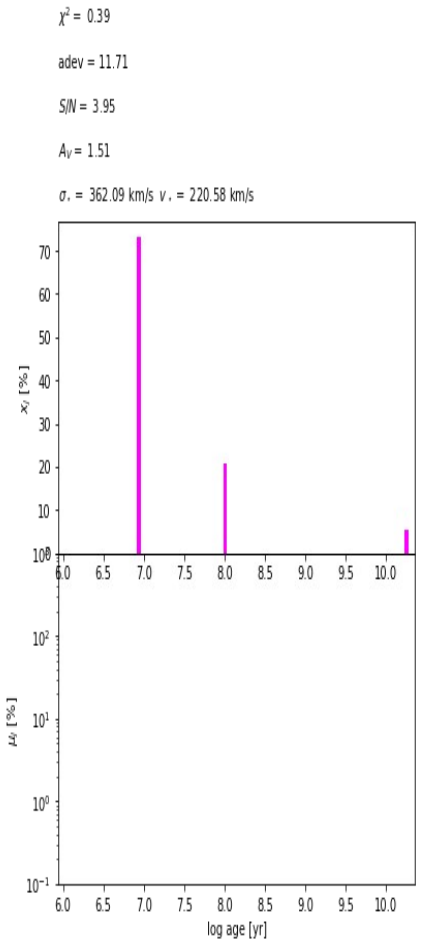

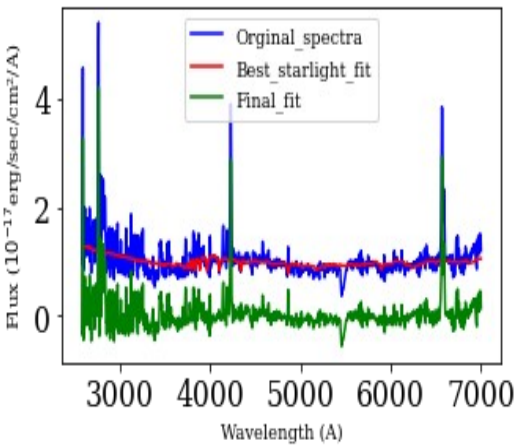

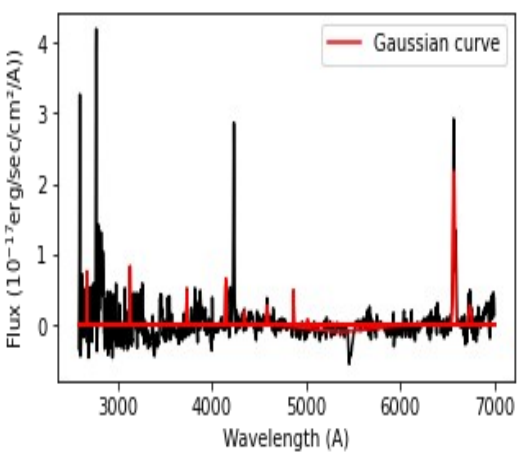

206401 (z_{spec} =1.3363)

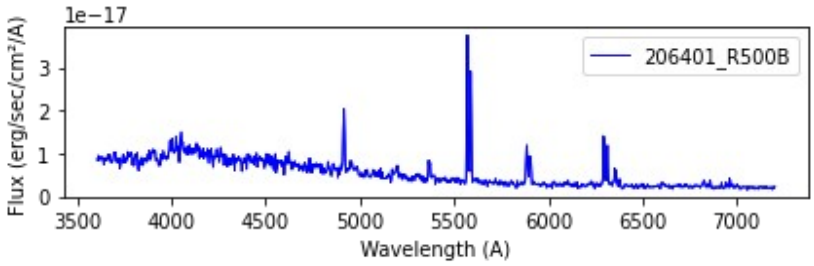

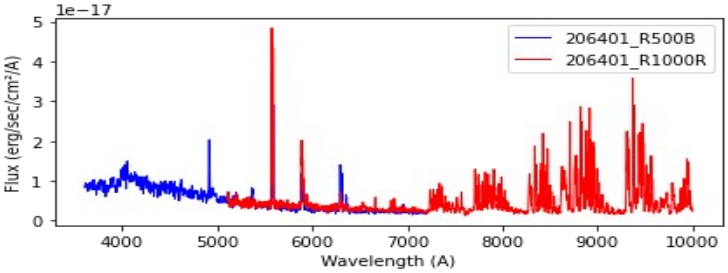

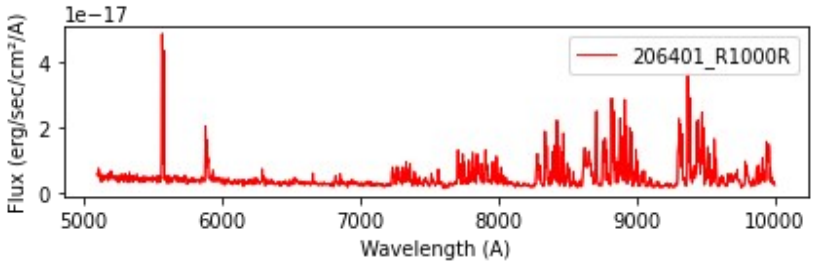

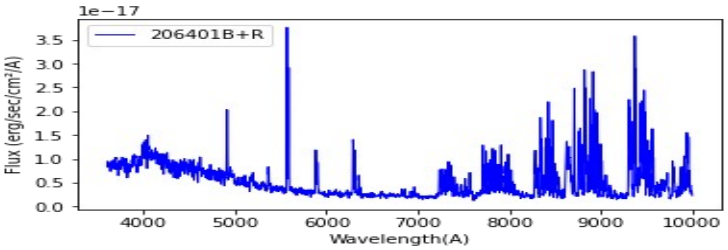

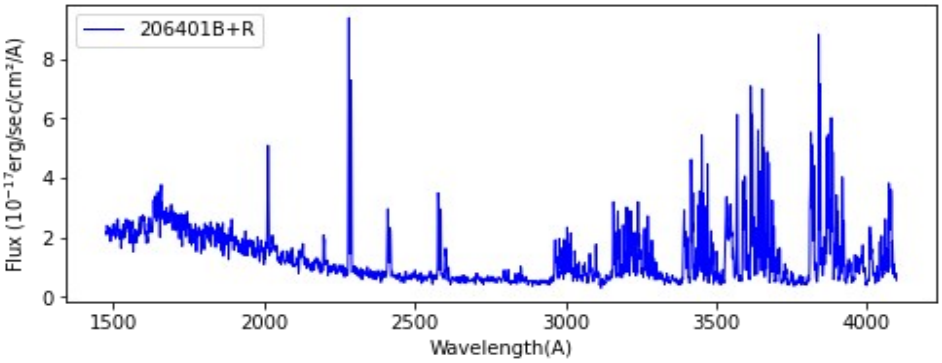

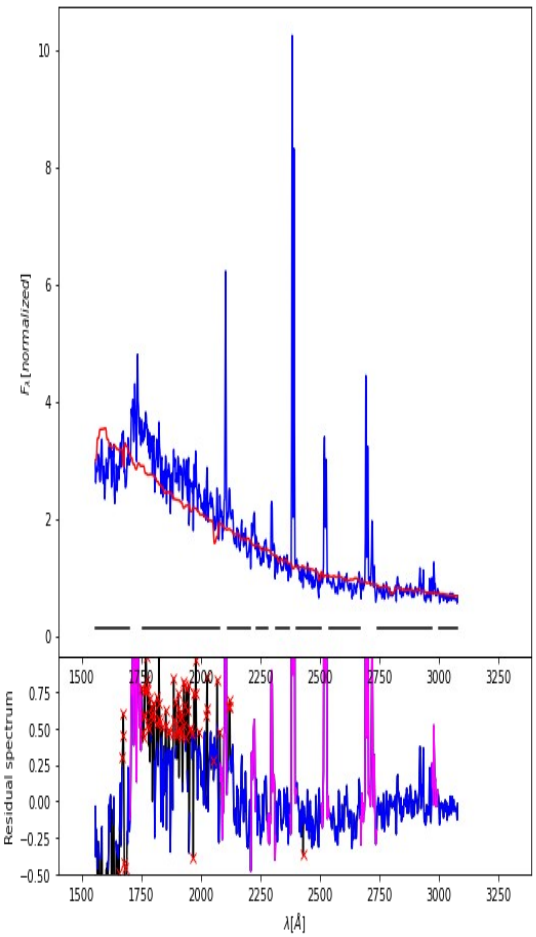

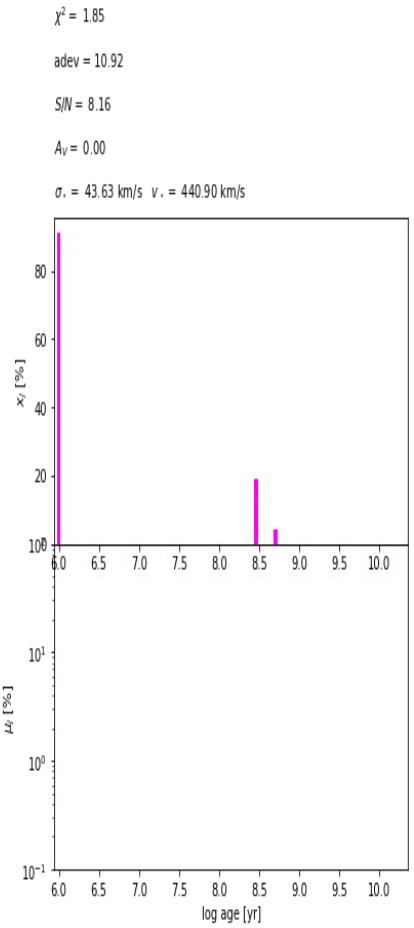

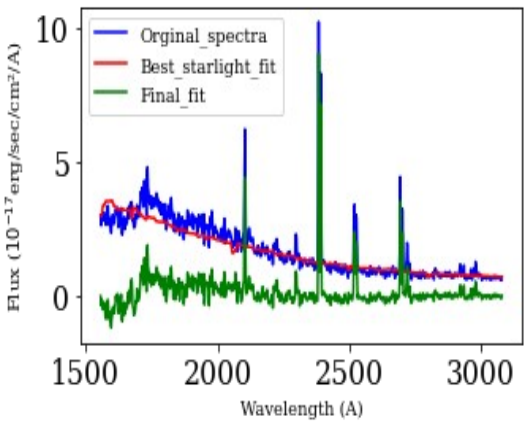

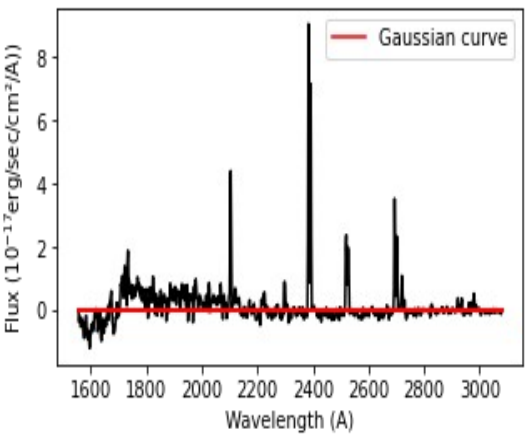

206406 (z_{spec} =0.711)

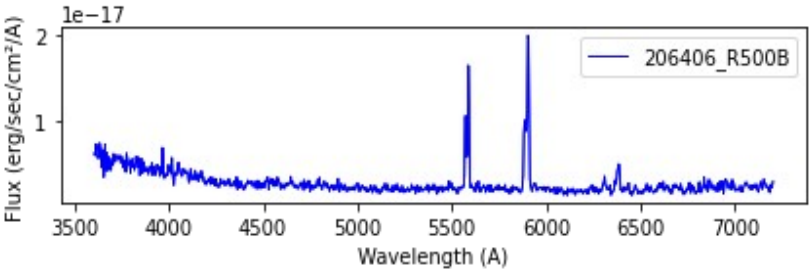

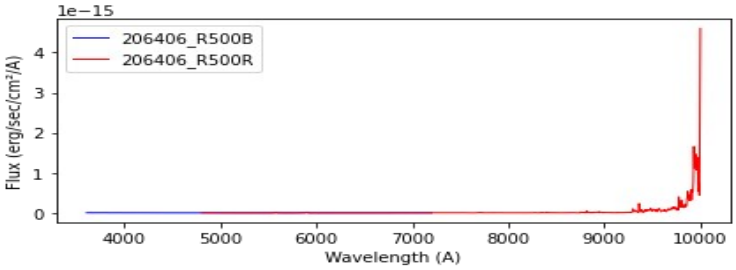

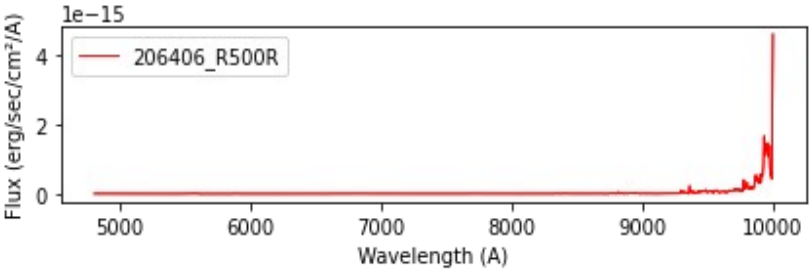

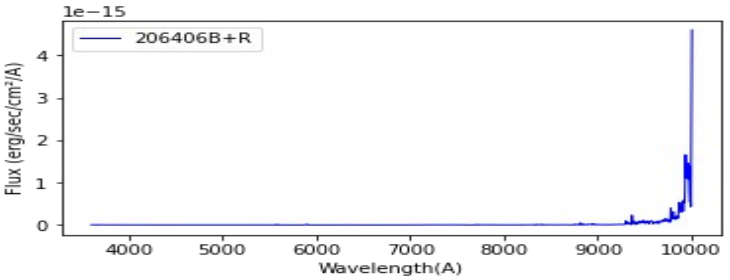

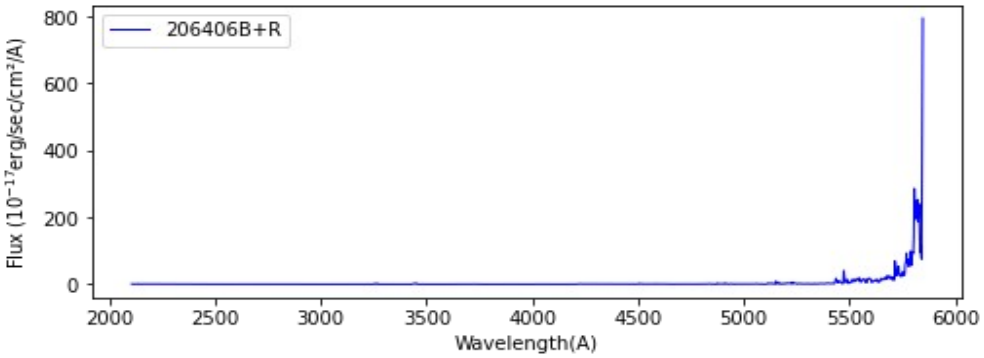

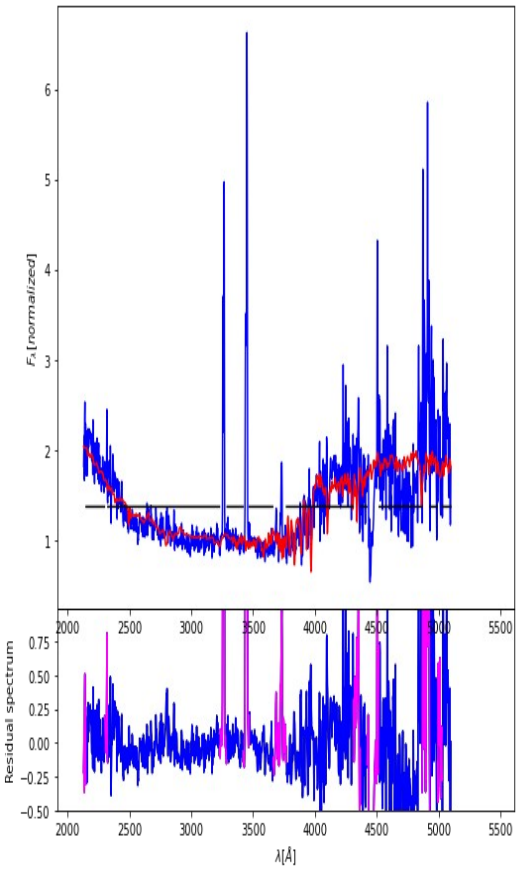

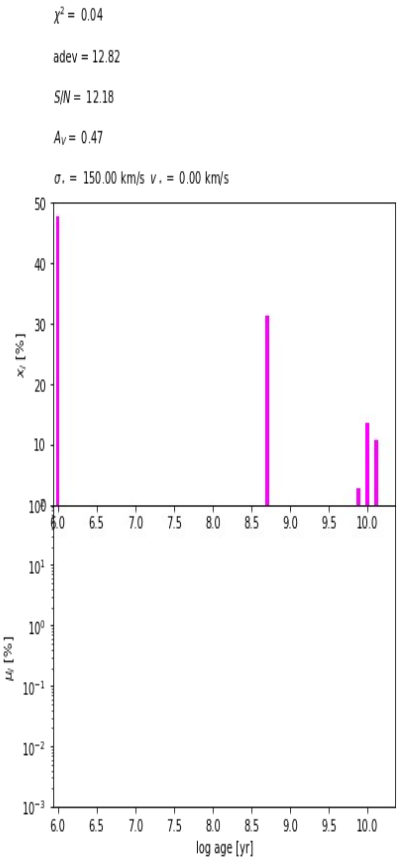

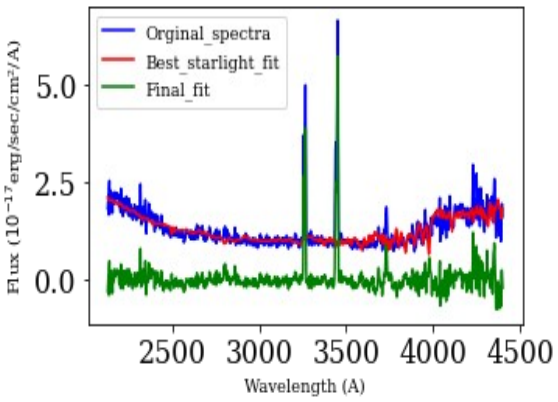

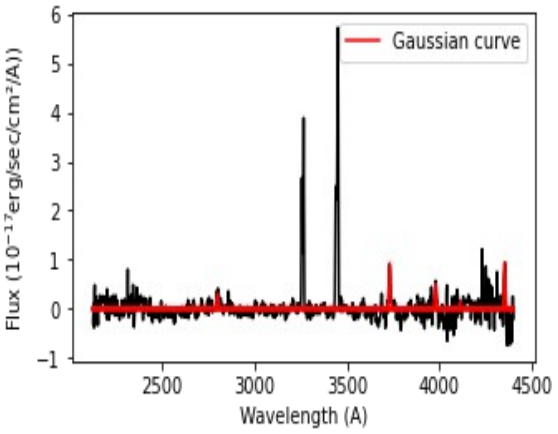

206418 (z_{spec} =0.4529)

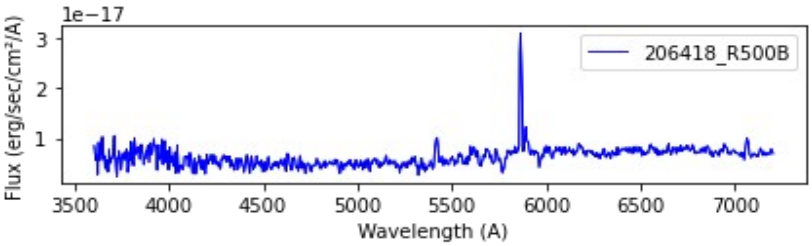

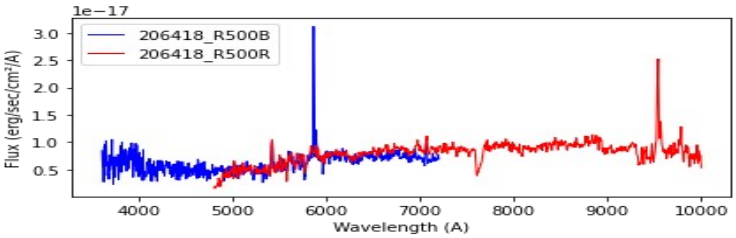

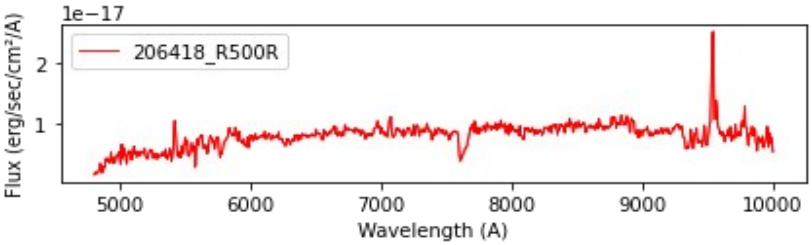

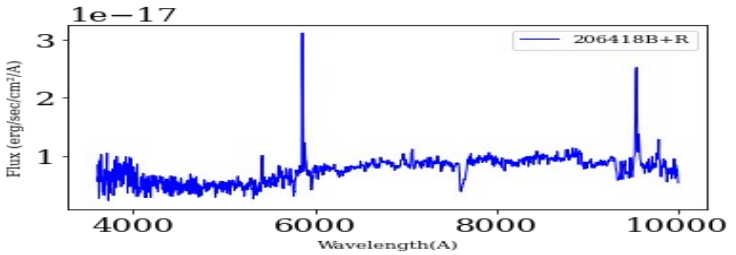

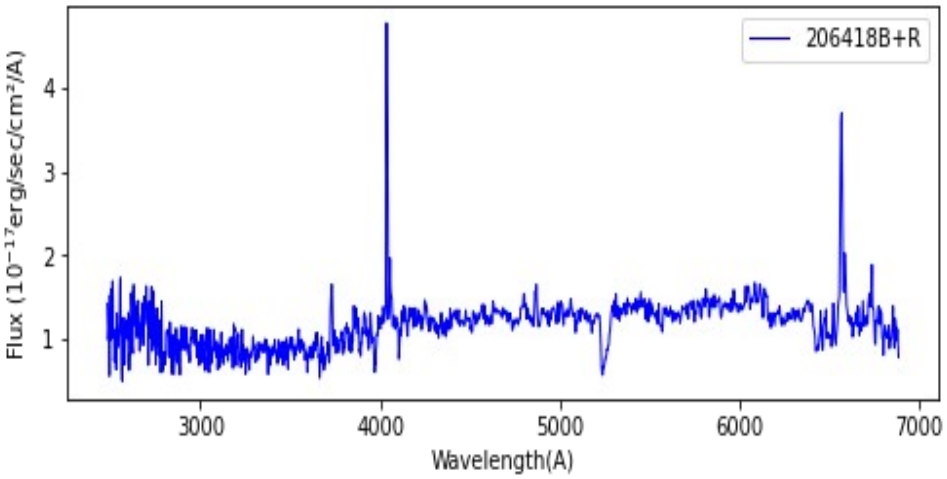

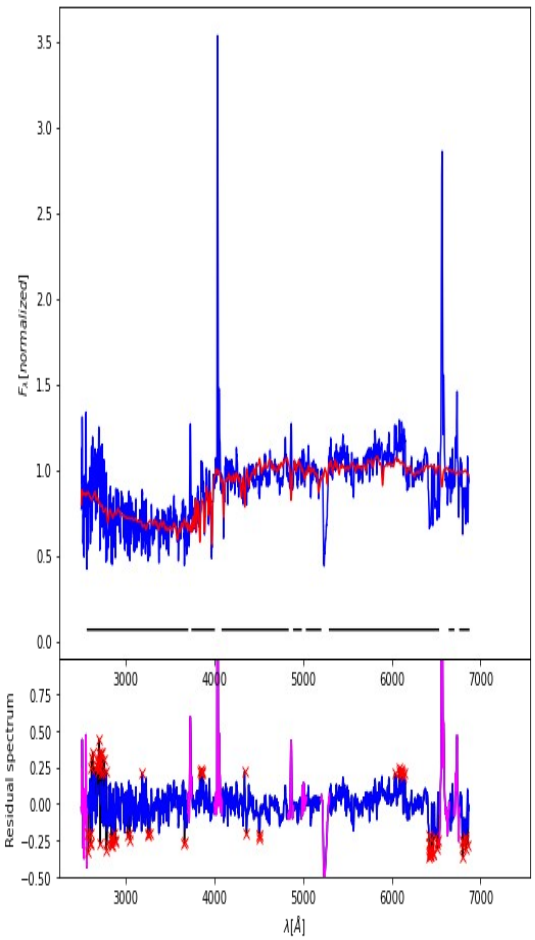

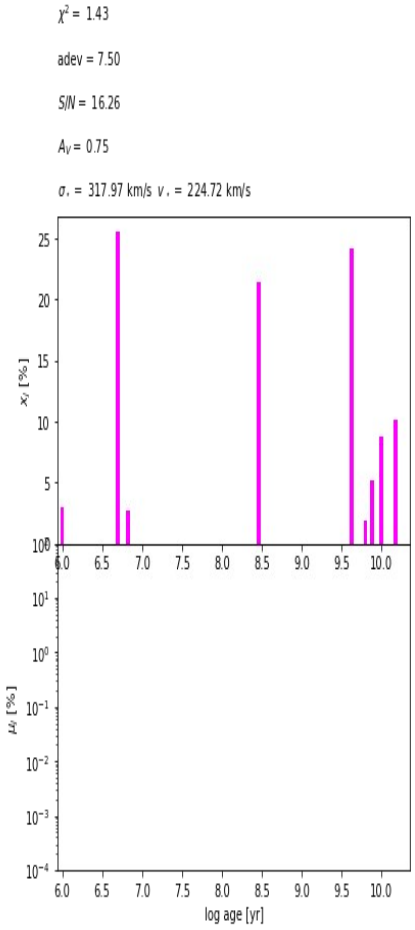

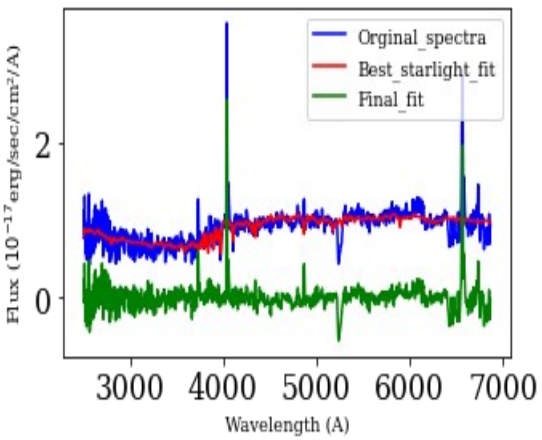

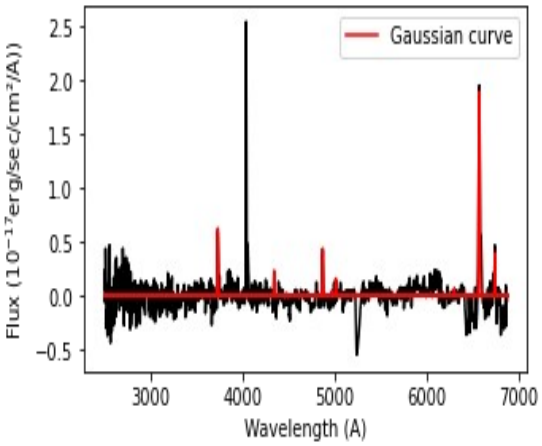

206425 (z_{spec} =0.3636)

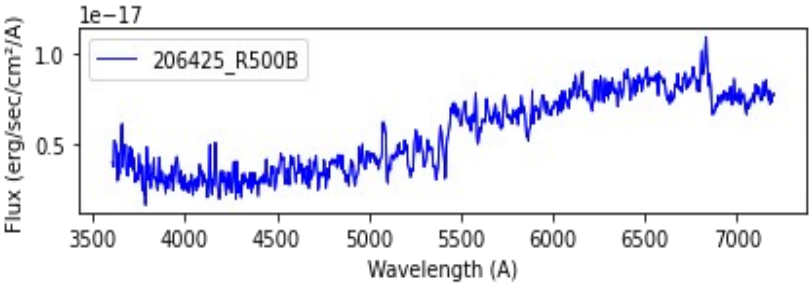

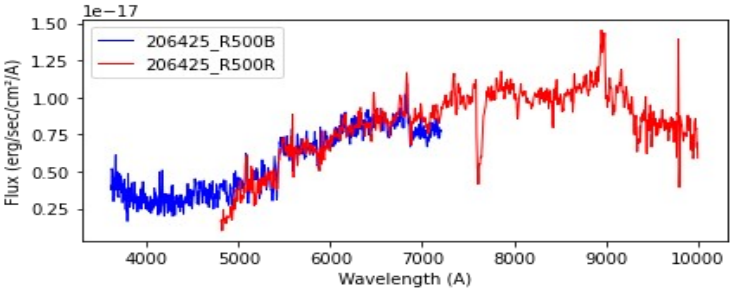

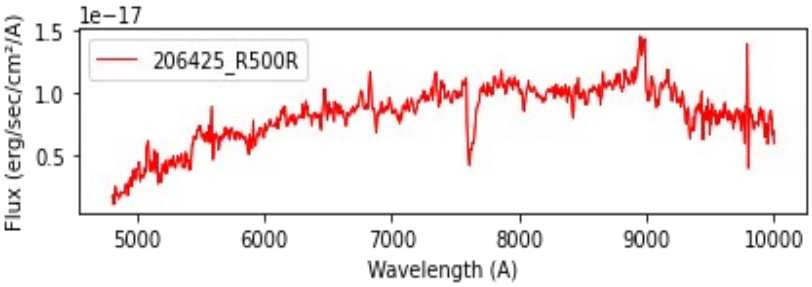

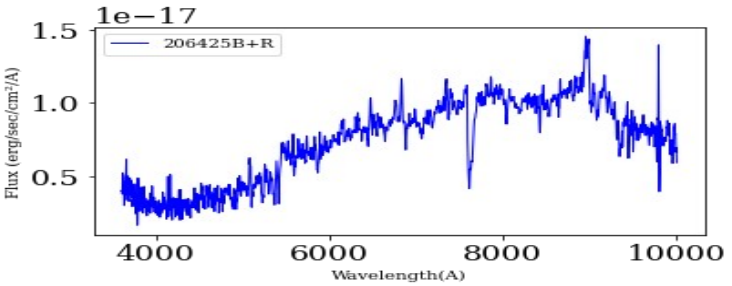

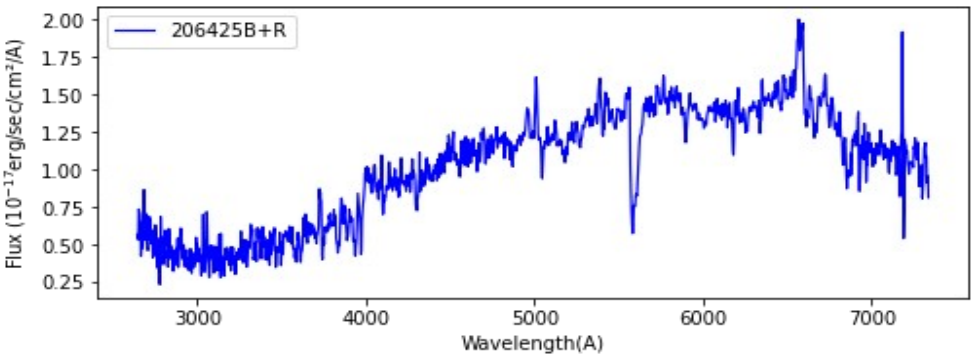

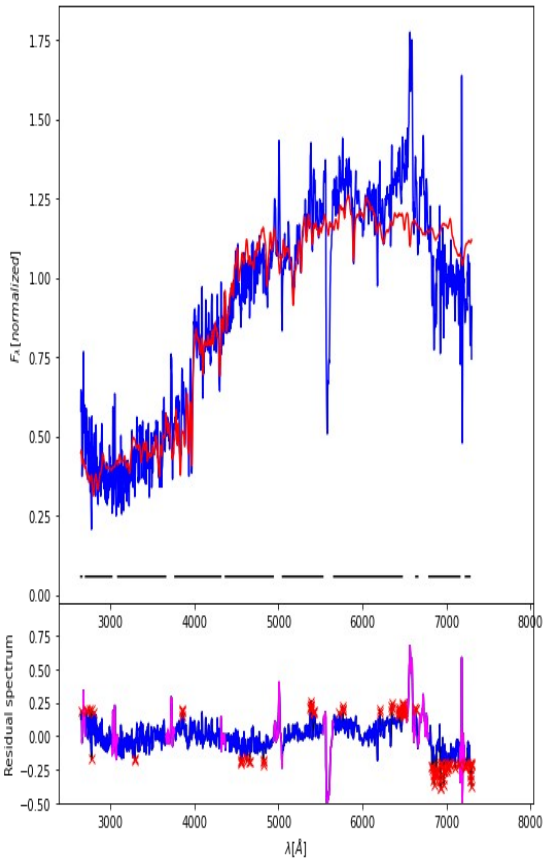

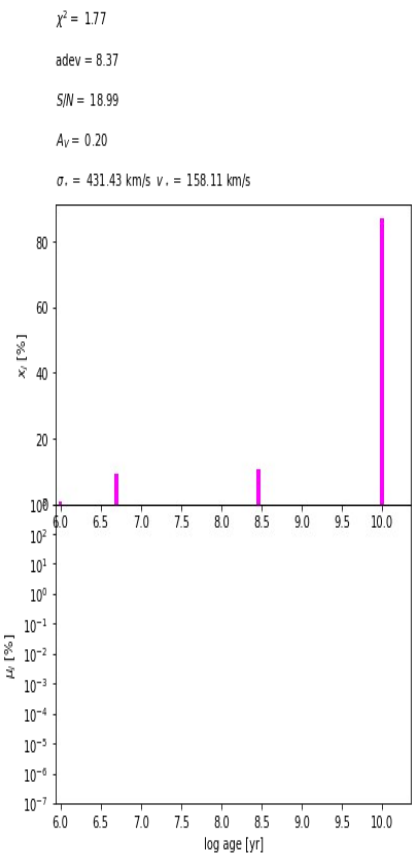

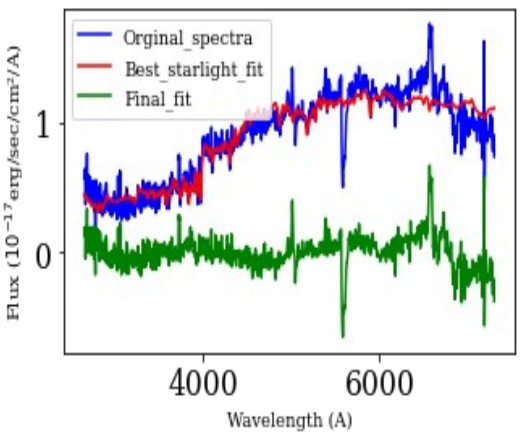

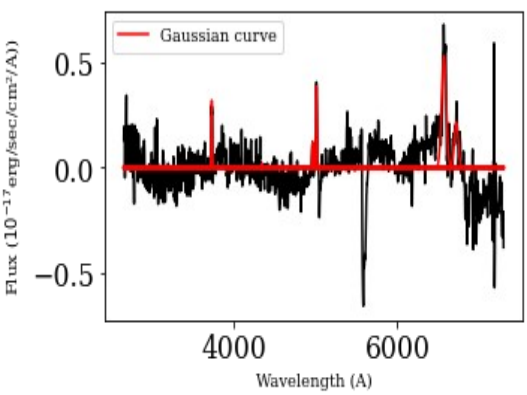

206434 (z_{spec} =1.018)

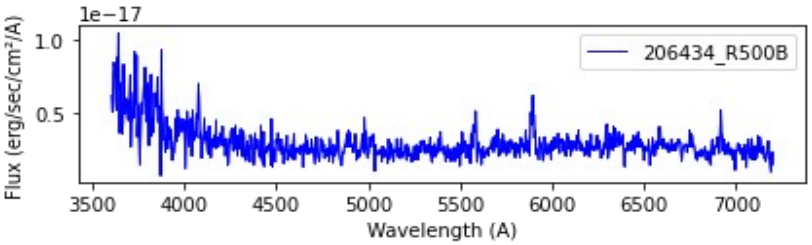

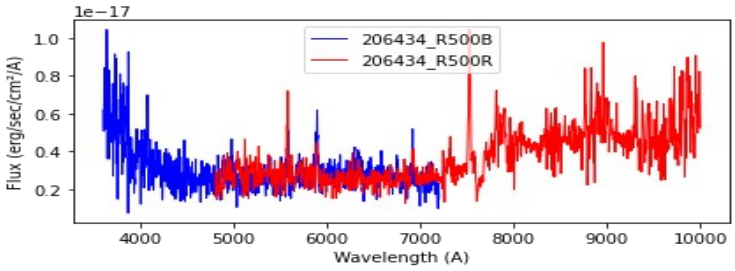

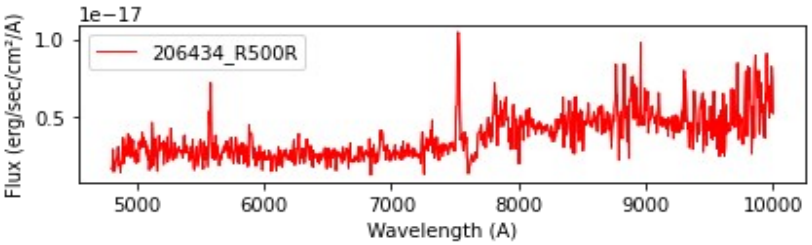

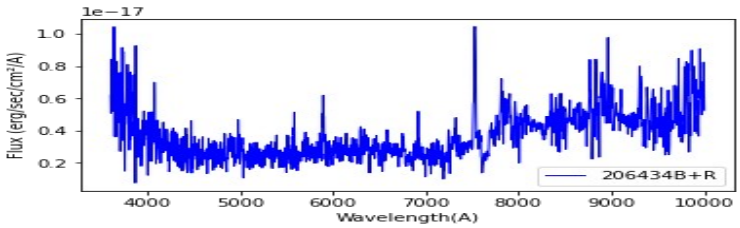

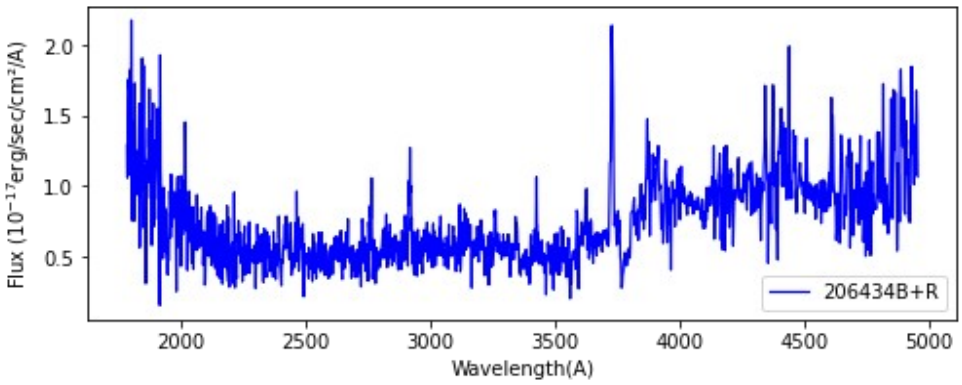

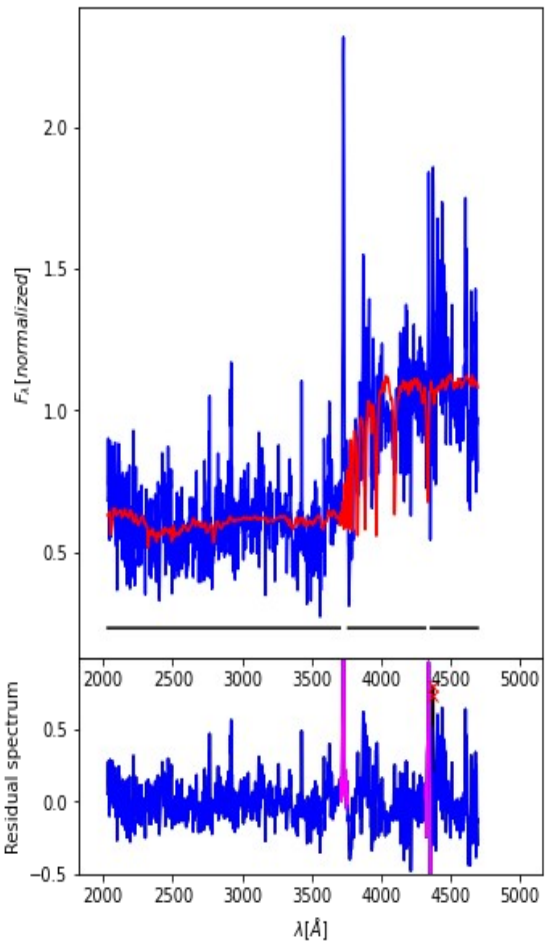

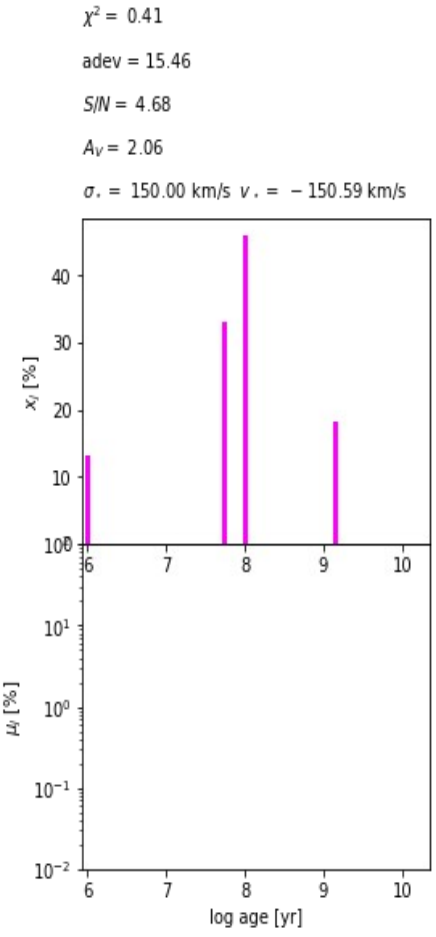

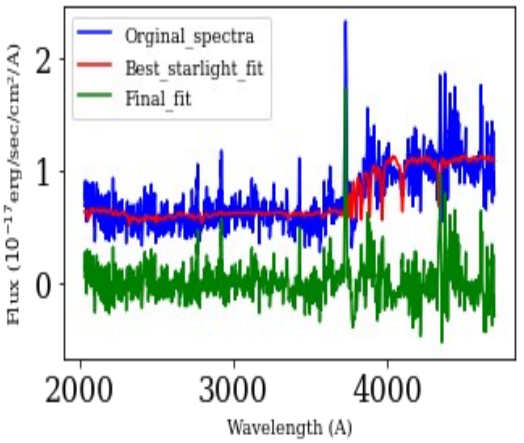

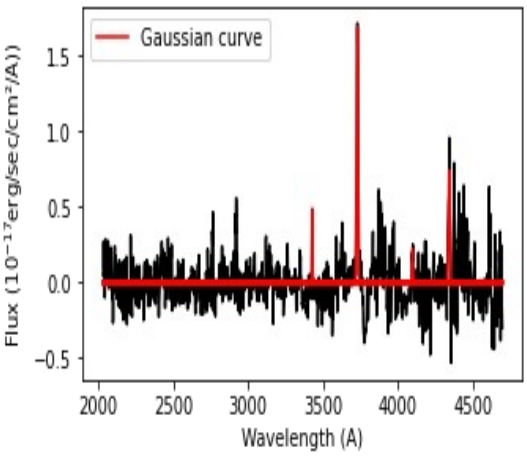

206447 (z_{spec} =0.8087)

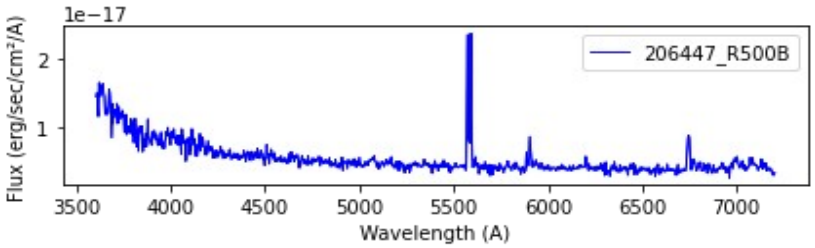

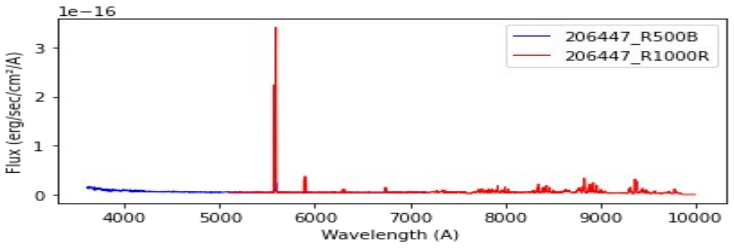

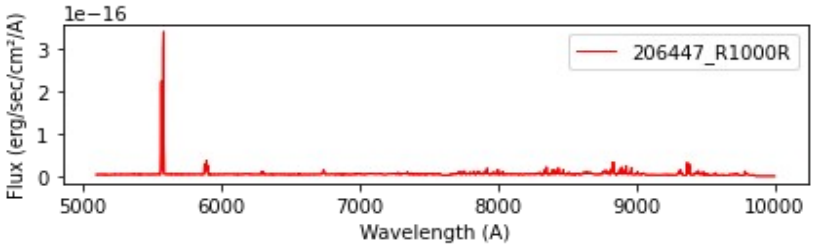

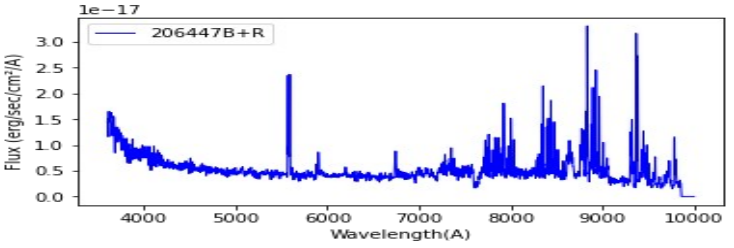

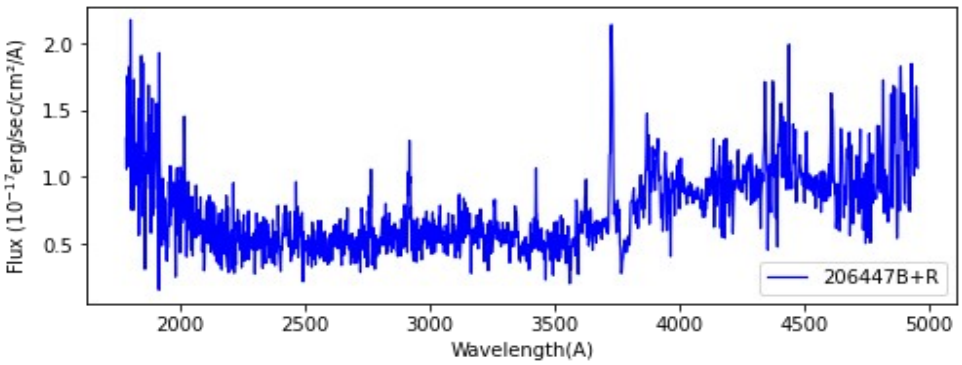

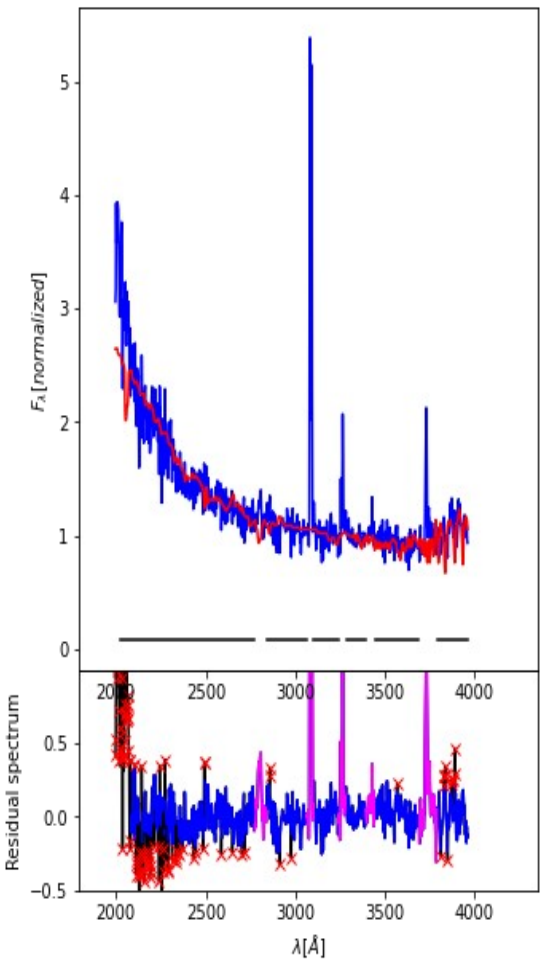

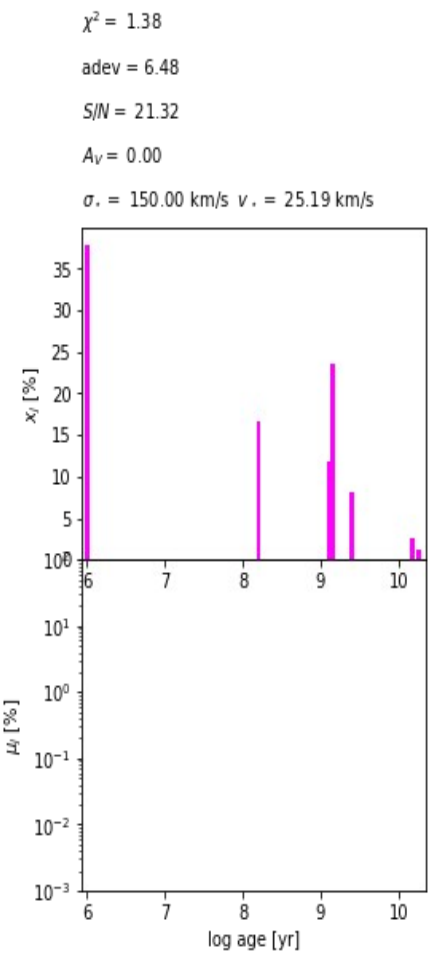

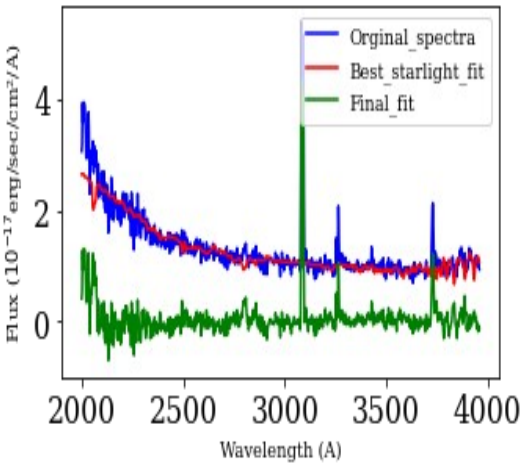

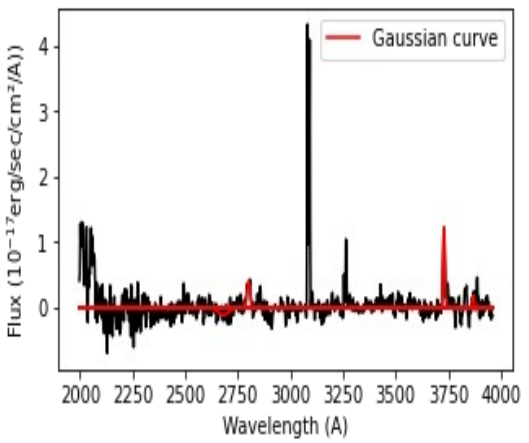

206474 (z_{spec} =0.503)

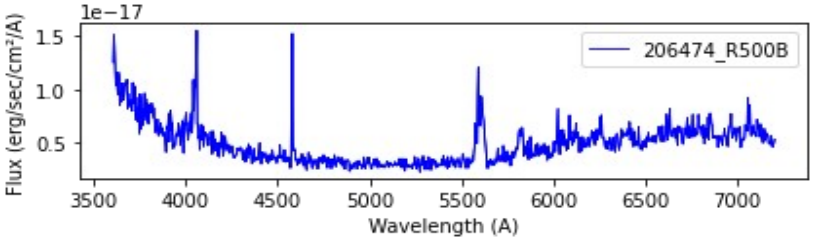

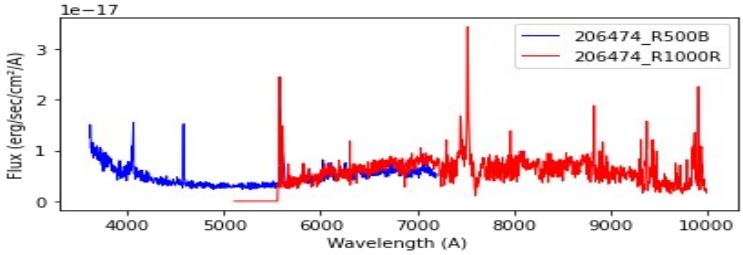

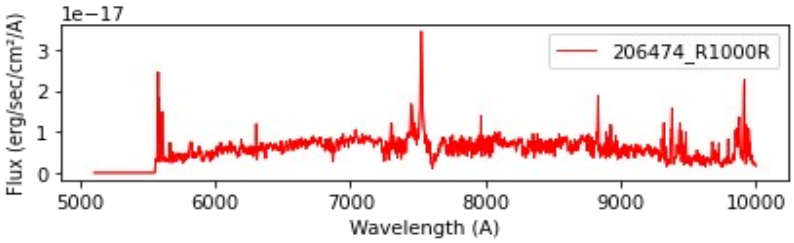

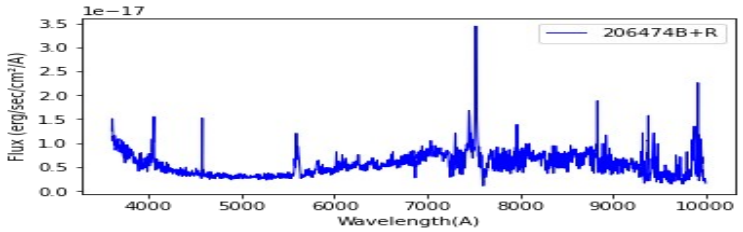

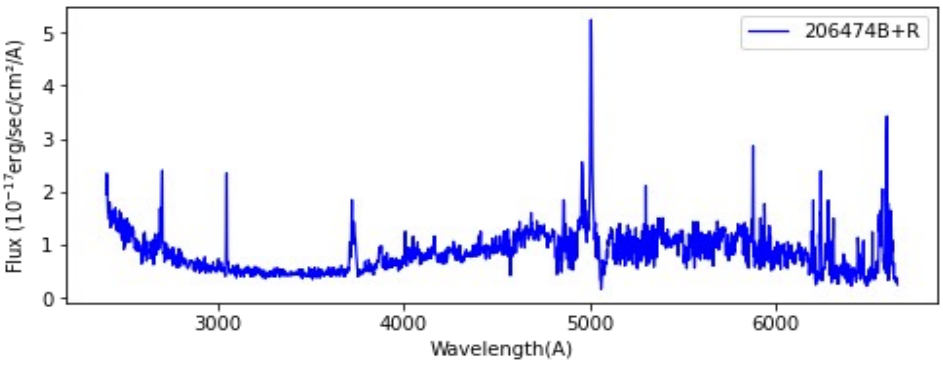

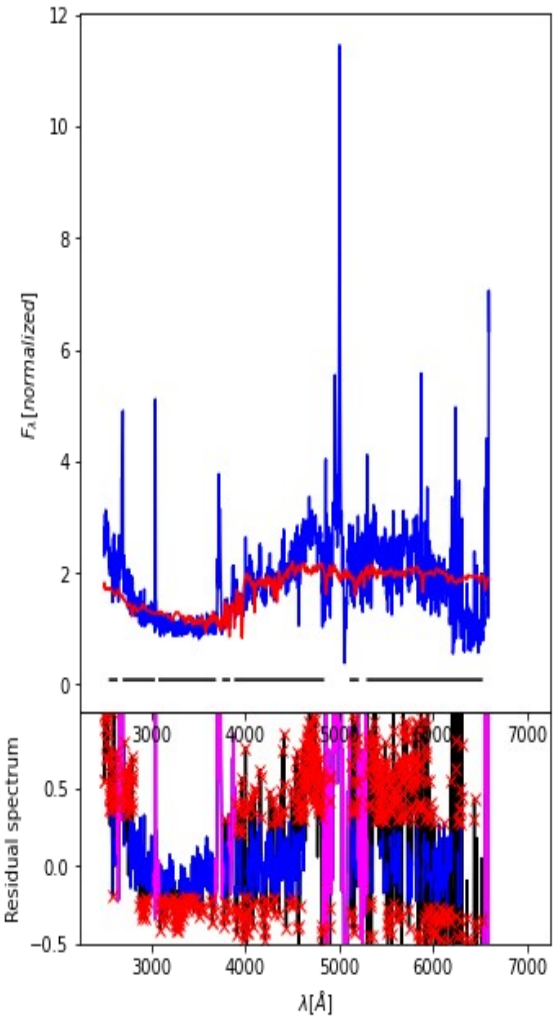

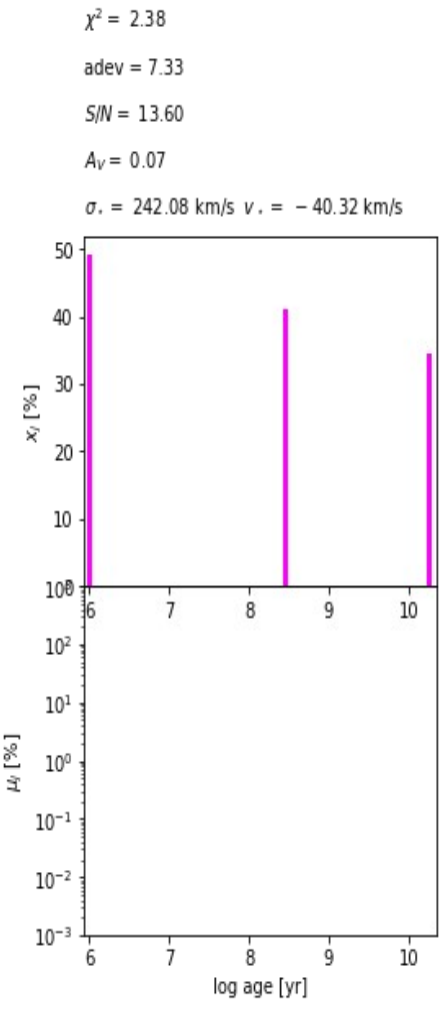

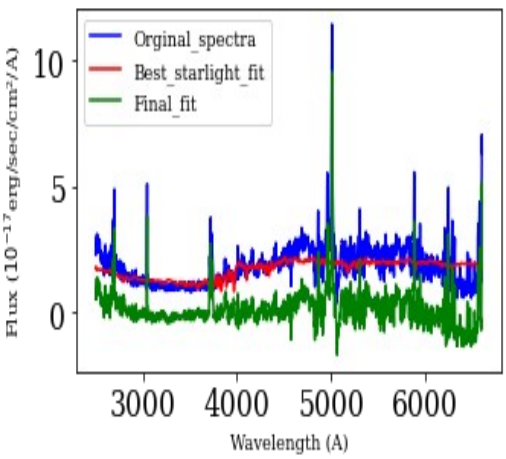

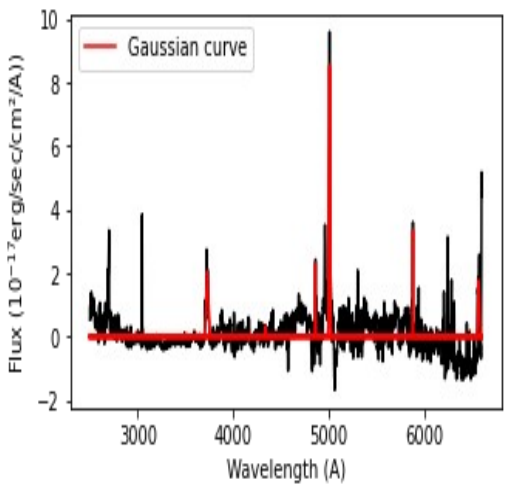

206490 (z_{spec} =0.2055)

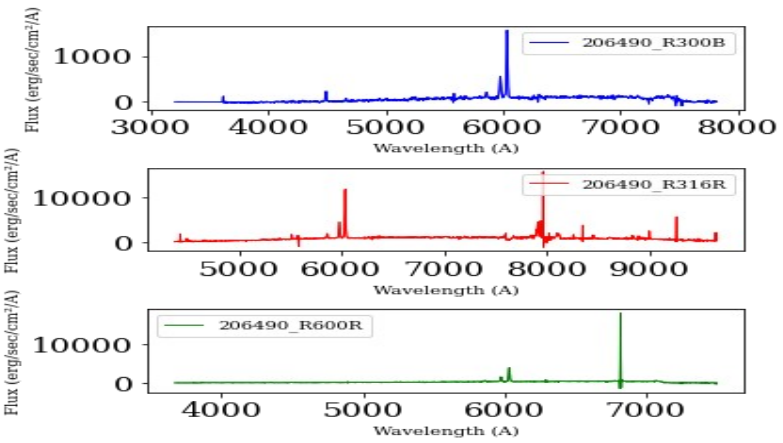

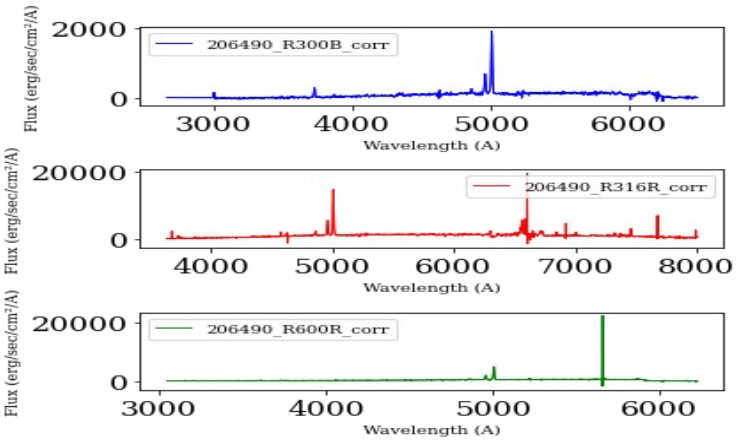

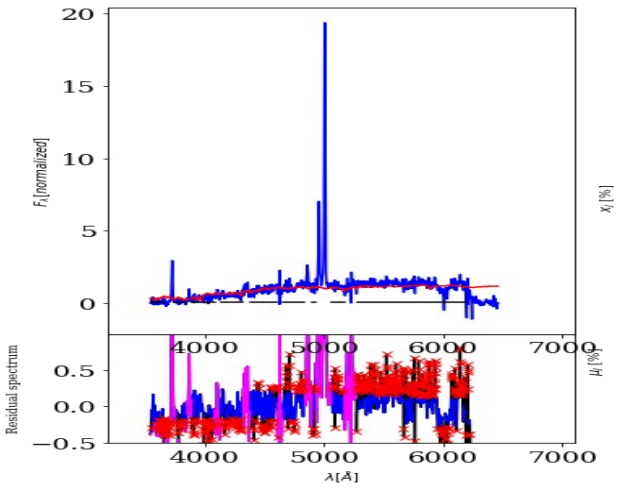

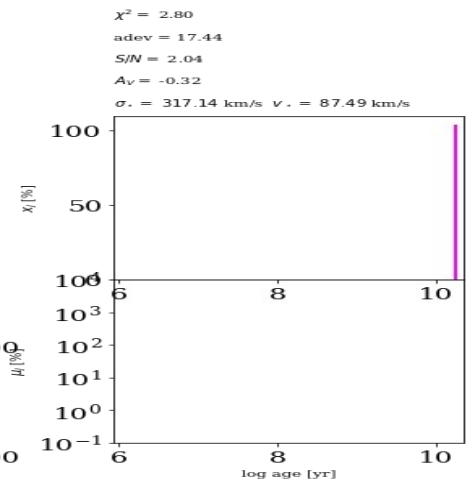

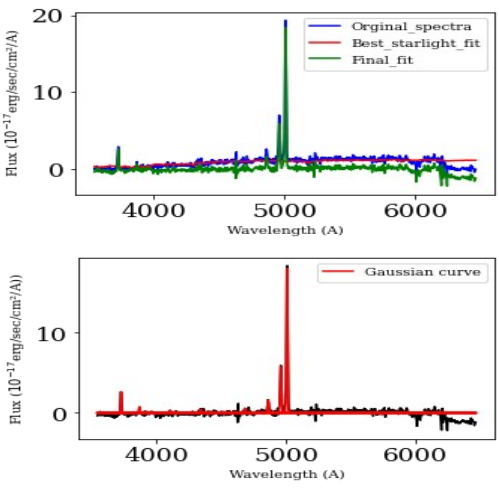

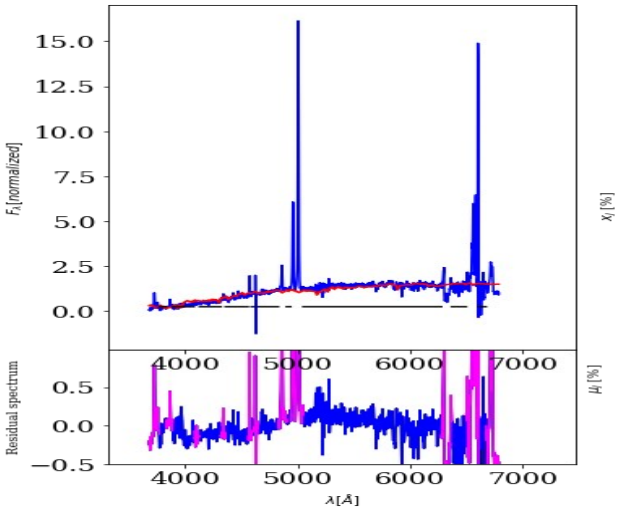

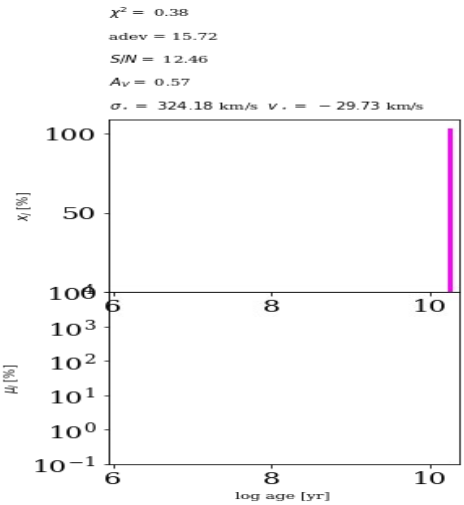

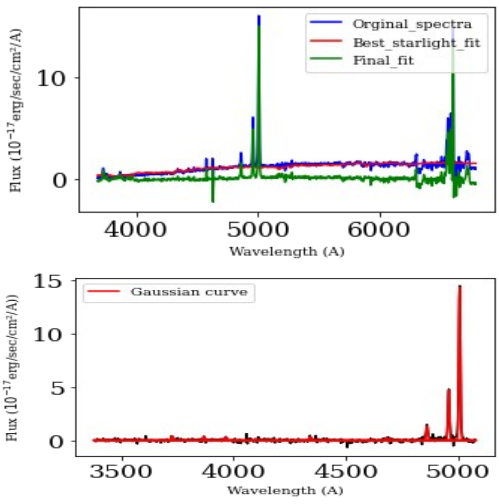

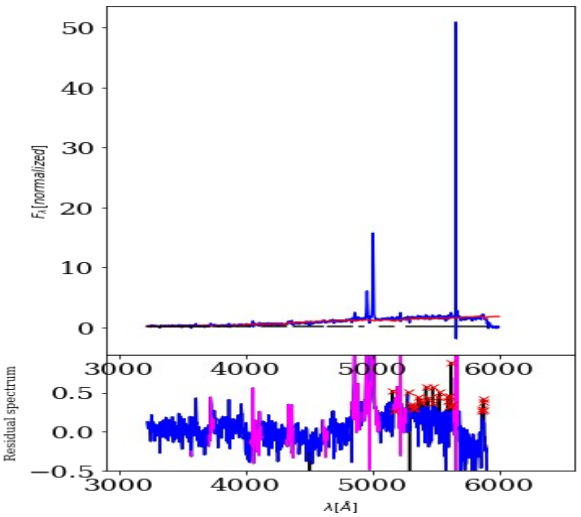

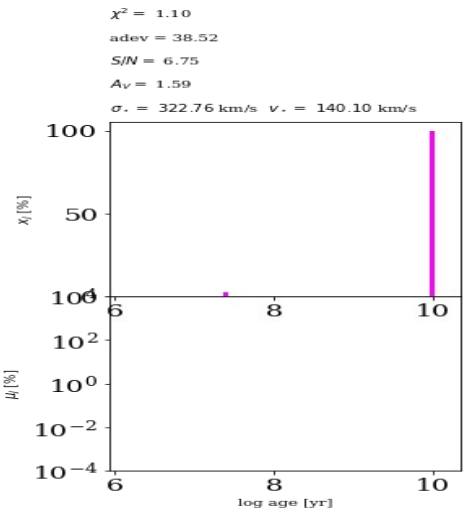

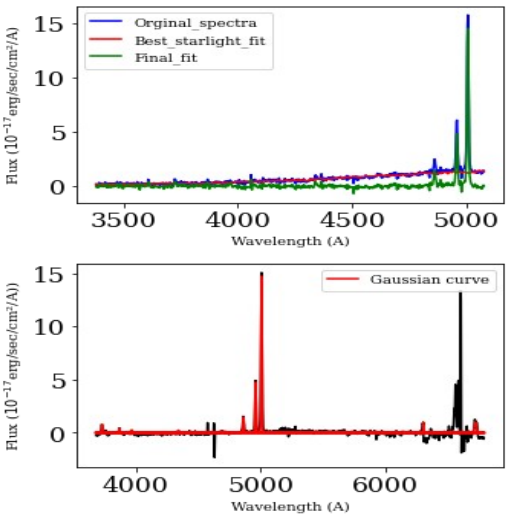

206501 (z_{spec} =0.758)

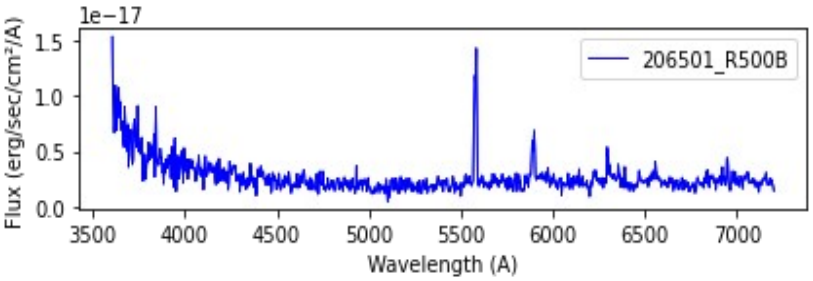

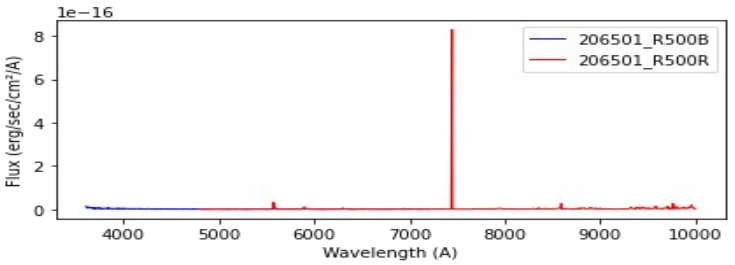

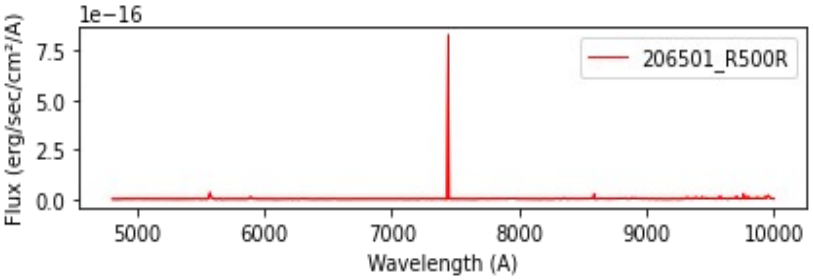

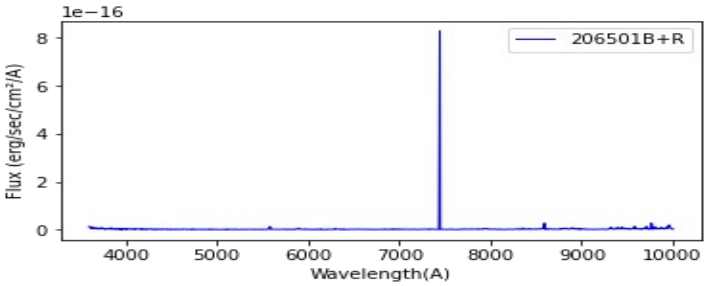

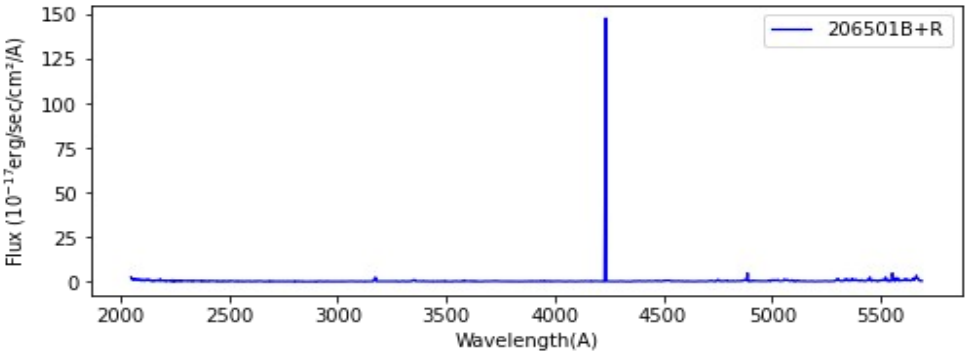

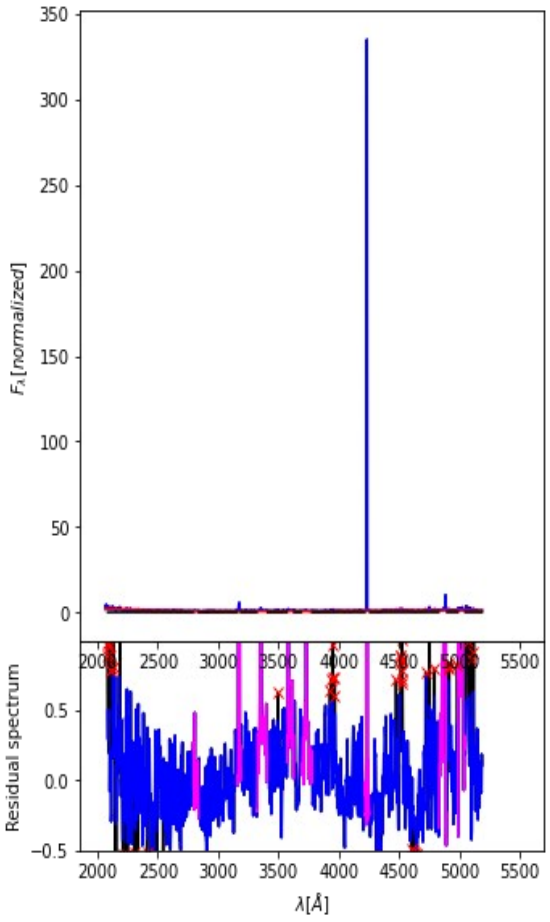

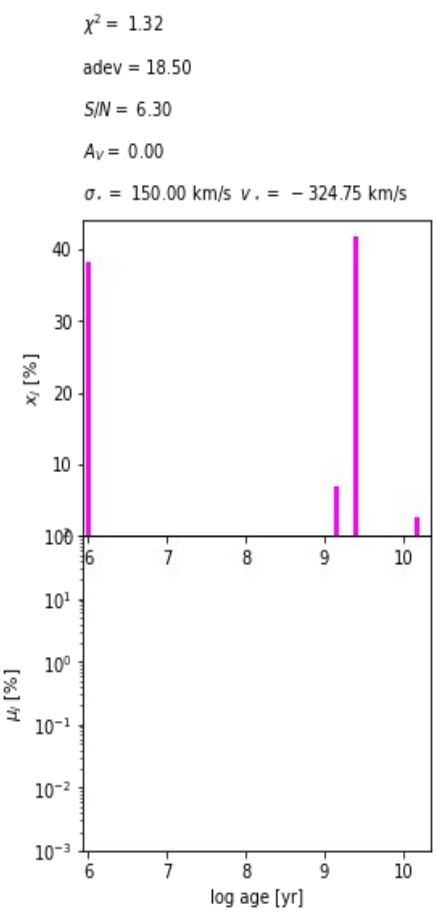

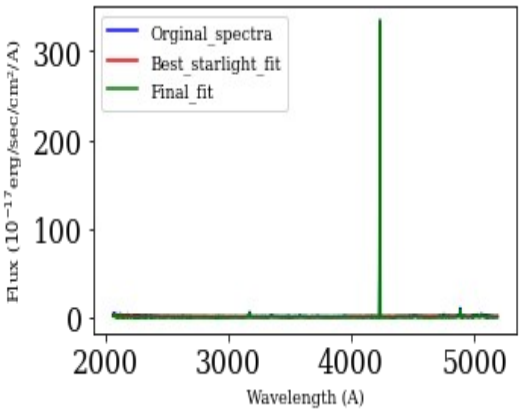

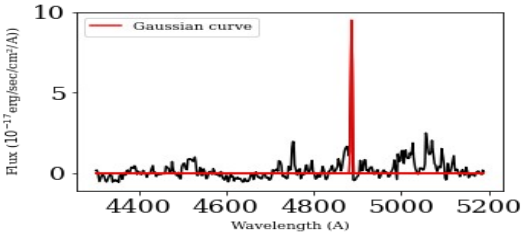

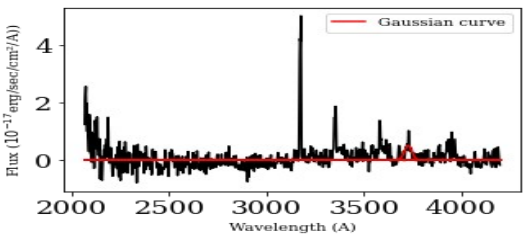

206511 (z_{spec} =0.353)

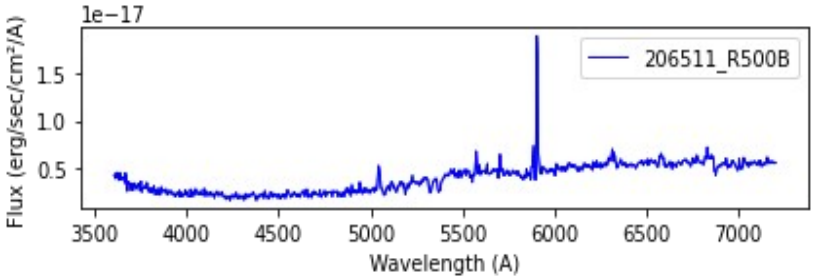

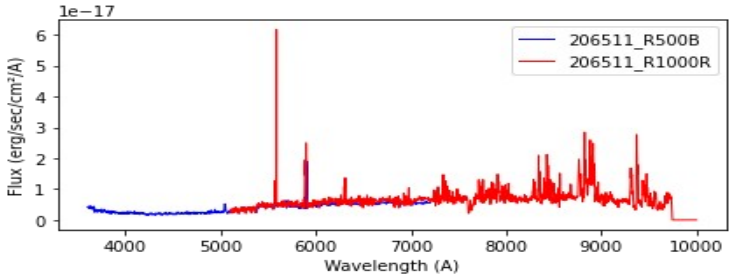

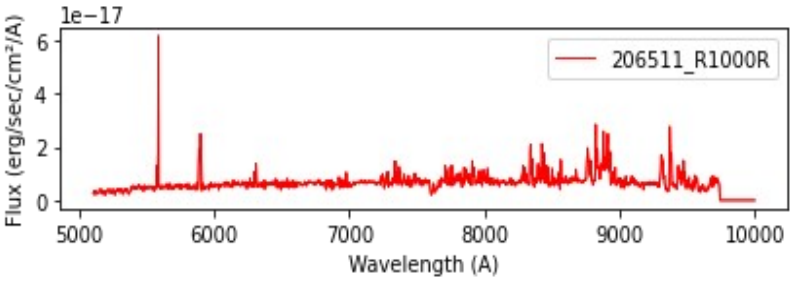

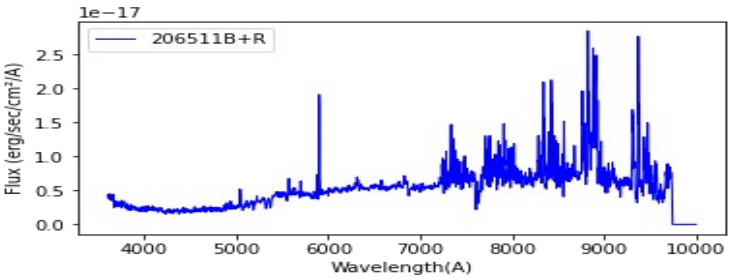

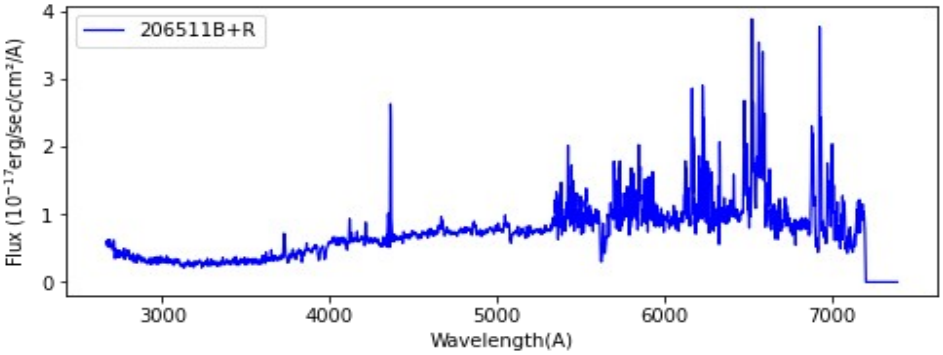

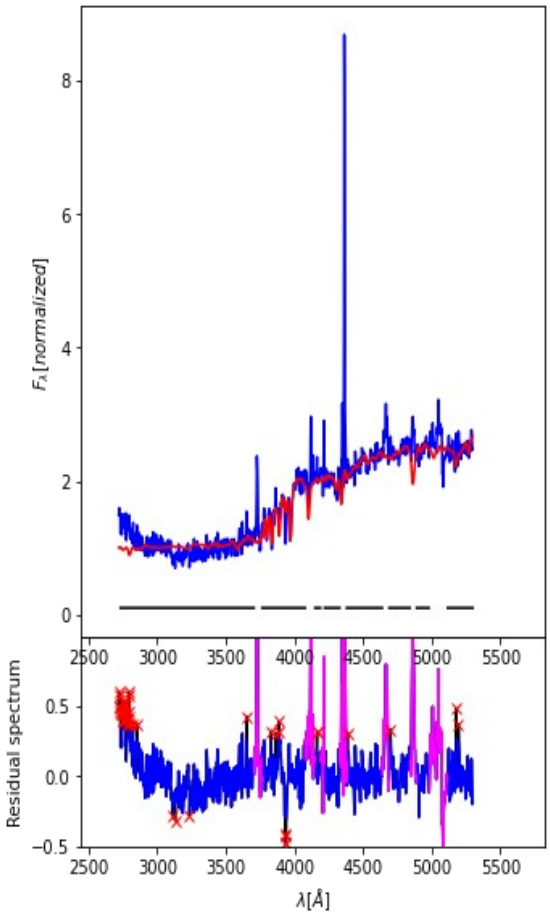

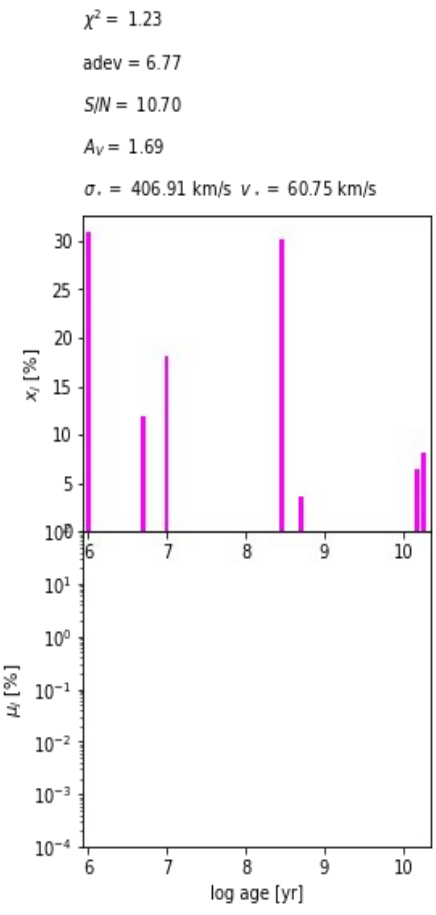

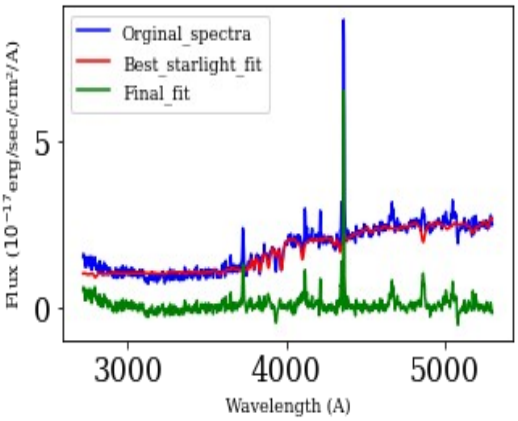

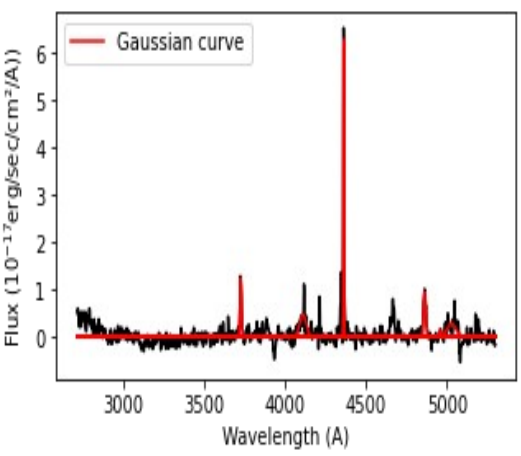

206529 (z_{spec} =0.887)

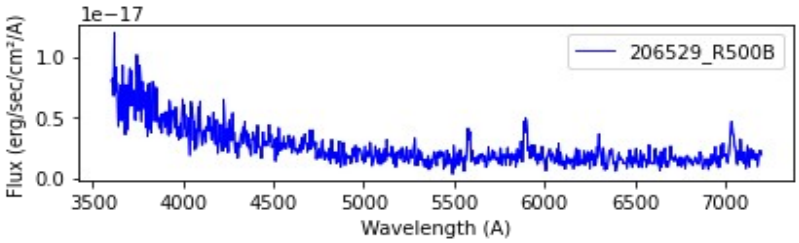

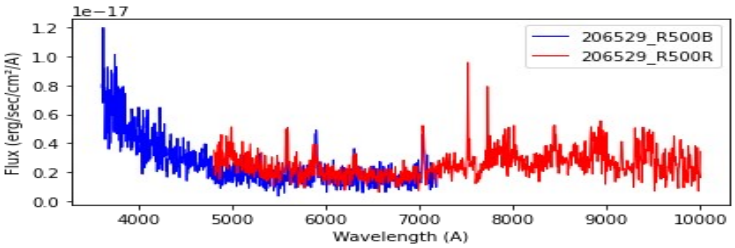

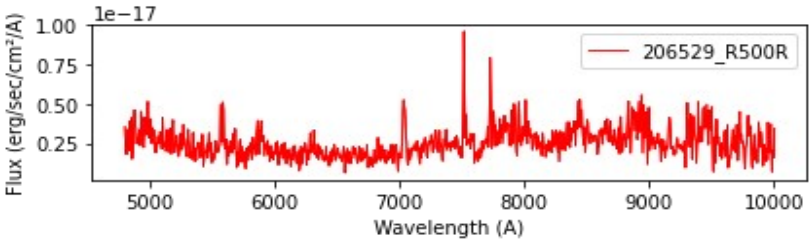

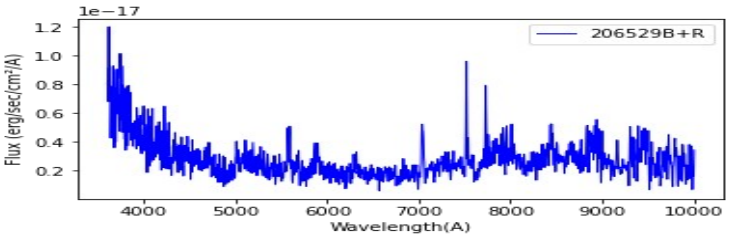

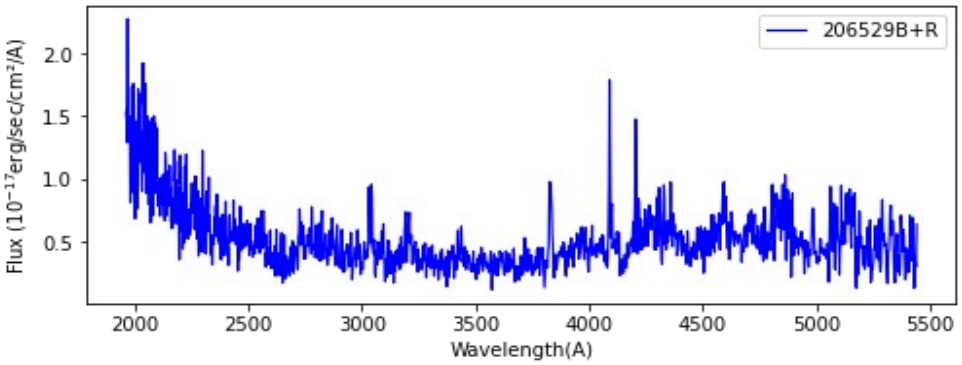

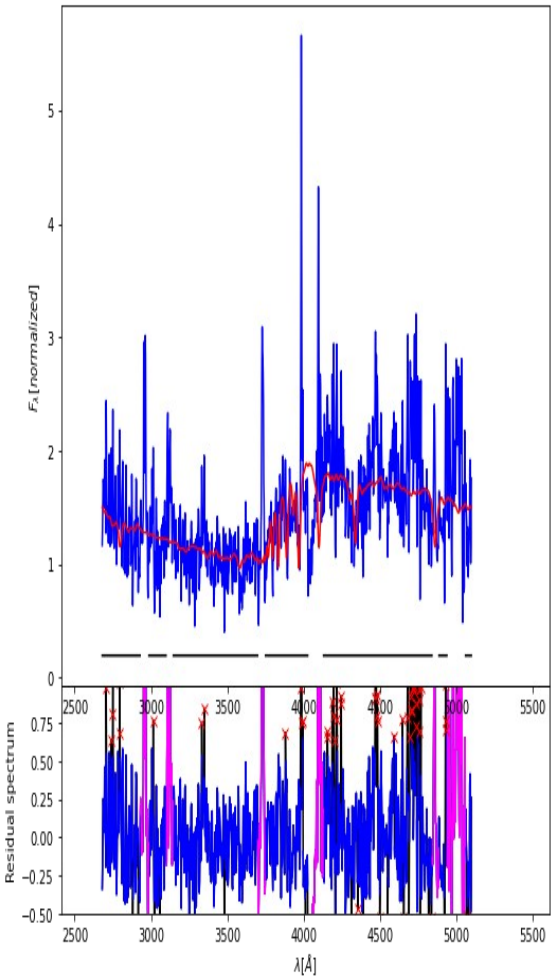

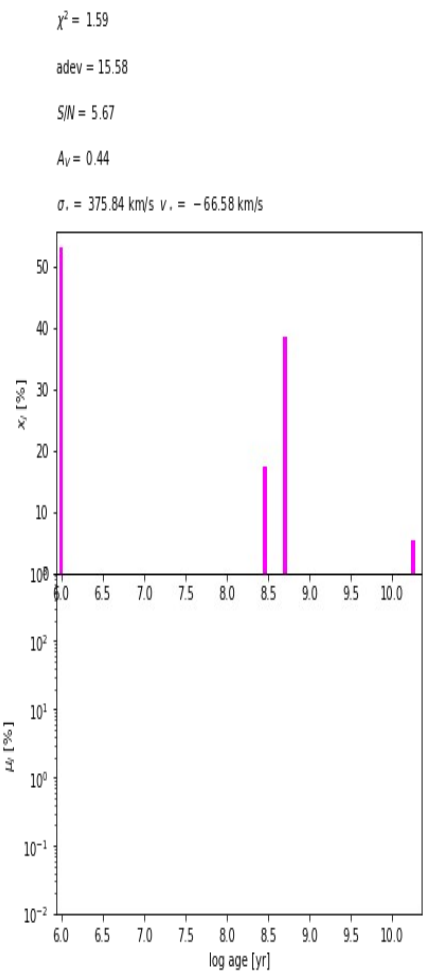

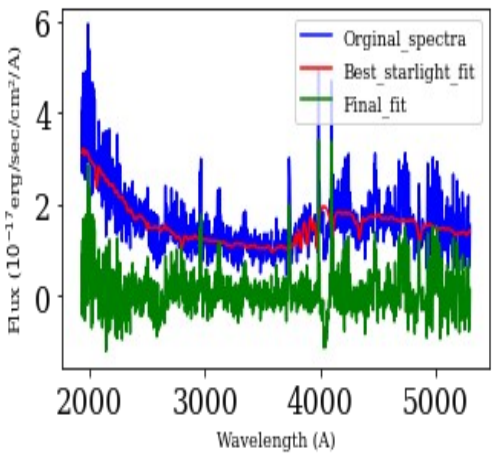

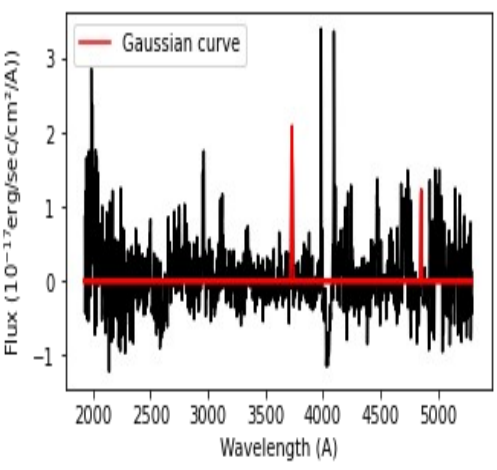

206545(z_{spec} =2.3679)

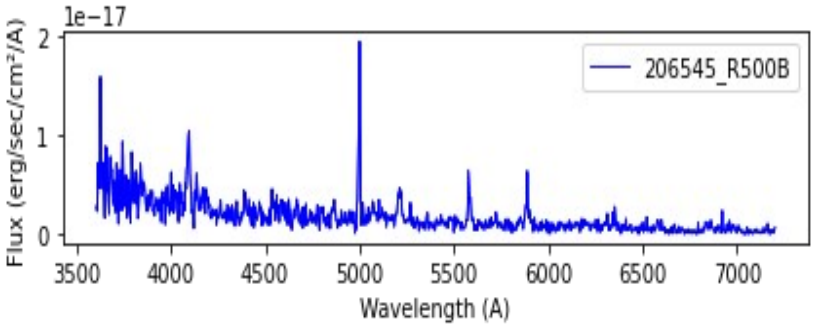

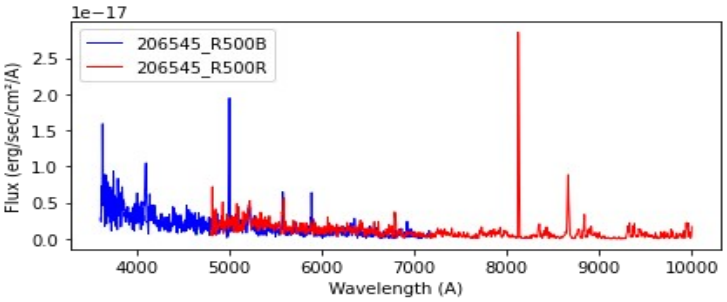

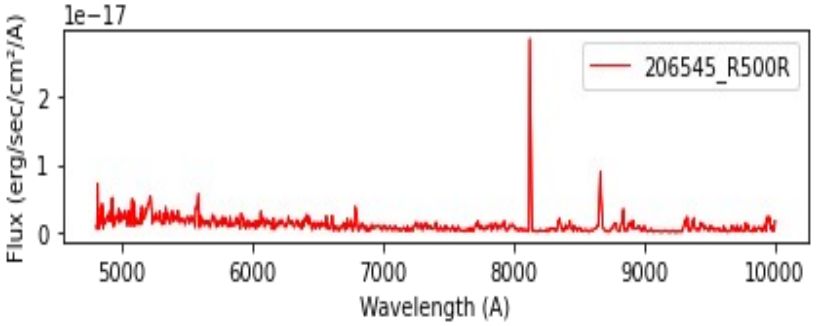

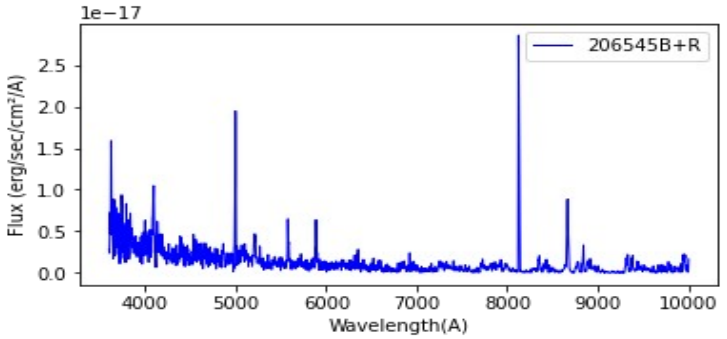

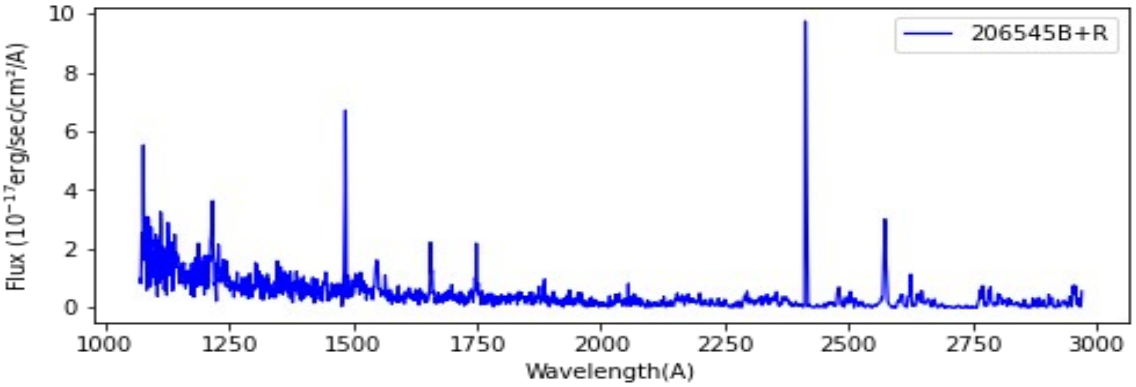

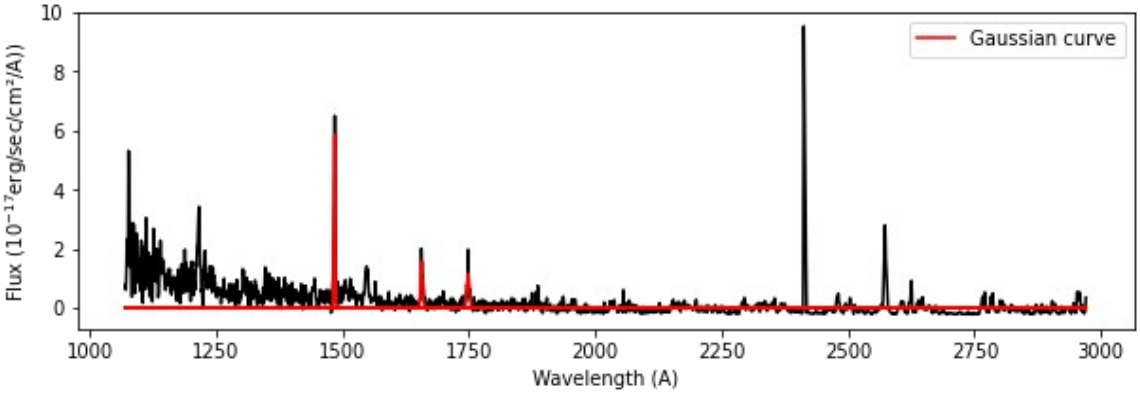

206547 (z_{spec} =0.788)

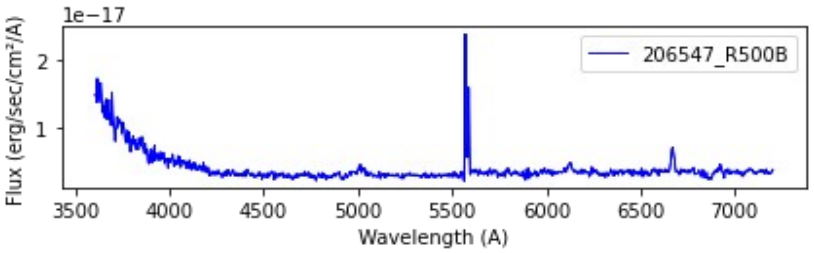

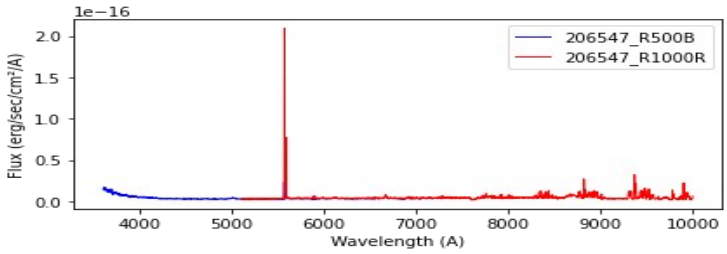

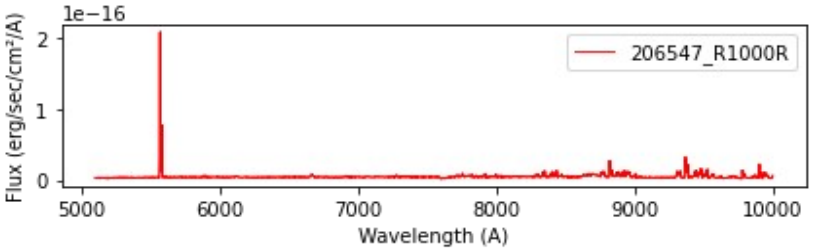

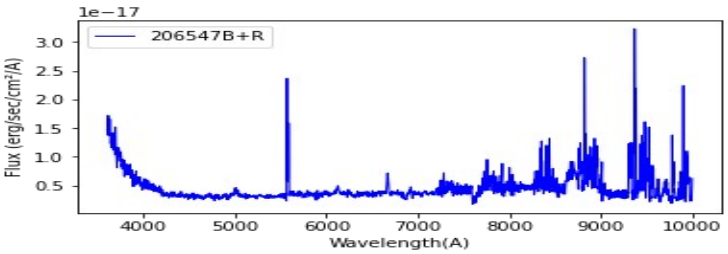

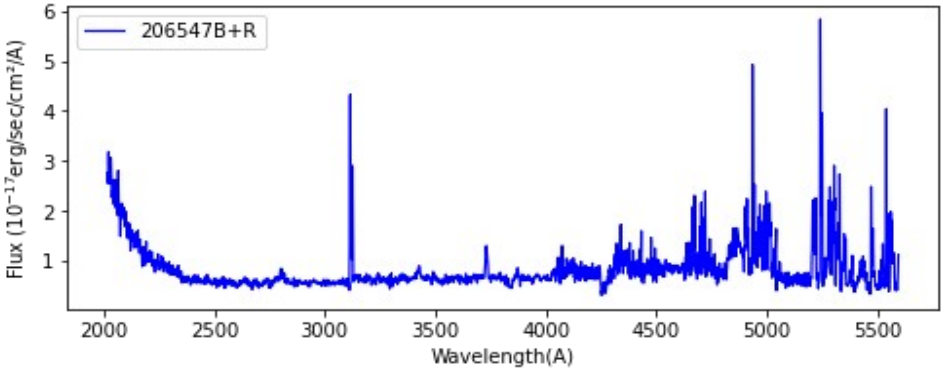

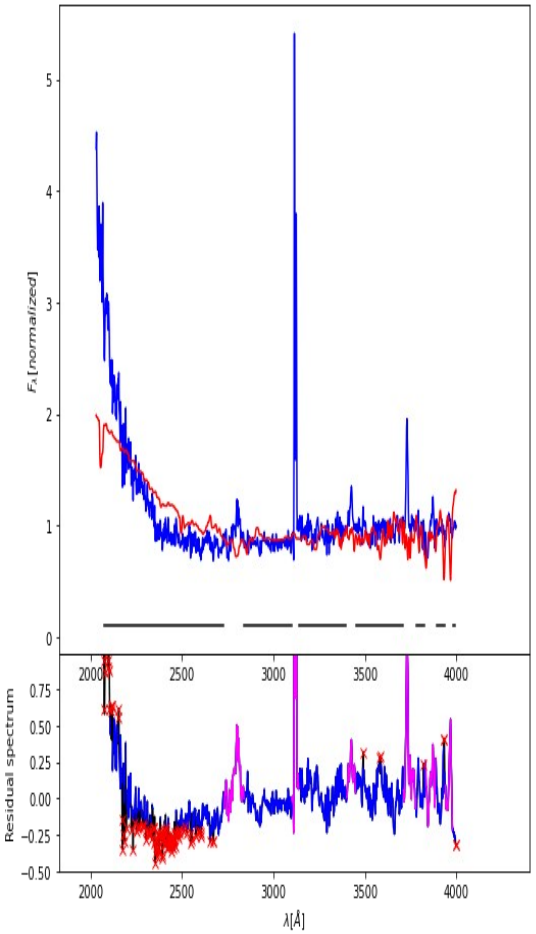

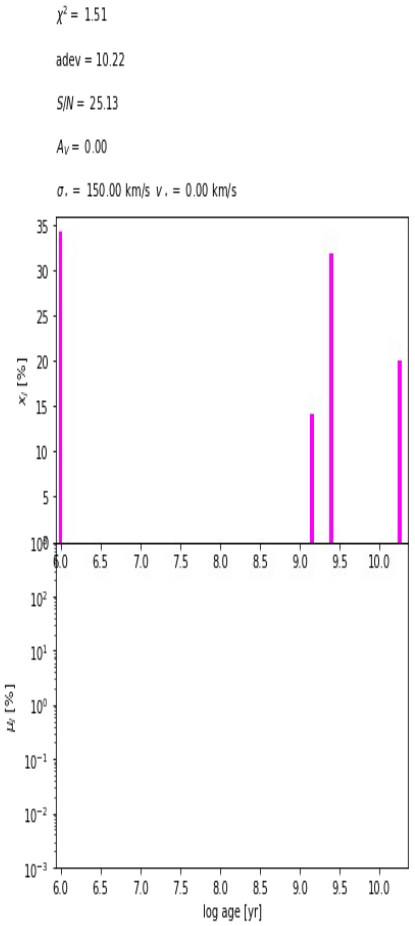

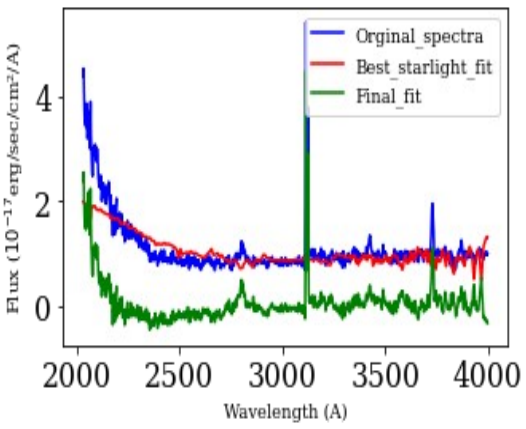

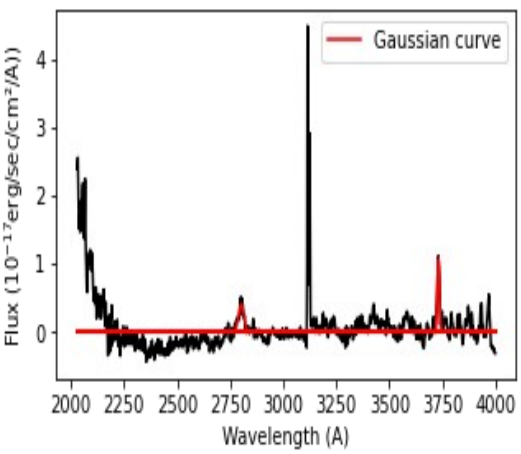

206583 (z_{spec} =0.8939)

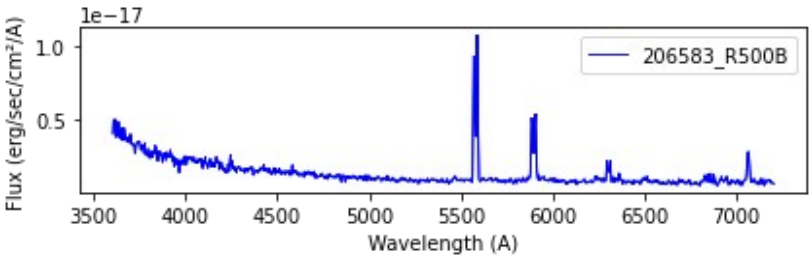

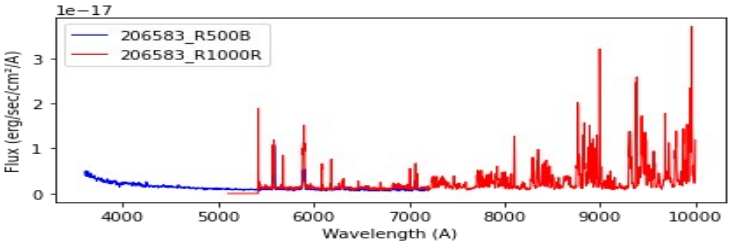

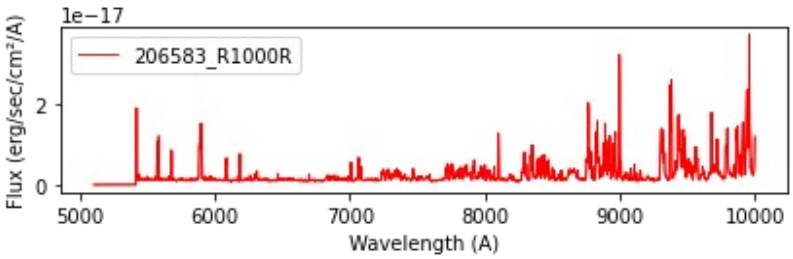

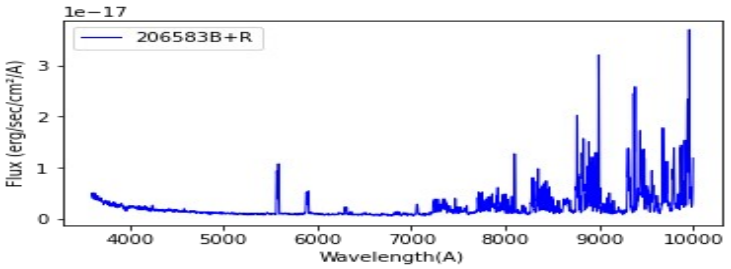

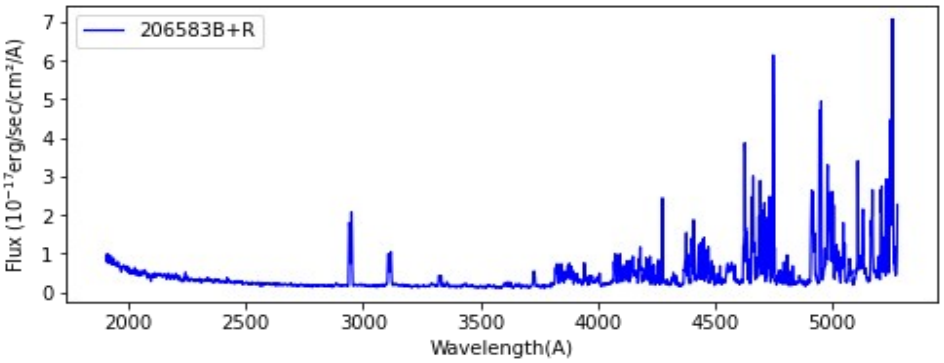

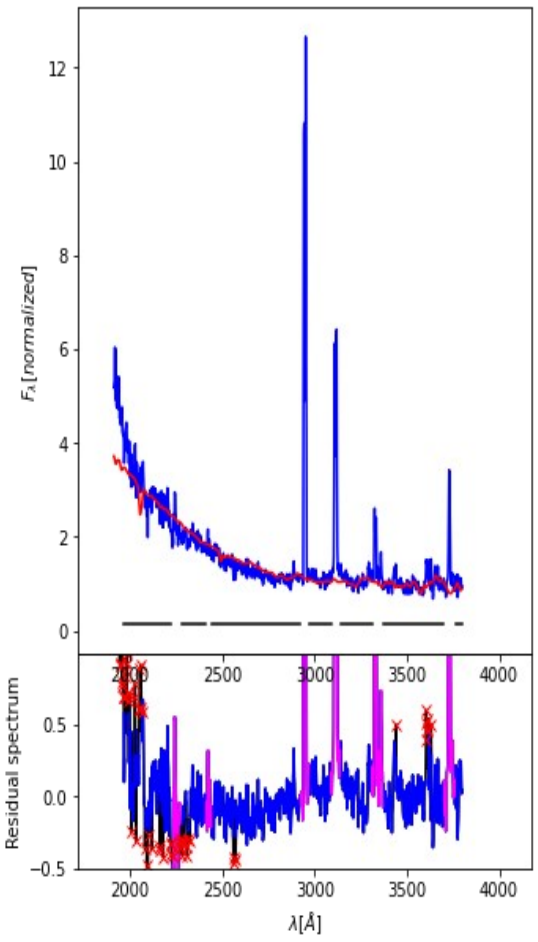

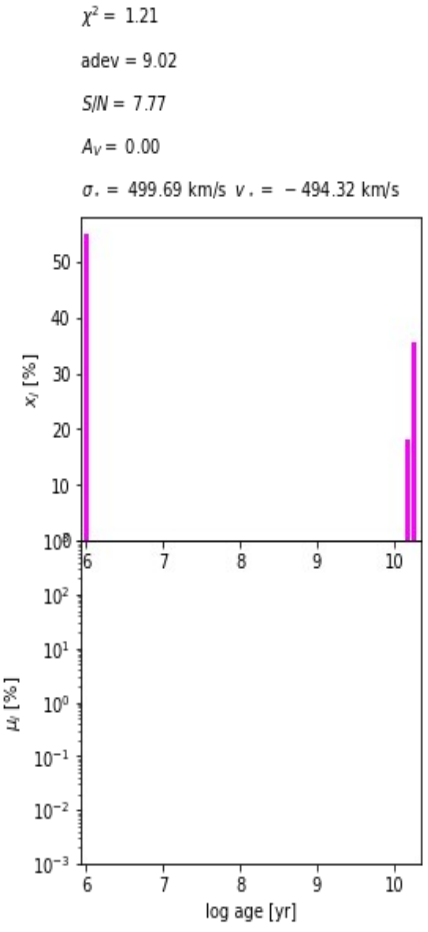

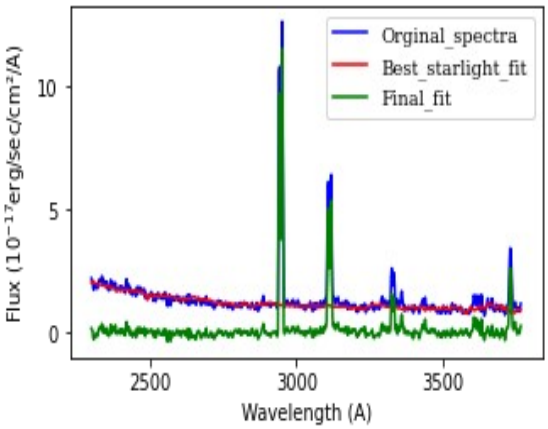

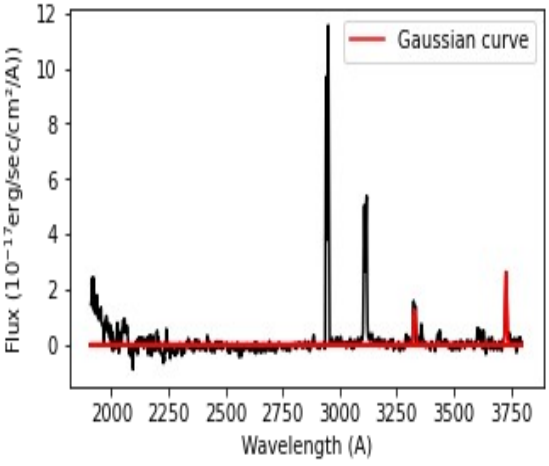

206586 (z_{spec} =1.447)

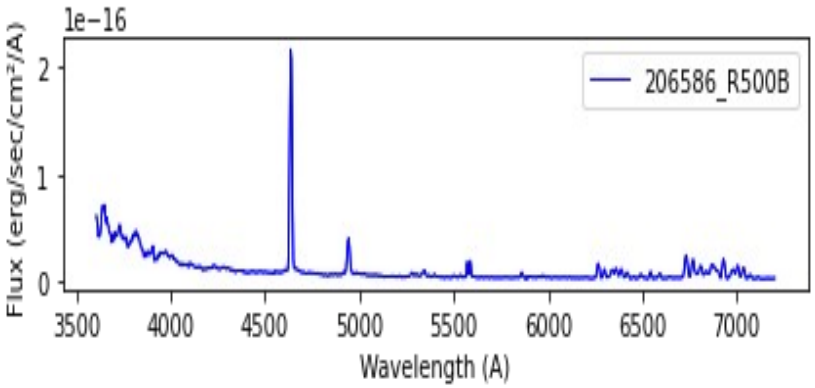

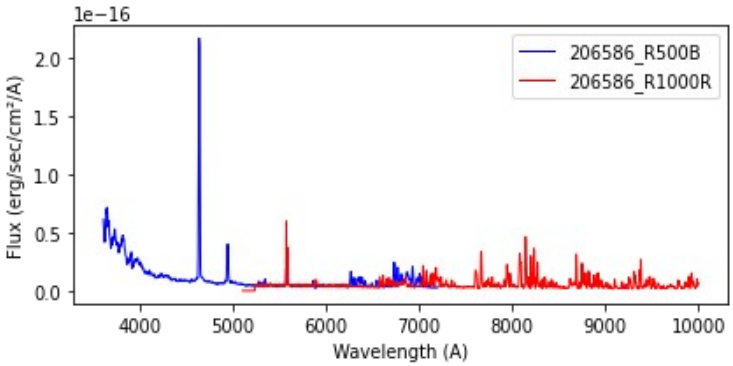

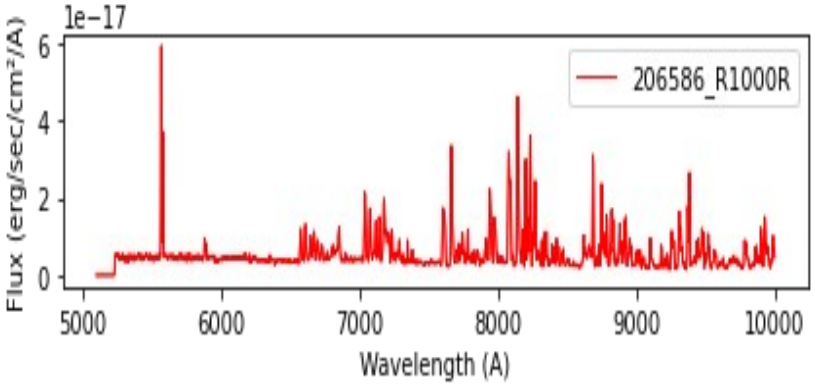

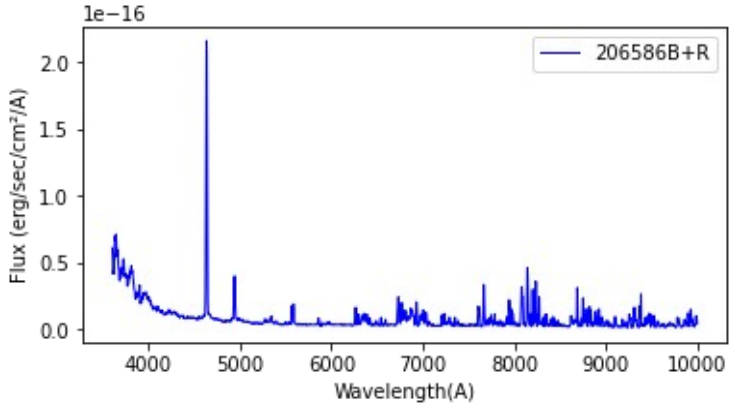

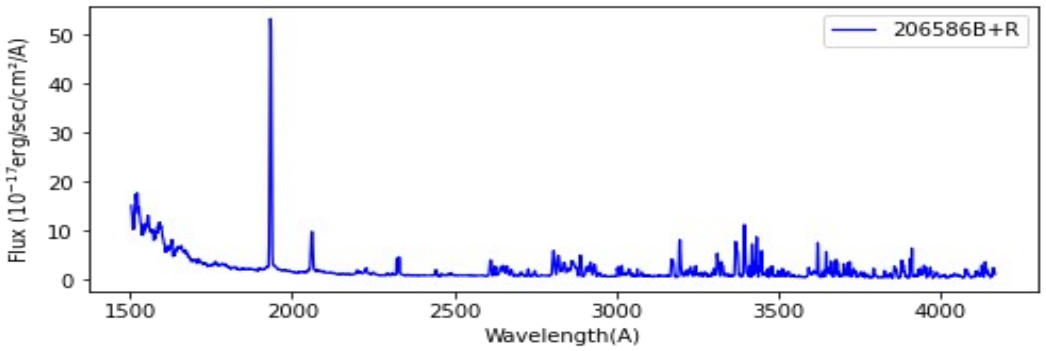

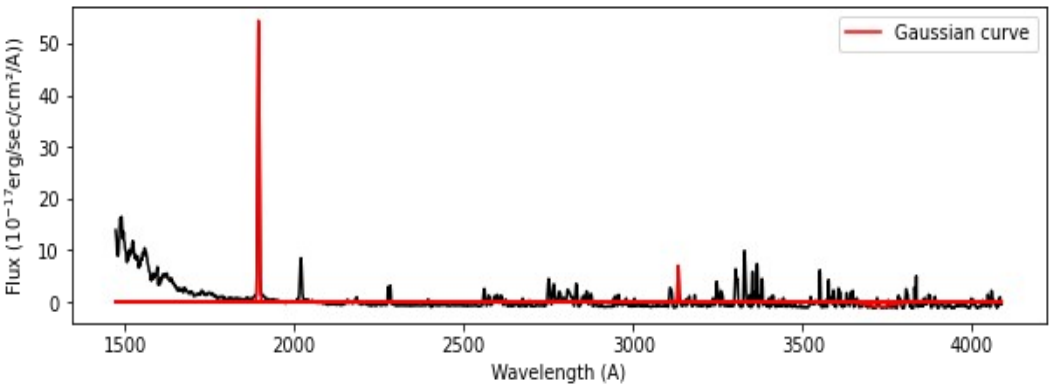

206589 (z_{spec} =0.6649)

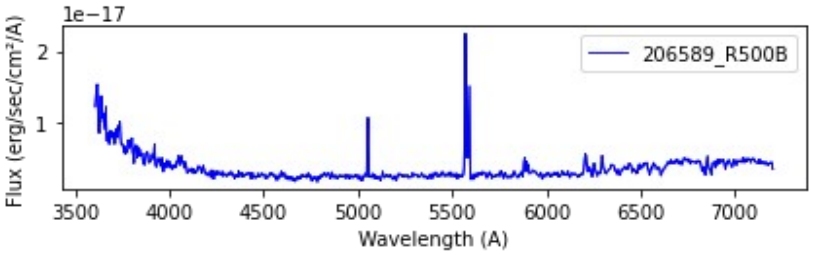

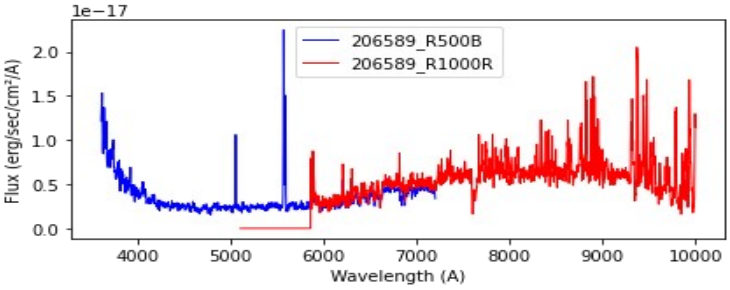

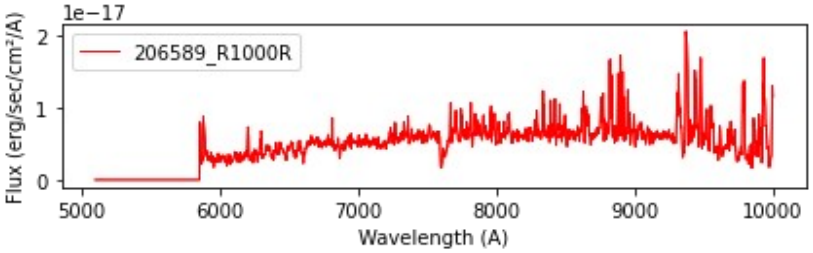

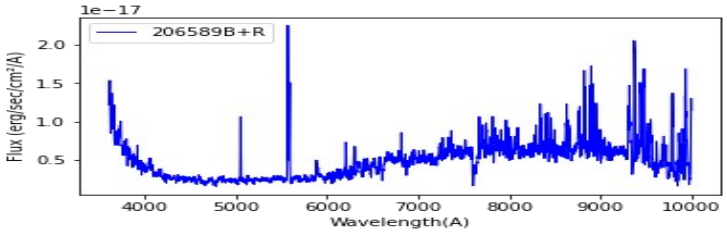

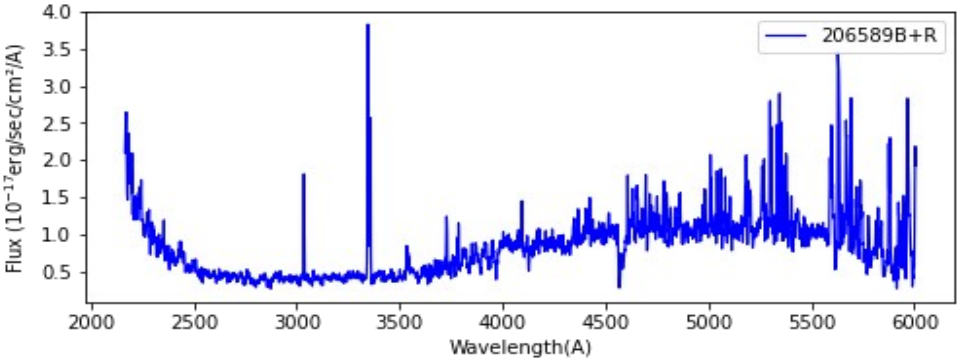

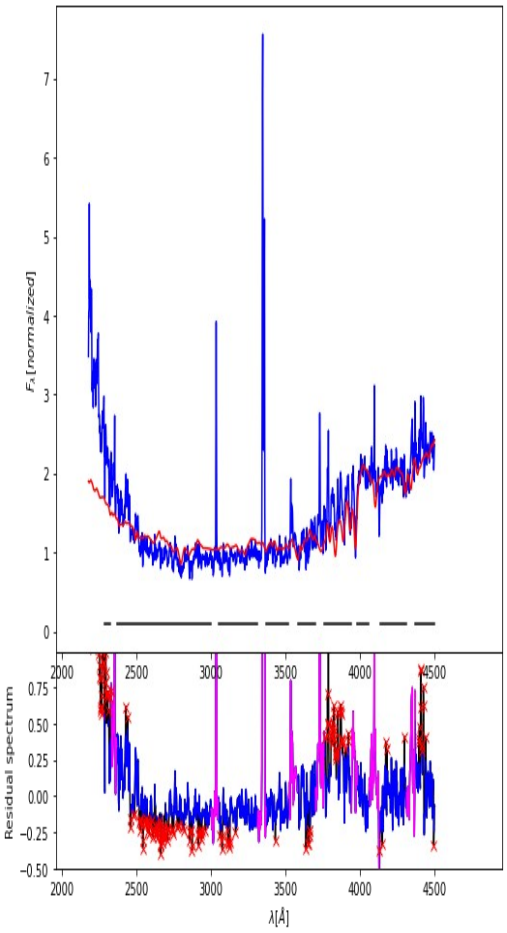

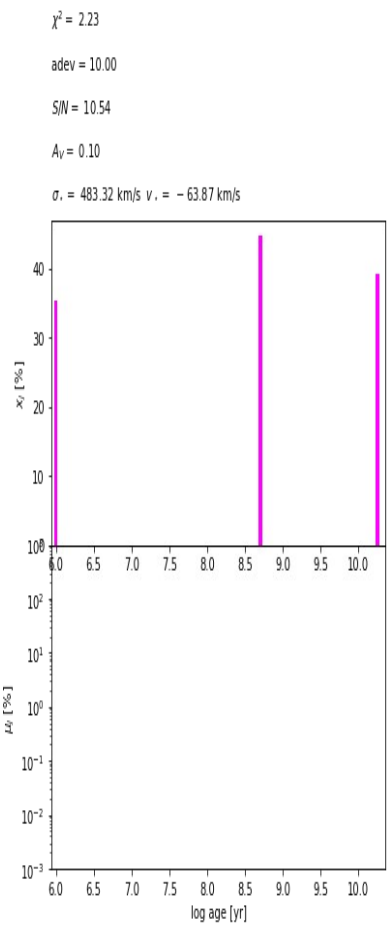

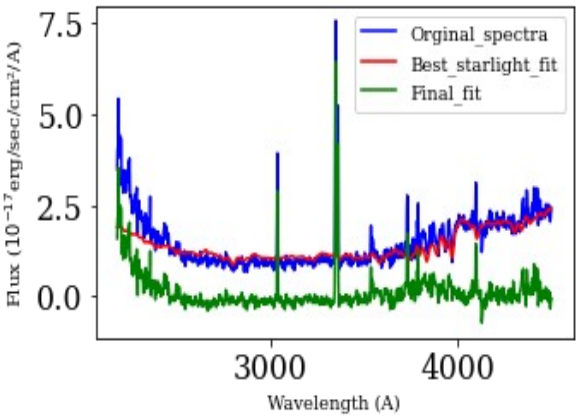

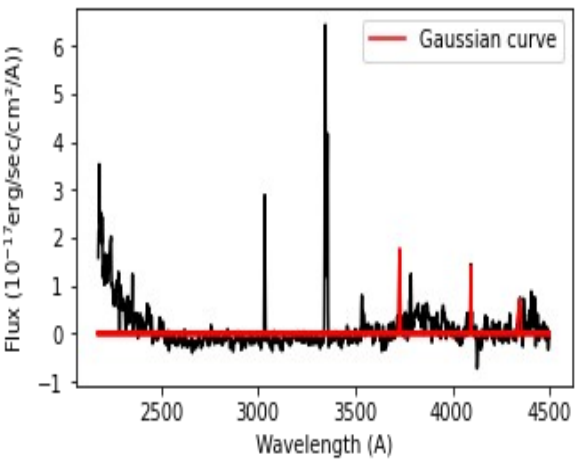

206598 (z_{spec} =0.9884)

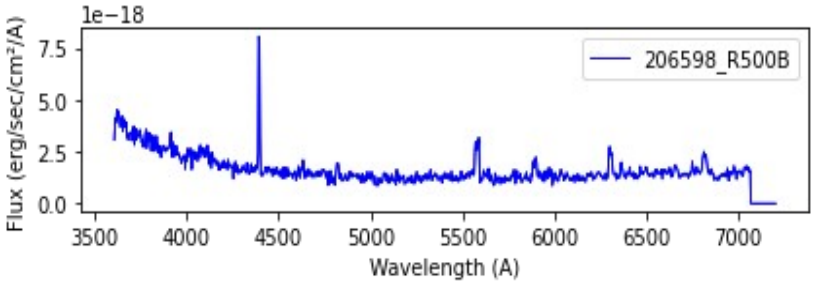

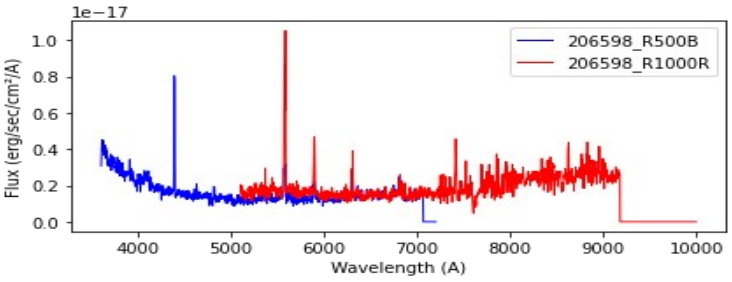

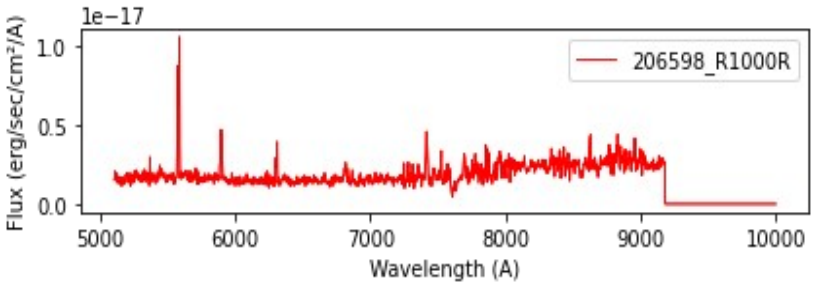

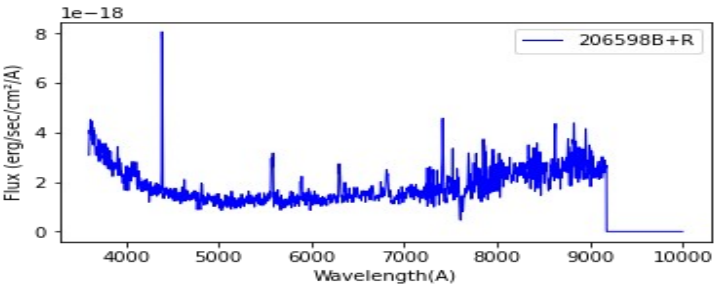

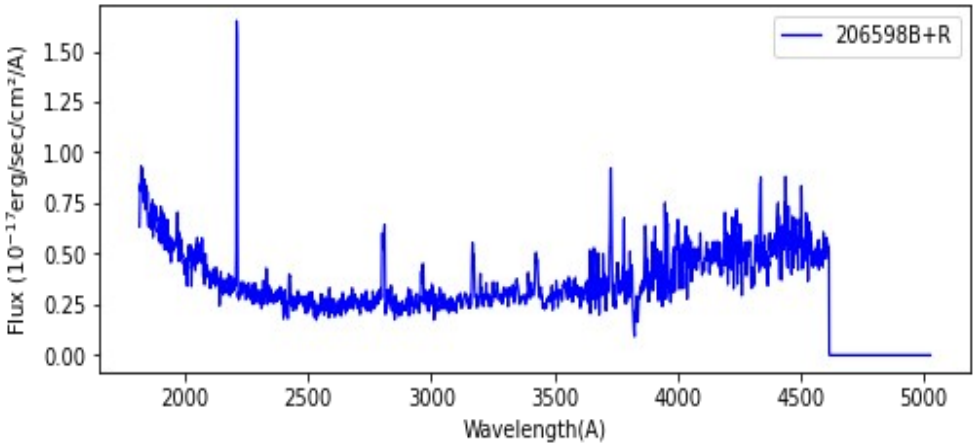

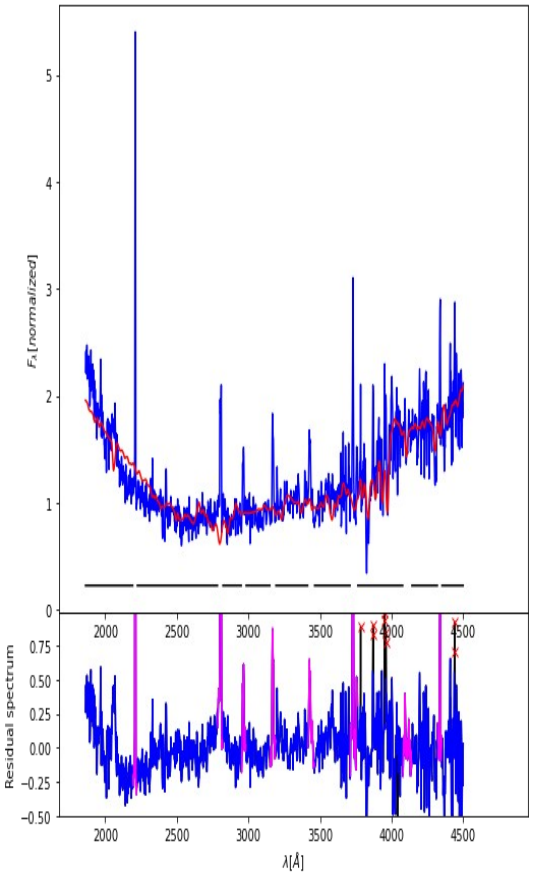

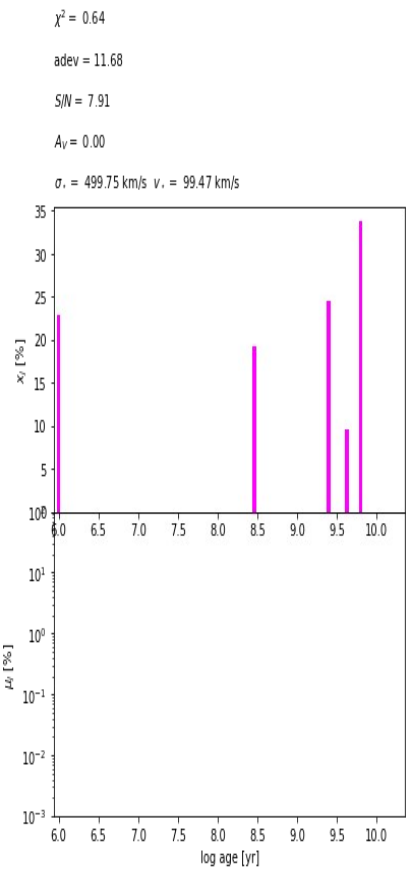

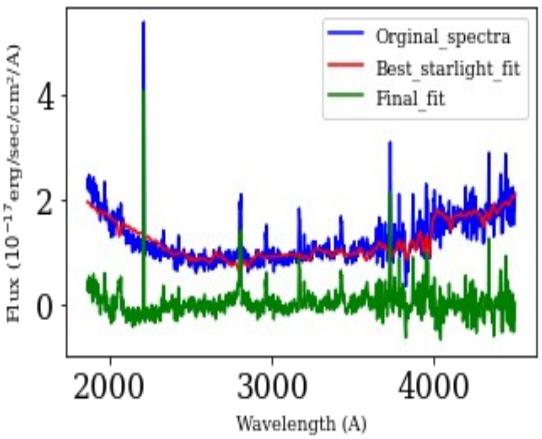

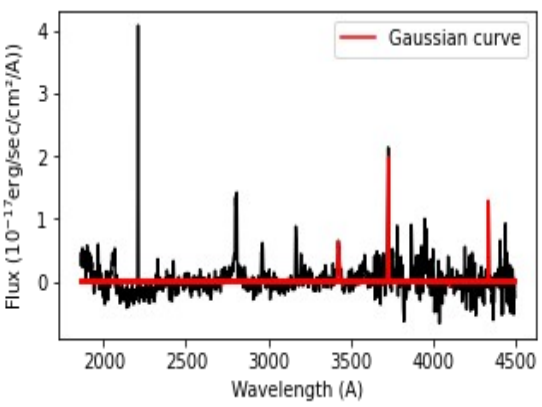

206603 (z_{spec} =2.5185)

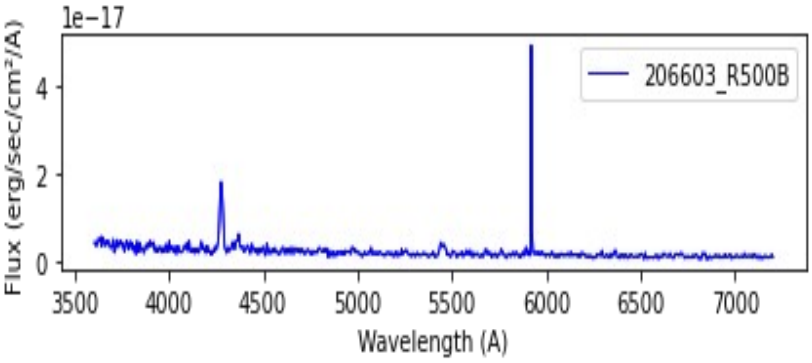

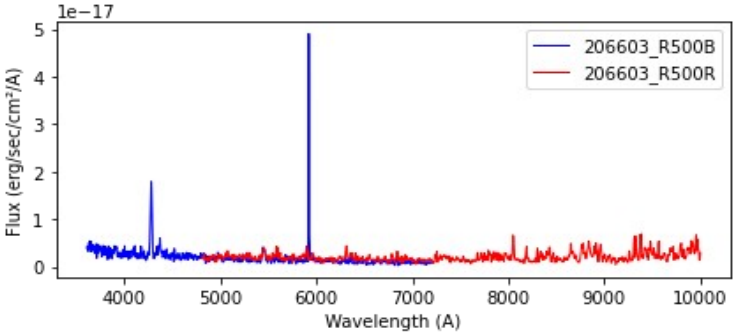

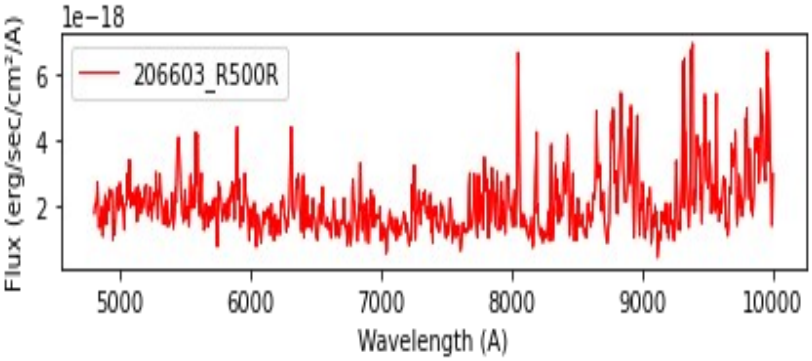

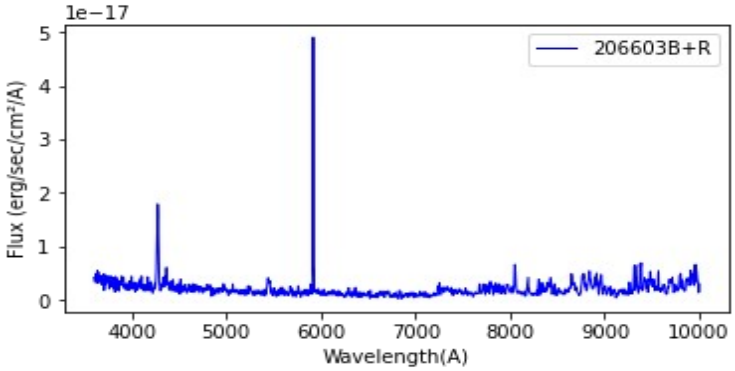

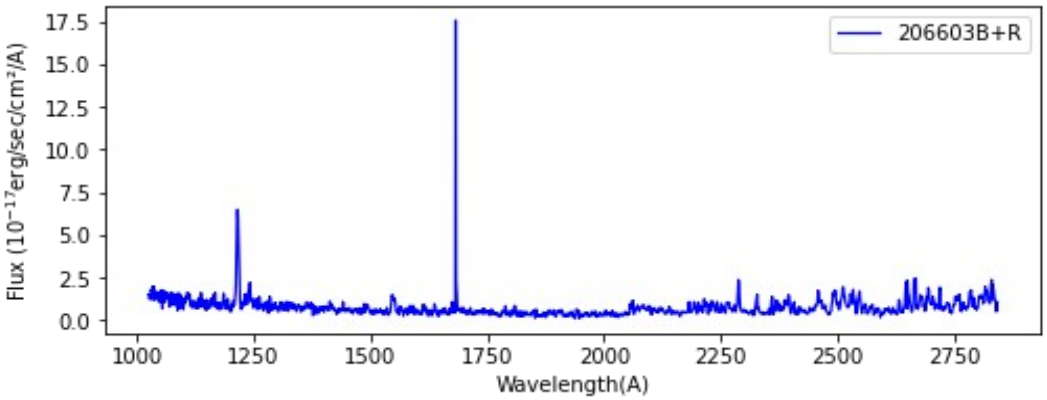

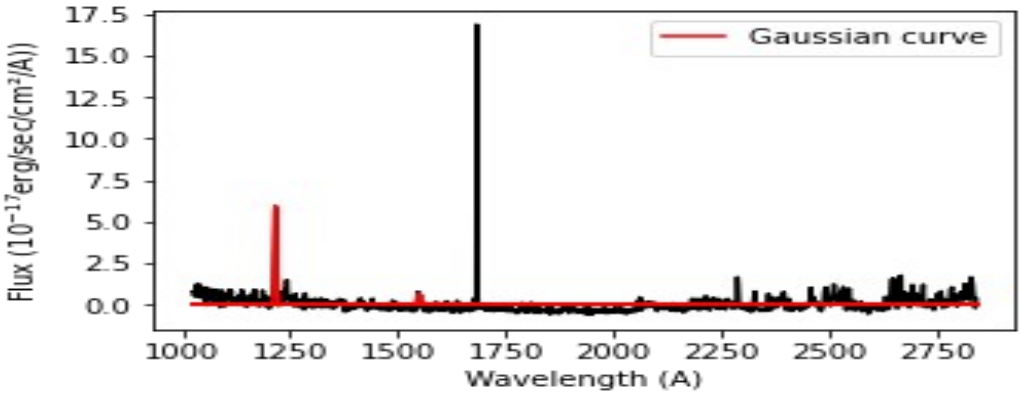

206608 (z_{spec} =0.695)

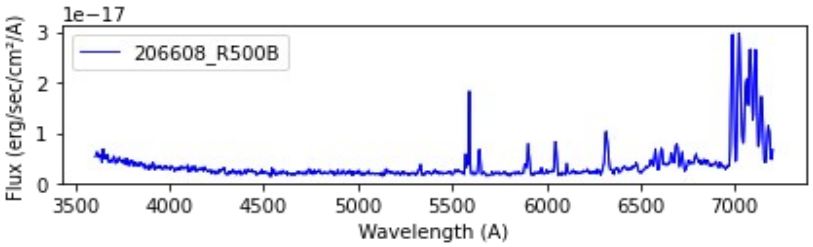

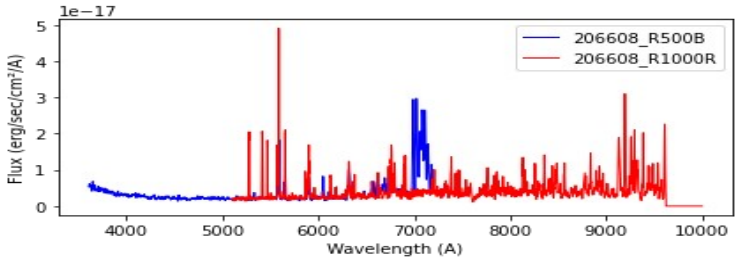

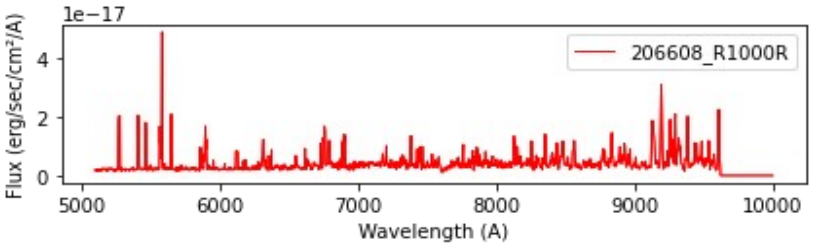

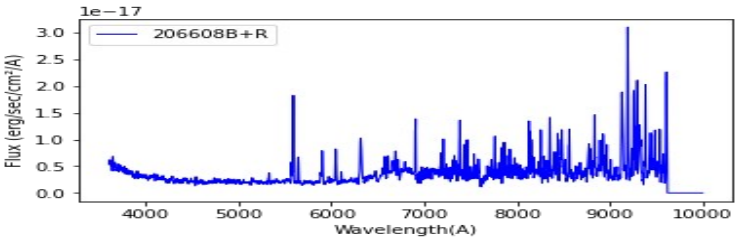

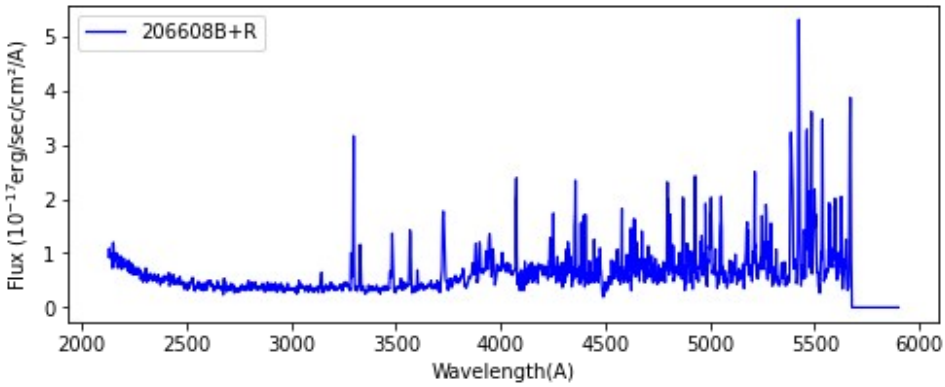

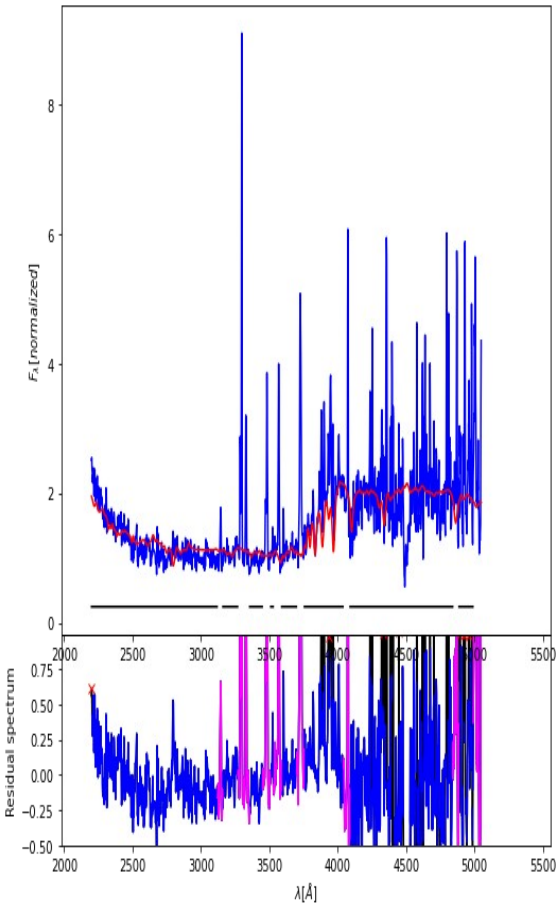

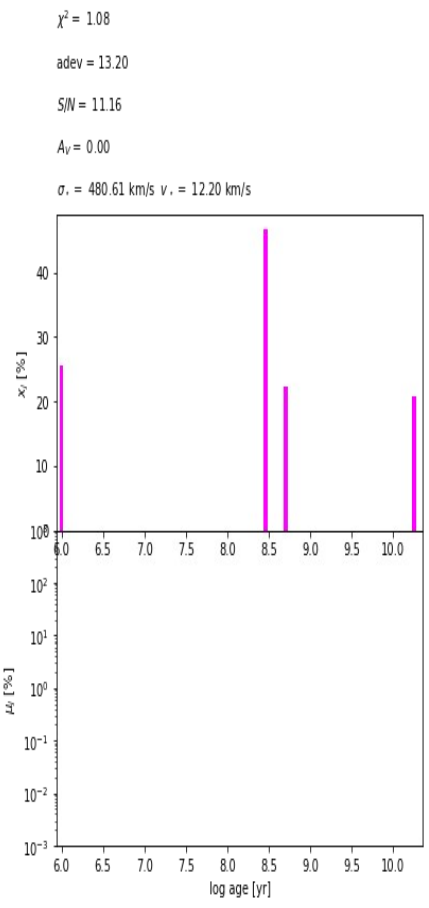

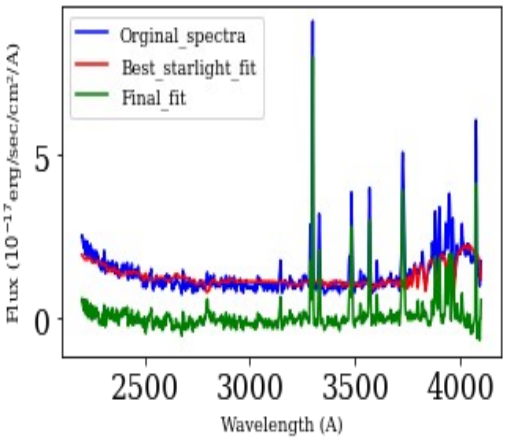

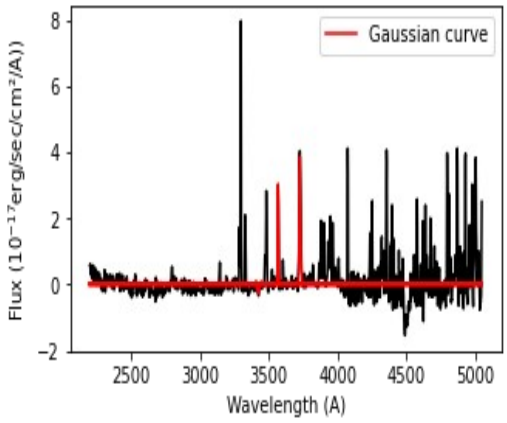

206626 (z_{spec} =0.3527)

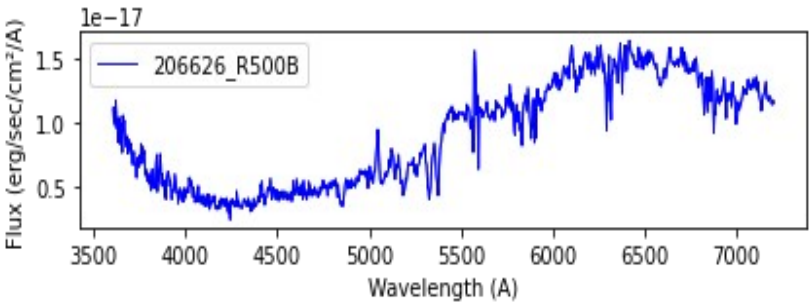

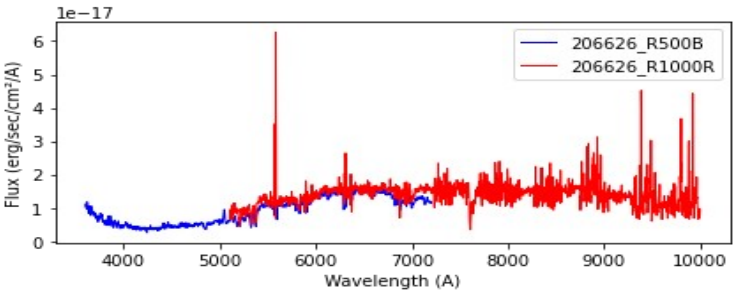

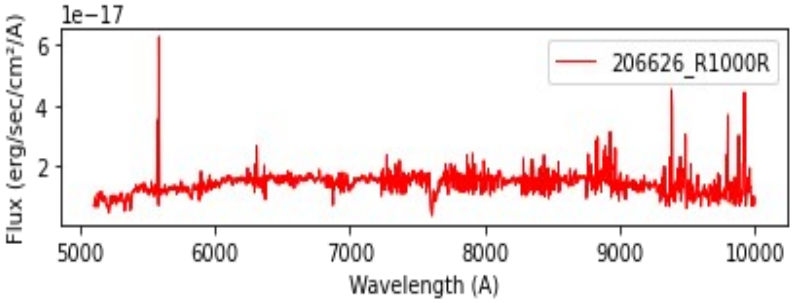

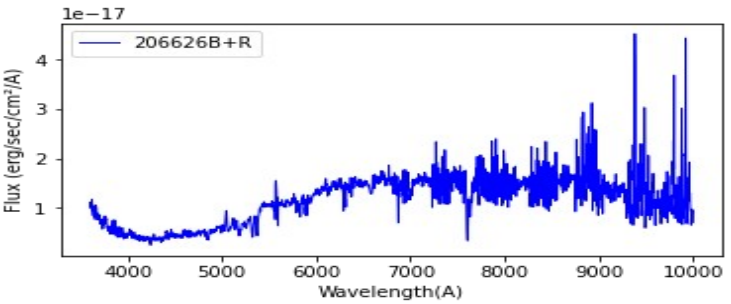

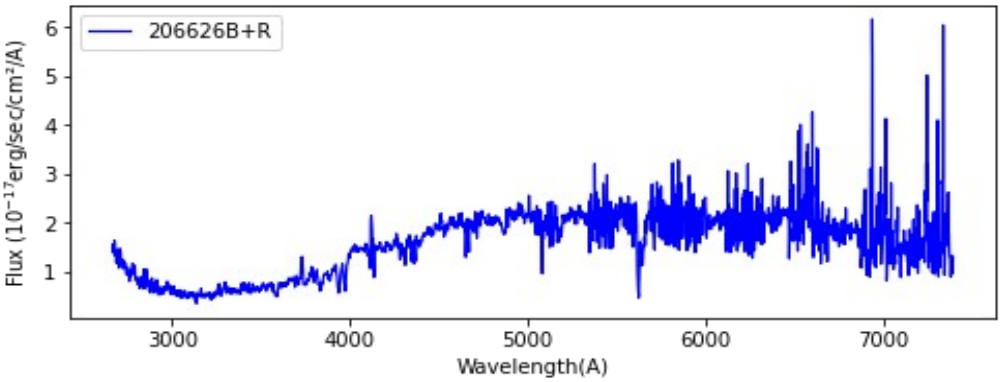

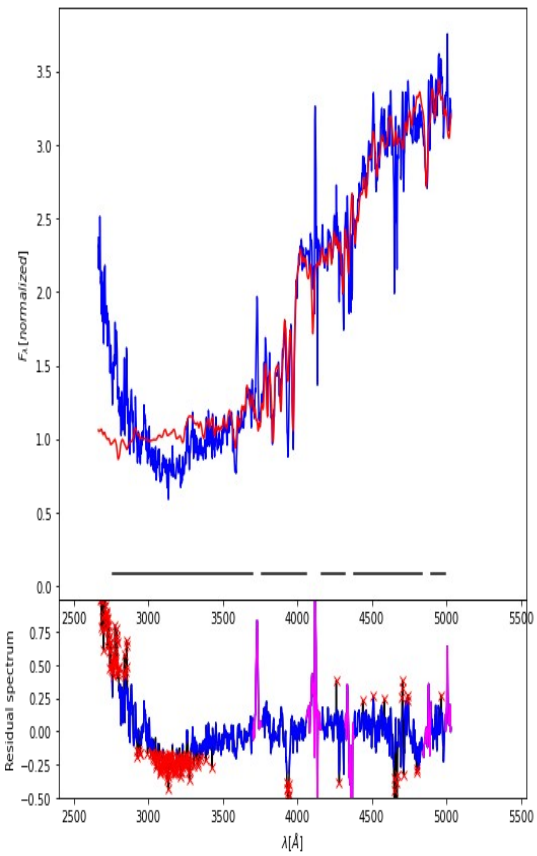

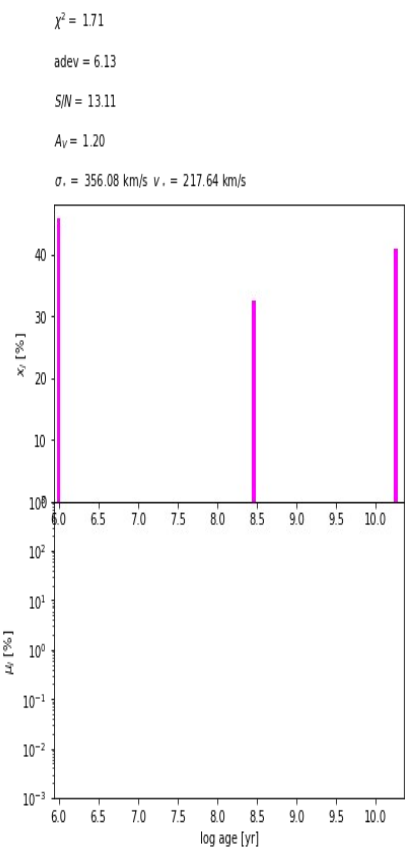

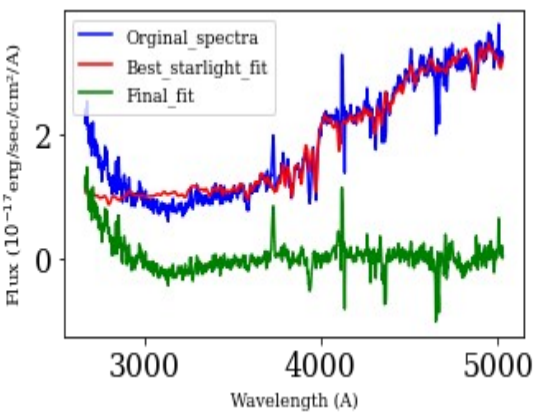

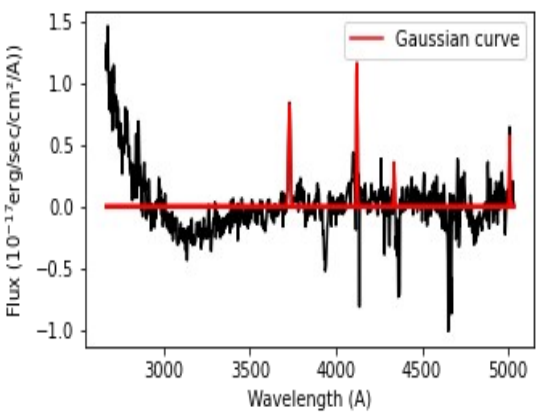

206650 (z_{spec} =0.1499)

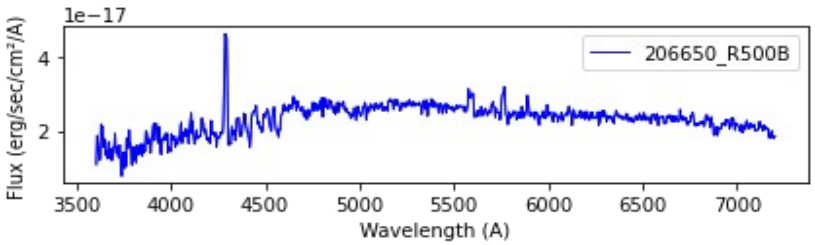

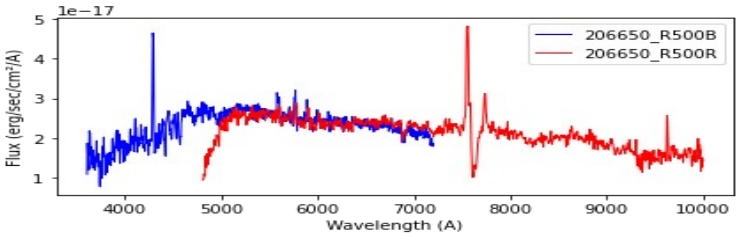

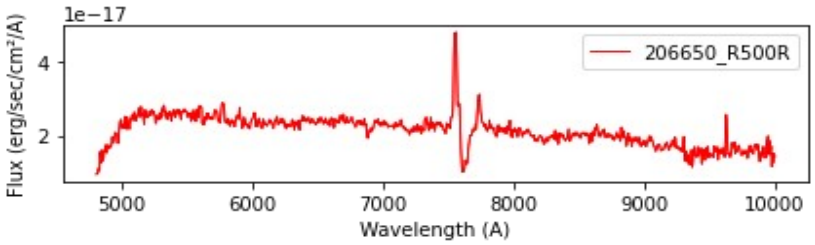

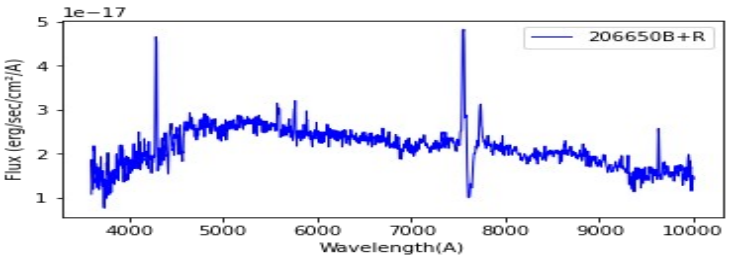

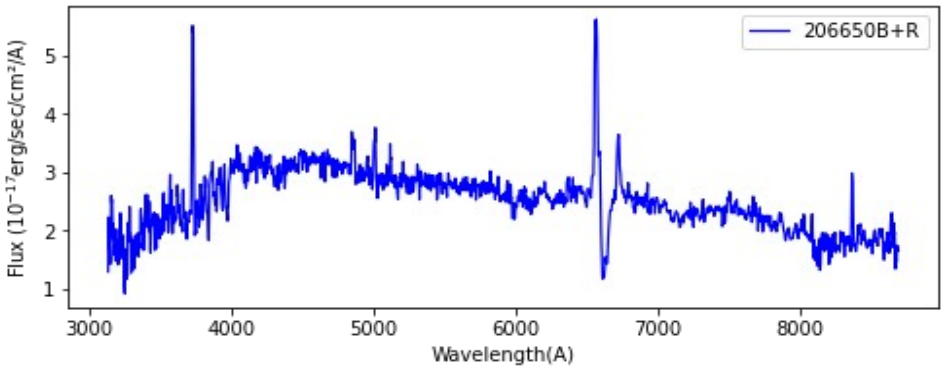

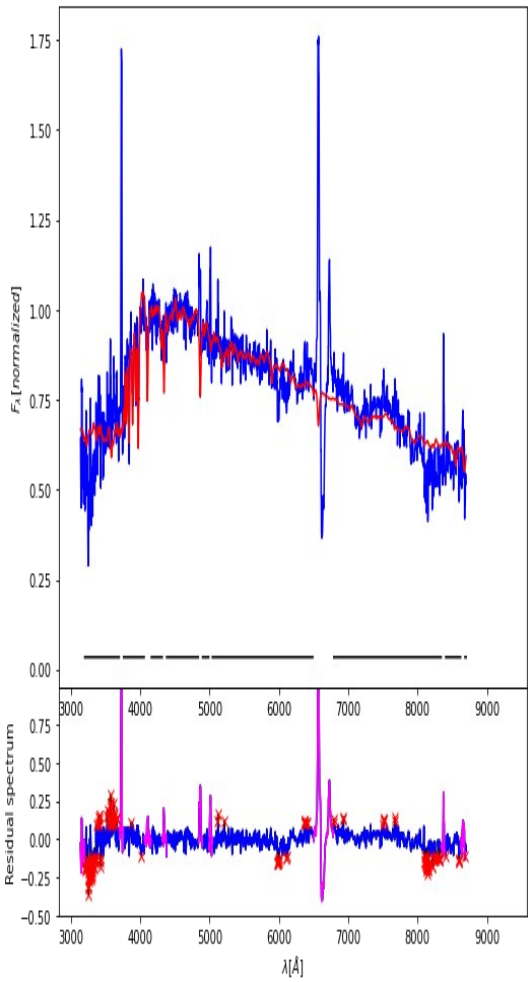

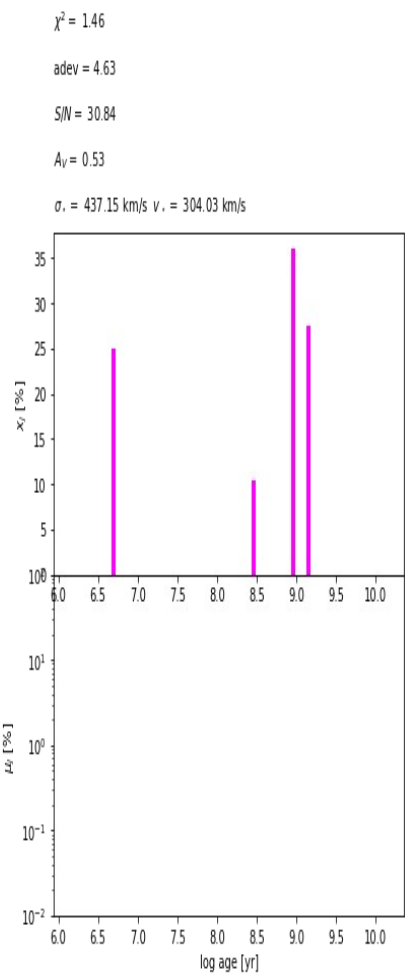

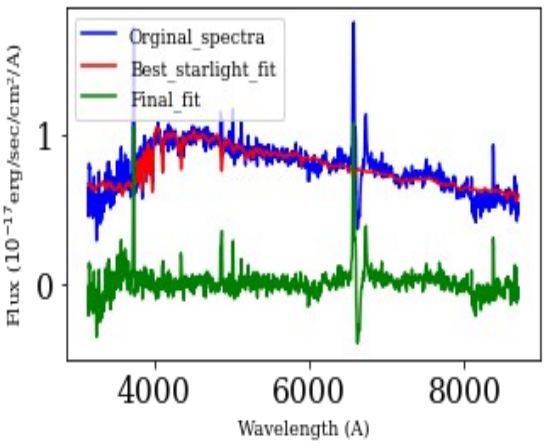

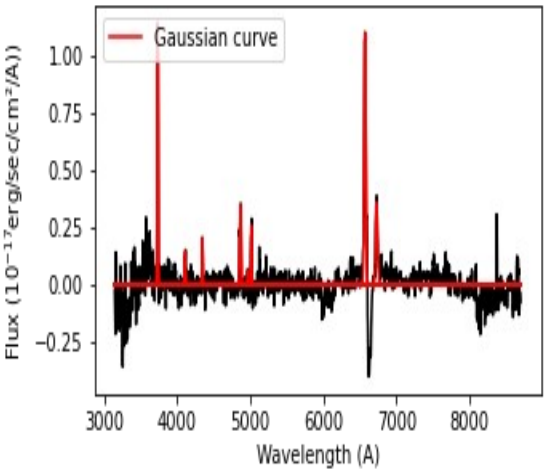

206651 (z_{spec} =0.802)

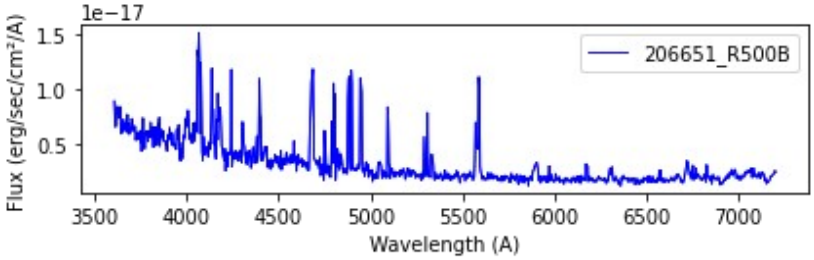

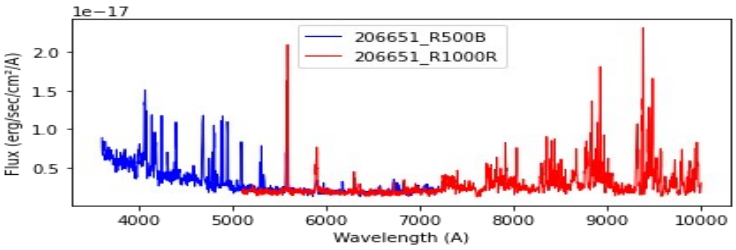

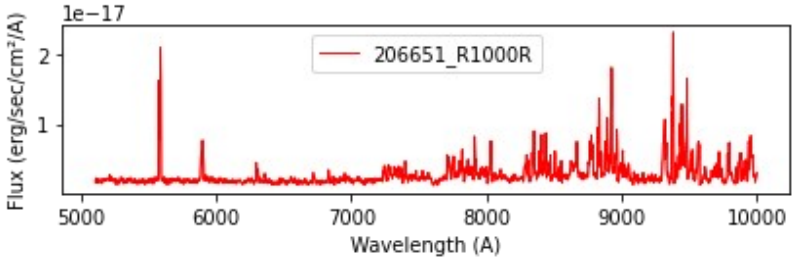

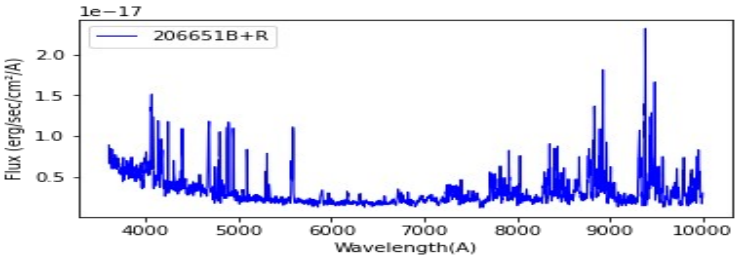

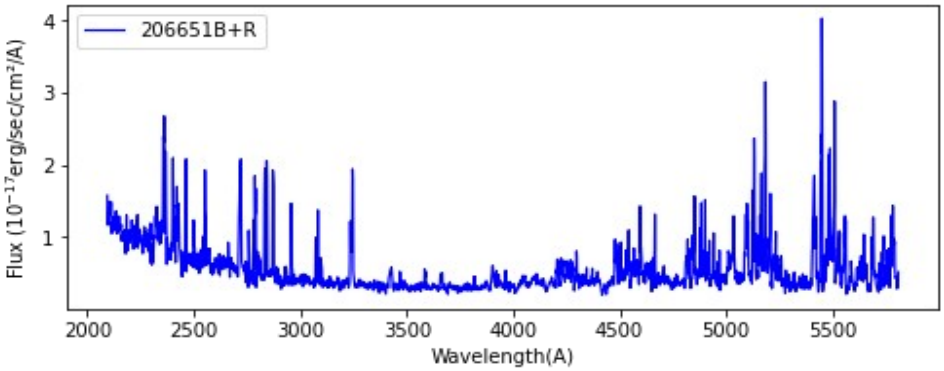

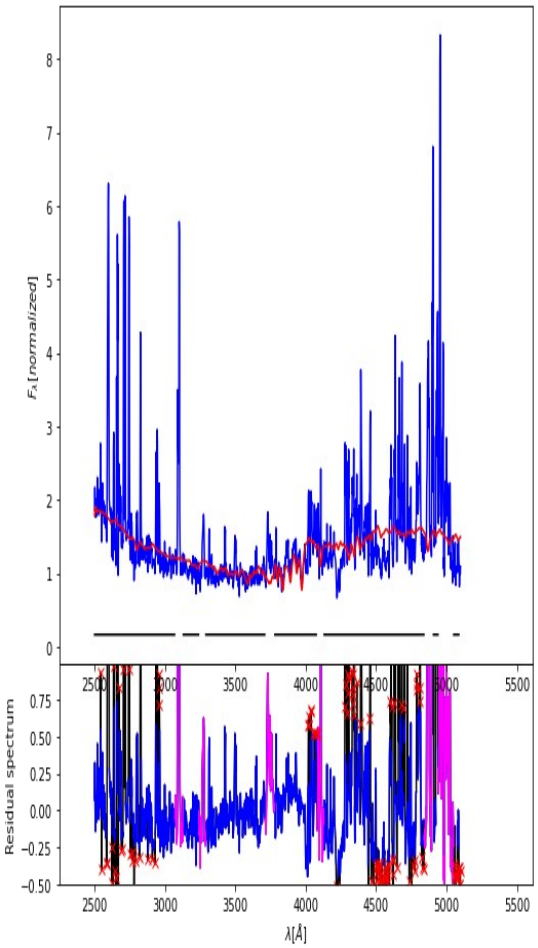

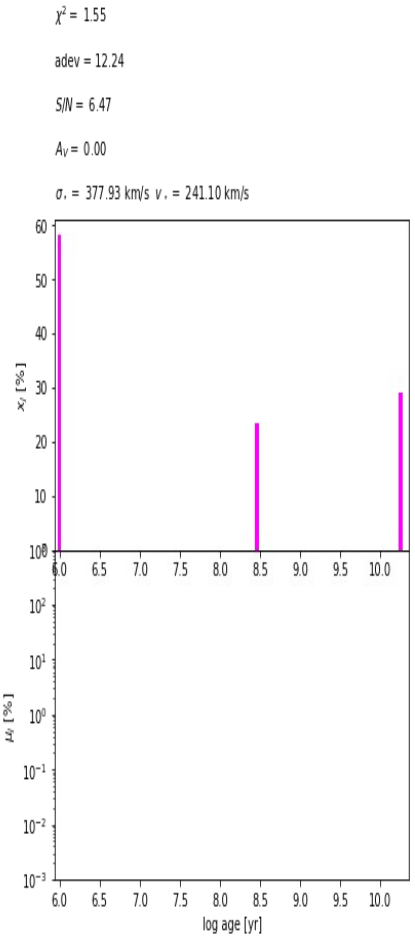

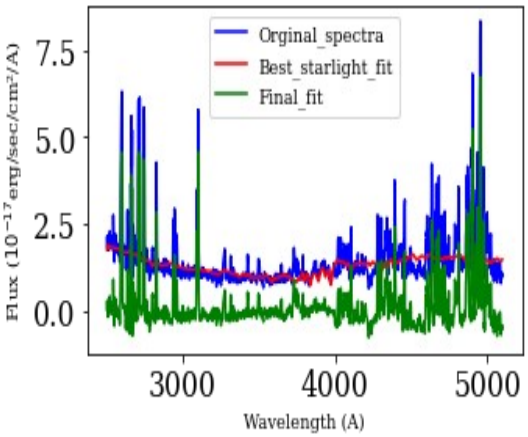

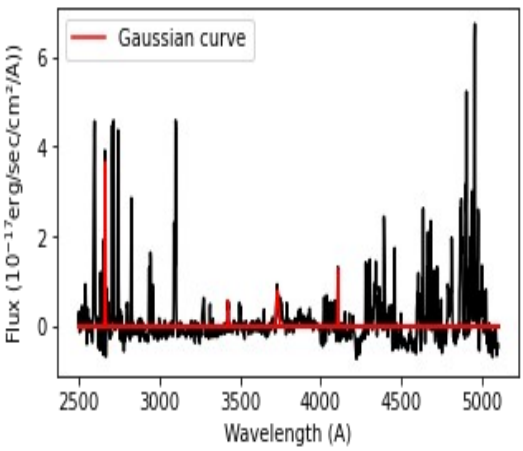

206684 (z_{spec} =0.876)

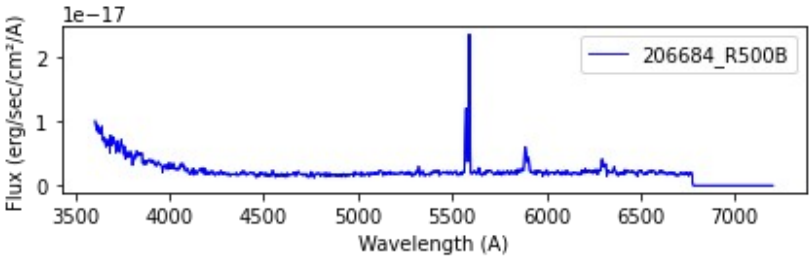

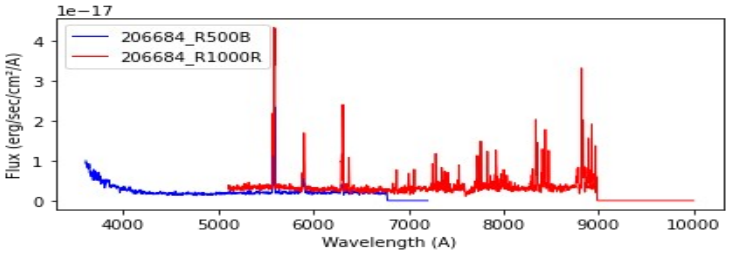

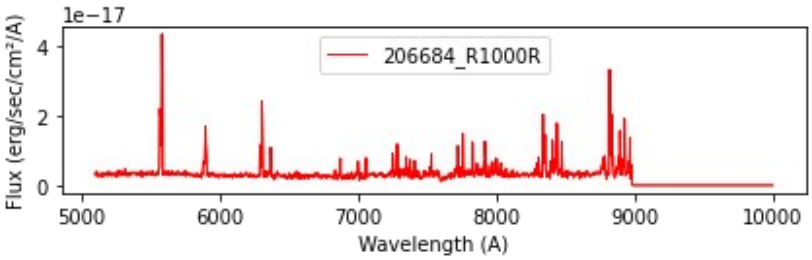

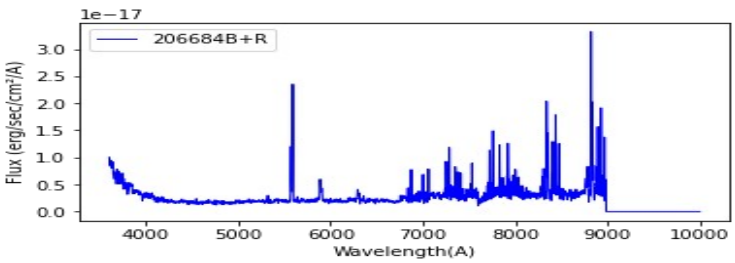

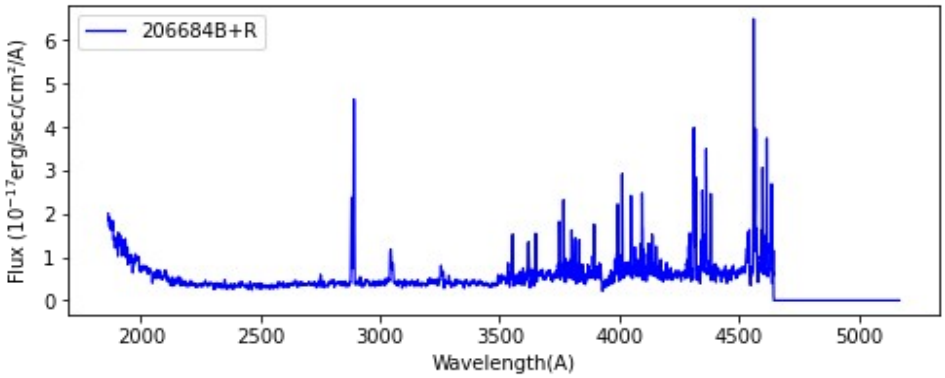

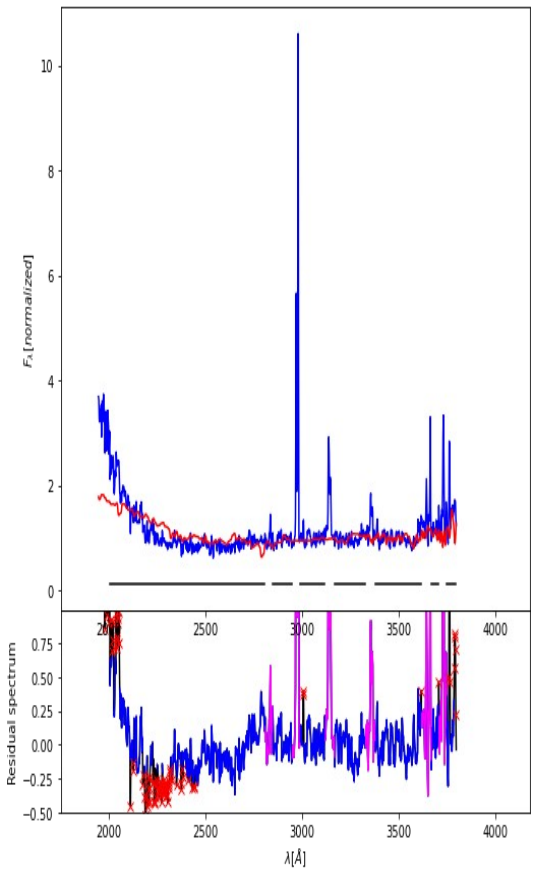

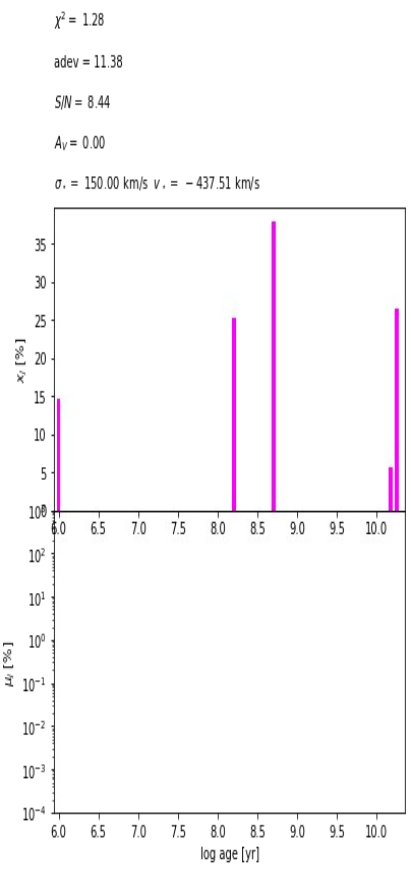

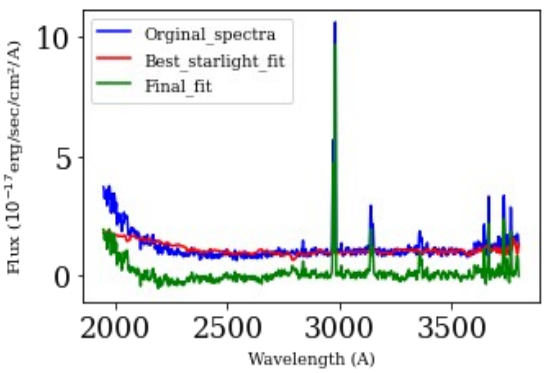

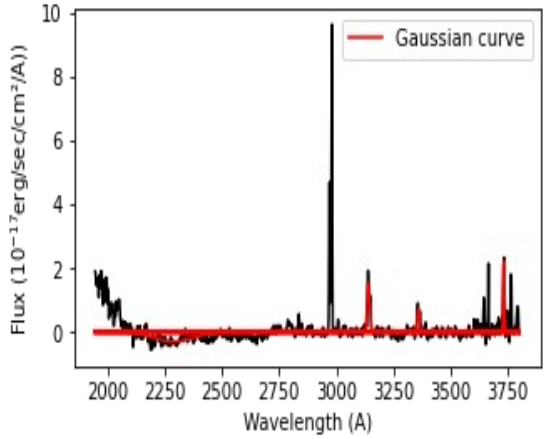

206776 (z_{spec} =0.2033)